

# Chasing metamorphic supernovae with Zwicky Transient Facility, SEDM-KP, and AI

Thesis by  
Yashvi Sharma

In Partial Fulfillment of the Requirements for the  
Degree of  
Doctor of Philosophy

The logo for the California Institute of Technology (Caltech), featuring the word "Caltech" in a bold, orange, sans-serif font.

CALIFORNIA INSTITUTE OF TECHNOLOGY  
Pasadena, California

2025  
Defended April 25, 2025

© 2025

Yashvi Sharma

ORCID: 0000-0003-4531-1745

All rights reserved

## ACKNOWLEDGEMENTS

This thesis marks the end of an incredible journey—filled with many challenges, growth, and unforgettable moments. I feel lucky to have had the support, kindness, and encouragement of some truly wonderful people along the way:

Starting with my advisor, Shrinivas R. Kulkarni—I'm incredibly grateful for your support and encouragement (and the occasional reality check) throughout my academic journey, especially when I was deliberating my career pivot. Your trailblazing approach towards venturing into new fields, as well as your belief in my capabilities, kept me motivated. I learned to get into the nitty-gritty of instrument and telescope operations from you, which helped me immensely with the SEDM-KP project. Despite its challenges, I'm truly thankful for the opportunity to lead such a project! I also appreciate the resources and the network you provided to get me the scientific support I needed.

I want to express heartfelt gratitude towards my scientific co-advisor, Jesper Sollerman. This thesis would not be possible without your help and expertise regarding all things supernovae. You have taught me so much about supernovae and scientific writing. I sincerely appreciate your incredible attention to detail on all our papers and for hosting me at Stockholm University.

I am deeply grateful to Ashish Mahabal for providing scientific and career guidance related to AI in science and teaching me everything about deep learning. Your advice was crucial in forging my future career path. I truly appreciate your patience and continuous support in taking the AI project to the finish line.

I thank the members of my thesis committee—Mansi Kasliwal, Vikram Ravi, Sterl Phinney, and Chris Martin for their advice and support, and I am grateful to Lynne Hillenbrand for her support as the option representative during graduate school.

I am incredibly lucky to have been supported by several individuals who helped me get started on my PhD journey and inspired me throughout it. Christoffer Fremling—being mentored by you on the BTS SURF project and learning from you about transients and observing is what inspired me to apply for graduate school. You have been incredibly kind and supportive and the best mentor anyone could ask for. Mansi—your infectious enthusiasm towards astronomy motivated me to become the most efficient astronomer I can be. Your guidance meant a lot, and as a leading woman in science, you continue to be an inspiration to me. Varun Bhalerao—thank

you for kick-starting my academic journey, being an incredible advisor, introducing me to astronomy, and routinely checking in during my PhD.

I am indebted to the amazing SEDM-KP team, who conquered every challenge in the project and went through all the ups and downs of the SEDM-KP project with me. Don Neill for his expert leadership as the initial project manager; Dan McKenna for being an excellent telescope engineer and teaching me all about telescope mechanics; Lauren Fahey and Jason Fucik for their excellent engineering work and keeping me involved throughout; Michael Coughlin for being an amazing project scientist and for all his assistance with Fritz and Skyportal; Larry Lingvay for being an amazing project manager and for his support; Saarah Hall and Mitchell Karmen for being amazing colleagues, excellent students, and super fun road trip buddies; Josiah Purdum, Alex Reedy, Brendan King, Alex Criswell, Ben Roulston, Yu-Jing Qin, and Tomas Ahumada for assisting with installation and operations; Shri Kulkarni, Adam Miller, Michael Coughlin, Suvi Gezari, and Brad Cenko for conceiving and supporting this project; Larry Reddell and the Kitt Peak E&M staff for their excellent support with mountain facilities; and finally Gita Patel, Linda Donnelly, Ruth Loisel, and Stephanie Petty for their quick assistance with all the logistics.

To my colleagues and mentors in the Caltech time-domain group, my thesis would not be possible without your mentorship and I am so thankful to: Igor Andreoni for the fun work trips and teaching me all about EMGW follow-up; Anna Ho for teaching me the ropes of observing and how to survive Shri's meetings; Kishalay De for tolerating all my annoying questions about light curve modeling; Yuhan Yao for being my Keck observing partner and shopping partner; Lin Yan for the thorough feedback on all my papers; and Yu-Jing Qin and Tomas Ahumada for joining me on the Kitt Peak observing runs and making them more fun. I sincerely appreciate the support and feedback of the larger ZTF collaboration and the amazing science working groups. Steve Schulze, Adam Miller, Dan Perley, Avishay Gal-Yam, Claes Fransson, Lin Yan, Kate Maguire, Matthew Graham, Michael Coughlin, and Dmitry Duev for your insights and support on my projects. I am incredibly thankful to Palomar and Keck staff for their help during the many observing nights.

I am grateful to the wonderful colleagues in the Caltech time-domain group for scientific feedback, shared observing runs, but most importantly, their friendship and all the fun group outings—Tomas, Robert, Shreya, Yuhan, Viraj, Kaustav, Sam, Nicholas, Theo, Aishwarya, and others. I am thankful to the amazing graduate student community of Caltech astronomy for their support and friendship: Sarah

(and Fido) for being amazing first-year office mates; Sam Wu, Zhuyun, Sam Rose, Jean, Nitika and Shreya for letting me chitchat away for hours in the office; Evan, Max, Sam, Sarah, Zhuyun, and Viraj for helping me survive the first year and all the fun cohort outings; and Dillon for being a wonderful first-year grad mentor.

To the amazing Caltech Tango community—Josh, Terry, Desiree, Cameron, Thomas, Vincent, Nadine, Ellis, and others, thank you for creating this wholesome community, making me feel welcome, and teaching me the wonderful dance that is Tango.

To my current and former housemates—Nitika, Shreya, Jean, Kaustav, Pranav, and Viraj, I am incredibly lucky to have shared a home, conversations (and gossip) over food and tea, and many Diwali celebrations with you all. Thank you so much for taking great care of my cats whenever I had to travel. To Pranav Kulkarni—thank you for being a great friend and figuring out grad school and Pasadena with me.

No words are enough to thank my best friend, my pal, my rotten soldier—Viraj Karambelkar. I am incredibly thankful for constant support and encouragement, for putting up with my doomsday wishes right before exams, for the mountain of feedback on my writing, and for being the most amazing partner one could ask for.

To my cats, Merry and Pippin, who can not read this or understand how grateful I am to them for keeping me sane and happy during my PhD, I will buy many, many treats for you.

To my mentors from undergraduate days—Varun Bhalerao, Urjit Yajnik, Pradeep Sarin, Vikram Rentala, Luca Baiotti, thank you for setting me on the path to this PhD. To my friends from undergraduate days—Tanya C., Shobhna, Snehal, Anju, Tanya G., Megha V., Katy, Meeta, Asha, Simi, Jani, Pareek, Aloo and my school friends—Megha G. and Ritu, thank you so much for your friendship and support throughout the years.

Last but not least, I would like to thank my family for always supporting me in my endeavors and encouraging my interests. My parents—Raj Rani and Om Prakash Sharma, all my perseverance and grit came from watching them endure life's toughest challenges with a smile. My sisters—Vasudha and Surbhi Sharma, for listening to my endless babbling, protecting me, and nurturing my creativity. I would like to thank the cousins I grew up with—Venu, Renu, Karuna, Varuna, and Gautam, my cousin-in-laws—Hitesh, Harry, Monica, and others, and all my extended family for their immense love and support.

## ABSTRACT

Modern time-domain astronomy has entered a data-rich era. Propelled by wide-field, high-cadence surveys like the Zwicky Transient Facility (ZTF) have vastly expanded our understanding of supernova (SN) diversity. However, the surge in discoveries has led to a classification bottleneck, particularly for spectroscopic follow-up, hindering the timely identification of rare or unusual transients. This thesis focuses on a class of unusually long-lived SNe with bumpy light curves, and also addresses the broader classification challenge through instrumentation and the application of artificial intelligence.

Two rare SN classes are examined in depth through systematic samples: (i) SNe Ia-CSM, which initially have SNe Ia-like spectra but later transform into Type II-like SNe strongly interacting with circumstellar material (CSM), challenging our understanding of their progenitor systems; and (ii) double-peaked stripped-envelope supernovae (SESNe), where multiple light curve peaks suggest contributions from diverse energy sources including double-nickel distribution, CSM interaction, or magnetar engines. I derive constraints on the observed rates of SNe Ia-CSM with the systematic sample, and identify spectroscopic features that can differentiate between the strongly-interacting spectra of SNe Ia-CSM from SNe II. I discuss the diversity of double-peaked SESN light curves in the context of the plethora of suggested powering mechanisms and derive light curve properties that can help narrow down the possibilities.

To enable more effective discovery and classification of such events, this thesis also presents instrumental and computational advances. I detail the commissioning of a new low-resolution robotic spectrograph, SEDM-KP, on the Kitt Peak 84-inch telescope, designed to extend spectroscopic classification to fainter transients. Additionally, I introduce a deep-learning-based tool, *CCSNscore*, which achieves high accuracy in automated core-collapse supernova classification from low-resolution spectra, significantly reducing human workload and latency in reporting.

Together, these contributions advance our ability to identify, classify, and study the growing zoo of transient phenomena and lay the groundwork for managing the deluge of discoveries anticipated in the Rubin Observatory era.

## PUBLISHED CONTENT AND CONTRIBUTIONS

Sharma, Y. et al. (2025). “CCSNscore: A Multi-input Deep Learning Tool for Classification of Core-collapse Supernovae Using SED-machine Spectra”. In: *PASP* 137.3, p. 034507. DOI: 10.1088/1538-3873/adbf4b.

YS contributed to the survey and instrument operations for data acquisition, collected data from literature, developed and trained the deep learning model, wrote the open-source software and wrote the manuscript.

Sharma, Y. et al. (May 2024). “Dramatic Rebrightening of the Type-changing Stripped-envelope Supernova SN 2023aew”. In: *ApJ* 966.2, 199, p. 199. DOI: 10.3847/1538-4357/ad3758.

YS contributed to the survey that led to the transient identification, contributed to observing programs for its characterization, conducted data analysis, and wrote the manuscript.

Sharma, Y. et al. (May 2023). “A Systematic Study of Ia-CSM Supernovae from the ZTF Bright Transient Survey”. In: *ApJ* 948.1, 52, p. 52. DOI: 10.3847/1538-4357/acbc16.

YS contributed to the survey that led to the sample collection and data acquisition, conducted data analysis, and wrote the manuscript.

## TABLE OF CONTENTS

Acknowledgements . . . . .	iii
Abstract . . . . .	vi
Published Content and Contributions . . . . .	vii
Table of Contents . . . . .	vii
List of Illustrations . . . . .	x
List of Tables . . . . .	xxii
Chapter I: Introduction . . . . .	1
1.1 Metamorphing Type Ia: SNe Ia-CSM . . . . .	5
1.2 Metamorphing Type Ibc: Double-peaked SNe . . . . .	5
1.3 Instrumentation and AI for optimal classification of SNe . . . . .	7
Chapter II: A Systematic Study of Ia-CSM Supernovae from the ZTF Bright Transient Survey . . . . .	10
2.1 Introduction . . . . .	11
2.2 Observations and Data reduction . . . . .	14
2.3 Analysis . . . . .	20
2.4 Discussion . . . . .	46
2.5 Summary . . . . .	49
2.6 Acknowledgment . . . . .	49
2.7 Appendix A: Ambiguous SN Ia-CSM/IIIn in BTS . . . . .	51
Chapter III: Dramatic rebrightening of the type-changing stripped-envelope supernova SN 2023aew . . . . .	54
3.1 Introduction . . . . .	55
3.2 Observations . . . . .	56
3.3 Analysis . . . . .	61
3.4 Discussion . . . . .	76
3.5 Summary and conclusions . . . . .	82
3.6 Acknowledgement . . . . .	83
3.7 Appendix A: Photospheric phase line strengths and velocities . . . . .	85
3.8 Appendix B: Note added in proofs . . . . .	86
3.9 Appendix C: Photometry tables . . . . .	87
Chapter IV: Twin peaks: SN 2021uvy and SN 2022hgk in the landscape of double-peaked stripped envelope supernovae . . . . .	89
4.1 Introduction . . . . .	90
4.2 Observations . . . . .	92
4.3 Analysis . . . . .	97
4.4 Discussion . . . . .	109
4.5 Summary . . . . .	114
4.6 Acknowledgement . . . . .	115
4.7 Appendix A: Photometry Data . . . . .	117

4.8 Appendix B: Spectroscopy Data . . . . .	117
Chapter V: Commissioning the Spectral Energy Distribution Machine at Kitt Peak 2.1-m telescope . . . . .	119
5.1 Introduction . . . . .	120
5.2 Instrument overview . . . . .	122
5.3 Operations . . . . .	126
5.4 Data Processing Software . . . . .	130
5.5 Performance . . . . .	132
5.6 Summary . . . . .	140
5.7 Acknowledgment . . . . .	145
Chapter VI: CCSNscore: A multi-input deep learning tool for classification of core-collapse supernovae using SED-Machine spectra . . . . .	146
6.1 Introduction . . . . .	147
6.2 Dataset . . . . .	150
6.3 Parallel binary classifiers . . . . .	156
6.4 Optimization and training . . . . .	158
6.5 Performance . . . . .	160
6.6 Real-time implementation . . . . .	169
6.7 Discussion and Summary . . . . .	170
6.8 Acknowledgment . . . . .	174
6.9 Appendix A: SNID ROC curve . . . . .	175
Chapter VII: Summary . . . . .	176
7.1 Probing the extent of CSM in SNe Ia . . . . .	176
7.2 Building systematic samples of double-peaked SESNe . . . . .	176
7.3 SEDM-KP, a new supernova classifier on the horizon . . . . .	177
7.4 Future of AI in supernova classification . . . . .	177
Bibliography . . . . .	179

## LIST OF ILLUSTRATIONS

<i>Number</i>	<i>Page</i>
1.1 The supernova classification scheme (adapted from astrobit.es article by Ashley Villar— <a href="https://astrobit.es.org/2016/12/02/classifying-supernovae/">https://astrobit.es.org/2016/12/02/classifying-supernovae/</a> ). New supernova classes are emerging more frequently with surveys like ZTF. . . . .	1
1.2 Pie charts depicting the fraction of classified supernovae by subtypes in ZTF’s flux-limited Bright Transient Survey (BTS; Fremling et al. 2020). Figure from Perley et al. (2020). . . . .	2
1.3 <i>Left:</i> Histogram of SNIascore values (probability of a sample being a SN Ia) predicted for true SNe Ia (red) and other transients (blue). For a well-performing classifier, this distribution should be bimodal with true SNe Ia getting a higher SNIascore. <i>Right:</i> True positive rate (true SNe Ia that get classified as SNe Ia) vs. false positive rate (other SNe that get classified as SNe Ia) of SNIascore, compared with the same for SNID and DASH. SNIascore performs much better than either SNID or DASH on SEDM data. Figure 4 from Fremling et al. (2021). . . . .	8
2.1 Optical light curves of the ZTF BTS SN Ia-CSM sample. The SNe Ia-CSM have longer durations than the average SN Ia, with some variety, like bumpy light curves or long plateaus. The one SN marked with an asterisk (SN 2020uem) has an unconstrained explosion time estimate ( $\sim\pm 50$ d). The decline rate from Cobalt decay is marked with a black dashed line, and the light curve decline rates measured from $r$ -band data are shown in the subplot legends. . . . .	18

- 2.2 *Top:* Location of our 12 SNe Ia-CSM in the peak absolute magnitude vs. rest-frame duration above half max phase space. The colored points are the BTS SNe Ia-CSM, and the gray points are the rest of the BTS SNe Ia. Also shown with empty triangles are the SNe Ia-CSM from S13. The vertical arrows mark the upper limits to peak absolute magnitudes, and horizontal arrows mark the lower limits to durations of SNe not having pre-peak coverage. *Bottom:* Change in magnitude 30 days after peak ( $\Delta m_{30}$ ) vs. rest-frame duration above 20% of peak-flux for BTS SNe Ia and SNe Ia-CSM. These criteria were used to filter out potential SNe Ia-CSM from all SNe Ia and demonstrate that SNe Ia-CSM occupy a distinct portion in this phase space. However, some gray points (not SN Ia-CSM) remain on the longer duration side and are the false positive cases described in §2.1. . . . . 23
- 2.3 Color evolution ( $g - r$ ) of BTS SNe Ia-CSM from  $r$ -band maximum (plotted in black) compared with SNe 2005gj, 1997cy, 1999E (Ia-CSM), SN 2012ca (IIn/Ia-CSM), SN 2010jl (IIn), SN 1991T (SN Ia), and ZTF SNe Ia (gray lines). As can be seen for up to  $\sim 150$  days, our SNe Ia-CSM tend to be redder than SNe Ia and at late times develop a plateau similar to other interacting SNe (IIn/Ia-CSM). . . . . 25
- 2.4 unWISE detections in the W1 and W2 bands of BTS SNe Ia-CSM. The W1 and W2 points are marked with black and red filled stars, respectively. Spitzer IRAC photometry of SNe IIn (blue and orange crosses) and two SNe Ia-CSM from Fox et al. (2011) (SNe 2008cg and 2008J in empty triangle and square) are also shown for comparison. Nine out of twelve BTS SNe Ia-CSM are as bright in mid-IR as other interacting SNe ( $\sim -16$  to  $\sim -19$ ). The upper limits for SN 2020abfe are shown in black and red filled upside-down triangles. . . . . 27

- 2.5 Pseudo-bolometric luminosity light curves of BTS SNe Ia-CSM compared with pseudo-bolometric light curves of SNe 1991T, 1997cy, 1999E, 2002ic, 2005gj, 2013dn, and PTF11kx from literature. The light curves in each filter having more than 10 epochs were interpolated using Gaussian process regression to fill in the missing epochs, and at each epoch, the fluxes between the bands were linearly interpolated and integrated over the optical wavelength range spanned by ZTF and ATLAS filters to get the pseudo-bolometric luminosity. For BTS SNe, the phases are with respect to the estimated explosion epochs, while for comparison SNe, the phases are with respect to discovery. . . . . 29
- 2.6 Spectral series of all SNe Ia-CSM presented in this paper. The rest-frame phases are shown alongside the spectra in each subplot and have been calculated using the explosion epoch estimate. The colors depict different instruments used to obtain this data. Major emission lines are marked with vertical dashed lines. . . . . 30
- 2.7 *Top left:* Early-time spectra of BTS SNe Ia-CSM with phases between 0 and 30 days since explosion compared to spectra of SNe 2011jb, 2005gj, 1991T, and PTF11kx (phases in days since discovery). *Top right:* Late-time spectra of BTS SNe Ia-CSM (phases ranging from 40 to 370 days since explosion) compared to spectra of SNe 2011jb, 2005gj, 2010jl, and PTF11kx (phases in days since discovery). *Bottom left and right:*  $H\alpha$  line profiles (post continuum removal) with the blue side reflected across the peak flux, marked by dashed lines. SNe 2020aekp, 2020abfe, 2020xtg, and 2020uem in the right panel, and SNe 2018crl, 2018gkx, 2018evt, 2019agi, 2019ink, 2019rvb, 2020onv, and 2020qxz in left panel. . . . . 33
- 2.8 Integrated fluxes and equivalent widths of  $H\alpha$  emission line with respect to SN phases for the BTS SN Ia-CSM sample. Broad component values are shown with filled markers and narrow component values with unfilled markers. SN 2018evt  $H\alpha$  luminosities and EWs presented in Yang et al. (2022) are also shown in gray circles. . . . . 36
- 2.9 Velocity of  $H\alpha$  emission line with respect to SN phases for the BTS SN Ia-CSM sample. Broad component values are shown with filled markers and narrow component values with unfilled markers. . . . . 37

- 2.10 Mass-loss rates estimated from the luminosity of the broad component of  $H\alpha$  for the BTS SNe Ia-CSM. A value of  $100 \text{ km s}^{-1}$  was assumed for the wind velocity. . . . . 37
- 2.11 Cumulative distributions of equivalent width of  $H\beta$  and He  $\lambda 5876$  emission lines calculated from the BTS SNe Ia-CSM (in grey) compared with the respective distributions presented in S13 for SNe Ia-CSM (blue) and SNe IIn (red). Vertical dashed lines mark the median EW of the distributions. . . . . 39
- 2.12 Cumulative distribution of  $H\alpha/H\beta$  intensity ratio (Balmer decrement) calculated from intermediate resolution spectra of the BTS SN Ia-CSM sample (grey shaded region). The red line is the distribution of Balmer decrement of SNe IIn measured in S13, and the blue line is the SN Ia-CSM Balmer decrement distribution from S13. The black circles are a few representative points indicating the high Balmer decrement values and the uncertainties on them. The vertical dashed line is the median Balmer decrement measured from BTS SNe Ia-CSM. 41
- 2.13 Host galaxies of BTS SN Ia-CSM (black circles) on SFR vs stellar mass plot with Galaxy-zoo spiral (blue contours) and elliptical (red contours) galaxies for comparison. BTS SN Ia hosts are also shown for comparison in green circles. Equal sSFR lines are marked with grey dashed lines. . . . . 43
- 2.14 Precursor rate as a function of magnitude calculated from BTS SN Ia-CSM pre-explosion ZTF forced photometry stacked in 7-day bins. The different colored shaded regions correspond to different ZTF bands (*r*-red, *g*-green, *i*-grey). The solid lines depict the upper limits on the fraction of the time a precursor of the corresponding magnitude would have been detected, which is consistent with the ZTF non-detections. . . . . 45

- 3.1 Light curve of SN 2023aew. The TESS observations cover the rise of the first peak and are shown in gray squares, with  $5\sigma$  significance denoted with full markers and  $3\sigma$  with empty markers. The spectroscopic epochs are marked with black lines at the top. Also shown for comparison are absolute magnitude  $r$ -band light curves of SNe 1993J (Iib), 2011dh (Iib), 2005bf (Ib-pec), 2007gr (Ic), 2009ip (IIn), iPTF13bvn (Ib), and the type-changing 2017ens (Ic to IIn). SNe 1993J and 2011dh are shifted to match their first detection with the SN 2023aew explosion epoch. Other comparison SNe are shifted by  $\sim 100$  days to match the start of the second peak. The overall light curve shape is somewhat similar to that of SN 2009ip but is broader, with the second peak having similar broadness as SN 2017ens. . . . . 58
- 3.2 Spectral sequence of SN 2023aew from day 34 to day 281. The black lines are smoothed spectra (using a median filter), and the colored lines are original spectra, with different colors depicting different instruments. Some important spectral lines are marked with gray dashed lines. In the left panel, the Balmer lines are visible in the first spectrum at 34 days, then  $H\alpha$  seemingly shows up again in the nebular phase spectra in the third panel. . . . . 63
- 3.3  $g - r$  and  $r - i$  color curves of SN 2023aew. Shown for comparison are  $V - R$  color curves of SNe 1993J, 1998bw, 2007gr, and 2009ip, and  $g - r$  color curves of SN 2017ens and iPTF13bvn. . . . . 65
- 3.4 Bolometric (filled red circles) and pseudo-bolometric (open red circles) light curves of SN 2023aew along with some comparison SNe. Gray open circles denote the pseudo-bolometric luminosity approximation from TESS observations. Also shown (blue squares) is an alternative estimate of the bolometric light curve obtained by applying bolometric corrections to  $g$ -band data following Lyman et al. (2014). The  $^{56}\text{Ni}$  radioactivity power fits to the bolometric and pseudo-bolometric light curves following the Arnett method are plotted in light-red color for the second peak and gray color for the first peak. . . . . 66

3.5	Rise time versus decline time (peak to half-peak in the $r$ band) of the Bright Transient Survey sample of supernovae (colored points) and broad light-curve SESNe from Karamehmetoglu et al. (2023) (empty black squares). The first peak of SN 2023aew is marked with the smaller black star (rise time from TESS data), and the second peak is marked with the larger black star ( $r$ band data). . . . .	68
3.6	SN 2023aew spectral comparison at different phases compared to mean spectra of SNe I Ib, SNe Ib, and SNe Ic from Liu et al. (2016). . . . .	70
3.7	A near-infrared spectrum of SN 2023aew obtained with Keck2/NIRES, smoothed using a median filter of kernel size of 9 pixels (in black). Tentative line identifications are marked with blue dashed lines. . . . .	71
3.8	<i>Upper panel:</i> SN 2023aew in the logarithmic phase-space of [O I] width versus [O I]/[Ca II] flux ratio for SESNe published in Fang et al. (2022, their fig. 7a). <i>Lower panel:</i> $L_N/L_O$ versus $L_O/L_{Ca}$ for SESNe published in Fang et al. (2019, their fig. 3). ‘cI Ib’ and ‘eI Ib’ refer to compact and extended SNe I Ib, respectively. Values for SN 2023aew are shown in purple stars and derived from late-time spectra (phases ranging from 200 to 281 days from explosion) with the transparency decreasing with increasing phase. The SN nebular spectra used in Fang et al. (2019) range from 150 to 300 days after the peak, while for SN 2023aew they range from 75 to 150 days after the second peak. SN 2023aew consistently shows higher values on the [N II]/[O I] axis, which suggest the presence of $H\alpha$ contaminating (or rather dominating) the [N II] lines at these phases. . . . .	73
3.9	Line profiles of nebular [O I], [Ca II], Mg I, and $H\alpha$ /[N II] complex from 207 days to 281 days. Dashed vertical lines mark the rest wavelengths and dotted vertical lines mark the blueshifted ( $\sim 1500$ km s $^{-1}$ ) components. The blueshifted component in all lines appears to be increasing in strength with phase. . . . .	74
3.10	Comparison of SN 2023aew with the canonical precursor Type IIn SN 2009ip, but also with the analogous SESN SN 2023plg, showing both a similar luminous, long-lived declining precursor and a bright second peak. Light curves shifted to match the rise of the main peak. SN 2023plg also exhibits a Type Ibc SN spectrum. . . . .	80

3.11	Absorption velocity and pseudo-equivalent width (pEW) evolution with phase for He I $\lambda$ 5876, H $\alpha$ and O I $\lambda$ 7774. Shown for comparison are running weighted averages of velocities and pEWs for SNe I Ib, Ib, and Ic with error bars of 1000 km s <sup>-1</sup> and 10 Å respectively from Liu et al. (2016). . . . .	85
4.1	Light (top) and color (bottom) curves of SN 2021uvy (left) and SN 2022hgk (right). The 5 $\sigma$ detections are shown with solid markers and 3 $\sigma$ upper limits with transparent markers. All photometry is corrected for MW extinction. Absolute magnitudes are K-corrected (by adding $-2.5\log_{10}(1+z)$ ) and obtained using Planck Collaboration et al. (2020) cosmology. The <sup>56</sup> Co decay rate (radioactive power) is shown with a dotted gray line. The spectral phases are marked on the top axis with red vertical lines. The explosion epochs are shown with gray dashed lines. . . . .	94
4.2	Spectral sequences of SN 2021uvy (left and center) covering epochs from -15 to 384 rest-frame days since its first peak and of SN 2022hgk (right) covering epochs from 17 to 95 rest-frame days since its first peak. Some characteristic spectral lines are marked with vertical gray dashed lines. Spectra are smoothed with a median filter of window size 5. . . . .	96
4.3	Light curves ( <i>r</i> -band) of our sample of double-peaked SESNe, shifted vertically for clarity and with their first peaks aligned. Also shown for comparison are SN 2005bf and PTF11mnb (dashdot lines). All absolute magnitudes have been calculated using the same cosmology. . . . .	100
4.4	Evolution of the bolometric luminosity (top), blackbody temperature (second), blackbody radius (third), and <i>g</i> - <i>r</i> color (bottom) with time of SN 2021uvy (black circles) and SN 2022hgk (blue squares). Shown for comparison are SN 2019cad (red), SN 2019stc (magenta), PS1-14bj (green), and SN 1998bw (gray). SN 2021uvy and SN 2019stc show similar evolution during their first light-curve peaks but diverge in behavior during the second peaks. SN 2021uvy develops a gradual rise in temperature during the second peak, similar to PS1-14bj, which also correlates with the lack of color evolution for both these SNe. The properties of SN 2022hgk closely resemble those of SN 2019cad. . . . .	103

- 4.5 *Left:* First-peak spectra of SN 2021uvy (black) compared with those of SNe 2019stc (magenta), 2020acct (brown), and PS1-14bj (green), with phases reported with respect to the first peak. Similar to normal SESNe, the first-peak spectra of SNe 2019stc, 2021uvy and PS1-14bj are dominated by Ca II, Mg I], Fe II and O I. SN 2020acct, on the other hand, shows signs of CSM interaction at this phase. *Right:* Second-peak spectra of SNe 2021uvy (black) and 2022hgk (blue) compared with those of SNe 2005bf (purple), 2019cad (red), 2019stc (magenta), 2020acct (brown), and PS1-14bj (green), with phases reported with respect to the second peak (except for PS1-14bj). SN 2022hgk shows a close spectroscopic resemblance to the peculiar Type Ib SN 2005bf around their main (second) peaks. All spectra are smoothed with a median filter of window size 5 (except for SN 2020acct). . . . . 106
- 4.6 *Top:* Comparison of nebular spectra of SN 2021uvy (black) with SNe 2019stc (magenta), 2020acct (brown), 2022xxf (cornflowerblue) and 2023aew (gold). *Bottom:* Comparison of nebular spectra of SN 2022hgk (blue) with SNe 2005bf (purple) and 2019cad (red). All spectral phases are reported with respect to the first peak. . . . . 107
- 4.7 *Left:* Peak absolute magnitudes of the second peak vs. the first peak for the double-peaked SESN sample, and the shock-cooling powered double-peaked SESNe presented in Das et al. (2024). There appears to be a correlation between the peak magnitudes, which is strongest for the Das et al. (2024) SESNe (p-value  $< 10^{-5}$ ) but also significant for our double-peaked SESN sample (p-value = 0.005). *Right:* Magnitude difference vs. rest-frame duration between the two peaks. Again, the potentially double-nickel powered SESNe form a tight group in this phase space. . . . . 109
- 5.1 A schematic of the KP84 telescope showing where the instrument and electronics are mounted. *Image Credit:* Coughlin et al. (2019). . 122
- 5.2 *Left:* A picture of SEDM on the Palomar 60-inch telescope. *Right:* A picture of SEDM-KP on the Kitt Peak 84-inch telescope. Note that the imaging/guide camera in SEDM is located out of the plane of the instrument, but in SEDM-KP is located inside the instrument in the same plane. . . . . 123

- 5.3 A schematic of the SEDM-KP design, showing the spectrograph channel and the imaging channel components. The light window is located under the pick-off assembly (inside the yellow circle). *Image Credit:* Lauren Fahey (Caltech Optical Observatories). . . . . 124
- 5.4 *Left:* A picture of the multi-lenslet array. *Right:* The geometry of the hexagonal micro-pupil images on the IFU CCD plane. Each micro-pupil image is 0.72'' across, with 0.62'' distance between centers of adjacent hexagons. *Image Credit:* Jason Fucik (Caltech Optical Observatories). . . . . 125
- 5.5 Comparison of the simulated resolutions as a function of wavelength for SEDM (blue) and SEDM-KP (black). SEDM-KP has a higher than SEDM resolution for  $\lambda \lesssim 5000 \text{ \AA}$  and lower than SEDM resolution for  $\lambda \gtrsim 5000 \text{ \AA}$ . Simulated data generated by Jason Fucik (Caltech Optical Observatories). . . . . 125
- 5.6 *Left:* Example of an autofocus loop routine showing the quadratic dependence of FWHM on telescope secondary focus position. *Right:* Plot showing best focus position as a function of dome temperature. The dark points are from good-quality quadratic fits on autofocus loops, gray points are from poor-quality quadratic fits (extrapolated, poor seeing, etc.). The linear relation is used to set the initial central position for autofocus loops. . . . . 128
- 5.7 *Top left:* Spectral traces from micro-pupils on the IFU CCD for a dome flat image. The extracted trace boundaries are shown in red. *Top right:* The hexagonal grid formed by micro-pupil images on the IFU CCD plane, each micro-pupil image forms a spatial pixel or a "spaxel". The bright target (in this case, a standard star) is clearly visible in the image, and the dotted area is used for PSF modeling. *Bottom:* Example of a wavelength solution for one spaxel using the arc lamps (Xe, Hg, Cd). The solution curve maps the pixels along the length of the trace to wavelengths. . . . . 130
- 5.8 Flow chart of all the photometric data reduction steps that are executed using the MIRAR framework for SEDM-KP data. *Image Credit:* Saarah Hall (CIERA, Northwestern University). . . . . 132

- 5.9 Motor current data collected for diagnosing the KP84 mechanical issues. *Top panels:* DEC axis motor current as a function of DEC encoder position during a long slew from North – South (blue) and South – North (orange) limits. *Bottom panels:* HA axis motor current as a function of time while the telescope is tracking. On the left are plots before servicing and tuning of the telescope mechanics, which show clear stick-slip oscillations. On the right are plots after the servicing, which show a much-improved performance of the telescope axes during slewing and tracking. Data collected with the help of Dan McKenna (COO). . . . . 133
- 5.10 *Left:* Quiver plot showing astrometric solution uncertainties in RA and DEC derived from a field containing 72 reference catalog-matched stars. *Right:* Zero-point as a function of PS1  $g - r$  color for the same field in a  $g$ -band image. There is a negligible effect of color-term on our ZP fitting. *Image Credit:* Saarah Hall (CIERA, Northwestern University). . . . . 135
- 5.11 A false color image of Crab Nebula (M1) created using  $gri$ -band images taken with SEDM-KP. *Image Credit:* Mitchell Karmen (STScI). 136
- 5.12 *Left panels:* A zoomed-in snapshot of the cadmium arc lamp calibration image (top) showing the halo effect around bright Cd lines caused by the birefringent component in the spectrograph optical path, and the corresponding wavelength solution uncertainties map (bottom). *Right panels:* The same images after the birefringent component was replaced. The Cd snapshot looks much sharper, with a darker background due to less scattered light and a clear 2-pix space between adjacent traces. The wavelength solution is improved and  $< 20 \text{ \AA}$  for the upper half spaxels but has higher uncertainties in the lower half due to minor misalignment of the tri-prism. . . . . 137
- 5.13 Evolution of SEDM and SEDM-KP's efficiency over time after key upgrades. SEDM-KP's final efficiency is  $1.6\times$  higher in the redder bands and  $4\times$  higher in the bluer bands compared to its initial efficiency and  $2\times$  higher than that of SEDM in redder bands. The efficiency number includes the effect of the telescope's primary and secondary mirror reflectances. . . . . 138

5.14	Example of a summary report page generated by <code>pysedm</code> for each observation taken. The plot shows PSF modeling quality, flexure correction fits, and the extracted spectrum (with uncertainties on the fluxes). This particular example is of a Type II supernova. . . . .	139
5.15	Spectra of some bright Type II SNe from TNS collected with SEDM-KP, with wavelengths transformed to the rest-frame, and with the hydrogen Balmer series marked with vertical dotted lines. . . . .	140
5.16	Comparison of a SEDM (2160 s exposure time) and a SEDM-KP (900 s exposure time) spectrum of the same supernova (SN 2024cld) taken around similar phase. Given that the KP84 effective area is $2\times$ that of P60 and the SEDM-KP exposure time here is $0.42\times$ that of SEDM, both spectra should have roughly the same SNR, but we see that SEDM-KP has a much better SNR than SEDM, especially in the redder bands. . . . .	141
6.1	Distribution of properties of the training and test sets (gold and bronze). The first row contains pie charts depicting the highly imbalanced distribution of samples by CCSN subtype. The next four rows depict the property distribution for hydrogen-rich (Type II in blue) and hydrogen-poor (Type Ibc in red) SN samples separately, with the second row showing spectral phase distribution, the third row showing the distribution of the number of spectra per unique SN, the fourth row showing redshift distribution of the unique SNe and the fifth row showing the peak apparent magnitude distribution of unique SNe. The mean values of all distributions are marked with dotted vertical lines. . . . .	150
6.2	Training data samples representing the various transient types (rows). The first column shows the raw (red) and processed (black) normalized spectra, the second column shows the raw and GP-interpolated $r$ - and $g$ -band normalized light curves, and the third and fourth columns show $\delta m - \delta t$ representations of the $r$ - and $g$ -band GP-interpolated light curves, respectively. . . . .	154
6.3	Multi-channel network architecture of CCSNscore. We found two bidirectional LSTM layers optimal for the spectrum channel, and three LSTM layers optimal for the light curve channels. . . . .	157

- 6.4 Performance of layer 1 binary classifiers on gold and bronze test sets. *Left:* Distribution of binary classifier predicted probabilities for positive class (blue) vs. negative class (red) for H-rich and H-poor classifiers. The gold test set distribution is depicted as filled bars, and the bronze set distribution as empty steps. *Right:* ROC curve from the two layer-1 binary classifiers (blue and red), with SNID (purple) and DASH (teal) for comparison. The gold set curves are depicted with solid lines and the bronze set curves with dotted lines. The black vertical dashed line marks a 2% false positive rate. . . . . 161
- 6.5 Results from the layer 1 (H-rich vs. H-poor) models. The four columns of confusion matrices (CM) are for the four input cases—‘only spectra’, ‘spectra + 1D LC’, ‘spectra +  $\delta m - \delta t$ ’, and ‘spectra + 1D LC +  $\delta m - \delta t$ ’. The top row of CMs in each subfigure is for the gold test set, and the bottom row of CMs is for the bronze test set. . . 163
- 6.6 Confusion matrices for the whole test set derived from the layer 2 models. The four columns in subfigures are for the four input cases—‘only spectra’, ‘spectra + 1D LC’, ‘spectra +  $\delta m - \delta t$ ’, and ‘spectra + 1D LC +  $\delta m - \delta t$ ’. These confusion matrices were constructed considering all of the test samples’ classifications. . . . . 168
- 7.1 A schematic of CCSNscore’s workflow. Though it primarily uses SEDM spectra, CCSNscore’s multi-modal architecture allows for the use of ZTF  $g$  and  $r$ -band light curves in inference. Additional spectral quality criteria have also been implemented to determine if a spectrum is of good quality (good SNR, SN-like features) to generate reliable predictions. . . . . 178

## LIST OF TABLES

<i>Number</i>	<i>Page</i>
2.1 Properties of the 12 BTS SNe Ia-CSM. . . . .	15
2.2 Description of spectrographs used for follow-up and the corresponding data reduction pipelines. . . . .	19
2.3 Summary of optical spectra. . . . .	20
2.4 Explosion time epoch estimates derived from pre-peak multi-band light curves. For 6 out of 12 SNe Ia-CSM, we were able to fit a power-law model to multi-band data following Miller et al. (2020b). For the remaining 6 SNe, the explosion epoch was estimated by taking the mean of the first $5\sigma$ detection and last upper-limit before the first detection. . . . .	22
2.5 Summary of H $\alpha$ line properties obtained from two-component Gaussian fitting. . . . .	38
3.1 Description of spectrographs used for follow-up and the corresponding data reduction pipelines. . . . .	61
3.2 Summary of optical and NIR spectra. . . . .	62
3.3 Log of TESS-Red band observations of $3\sigma$ significance (full table available online). . . . .	87
3.4 Log of UVOT observations of $3\sigma$ significance (full table available online). . . . .	87
3.5 Log of XRT observations. . . . .	87
3.6 Log of optical photometry of $5\sigma$ significance (full table available online). . . . .	88
4.1 Sample of published double-peaked SESNe in the ZTF archive. . . .	97
4.2 Light curve parameters of our double-peaked SESN sample. The rise and fade times are calculated between peak flux and half-of-peak flux. The superscripts ‘1’ and ‘2’ denote the first and second peak parameters, respectively. The rise times, fade times, and duration between the two peaks ( $\Delta t^{21}$ ) are reported in rest-frame days. . . . .	99
4.3 Peak bolometric and pseudo-bolometric luminosities and estimated radiated energies in the two peaks of our double-peaked SESN sample. The superscripts ‘1’ and ‘2’ denote the first and second peaks, respectively. SN 2021uvy has $\sim 32\times$ more energy radiated than SN 2022hgk. . . . .	104

4.4	Log of optical photometry of SN 2021uvy and SN 2022hgk of $>5\sigma$ significance (full table available online). . . . .	117
4.5	Log of UVOT observations of SN 2022hgk of $>3\sigma$ significance (full table available online). . . . .	117
4.6	Summary of optical spectra of SNe 2021uvy, 2022hgk, and 2020acct. We report phases (in rest-frame days) calculated with respect to both the first peak of the light curve and the estimated explosion epoch (inside parentheses). . . . .	118
5.1	Specifications of the EMCCD and the IFU CCD. . . . .	126
5.2	Timeline of the project. . . . .	141
6.1	Total number of samples in the training and test sets per binary classifier. The total number of training samples (including augmented data) per class is listed outside brackets in the second column, while the real number of training samples is listed inside brackets. The number of samples in the gold test set is listed outside brackets in the third column, while the number of samples in the bronze set is listed inside brackets for Layer 1. The amount of augmented data added to each classifier in a layer is such that the samples per class are roughly balanced. . . . .	158
6.2	Hyperparameter ranges for tuning binary classifiers with <code>kerastuner</code> . . . . .	160
6.3	Performance metrics of the layer 1 task models on the gold and bronze test sets. The total accuracy in the final row shows the combined performance on the gold and bronze sets. . . . .	166
6.4	Performance of the layer 1 ‘only spectra’ model predictions on the test samples that pass the TNS reporting criteria. The true positive rate and precision values are reported separately by phase ( $\leq 10$ days or $> 10$ days) and the true type (II and Ibc). The number of samples that pass the different TNS criteria is shown in brackets in the first column. . . . .	171

## Chapter 1

## INTRODUCTION

The advent of high-cadence, wide-field robotic optical surveys has transformed our view of supernovae (SN). Since the first systematic supernova survey (Zwicky 1938), we have come a long way in understanding the diversity of these cosmic explosions, with modern surveys such as the Zwicky Transient Facility (ZTF; Bellm et al. 2019; Graham et al. 2019; Dekany et al. 2020). Where supernovae were once grouped into a handful of spectroscopic classes (Filippenko 1997), we now recognize a rich zoo of subtypes within those broad categories, each distinguished by complex photometric and spectroscopic behavior (see Figure 1.1).

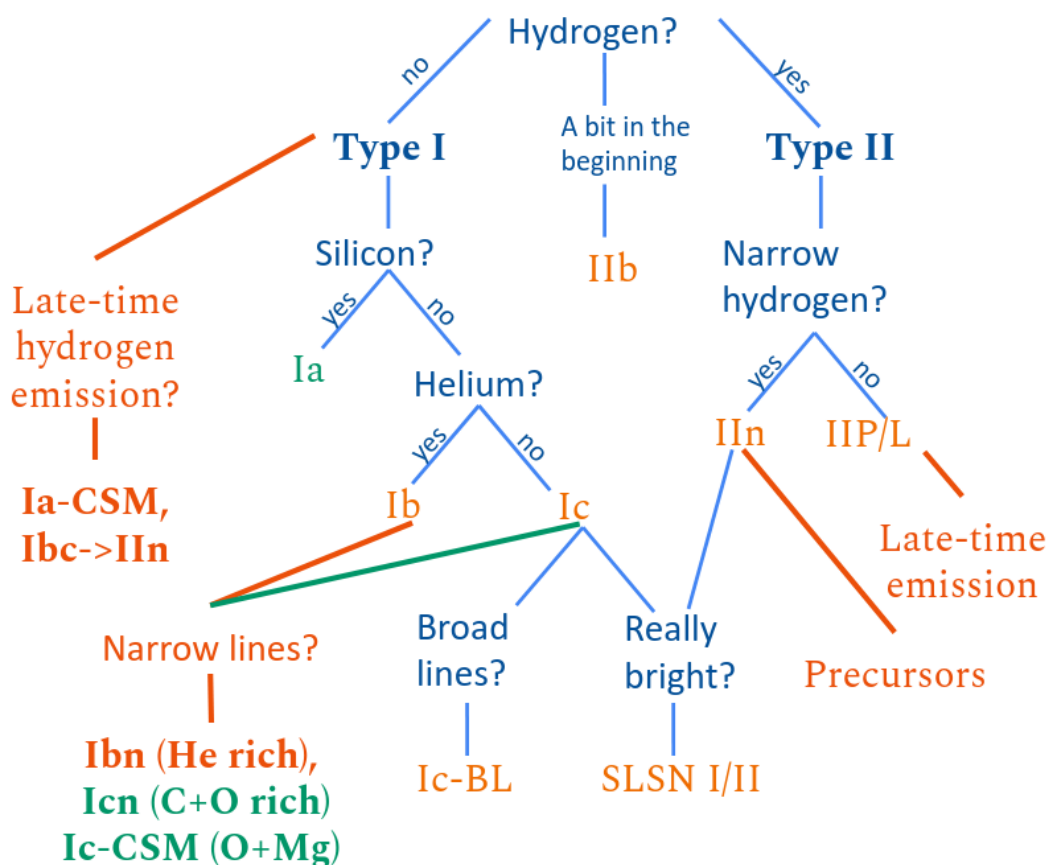


Figure 1.1: The supernova classification scheme (adapted from *astrobit*es article by Ashley Villar—<https://astrobit.es.org/2016/12/02/classifying-supernovae/>). New supernova classes are emerging more frequently with surveys like ZTF.

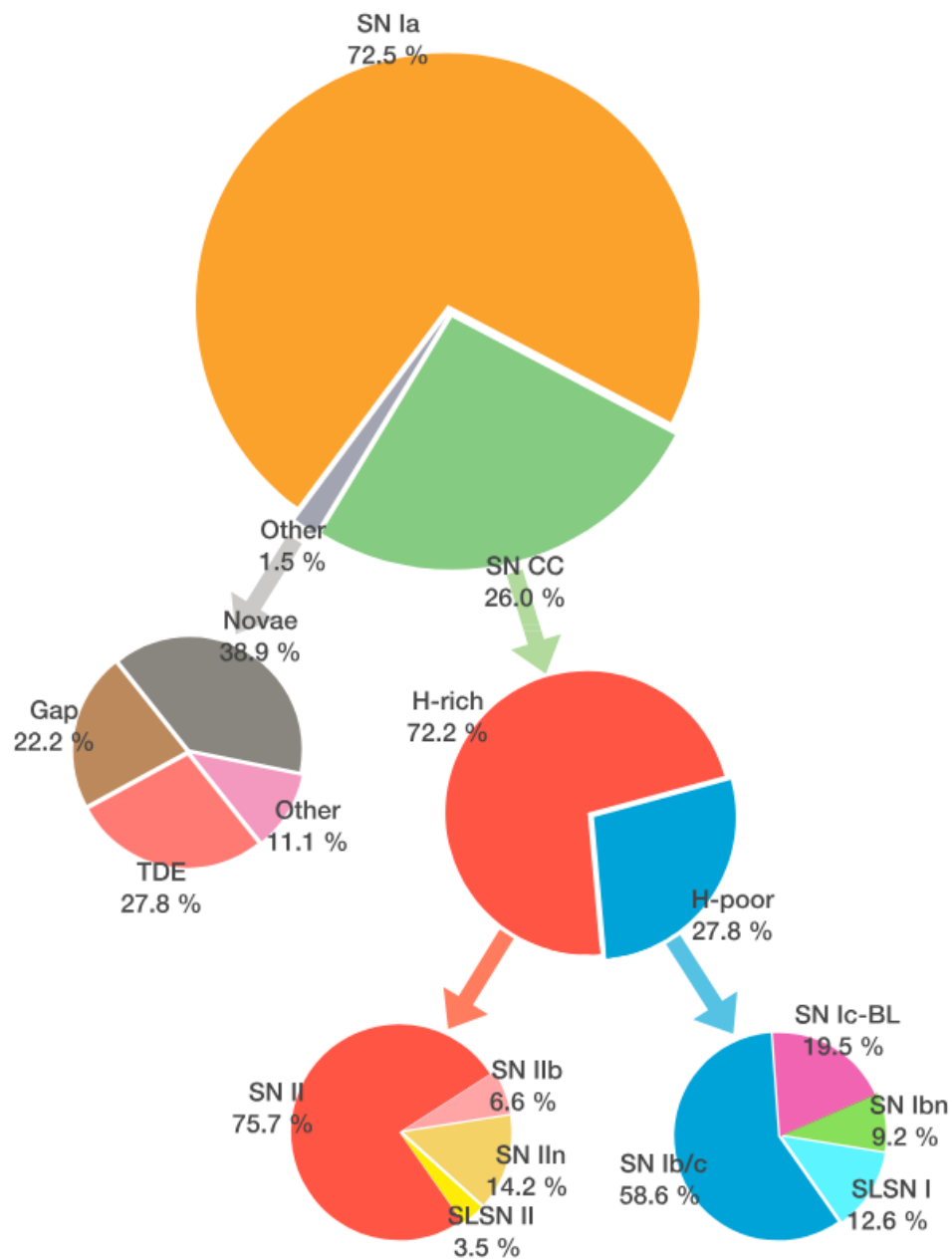


Figure 1.2: Pie charts depicting the fraction of classified supernovae by subtypes in ZTF's flux-limited Bright Transient Survey (BTS; Fremling et al. 2020). Figure from Perley et al. (2020).

The light curves of these SNe exhibit a remarkable diversity in their duration, morphology, and luminosities—some exhibiting extended plateaus (Dilday et al. 2012) and ultra-long durations (Zhang et al. 2012; Arcavi et al. 2017), others showing pronounced undulations or multiple peaks (Anupama et al. 2005; Pastorello et al. 2013; Chen et al. 2024; Angus et al. 2024) and spanning a luminosity range from subluminous (Pastorello et al. 2004) to superluminous events (Quimby 2011). Spectroscopic transformations can accompany the major light curve variations, especially if the supernova has extended circumstellar material (CSM) to interact with (Silverman et al. 2013b; Sollerman et al. 2020; Kuncarayakti et al. 2023). Rare and hypothesized spectroscopic subtypes are being discovered with increasing frequency (Gal-Yam et al. 2021; Perley et al. 2022b; Kuncarayakti et al. 2022; Gal-Yam et al. 2024; Schulze et al. 2024b), pointing to a wider variety of progenitor systems and powering mechanisms than previously appreciated.

Some of this diversity arises from variations in the immediate circumstellar environment. Interactions between SN ejecta and dense CSM, for instance, can dramatically alter the light curve and spectral features (Smith 2017; Khatami et al. 2024), sometimes masking the intrinsic nature of the explosion (e.g., thermonuclear explosion of white dwarf inside a dense CSM; Wang et al. 2004; Silverman et al. 2013b). The origin of the CSM depends on the progenitor. It could be from mass-loss winds (Smith 2014) or eruptive luminous blue variable (LBV) episodes (Humphreys et al. 1994). Multiple rebrightenings can occur when shells of previously ejected material collide, as in the case of pulsational pair-instability SNe (Barkat et al. 1967; Rakavy et al. 1967; Woosley 2017). In other cases, the newly formed compact object can act as a central engine and inject energy into the SN ejecta (e.g., magnetar; Ostriker et al. 1971; Gaffet 1977; Kasen et al. 2010; Woosley 2010 or fallback accretion; Chevalier 1989; Zhang et al. 2008; Dexter et al. 2013; Moriya et al. 2019a) which can produce long-lived, luminous transients that cannot be explained by just radioactive power from  $^{56}\text{Ni}$  decay (Arnett 1982). Disentangling the roles of progenitor type, explosion mechanism, and post-explosion environment is critical for understanding these systems.

While high-cadence surveys have enabled the discovery of large numbers of SNe, it is spectroscopy that allows us to classify them and understand their nature. However, transient astronomy is increasingly experiencing a classification bottleneck. Systematic surveys that target spectroscopic completeness are limited to bright transients ( $m_{peak} \leq 18.5$  mag; Fremling et al. 2020; Perley et al. 2020), leaving a vast

population of fainter events uncharacterized. Fully-robotic dedicated spectrographs on relatively small apertures (1–2 meter class) that are optimized for transient classification have proven their utility in managing this bottleneck; however, in the upcoming Rubin (Ivezic et al. 2019) era, this situation will be made worse. Thus, there is a need for dedicated robotic follow-up facilities for classifying transients.

The modern transient pipeline—from robotic discovery machines to automated triggering (Andreoni et al. 2021; Rehemtulla et al. 2024) to robotic spectroscopy is largely autonomous. However, the next step, deducing classifications from spectra, requires an astronomer’s input. Moreover, even with the current spectroscopic data volume, visual analysis of the spectra for classification is a cumbersome and time-consuming manual task that delays sorting interesting SNe from the typical ones. This is a big-data classification problem and thus well-suited for artificial intelligence (AI). Recent advances in deep learning can offer solutions for diverse astronomical problems and datasets. Leveraging AI for rapid transient classification and dissemination will allow for the timely addition of confirmed SNe to the public servers and thus help quickly identify rare, extreme, and new types of SNe for further follow-up. Studying these peculiar SNe systematically offers insight into the deathly throes toward the very end of the stellar life cycle and increases our understanding of interactions between binary companions, eruptive mass loss, compact object formation, etc. However, it is easier said than done, as most AI models are data-hungry, but the rate of occurrence of transients in a flux-limited survey is not evenly distributed (see Figure 1.2), which in turn causes the models to be biased and not perform robustly.

This thesis aims to address the phenomena behind some subsets of transients characterized by long-lived and/or bumpy light curves that fall outside the well-studied classes, such as Type IIn. These include: i) Type Ia-CSM SNe, where thermonuclear explosions appear to interact with massive hydrogen-rich circumstellar environments, raising questions about the nature of the progenitor system and whether the explosion is truly of Type Ia origin; and ii) double-peaked Type Ibc supernovae, where core-collapse SNe show two distinct but related peaks which often need a combination of powering mechanisms to explain. In addition to characterizing these rare transients, this thesis also addresses the observational challenge of rapid and accurate classification amidst an ever-growing stream of candidates through a new spectrograph and a deep-learning-based automatic classification tool, enabling timely spectroscopic follow-up and in-depth study.

### 1.1 Metamorphing Type Ia: SNe Ia-CSM

Several subtypes of core-collapse supernovae (CCSNe) exhibit strong interaction with circumstellar material. SNe IIn (Schlegel 1990; Filippenko 1997) are thought to originate from massive stars like luminous blue variables (LBVs), with CSM shaped by eruptive mass loss (Gal-Yam et al. 2007; Kiewe et al. 2012; Smith 2014). In contrast, the hydrogen- and/or helium-poor CSM seen in SNe Ibn (Pastorello et al. 2008; Foley et al. 2007; Chugai 2009; Hosseinzadeh et al. 2017) and SNe Icn (Gal-Yam et al. 2022; Perley et al. 2022b; Pellegrino et al. 2022) likely stems from wind-driven or binary stripping of massive Wolf-Rayet progenitors. A rare subclass of thermonuclear SNe Ia, known as SN Ia-CSM, also shows strong interaction with hydrogen-rich CSM. This class of objects shows a spectral metamorphosis—from appearing normal Type Ia-91T-like at early times to transforming into Type IIn-like soon after. SNe Ia-CSM challenge the progenitor debate between the double-degenerate (DD) scenario (Webbink 1984; Iben et al. 1984) (binary white dwarf merger) and the single-degenerate (SD) channel (Whelan et al. 1973) (accretion from a non-degenerate companion onto the white dwarf, triggering thermonuclear runaway). While DD scenarios have strong observational support from nearby SNe Ia (Nugent et al. 2011; Li et al. 2011; Bloom et al. 2011; Brown et al. 2012), Ia-CSM events provide strong evidence for the SD channel.

Notable examples of Type Ia-CSM SNe include SNe 2002ic (Hamuy et al. 2003) and 2005gj (Aldering et al. 2006), but these SNe were strongly interacting from very early times, and thus their SNe Ia origin was unclear. PTF11kx (Dilday et al. 2012) was the first supernova that showed a clear SN Ia-like evolution for  $\sim 60$  days and then evolved into resembling SNe 2002ic and 2005gj. Despite strong spectral similarities with SNe IIn once interaction begins, SNe Ia-CSM appear to differ subtly in some observational properties, specifically  $H\beta$  and helium line strengths (Silverman et al. 2013b). The only prior sample study, Silverman et al. (2013b), analyzed a sample of 16 SN Ia-CSM collected from various surveys that does not allow for putting robust constraints on their rates. In Chapter 2, I present 12 new SNe Ia-CSM discovered by ZTF collected systematically as part of the Bright Transient Survey. I quantitatively analyze the differences between the interaction-dominated spectra of SNe Ia-CSM and SNe IIn and put strong constraints on their observed rates.

### 1.2 Metamorphing Type Ibc: Double-peaked SNe

Stripped-envelope supernovae (SESNe) are the explosions of massive stars ( $\gtrsim 8 M_{\odot}$ ) that have lost most or all of their outer envelopes. They include Types I Ib (some H), Ib

(no H, some He), and Ic (neither H nor He). Hundreds of SESNe have been observed in the last decade and have shed light on several aspects of their progenitors and powering mechanisms. Binary interaction appears essential for envelope stripping, supported by low ejecta masses, observed rates (Smith 2011), and post-explosion companion detection in SN 2022jli (Chen et al. 2024). Light-curve modeling often relies on  $^{56}\text{Ni}$ -powered analytic models (Arnett 1982), but some SESNe require alternative mechanisms to explain unusual features or high luminosities (Sollerman et al. 2022; Rodríguez et al. 2024). However, in the last few years, time-domain surveys have revealed a growing number of SESNe that exhibit double-peaked light curves. These unusual SESNe do not constitute a uniform group, but show a wide range of photometric and spectroscopic behavior with pockets of homogeneity.

Some double-peaked SESNe show a rapid early decline ( $t_{1/2} \lesssim 5$  days), often attributed to shock cooling in extended envelopes or nearby CSM (Nakar et al. 2014; Piro 2015; Jin et al. 2021; Crawford et al. 2025; Das et al. 2024), while others display diverse light-curve morphologies, durations, and luminosities. Several powering mechanisms (or combinations thereof) have been proposed for the latter, namely double-nickel distribution (Folatelli et al. 2006; Gutiérrez et al. 2021; Orellana et al. 2022), delayed or variable magnetar spin-down energy injection (Moriya et al. 2022), CSM interaction (Khatami et al. 2024), fallback accretion (Dexter et al. 2013), eruptive precursors (Damineli et al. 1997; Woosley et al. 2015), and pulsational pair-instability events (Woosley 2017). While some mechanisms have distinctive signatures (e.g., narrow emission lines for CSM interaction), many can produce similar light curves with fine-tuning, complicating the interpretation of these SNe's origin. Therefore, models must predict certain specific observable signatures (for example, changes in the light curve shape, colors, or spectral line profiles) or have restrictions on the feasibility of some light curve properties (for example, duration between peaks, relative brightness of the peaks, or rise and decline rates), which can narrow down the possible powering mechanism. However, these peculiar objects and the plethora of proposed models are seldom analyzed as a group; doing so could illuminate missing connections and reduce the need for fine-tuning models to individual objects.

In Chapters 3 and 4, I present new observations and analysis of three unusual double-peaked SESNe discovered by ZTF: SN 2023aew, SN 2021uvy, and SN 2022hgk. All three SESNe differ in peak luminosities, timescales, and light curve shapes. For SN 2023aew, I explore all possible powering mechanisms in Chapter 3. In

Chapter 4, I analyze a sample of 12 published double-peaked SESNe from the ZTF archive to investigate whether specific light-curve features correlate with particular powering scenarios and assess their potential as a photometric subclass.

### 1.3 Instrumentation and AI for optimal classification of SNe

To date, the most efficient among current transient classification instruments is the SED-Machine (Blagorodnova et al. 2018; Rigault et al. 2019) on the Palomar 60-inch telescope (P60) in Southern California—an ultra-low resolution ( $R \sim 100$ ) IFU spectrograph that has classified  $> 5500$  transients on the Transient Name Server (TNS; 42% of total classifications on TNS since the beginning of ZTF,  $2\times$  more than the next best instrument, see Kulkarni 2020). Being robotic, SEDM also has low overheads, can be integrated easily with automated follow-up triggering systems, and has a fast turnaround, which is the need of the hour for follow-up of fast transients like gamma ray burst (GRB) afterglows (Ho et al. 2020), fast blue optical transients (Ho et al. 2019; Ho et al. 2023), and electromagnetic counterparts of gravitational waves (EMGW; Abbott et al. 2017; Kasliwal et al. 2017). Despite the remarkable success of SEDM for bright transients, large-scale classification efforts still suffer from two bottlenecks.

First, SEDM’s sensitivity limits it to transients brighter than  $\sim 19$  magnitude ( $r$  band). With another SEDM-like instrument on a larger aperture telescope that has the same robotic capabilities, the spectroscopic completeness of flux-limited surveys can be pushed deeper. For my thesis, I led the commissioning of SEDM-KP—an upgraded iteration of SEDM on the robotic 84-inch telescope (KP84) at Kitt Peak National Laboratory in Tucson, Arizona. Working with the Caltech Optical Observatories (COO) engineering team, I refined and tested the robotic operations software and troubleshooted the numerous engineering challenges encountered with the telescope and the instrument. I also established the automatic IFU data reduction pipeline. In Chapter 5, I detail the commissioning process and initial performance of SEDM-KP compared to SEDM.

Second, SN classification is largely a manual task. Traditional classification aids such as SNID (Blondin et al. 2007), Superfit (Howell et al. 2005), and Gelato (Harutyunyan et al. 2008) rely on supernova template matching, often requiring user input and struggling with low signal-to-noise data or spectra with host galaxy contamination. These methods are also slow and scale poorly to the large volumes of data produced by modern surveys. Deep learning offers a scalable alternative and

was first explored for SN classification by Muthukrishna et al. (2019a), in which the authors presented DASH—a deep-learning multi-type classifier trained using SNID templates. Fremling et al. (2021) found that DASH did not perform well on SEDM’s low-resolution data and thus developed *SNIascore*—a deep-learning classifier specifically tailored to SEDM. With  $> 90\%$  accuracy and  $< 0.6\%$  false positive rate (see Figure 1.3), *SNIascore* automated half the classification workload for BTS and enabled robust submissions of classifications to TNS within  $\sim 11$  minutes of spectrum acquisition. Alongside BTSbot (Rehemtulla et al. 2024), it enabled the first fully automated discovery-to-classification pipeline (Rehemtulla et al. 2023). While SNe Ia classification benefits from their spectral homogeneity and abundance in flux-limited surveys, core-collapse SNe (CCSNe) are more diverse and harder to classify, especially with ultra-low resolution data. Within BTS, the majority of CCSNe are hydrogen-rich Type II ( $\sim 72\%$ ), dominated by SNe IIP/L ( $\sim 76\%$  of Type II), while stripped-envelope SNe (SESNe) include SNe Ibc ( $\sim 59\%$ ), Ic-BL, SLSNe, and rare subtypes like Icn and Ibn (Perley et al. 2020). This class imbalance, spectral heterogeneity, and low resolution of SEDM complicate automated classification for CCSNe, especially for subtypes requiring the resolution of narrow features ( $\sim 100 \text{ km s}^{-1}$ ).

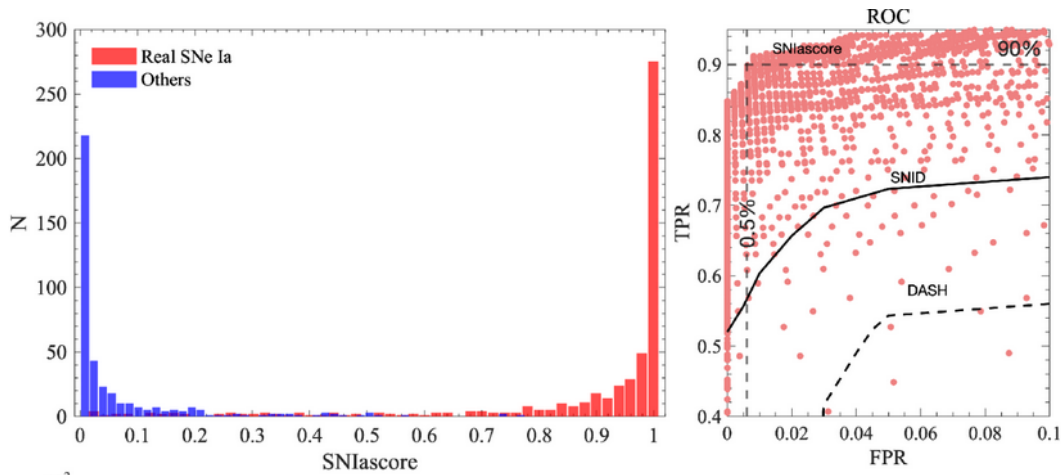


Figure 1.3: *Left:* Histogram of SNIascore values (probability of a sample being a SN Ia) predicted for true SNe Ia (red) and other transients (blue). For a well-performing classifier, this distribution should be bimodal with true SNe Ia getting a higher SNIascore. *Right:* True positive rate (true SNe Ia that get classified as SNe Ia) vs. false positive rate (other SNe that get classified as SNe Ia) of SNIascore, compared with the same for SNID and DASH. SNIascore performs much better than either SNID or DASH on SEDM data. Figure 4 from Fremling et al. (2021).

To address this, I developed *CCSNscore*, a deep learning-based classifier for CCSNe

trained on SEDM spectra, spectra from the Open Supernova Catalog data (Guillochon et al. 2017), and ZTF photometry. The tool was optimized for handling the challenges of heterogeneity, noise, and low-resolution data in core-collapse SN classification. In Chapter 6, I present its performance and limitations on a defined test sample and the expected performance during real-time implementation.

*Chapter 2*

A SYSTEMATIC STUDY OF IA-CSM SUPERNOVAE FROM THE  
ZTF BRIGHT TRANSIENT SURVEY

Sharma, Y. et al. (May 2023). “A Systematic Study of Ia-CSM Supernovae from the ZTF Bright Transient Survey”. In: *ApJ* 948.1, 52, p. 52. DOI: 10.3847/1538-4357/acbc16.

Yashvi Sharma<sup>1</sup>, Jesper Sollerman<sup>2</sup>, Christoffer Fremling<sup>1</sup>, Shrinivas R. Kulkarni<sup>1</sup>, Kishalay De<sup>3</sup>, Ido Irani<sup>4</sup>, Steve Schulze<sup>5</sup>, Nora Linn Strotjohann<sup>4</sup>, Avishay Gal-Yam<sup>4</sup>, Kate Maguire<sup>6</sup>, Daniel A. Perley<sup>7</sup>, Eric C. Bellm<sup>8</sup>, Erik C. Kool<sup>2</sup>, Thomas G. Brink<sup>9</sup>, Rachel Bruch<sup>4</sup>, Maxime Deckers<sup>6</sup>, Richard Dekany<sup>10</sup>, Alison Dugas<sup>11</sup>, Alexei V. Filippenko<sup>9</sup>, Samantha Goldwasser<sup>4</sup>, Matthew J. Graham<sup>1</sup>, Melissa L. Graham<sup>8</sup>, Steven L. Groom<sup>12</sup>, Matt Hankins<sup>13</sup>, Jacob Jencson<sup>14</sup>, Joel P. Johansson<sup>5</sup>, Viraj Karambelkar<sup>1</sup>, Mansi M. Kasliwal<sup>1</sup>, Frank J. Masci<sup>12</sup>, Michael S. Medford<sup>15,16</sup>, James D. Neill<sup>1</sup>, Guy Nir<sup>9</sup>, Reed L. Riddle<sup>10</sup>, Mickael Rigault<sup>17</sup>, Tassilo Schweyer<sup>2</sup>, Jacco H. Terwel<sup>6,18</sup>, Lin Yan<sup>1</sup>, Yi Yang<sup>9</sup>, and Yuhan Yao<sup>1</sup>

<sup>1</sup>Division of Physics, Mathematics and Astronomy, California Institute of Technology, Pasadena, CA, 91125, USA

<sup>2</sup>Department of Astronomy, The Oskar Klein Center, Stockholm University, AlbaNova, SE-10691 Stockholm, Sweden

<sup>3</sup>MIT-Kavli Institute for Astrophysics and Space Research, Cambridge, MA, 02139, USA

<sup>4</sup>Department of Particle Physics and Astrophysics, Weizmann Institute of Science, 234 Herzl Street, 76100 Rehovot, Israel

<sup>5</sup>Department of Physics, The Oskar Klein Center, Stockholm University, AlbaNova, SE-10691 Stockholm, Sweden

<sup>6</sup>School of Physics, Trinity College Dublin, the University of Dublin, College Green, Dublin, Ireland

<sup>7</sup>Astrophysics Research Institute, Liverpool John Moores University, Liverpool Science Park, 146 Brownlow Hill, Liverpool, L3 5RF, UK

<sup>8</sup>DIRAC Institute, Department of Astronomy, University of Washington, 3910 15th Avenue NE, Seattle, WA, 98195, USA

<sup>9</sup>Department of Astronomy, University of California, Berkeley, CA, 94720-3411, USA

<sup>10</sup> Caltech Optical Observatories, California Institute of Technology, Pasadena, CA, 91125, USA

<sup>11</sup> Institute for Astronomy, University of Hawai'i, Honolulu, HI, 96822, USA

<sup>12</sup> IPAC, California Institute of Technology, 1200 E. California Boulevard, Pasadena, CA, 91125, USA

<sup>13</sup> Arkansas Tech University, Russellville, AR, 72801, USA

<sup>14</sup> Steward Observatory, University of Arizona, 933 North Cherry Avenue, Tucson, AZ, 85721-0065, USA

<sup>15</sup> Department of Astronomy, University of California, Berkeley, Berkeley, CA, 94720, USA

<sup>16</sup> Lawrence Berkeley National Laboratory, 1 Cyclotron Road, Berkeley, CA, 94720, USA

<sup>17</sup> Université Clermont Auvergne, CNRS/IN2P3, Laboratoire de Physique de Clermont, F-63000 Clermont-Ferrand, France

<sup>18</sup> Isaac Newton Group (ING), Apt. de correos 321, E-38700, Santa Cruz de La Palma, Canary Islands, Spain

## Abstract

Among the supernovae (SNe) that show strong interaction with the circumstellar medium, there is a rare subclass of Type Ia supernovae, SNe Ia-CSM, that show strong narrow hydrogen emission lines, much like SNe IIn but on top of a diluted Type Ia spectrum. The only previous systematic study of this class (Silverman et al. 2013b) identified 16 SNe Ia-CSM, 8 historic, and 8 from the Palomar Transient Factory (PTF). Now using the successor survey to PTF, the Zwicky Transient Facility (ZTF), we have classified 12 additional SNe Ia-CSM through the systematic Bright Transient Survey (BTS). Consistent with previous studies, we find these SNe to have slowly evolving optical light curves with peak absolute magnitudes between  $-19.1$  and  $-21$ , spectra having weak  $H\beta$ , and large Balmer decrements of  $\sim 7$ . Out of 10 SNe from our sample observed by NEOWISE, 9 have  $3\sigma$  detections, with some SNe showing a reduction in red wing of  $H\alpha$ , indicative of newly formed dust. We do not find our SN Ia-CSM sample to have a significantly different distribution of equivalent width of He I  $\lambda 5876$  than SNe IIn as observed in Silverman et al. (2013b). The hosts tend to be late-type galaxies with recent star formation. We derive a rate estimate of  $29_{-21}^{+27} \text{ Gpc}^{-3} \text{ yr}^{-1}$  for SNe Ia-CSM which is  $\sim 0.02\text{--}0.2\%$  of the SN Ia rate. We also identify 6 ambiguous SNe IIn/Ia-CSM in the BTS sample, and including them gives an upper limit rate of  $0.07\text{--}0.8\%$ . This work nearly doubles the sample of well-studied Ia-CSM objects in Silverman et al. (2013b), increasing the total number to 28.

## 2.1 Introduction

When it comes to supernovae (SNe) interacting with circumstellar material (CSM), a number of sub-types of core-collapse SNe (CCSNe) show signs of strong interaction, like SNe IIn (Schlegel 1990; Filippenko 1997), SNe Ibn (Pastorello et al. 2008; Foley et al. 2007; Chugai 2009; Hosseinzadeh et al. 2017) and most recently SNe Icn (Gal-

Yam et al. 2021; Gal-Yam et al. 2022; Perley et al. 2022b). SN IIn progenitors are generally thought to be massive stars (like Luminous Blue Variables, LBVs) that lose their hydrogen envelopes to wind-driven mass loss and outbursts (Gal-Yam et al. 2007; Gal-Yam et al. 2009; Kiewe et al. 2012; Taddia et al. 2013; Smith 2014). Helium-rich but hydrogen-deficient CSM in the case of SNe Ibn (Pastorello et al. 2008; Foley et al. 2007; Chugai 2009) and both hydrogen and helium deficient CSM in SNe Icn (Gal-Yam et al. 2022; Perley et al. 2022b; Pellegrino et al. 2022) are thought to arise from high-velocity wind mass loss or stripping of the envelope in binary configurations of massive Wolf-Rayet (WR) like stars. For SNe IIn in most cases, the mass-loss rate derived from the CSM velocity is consistent with estimates from LBV-like eruptive mass loss.

However, there exists a rare subtype of thermonuclear supernovae (SNe Ia) which also interacts strongly with CSM, i.e., SNe Ia-CSM. This class poses a challenge to the progenitor debate of SNe Ia. There is some consensus on there being at least two major progenitor channels for SNe Ia; the double-degenerate (DD) channel (Webbink 1984; Iben et al. 1984) which is the merging of two C/O white dwarfs and the single-degenerate (SD) channel (Whelan et al. 1973) where the white dwarf accretes enough material from a non-degenerate companion to explode. Although there are more arguments for the DD scenario from observations of nearby SNe Ia (Nugent et al. 2011; Li et al. 2011; Brown et al. 2012; Bloom et al. 2011), the strongest observational evidence for the SD scenario are SNe Ia with CSM.

Indications of CSM around SNe Ia range from detection of time varying narrow Na ID absorption lines (Patat et al. 2007; Blondin et al. 2009; Simon et al. 2009) in high-resolution spectra (found in at least 20% of SNe Ia in spiral hosts, Sternberg et al. 2011; Maguire et al. 2013; Clark et al. 2021), to strong intermediate and narrow Balmer emission features in the spectra and large deviations of the light curves from the standard shape. The latter phenomena have been named SNe Ia-CSM (Silverman et al. 2013b), but were earlier referred to as “SNe IIna” or “SNe Ian” due to the strong similarity between their spectra and those of SNe IIn. The first two examples of this class studied in detail were SNe 2002ic (Hamuy et al. 2003; Deng et al. 2004; Wang et al. 2004; Wood-Vasey et al. 2004; Kotak et al. 2005; Chugai et al. 2004a) and 2005gj (Aldering et al. 2006; Prieto et al. 2007), but for a long time there was ambiguity regarding their thermonuclear nature (Benetti et al. 2006). These SNe were dominated by interaction from the first spectrum and were quite over-luminous compared to normal SNe Ia. The first clear example of

a thermonuclear SN Ia-CSM was PTF11kx (Dilday et al. 2012; Silverman et al. 2013a). It looked like a luminous SN Ia (99aa-like, Filippenko et al. 1999) at early phases but started showing interaction at  $\sim 60$  days from explosion and thereafter strongly resembled SNe 2002ic and 2005gj at late times. Higher resolution spectra taken at early times indicated multiple shells of CSM with some evacuated regions in between. Dilday et al. (2012) suggested a symbiotic nova progenitor involving a WD and a red giant (similar to RS Ophiuchi) could produce such CSM distribution; however, later studies argued that the massive CSM of PTF11kx was inconsistent with the mass-loss rates from symbiotic nova systems (Silverman et al. 2013a; Soker et al. 2013b).

Ever since, a handful of SNe of this class have been studied in detail to investigate their progenitors and to distinguish them from their spectroscopic cousins, the Type IIn SNe. Both SN Ia-CSM and SN IIn spectra share a blue quasi-continuum, a strong  $H\alpha$  feature with an intermediate and a narrow component, and often a broad Ca NIR triplet feature, but they differ with regards to the line strength of  $H\beta$ , strength/presence of helium, and presence of emission lines from intermediate mass elements often found in CCSNe. There are some individual SNe with unclear type often referred to as SN Ia-CSM/IIn, like SN 2012ca, for which some papers argue for core-collapse (Inserra et al. 2014; Inserra et al. 2016) and others for a thermonuclear origin (Fox et al. 2015). This ambiguity becomes more dominant as the underlying SN flux gets smaller compared to the interaction power (Leloudas et al. 2015). Silverman et al. (2013b, hereafter S13) is the only study to analyze a sample of SNe Ia-CSM, 16 objects in total, including 6 previously known, 3 re-discovered (re-classified SNe IIn), and 7 new from the Palomar Transient Factory (PTF). Their paper presents the common properties of optical light curves, spectra, and host galaxies and contrasts them against SN IIn properties. In this paper, we present 12 new SNe Ia-CSM discovered as part of the Zwicky Transient Facility’s (ZTF; Bellm et al. 2019; Graham et al. 2019; Dekany et al. 2020) Bright Transient Survey (BTS; Fremling et al. 2020; Perley et al. 2020) and analyze their optical light curves, spectra, hosts, and rates. Throughout this paper, we have compared the results derived from our sample to those in S13.

This paper is organised as follows: we first discuss the sample selection criteria, the photometric and spectroscopic data collection in §2, and then the analysis of light- and color-curves and the bolometric luminosities is done in §3.1. The analysis of early and late-time spectra and emission line identification is presented in §3.2, and

analysis of the host galaxies is provided in §3.3. The rates are estimated from the BTS survey in §3.4. We end with a discussion about the nature of SN Ia-CSM progenitors and a summary in §4 and §5.

## 2.2 Observations and Data reduction

In this section, we outline our selection criteria and present the optical photometry and spectroscopic observations of the 12 SNe Ia-CSM in our sample.

### Selection Criteria

To carefully curate our sample of SNe Ia-CSM, we used the BTS sample and its publicly available BTS Sample Explorer<sup>1</sup> website to obtain the list of all classified Type Ia sub-types during the period 2018-05-01 to 2021-05-01. We then filter out oddly behaving Type Ia SNe based on their light-curve properties. We used two criteria: the primary being rest-frame duration considering flux above 20% of peak flux, and the second being change in magnitude after 30 days from peak ( $\Delta m_{30}$ ). We calculated these two properties from either  $g$  or  $r$ -band light curves (whichever had the maximum number of detections) grouped into 3-day bins and used Gaussian Process Regression<sup>2</sup> to interpolate the light curves where coverage was missing. For the first filtering, we calculated the mean ( $\mu \approx 35$  days) and standard deviation ( $\sigma \approx 16$  days) of the duration distribution and selected everything that had a duration greater than  $\mu + 3\sigma$ . Given the large sample size ( $N = 3486$ ), the standard error on the mean is  $\sim 0.5$  days. Hence, our duration cut of  $3\sigma$  is suitable. This filtering selected 41 out of 3,486 BTS SNe Ia. Then, from these 41 SNe, we calculated the mean and standard deviation of the  $\Delta m_{30}$  distribution and removed SNe that were more than  $1\sigma$  away from the mean on the higher side to reject the relatively steeply declining long SNe, which resulted in 35 SNe being kept. Again, the mean and standard deviation of the  $\Delta m_{30}$  distribution of these 41 long-duration SNe are 0.48 mag and 0.27 mag, respectively, and the standard error on the mean is  $\sim 0.04$ , making our  $1\sigma$  cut suitable. Finally, we manually inspected the 35 selected SNe Ia to confirm their classification. Out of the 35 SNe that passed the above filtering criteria, 20 were just normal SNe Ia either caught late or missing some post-peak coverage in ZTF or had spurious detections that resulted in long duration estimates, 2 had incorrect duration estimate due to an interpolation error and were recalculated, and 1 (AT2020caa; Soraisam et al. 2021) had some detections before the SN explosion

<sup>1</sup><https://sites.astro.caltech.edu/ztf/bts/explorer.php>.

<sup>2</sup>Pedregosa et al. (2011) [https://scikit-learn.org/stable/modules/gaussian\\_process.html](https://scikit-learn.org/stable/modules/gaussian_process.html).

Table 2.1: Properties of the 12 BTS SNe Ia-CSM.

ZTF Name	IAU Name	$z$	$M_r^{\text{peak}}$ (mag)	Duration <sup>1</sup> (days)	Host Name	Host Mag <sup>2</sup> ( $m_r$ )
ZTF18aaykjei	SN 2018crl	0.097	-19.66	130	SDSS J161938.90+491104.5	18.89
ZTF18abuafp	SN 2018gkx	0.1366	-20.07	322	SDSS J135219.22+553830.2	18.23
ZTF18actuhrs	SN 2018evt	0.02378	-19.10	447	MCG-01-35-011	14.07
ZTF19aaeoqst	SN 2019agi	0.0594	<-18.76	>303	SDSS J162244.06+240113.4	17.82
ZTF19abidbqp	SN 2019ibk	0.04016	<-17.55	>576	SDSS J014611.93-161701.1	15.55
ZTF19acbjddp	SN 2019rvb	0.1835	-20.74	172	WISEA J163809.90+682746.3	20.44
ZTF20abmlrx	SN 2020onv	0.095	<-20.36	>154	WISEA J231646.31-231839.9	17.95
ZTF20abqkbfx	SN 2020qxz	0.0964	-20.00	166	WISEA J180400.99+740050.0	17.65
ZTF20accmutv	SN 2020uem	0.041	<-20.17	>279	WISEA J082423.32-032918.6	15.88
ZTF20aciwcuz	SN 2020xtg	0.0612	<-19.60	>336	SDSS J153317.64+450022.8	15.42
ZTF20acqikeh	SN 2020abfe	0.093	-20.24	171	SDSS J200003.30+100904.2	20.18
ZTF21aaabwzx	SN 2020aekp	0.046	-19.62	458	SDSS J154311.45+174843.7	18.41

<sup>1</sup> Rest frame duration above 20% of  $r$ -band peak flux, uncertainty of  $\pm 2 - 3$  days from ZTF cadence.

<sup>2</sup> Corrected for Galactic extinction.

which could be connected to a different SN (i.e. a sibling; Graham et al. 2022a).

The remaining 12 long-duration SNe Ia all turned out to be spectroscopically classified SNe Ia-CSM in BTS, and none of the classified BTS SNe Ia-CSM were missed in this filtering. No other SNe apart from these stood out in particular, indicating the classification reliability of the BTS sample. During the same period, 9 SNe Ia-CSM were reported to the Transient Name Server (TNS), out of which 7 are already in our sample, 1 was detected by ZTF but did not meet the BTS criteria, and 1 was not detected in ZTF as the transient location fell too close to the field edges and was masked by the automated image subtraction pipeline. Yao et al. (2019) presented early photometric observations of one SN Ia-CSM in our sample, SN 2018crl. Table 2.1 summarizes the coordinates, redshifts, peak absolute magnitudes, durations, host galaxy information, and Milky Way extinction for the 12 SNe Ia-CSM in our sample.

Furthermore, we re-checked the classifications of 142 SNe II<sub>n</sub> classified in BTS during the same period as above, in case any SN Ia-CSM was masquerading among them, and found 6 to have ambiguous classifications. These are discussed further in Appendix 2.7.

## Discovery

All SNe Ia-CSM were detected by the ZTF (Bellm et al. 2019; Graham et al. 2019; Dekany et al. 2020) and passed the criteria for the BTS (Fremming et al. 2020; Perley et al. 2020) automatic filtering, i.e., extra-galactic real transients with peak magnitudes brighter than 19 mag. These were saved and classified as part of BTS,

which aims to classify all transients brighter than 18.5 magnitude, and reported to the Transient Name Server<sup>3</sup> (TNS) during the period 2018-05-01 to 2021-05-01. Out of the 12 SNe, 6 were first reported to TNS (i.e., discovered) by ZTF (AMPEL, Nordin et al. 2019; Soumagnac et al. 2018 and BTS), 3 were first reported by GaiaAlerts (Hodgkin et al. 2021), 2 by ATLAS (Smith et al. 2020), and 1 by ASAS-SN (Shappee et al. 2014). For classification, 9 were classified by the ZTF group, 1 by ePESSTO (Smartt et al. 2015; Stein et al. 2018a), 1 by SCAT (Tucker et al. 2018; Payne et al. 2019), and 1 by the Trinity College Dublin (TCD) group (Prentice et al. 2020). The follow-up spectral series for these SNe were obtained as part of the BTS classification campaign, as many were difficult to classify with the ultra-low resolution spectrograph P60/SEDM (Blagorodnova et al. 2018) and hence were followed up with intermediate resolution spectrographs. The SEDM spectra were helpful in determining an initial redshift, but the template matches were unclear (matched to SN IIn as well as SN Ia-CSM and SN Ia-pec templates, some matched poorly to SN Ia/Ic at early times). SNe 2019agi (classification and spectrum taken from TNS), 2019rvb, 2020onv, 2020qxz, and 2020uem were classified as Ia-CSM  $\sim$ 1–2 months after discovery using spectra at phases of 42, 26, 38, 45, and 51 days, respectively. SNe 2018crl, 2018gkx, and 2019ibk were classified  $\sim$ 2–3 months after discovery using spectra at phases of 92, 75, and 103 days, respectively. SNe 2018evt, 2020abfe, and 2020aekp were classified  $\sim$ 4–5 months after discovery using the spectra at phases of 144, 146, and 132 days, respectively. SN 2020xtg immediately went behind the sun after its first detection in ZTF; therefore, its first spectrum (using SEDM) was taken at 91 days since explosion, which was dominated by strong  $H\alpha$  emission, and thus SN 2020xtg was initially classified as a Type II. As this SN was exhibiting a long-lasting light curve, an intermediate resolution spectrum was taken at 340 days, which matched very well to SN Ia-CSM, and therefore its classification was updated. SNe 2020uem and 2020aekp showed peculiar features and were followed up for more optical spectroscopy for single object studies (Cold et al. in prep).

### Optical photometry

To assemble our sample light curves, we obtained forced PSF photometry via the ZTF forced-photometry service (Masci et al. 2019; IRSA 2022) in  $g$ ,  $r$ , and  $i$  bands and also added data from the ATLAS (Tonry et al. 2018; Smith et al. 2020) forced-photometry service in  $c$  and  $o$  bands. The high cadence ZTF partnership survey

---

<sup>3</sup><https://www.wis-tns.org/>.

in the  $i$  band contributed some photometry to SNe 2018crl, 2018gkx, 2019agi, 2019ibk, and 2019rvb. The ZTF and ATLAS data were supplemented with data from the Rainbow camera (RC, Ben-Ami et al. 2012) on the robotic Palomar 60-inch telescope (P60, Cenko et al. 2006) and the Optical wide field camera (IO:O) on the Liverpool telescope (LT, Steele et al. 2004). The P60 data was processed with the automatic image subtraction pipeline FPipe (Fremming et al. 2016) using reference images from SDSS when available, and otherwise from Pan-STARRS1. The IO:O data was initially reduced with their standard pipeline<sup>4</sup>, then image subtraction was carried out using the method outlined in Taggart (2020). For SN 2018evt, some early time data available from ASAS-SN (Shappee et al. 2014; Kochanek et al. 2017) in the  $V$  band was obtained through their *Sky Patrol*<sup>5</sup> interface.

We corrected all photometry for Milky Way extinction with the Python package *extinction* (Barbary 2016) using the dust extinction function from Fitzpatrick (1999), the Schlafly et al. (2011) dust map, and an  $R_V$  of 3.1. Then we converted all measurements into flux units for analysis and considered anything less than a  $3\sigma$  detection an upper limit. There is moderate to good coverage in  $g$ ,  $r$ ,  $c$ , and  $o$  bands for all SNe in our sample. Figure 2.1 shows a multi-paneled figure of the light curves of the objects in our sample.

### Mid-IR photometry

The transients were observed during the ongoing NEOWISE all-sky mid-IR survey in the  $W1$  ( $3.4\ \mu\text{m}$ ) and  $W2$  ( $4.5\ \mu\text{m}$ ) bands (Wright et al. 2010; Mainzer et al. 2014). We retrieved time-resolved coadded images of the field created as part of the unWISE project (Lang 2014; Meisner et al. 2018). To remove contamination from the host galaxies, we used a custom code (De et al. 2020a) based on the ZOGY algorithm (Zackay et al. 2016) to perform image subtraction on the NEOWISE images using the full-depth coadds of the WISE and NEOWISE mission (obtained during 2010-2014) as reference images. Photometric measurements were obtained by performing forced PSF photometry at the transient position on the subtracted WISE images until the epoch of the last NEOWISE data release (data acquired until December 2021). Further analysis of the mid-IR photometry is presented in §2.3

<sup>4</sup><https://telescope.livjm.ac.uk/TelInst/Pipelines/>.

<sup>5</sup><https://asas-sn.osu.edu/>.

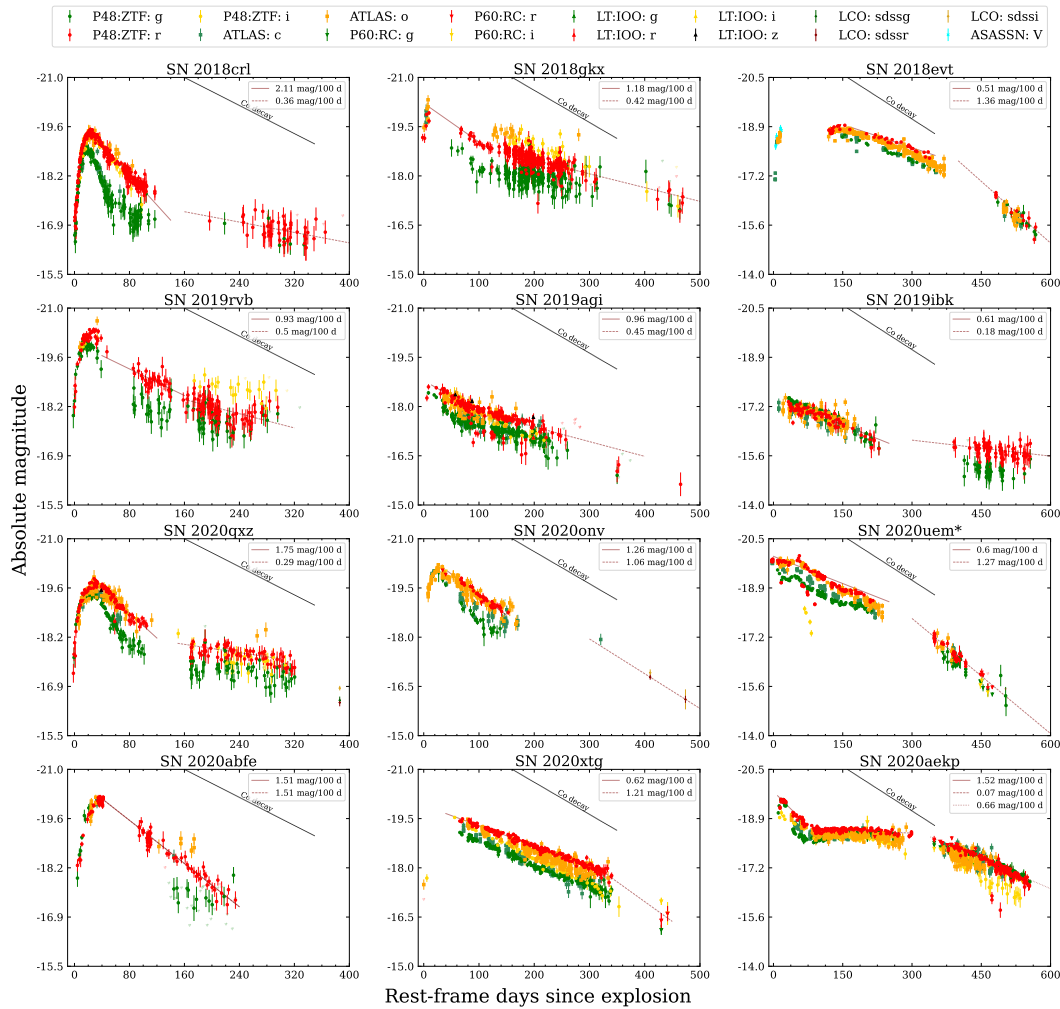


Figure 2.1: Optical light curves of the ZTF BTS SN Ia-CSM sample. The SNe Ia-CSM have longer durations than the average SN Ia, with some variety, like bumpy light curves or long plateaus. The one SN marked with an asterisk (SN 2020uem) has an unconstrained explosion time estimate ( $\sim\pm 50$  d). The decline rate from Cobalt decay is marked with a black dashed line, and the light curve decline rates measured from  $r$ -band data are shown in the subplot legends.

### Optical spectroscopy

The main instruments used for taking spectra and the software used to reduce the data are summarized in Table 2.2. Additionally, the spectrum Reguitti (2020) obtained using the Asiago Faint Object Spectrograph and Camera (AFOSC) on the 1.8-m telescope at Cima Ekar, and the spectrum Stein et al. (2018b) obtained using the ESO Faint Object Spectrograph and Camera version 2 (EFOSC2) on the ESO New Technology Telescope (NTT) were taken from TNS.

Table 2.2: Description of spectrographs used for follow-up and the corresponding data reduction pipelines.

Inst.	Telescope	Reduction Software
SEDM <sup>1</sup>	Palomar 60-inch (P60)	pySEDM <sup>2</sup>
ALFOSC <sup>3</sup>	Nordic Optical Telescope	IRAF <sup>4</sup> , PyNOT <sup>14</sup> , pypeit
DBSP <sup>5</sup>	Palomar 200-inch (P200)	IRAF <sup>6</sup> , DBSP_DRP <sup>7</sup>
KAST <sup>8</sup>	Shane 3-m	IRAF
LRIS <sup>9</sup>	Keck-I	LPipe <sup>10</sup>
SPRAT <sup>11</sup>	Liverpool Telescope	Barnsley et al. (2012)
DIS <sup>12</sup>	APO <sup>13</sup>	IRAF

<sup>1</sup> Spectral Energy Distribution Machine (Blagorodnova et al. 2018)

<sup>2</sup> Rigault et al. (2019)

<sup>3</sup> Andalucia Faint Object Spectrograph and Camera

<sup>4</sup> Tody (1986) and Tody (1993)

<sup>5</sup> Double Beam Spectrograph (Oke et al. 1982)

<sup>6</sup> Standard pipeline by Bellm et al. (2016) used prior to Fall 2020

<sup>7</sup> pypeit (Prochaska et al. 2020) based pipeline ([https://github.com/finagle29/dbsp\\_drp](https://github.com/finagle29/dbsp_drp)) used since Fall 2020

<sup>8</sup> Kast Double Spectrograph (Miller et al. 1987)

<sup>9</sup> Low Resolution Imaging Spectrometer (Oke et al. 1995)

<sup>10</sup> IDL based automatic reduction pipeline<sup>6</sup> (Perley 2019)

<sup>11</sup> Spectrograph for the Rapid Acquisition of Transients (Piascik et al. 2014)

<sup>12</sup> Dual Imaging Spectrograph

<sup>13</sup> Astrophysics Research Consortium telescope at the Apache Point Observatory

<sup>14</sup> <https://github.com/jkrogager/PyNOT>

The details for all optical spectra (61 for the sample in total) presented in this paper are provided in Table 2.3. Furthermore, all spectra were corrected for Milky Way extinction using `extinction` and the same procedure as for the photometry. The SN redshifts were derived using narrow host lines for the objects that did not already have a host redshift available in the NASA/IPAC Extragalactic Database<sup>7</sup> (NED). Photometric calibration was done for all spectra, i.e., they were scaled such that the synthetic photometry from the spectrum matched the contemporaneous host-subtracted ZTF *r*-band data. For SN 2018crl, a host galaxy spectrum taken using P200/DBSP was available, which was subtracted from the P200/DBSP SN spectrum taken at +92 days. For SN 2020aekp, more spectra beyond  $\sim 350$  days were obtained but will be presented in Cold et al. (in prep; 34 additional spectra up to  $\sim 600$  days).

<sup>7</sup><https://ned.ipac.caltech.edu/>.

Table 2.3: Summary of optical spectra.

SN	JD (−2450000)	Epoch (days)	Telescope/Instrument	Int (sec)	SN	JD (−2450000)	Epoch (days)	Tel./Instr.	Int (sec)
SN 2018crl	8282	9	APO/DIS	2400	SN 2020uem	9128	11	P60/SEDM	1800
	8288	15	P60/SEDM	2700		9136	18	P60/SEDM	1800
	8295	21	P60/SEDM	2700		9170	51	Ekar/AFOSC	1200
	8306	31	P60/SEDM	2700		9222	101	Lick-3m/KAST	3600
	8373	92	P200/DBSP	600		9252	130	Lick-3m/KAST	2700
(Host)	8627	324	P200/DBSP	900	9263	140	Lick-3m/KAST	2400	
SN 2018gkx	8457	75	Keck1/LRIS	300	9291	167	NOT/ALFOSC	900	
SN 2018evt	8343	9	NTT/EFOSC2	300	9481	349	P60/SEDM	2160	
	8465	127	P60/SEDM	1200	9492	360	Keck1/LRIS	600	
	8481	143	P60/SEDM	1200	9583	448	P60/SEDM	2160	
	8481	144	LT/SPRAT	1000	9586	451	P60/SEDM	2160	
	8534	195	P60/SEDM	1200	SN 2020xtg	9226	91	P60/SEDM	2160
SN 2019agi	8547	42	UH88/SNIFS	1820	9491	340	Keck1/LRIS	600	
SN 2019ibk	8691	35	P60/SEDM	2250	9606	448	Keck1/LRIS	1200	
	8695	39	P60/SEDM	2250	SN 2020abfe	9189	27	P60/SEDM	2700
	8697	41	P60/SEDM	2250	9319	146	Keck1/LRIS	400	
	8748	90	P60/SEDM	2250	SN 2020aekp	9224	19	P60/SEDM	2160
	8761	103	P200/DBSP	600	9342	132	P60/SEDM	2160	
SN 2019rvb	8766	14	P60/SEDM	2250	9343	132	NOT/ALFOSC	1200	
	8780	26	P200/DBSP	600	9362	151	P60/SEDM	2700	
SN 2020onv	9058	23	P60/SEDM	1800	9381	169	NOT/ALFOSC	2400	
	9062	27	P60/SEDM	1800	9404	191	P60/SEDM	2700	
	9069	33	P60/SEDM	1800	9425	211	NOT/ALFOSC	1800	
	9070	34	LT/SPRAT	750	9434	220	P60/SEDM	2700	
	9073	37	P60/SEDM	1800	9448	233	P60/SEDM	2700	
	9074	38	NOT/ALFOSC	450	9468	252	P60/SEDM	2700	
SN 2020qxz	9076	13	P60/SEDM	2250	9569	348	P60/SEDM	2700	
	9087	22	P60/SEDM	2250					
	9092	26	NOT/ALFOSC	1800					
	9098	32	P60/SEDM	2250					
	9101	34	NOT/ALFOSC	1200					
	9107	40	P200/DBSP	900					
	9112	45	Keck1/LRIS	300					
	9121	53	P60/SEDM	2250					
	9141	71	Keck1/LRIS	399					

These processed spectra were used for the rest of the analysis as detailed in §2.3 and will be available on WISEREP<sup>8</sup> (Yaron et al. 2012).

## 2.3 Analysis

### Photometry

#### Explosion epoch estimates

For the purpose of this paper, the ‘explosion time’ simply refers to the time when optical flux rises above the zero-point baseline (i.e., first light). We used pre-peak  $g, r, i$ -band ZTF photometry and  $c, o$ -band ATLAS photometry (binned in 1-day bins), when available, for our analysis. For each SN, the light curve was interpolated using Gaussian process regression to obtain the peak flux epoch, then a power-law (PL) model was fit using epochs from baseline to 60% of peak brightness in each band following Miller et al. (2020b). The PL fits converged in at least one

<sup>8</sup><https://www.wiserep.org/>.

band for six out of twelve BTS SNe Ia-CSM. For the rest, we simply took the middle point between the first  $5\sigma$  detection and the last upper limit before this detection as the explosion epoch, with half of the separation between these two points as the uncertainty.

The explosion time estimates, light curve bands used for the PL fits, and the  $1\sigma$  uncertainties on explosion times are listed in Table 2.4. The unfilled ‘PL fit filters’ column in the table are the SNe for which the PL fit did not converge and averages were used. For the PL fits, this typically constrains the time of explosion to within a fraction of a day. Given the high cadence of the ZTF survey, even in the cases where we use only the last non-detection, the uncertainty range is typically less than 3 days. Only for SN 2020uem is the date of explosion virtually unconstrained ( $\pm 57$  days) as it was behind the sun at the time of explosion.

Although for SN 2019ibk the explosion time is formally constrained with a  $\pm 3$  day uncertainty, this estimate was derived using only ATLAS  $o$ -band data right after the SN emerges from behind the sun. There is no clear rise observed over a few epochs, but two non-detections before a  $5\sigma$  detection. It is possible that the actual peak of this SN occurred earlier while it was behind the sun and the rising  $o$ -band points after it emerged are due to a second peak or bump (similar to SN 2018evt, in that case the actual rise was caught before the SN went behind the sun in ASAS-SN data). If the former explosion epoch estimate from the  $o$ -band is to be believed, then SN 2019ibk would be the most sub-luminous among the SNe Ia-CSM, peaking at  $-17.5$ .

### **Duration and absolute magnitudes**

Figure 2.2 shows the SNe Ia-CSM (colored squares) in our sample in the duration-luminosity and duration- $\Delta m_{30}$  phase space. In the top panel, the x-axis is duration above half-max and the y-axis is the peak absolute magnitude (see Table 2.1) when we have photometric coverage both pre-peak and post-peak. For SNe missing the pre-peak coverage, their discovery magnitude is taken to be the upper limit to peak absolute magnitude and the duration from discovery is the lower limit to duration above half-max (marked by arrows in Figure 2.2). The BTS SN Ia sample is shown in gray points, and we also show the SNe Ia-CSM presented in S13 with empty triangles for comparison in the top panel. In the bottom panel, the x-axis is duration above 20% of peak flux ( $\Delta t_{20}$ ) and the y-axis is  $\Delta m_{30}$ , the two parameters used in the selection criteria. Most of the SNe Ia-CSM lie on the longer duration and

Table 2.4: Explosion time epoch estimates derived from pre-peak multi-band light curves. For 6 out of 12 SNe Ia-CSM, we were able to fit a power-law model to multi-band data following Miller et al. (2020b). For the remaining 6 SNe, the explosion epoch was estimated by taking the mean of the first  $5\sigma$  detection and last upper-limit before the first detection.

IAU Name	PL fit filters	$t_o$ (MJD)	$1\sigma$ interval (days)
SN 2018crl	$g, r, o$	58271.83	[-0.48,+0.38]
SN 2018gkx	$r, o$	58371.34	[-0.64,+0.53]
SN 2018evt	-	58334.26	[-2.00,+2.00]
SN 2019agi	-	58502.48	[-1.51,+1.51]
SN 2019ibk	-	58654.61	[-2.99,+2.99]
SN 2019rvb	$g, r, i, o$	58749.16	[-0.79,+0.60]
SN 2020onv	$o$	59032.75	[-2.49,+1.10]
SN 2020qxz	$g, r, o$	59063.05	[-0.51,+0.45]
SN 2020uem	-	59117.03	[-56.63,+56.63]
SN 2020xtg	-	59130.14	[-0.04,+0.04]
SN 2020abfe	$g, r, o$	59159.36	[-2.16,+2.23]
SN 2020aekp	-	59204.53	[-5.50,+5.50]

brighter luminosity side, and are even more distinctly separated in the  $\Delta t_{20}$ - $\Delta m_{30}$  phase space. This makes the SN initial decline rate and duration useful tools for identifying thermonuclear SNe potentially interacting with CSM, if they have not revealed themselves already in their early time spectra. The gray points lying in the same phase space as SNe Ia-CSM are the false positive cases described in §2.1. Also worth noting is that the duration calculated by taking the flux above half of peak flux value does not capture the true duration of the light curve when the plateau phase falls below half-max as is the case for SN 2020aekp ( $> 500$  days light curve) but  $\Delta t_{20}$  and  $\Delta m_{30}$  do.

### Light and color curves

We have good pre-peak coverage in ZTF data for 8 of the 12 SNe in our sample<sup>9</sup>. SN 2018evt was discovered by ASAS-SN on JD 2458341.91 (Nicholls et al. 2018) and classified by ePESSTO the next day (Stein et al. 2018a), around 115 days before the first detection in ZTF when the SN came back from behind the sun. Hence, we have only one epoch of pre-peak photometry and one early spectrum for SN 2018evt.

Our mixed bag of SNe Ia-CSM show post-maximum decline rates ranging from 0.5 to

<sup>9</sup>except for SNe 2018evt, 2019ibk, 2020onv, and 2020uem.

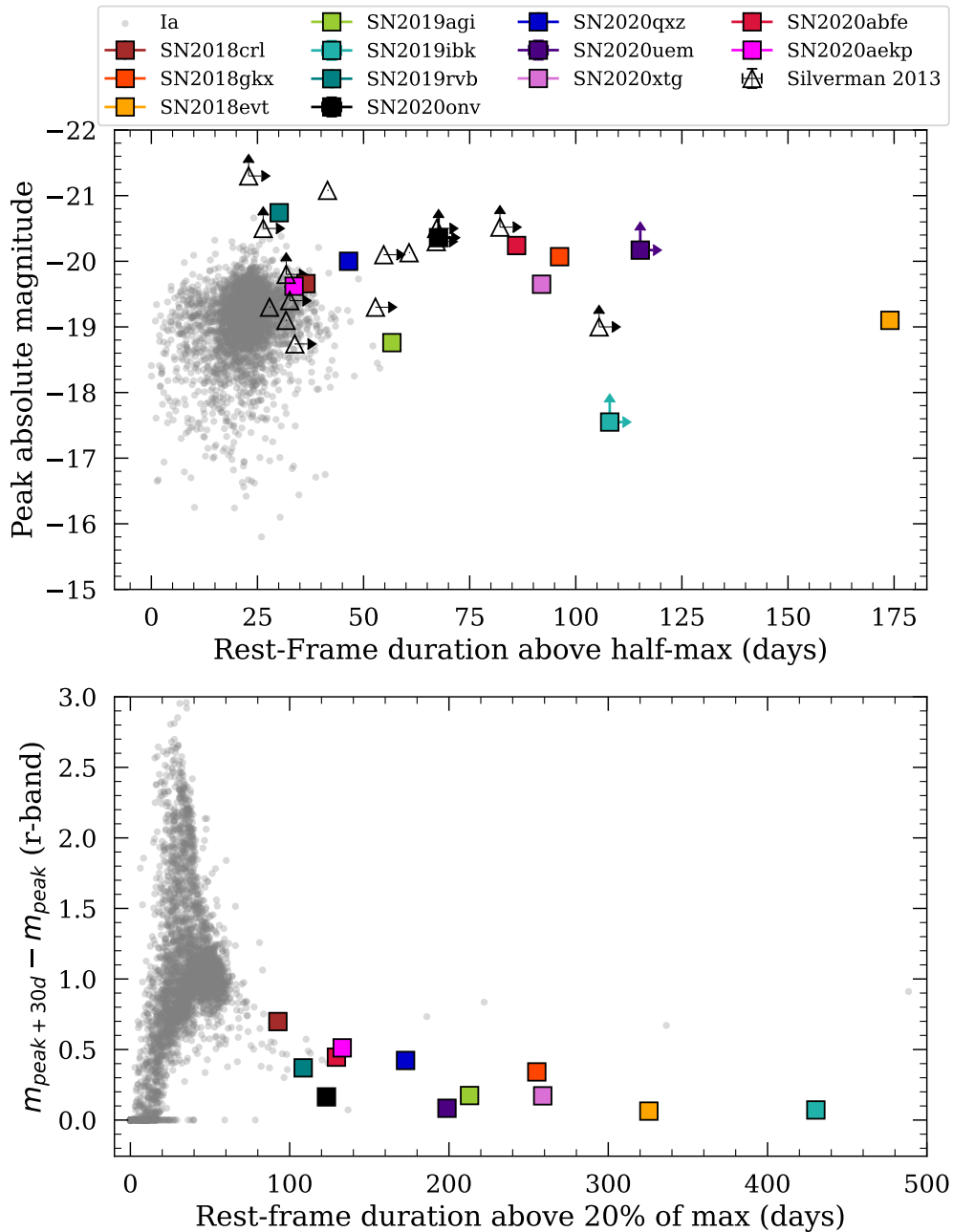


Figure 2.2: *Top:* Location of our 12 SNe Ia-CSM in the peak absolute magnitude vs. rest-frame duration above half max phase space. The colored points are the BTS SNe Ia-CSM, and the gray points are the rest of the BTS SNe Ia. Also shown with empty triangles are the SNe Ia-CSM from S13. The vertical arrows mark the upper limits to peak absolute magnitudes, and horizontal arrows mark the lower limits to durations of SNe not having pre-peak coverage. *Bottom:* Change in magnitude 30 days after peak ( $\Delta m_{30}$ ) vs. rest-frame duration above 20% of peak-flux for BTS SNe Ia and SNe Ia-CSM. These criteria were used to filter out potential SNe Ia-CSM from all SNe Ia and demonstrate that SNe Ia-CSM occupy a distinct portion in this phase space. However, some gray points (not SN Ia-CSM) remain on the longer duration side and are the false positive cases described in §2.1.

2.0 mag 100d<sup>-1</sup> in the  $r$  band from peak to  $\sim 100$  days post peak. The median decline rate is 1.07 mag 100d<sup>-1</sup>, which is much slower than the decline rates of normal SNe Ia. We see a variety of changes in decline rates after around 100 days from the peak. Two SNe (2020onv and 2020abfe) show no change and have a constant, slow decline throughout. Four SNe (2018gkx, 2019agi, 2019ibk and 2019rvb) evolve to a shallower slope going from  $\sim 0.6\text{--}1$  mag 100d<sup>-1</sup> to  $\sim 0.2\text{--}0.5$  mag 100d<sup>-1</sup>. Three SNe (2018crl, 2020qxz, and 2020aekp) show a major change in decline rate with the light curves becoming almost flat, and SN 2020aekp shifts back to a slow decline from this plateau after  $\sim 200$  days. In three cases, the decline rate actually becomes steeper, SN 2018evt goes from 0.52 mag 100d<sup>-1</sup> to 1.4 mag 100d<sup>-1</sup>, SN 2020uem goes from 0.52 mag 100d<sup>-1</sup> to 1.25 mag 100d<sup>-1</sup> and SN 2020xtg seems to go from 0.61 mag 100d<sup>-1</sup> to 1.35 mag 100d<sup>-1</sup> (even though there is only one epoch at late times to measure this change). The three SNe with fastest initial decline rates ( $\gtrsim 1.5$  mag 100d<sup>-1</sup> in the  $r$  band) are similar to SN 2002ic (initial decline of 1.66 mag 100d<sup>-1</sup> in  $V$ ) and PTF11kx (initial decline of 3.3 mag 100d<sup>-1</sup> in  $R$ ) and coincidentally are also the ones that evolve into a plateau. The rest of the sample have initial decline rates comparable to SN 1997cy (0.75 mag 100d<sup>-1</sup>) and SN 2005gj (0.88 mag 100d<sup>-1</sup>) (Inserra et al. 2016). From these observations, we can conclude that SNe Ia-CSM exhibit a range of slow evolution, indicating that there exists a continuum of phases at which strong CSM interaction begins to dominate the powering of the light curves for these SNe. It is, however, difficult to pinpoint the exact phase when interaction starts from the light curve without modeling. CSM interaction could be affecting the peak brightness significantly, even in cases where interaction only appears to dominate after a few weeks (SNe 2018crl, 2020qxz, and 2020aekp). Considering the average peak phase to be  $\sim 20$  days past explosion from the light curves and assuming an ejecta velocity of  $\sim 20000$  km s<sup>-1</sup>, the CSM is located at  $\sim 3.5 \times 10^{15}$  cm. This estimate can be refined by considering the phase of the earliest spectrum that shows interaction signatures (see §2.3). At late times, all the decline rates are slower than that expected from Cobalt decay (0.98 mag 100d<sup>-1</sup>), confirming that the power from CSM interaction dominates the light curve behavior for a long time.

Figure 2.3 shows the  $g - r$  color evolution of our sample SNe as a function of phase (rest-frame days from  $r$ -band maximum), comparing them with some famous SNe Ia-CSM (SNe 2005gj, 1997cy, 1999E), and SNe 2012ca (Ia-CSM/IIn), 2010jl (IIn), and 1991T (over-luminous Type Ia). The color evolution of normal SNe Ia from ZTF (Dhawan et al. 2022) is shown in grey lines. We use  $g - r$  colors when available,

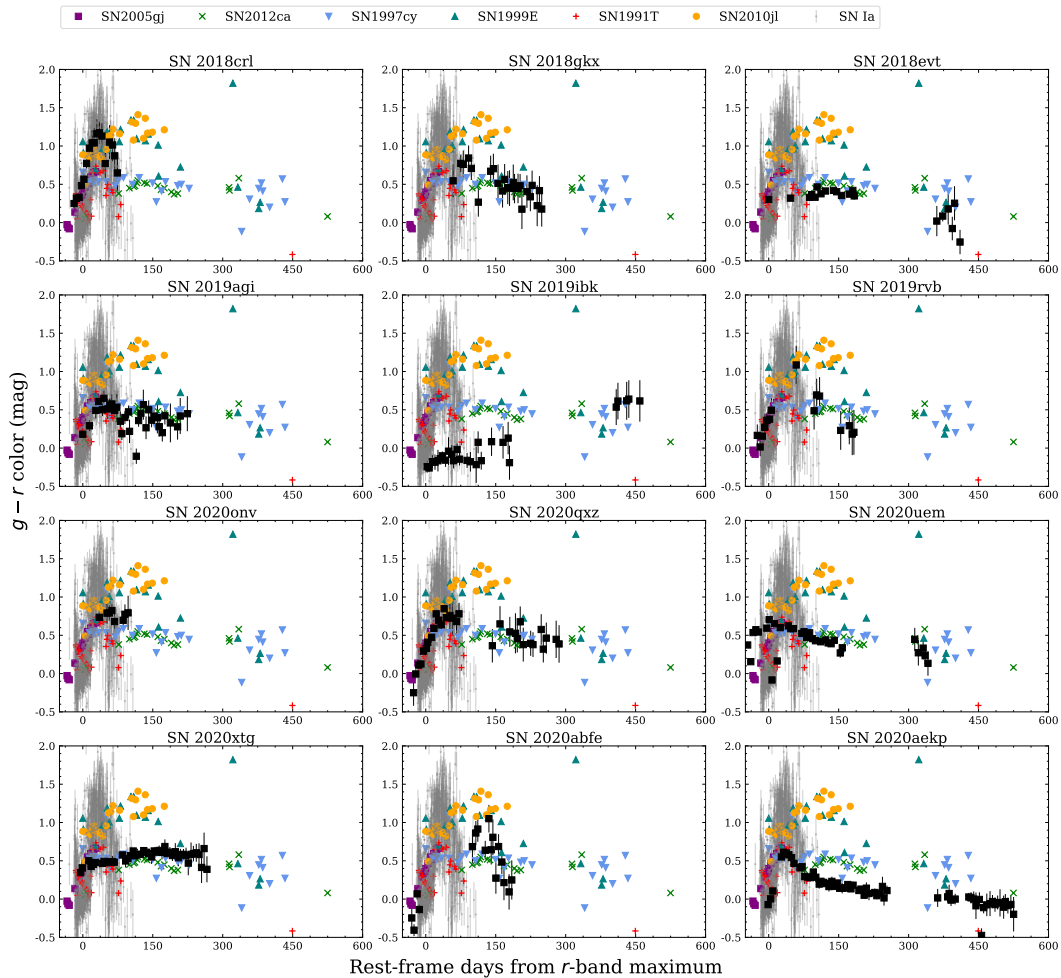


Figure 2.3: Color evolution ( $g - r$ ) of BTS SNe Ia-CSM from  $r$ -band maximum (plotted in black) compared with SNe 2005gj, 1997cy, 1999E (Ia-CSM), SN 2012ca (IIn/Ia-CSM), SN 2010jl (IIn), SN 1991T (SN Ia), and ZTF SNe Ia (gray lines). As can be seen for up to  $\sim 150$  days, our SNe Ia-CSM tend to be redder than SNe Ia and at late times develop a plateau similar to other interacting SNe (IIn/Ia-CSM).

otherwise, we estimate the  $g - r$  color by fitting Planck functions to estimate the black-body temperatures from the  $V - R$  colors. Our SNe Ia-CSM show similar color evolution as the older Type Ia-CSM/IIn interacting SNe, i.e., the  $g - r$  color increases gradually for about 100 days and then settles onto a plateau or slowly declines, and one object (SN 2019ibk) becomes redder at late times, similar to SN 2012ca. The interacting SNe are redder at late times compared to the normal SNe Ia.

### Mid-IR brightness comparison

Out of 12 SNe in our sample, only one observed (SN 2020abfe) did not have  $3\sigma$  detections post-explosion in the unWISE difference photometry light curves, and two (SNe 2019rvb and 2020qxz) did not have coverage post-explosion. The unWISE light curves for the rest of the SNe Ia-CSM having  $>3\sigma$  detections in W1 ( $3.3\ \mu\text{m}$ ) and W2 ( $4.6\ \mu\text{m}$ ) bands are shown in Figure 2.4 (black and red stars) along with *Spitzer* IRAC survey data of SN 2008cg (Ia-CSM, indigo and magenta empty triangles), SN 2008J (Ia-CSM, indigo and magenta empty squares), and some SNe IIn (blue and orange crosses) taken from Fox et al. (2011). The most nearby SN in our sample, SN 2018evt, is among the brightest ( $\sim 17$  AB mag) in MIR at least until  $\sim 1000$  days after the explosion and has a bumpy light curve. SNe 2019ibk and 2018crl, however, are the most luminous with an absolute magnitude of  $-18.7$  mag in the W1 band. The brightness of the BTS SNe Ia-CSM is comparable to other interacting SNe and spans a similar range ( $-16$  to  $-19$ ). However, SNe IIn have been detected until even later epochs (up to 1600 days) than SNe Ia-CSM, probably due to the larger number of SNe IIn at closer distances. SN 2020abfe has upper limits around  $\sim -18$  in W1 band and  $\sim -18.5$  in W2 band up to  $\sim 300$  days post explosion, shown with upside-down filled triangles. As the mid-IR luminosity can be fainter than these limits for SNe Ia-CSM (as can be seen for other nearby SNe in this sample), and SN 2020abfe is at a redshift of 0.093, it might just be out of reach for WISE.

The brightness of SNe Ia-CSM in mid-IR can be indicative of existing or newly formed dust. A clear signature of new dust is reduced flux in the red wing of the  $\text{H}\alpha$  emission line at late phases as the new dust formed in the cold dense shell behind the forward shock absorbs the far-side (redshifted) intermediate and narrow line emission (see bottom panel of Fig. 2.7). For our sample, this reduction in  $\text{H}\alpha$  red wing is the most pronounced for SN 2018evt.

### Bolometric luminosity

As the SN Ia-CSM luminosity is dominated by CSM interaction, their spectra comprise a pseudo-continuum on the blue side and strong  $\text{H}\alpha$  emission on the red side; hence, a blackbody fit to multi-band photometric data is not appropriate to estimate the bolometric luminosity. Instead, we calculate a pseudo-bolometric luminosity from the available multi-band optical data by linearly interpolating the flux between the bands and integrating over the optical wavelength range spanned by

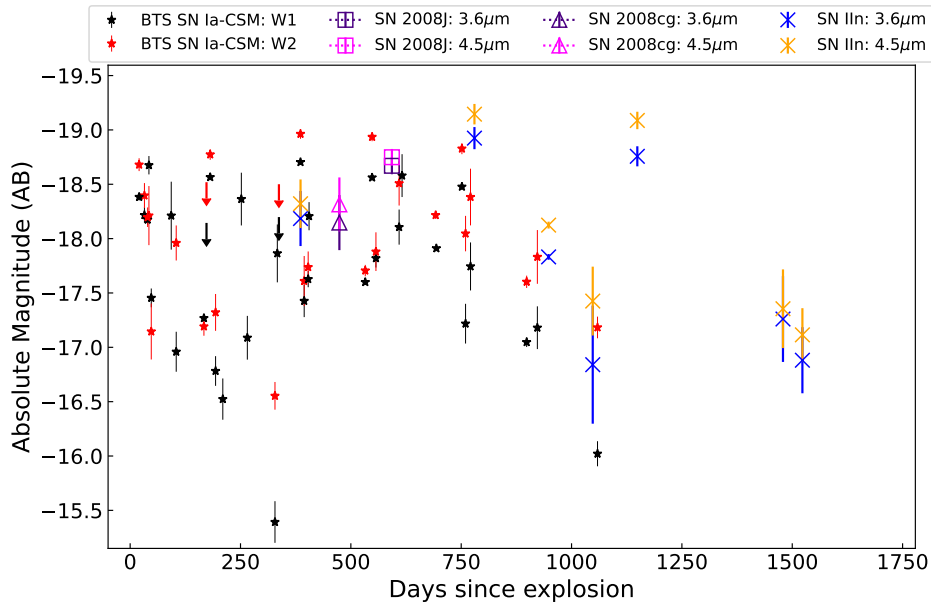


Figure 2.4: unWISE detections in the W1 and W2 bands of BTS SNe Ia-CSM. The W1 and W2 points are marked with black and red filled stars, respectively. Spitzer IRAC photometry of SNe IIn (blue and orange crosses) and two SNe Ia-CSM from Fox et al. (2011) (SNe 2008cg and 2008J in empty triangle and square) are also shown for comparison. Nine out of twelve BTS SNe Ia-CSM are as bright in mid-IR as other interacting SNe ( $\sim -16$  to  $\sim -19$ ). The upper limits for SN 2020abfe are shown in black and red filled upside-down triangles.

the ATLAS and ZTF bands. The individual band light curves are first interpolated using Gaussian process regression to fill in the missing epochs. This estimate places a strict lower limit on the bolometric luminosity.

In Figure 2.5 we show the pseudo-bolometric luminosity of our SN Ia-CSM sample in comparison with SN 1991T (Type Ia), SNe 1997cy, 1999E, 2002ic, 2005gj, 2013dn, and PTF11kx (Ia-CSM). Multi-band photometric data were taken from the Open Supernova Catalog (Guillochon et al. 2017) for SN 1991T (Filippenko et al. 1992; Ford et al. 1993; Schmidt et al. 1994) to generate the bolometric luminosity light curve through black body fitting. The pseudo-bolometric luminosity light curve for SN 1997cy was obtained from Germany et al. (2000), for SN 2013dn from Fox et al. (2015), and for SNe 2002ic, 2005gj, 1999E, and PTF11kx from Inserra et al. (2016).

All BTS SNe Ia-CSM show a slow evolution in bolometric luminosity, inconsistent with the decay of  $^{56}\text{Co}$  to  $^{56}\text{Fe}$ . The sample's overall luminosity decline rates are

comparable to those of SNe 1997cy and 2013dn, as shown in Figure 2.5. Only SNe 2018crl and 2020aekp seem to show early decline in their pseudo-bolometric light curves, similar to SN 1991T for about 40 days after peak, like SN 2002ic and PTF11kx. Another BTS interacting SN Ia, ZTF20aatxryt (Kool et al. 2022), was found to follow the PTF11kx light-curve evolution very closely, and as its light curve fell into a plateau, the SN started showing signs of interaction with a helium-rich CSM and evolved into a helium-rich SN Ia-CSM. We have excluded ZTF20aatxryt from the sample as we focus on typical SNe Ia-CSM interacting with hydrogen-rich CSM in this study. At late phases ( $\sim 300$  days), the SNe Ia-CSM are approximately 100 times brighter than normal SNe Ia at the same epoch. Therefore, at these late phases, the luminosity and spectral features of SNe Ia-CSM are entirely dominated by CSM-interaction with little emergent SN flux. From the pseudo-bolometric light curves, we place a lower limit on the total radiated energy for SNe Ia-CSM to be  $0.1\text{--}1.5 \times 10^{50}$  erg. This is well below the thermonuclear budget ( $E_{kin} \sim 10^{51}$  erg), but as this is a lower limit and some SNe in the sample have unconstrained peaks, the true total radiative energy might come close to the thermonuclear budget, requiring high conversion efficiency to achieve their luminosity.

### Spectroscopy

Figure 2.6 displays the spectral series obtained for the BTS SNe Ia-CSM. Most of the early time spectra were taken with the SEDM, the BTS workhorse instrument ( $R \sim 100$ ), which is not able to resolve the narrow CSM lines. Therefore, these SNe were followed up with higher resolution instruments to get more secure classifications. For each spectrum in Figure 2.6, the phase is provided with respect to the explosion epoch estimate given in Table 2.4. We have spectra ranging from a few to around 470 days from the explosion. Considering the well constrained explosion times of SN 2018evt, presence of narrow  $H\alpha$  in its first spectrum at 8 days since explosion and assuming a typical ejecta velocity of  $\sim 20000 \text{ km s}^{-1}$ , this implies that the CSM interaction start as close as  $\sim 1.4 \times 10^{15}$  cm.

Figure 2.7 shows the early time (left) and late time (right) spectral behavior of the BTS SNe Ia-CSM together with a few historical SNe for comparison, namely SNe Ia-CSM SN 2011jb (Silverman et al. 2013b), SN 2005gj, and PTF11kx, the Type Ia SN 1991T, and the well-observed Type II In SN 2010jl. Vertical gray regions mark typical SN Ia absorption features and [Fe II/III] line regions, and vertical dashed lines mark the Balmer emission lines. The sample spectra have been multiplied by a constant factor to magnify relevant spectral features. In the following paragraphs,

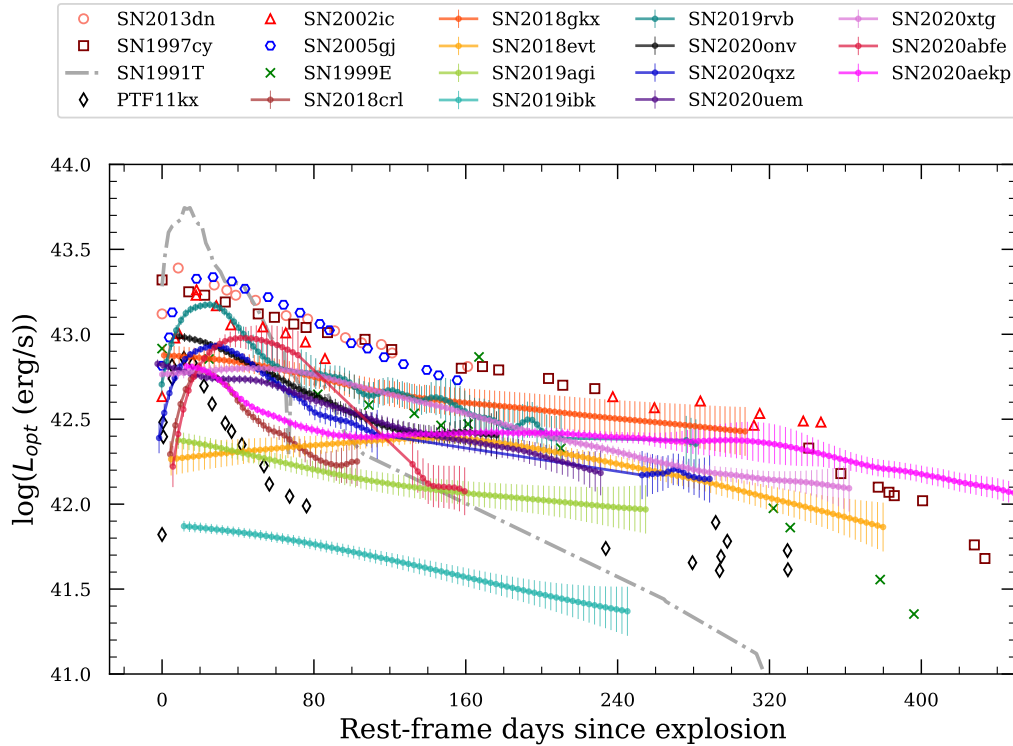


Figure 2.5: Pseudo-bolometric luminosity light curves of BTS SNe Ia-CSM compared with pseudo-bolometric light curves of SNe 1991T, 1997cy, 1999E, 2002ic, 2005gj, 2013dn, and PTF11kx from literature. The light curves in each filter having more than 10 epochs were interpolated using Gaussian process regression to fill in the missing epochs, and at each epoch, the fluxes between the bands were linearly interpolated and integrated over the optical wavelength range spanned by ZTF and ATLAS filters to get the pseudo-bolometric luminosity. For BTS SNe, the phases are with respect to the estimated explosion epochs, while for comparison SNe, the phases are with respect to discovery.

we compare the observations of some of the spectral features with previous analysis of this class (Silverman et al. 2013b; Fox et al. 2015; Inserra et al. 2016).

A few of our early time SNe Ia-CSM show underlying SN Ia absorption features like PTF11kx and SN 2002ic (most are, however, quite diluted and also affected by the low resolution and signal-to-noise ratio (SNR) of the SEDM spectra), the most notable being SNe 2018evt, 2020qvx, and 2020aekp. SNe 2020qvx and 2020aekp also have among the fastest initial post-peak decline rates in the sample, similar to PTF11kx, while coverage around peak is not available for SN 2018evt. On the other hand, SNe with slower decline rates similar to SN 1997cy and SN 2005gj have more SN IIn-like early time spectra dominated by blue pseudo-continuum and

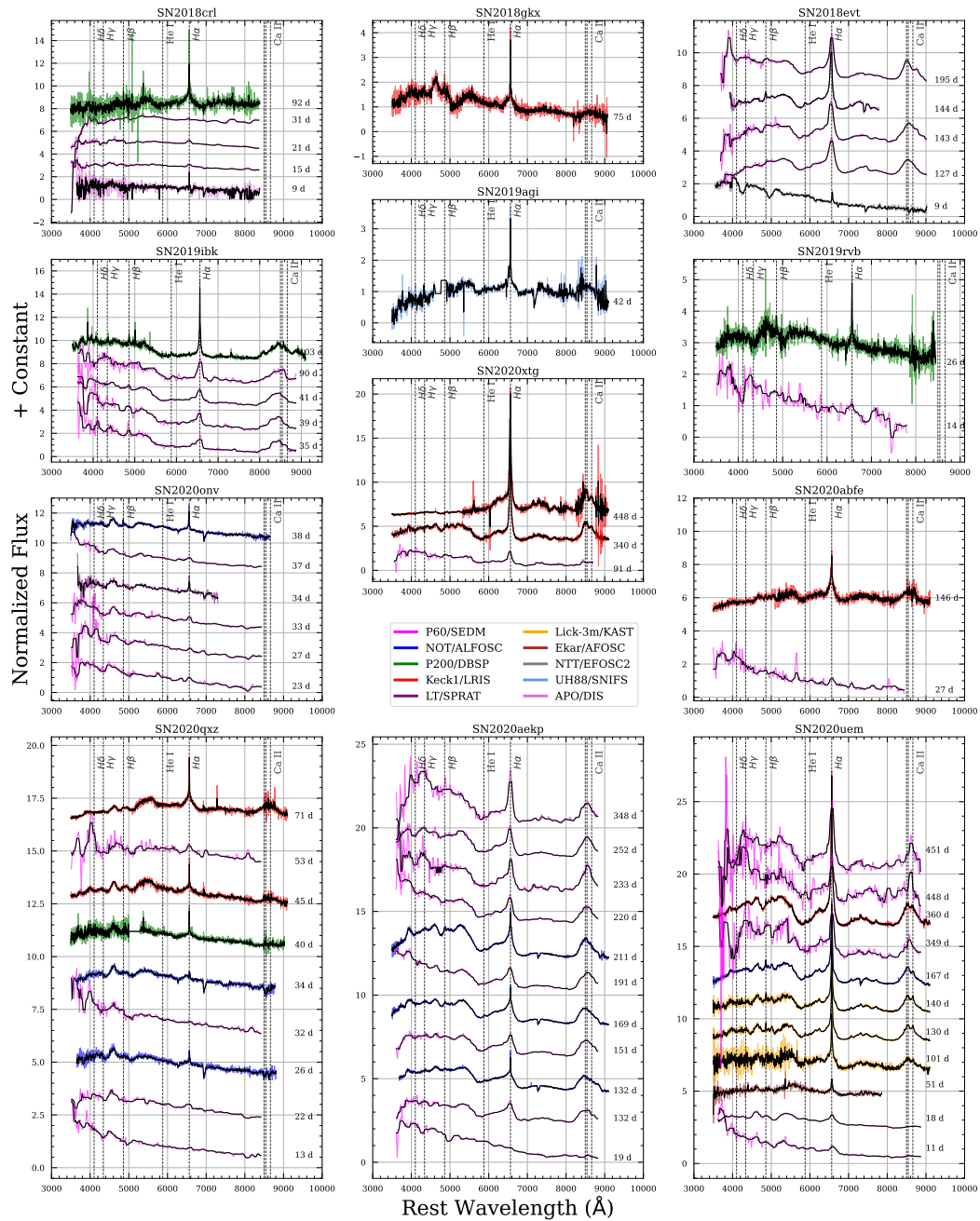


Figure 2.6: Spectral series of all SNe Ia-CSM presented in this paper. The rest-frame phases are shown alongside the spectra in each subplot and have been calculated using the explosion epoch estimate. The colors depict different instruments used to obtain this data. Major emission lines are marked with vertical dashed lines.

Balmer emission. The faster decline rate suggests we are still seeing some of the emission from the ejecta at those phases. To unveil the nature of the progenitor of interacting SNe, it is therefore necessary to obtain some spectroscopic follow-up before peak light. Spectroscopic data at the phase of transition to interaction-dominated luminosity would also help in deducing the extent and density structure of the optically thick CSM.

Late-time spectra of SNe Ia-CSM look very similar to those of SNe IIn, heavily dominated by  $H\alpha$  emission. The CSM interaction masks the underlying SN signature, and we instead see late-time spectra riddled with photoionized CSM lines. In some cases, the photosphere might lie in an optically thick cold dense shell (CDS) formed between the forward and reverse shocks, which obscures the ejecta completely (Smith et al. 2008; Chugai et al. 2004a). The continuum is also enshrouded under a blue quasi-continuum from a forest of iron-group element lines (S13) as identified and analyzed for SNe 2012ca and 2013dn by Fox et al. (2015).

The blue quasi-continuum blend of iron lines ([Fe III] lines around  $\sim 4700 \text{ \AA}$  and [Fe II] around  $\sim 5200 \text{ \AA}$ ) in the spectra of the BTS SN Ia-CSM sample (see Figure 2.7 top right panel) is the dominant feature blue-ward of  $5500 \text{ \AA}$  but the ratio of [Fe III]/[Fe II] is much weaker compared to for SNe Ia (like SN 1991T). This feature is more apparent in the SNe Ia-CSM like PTF11kx and SN 2002ic that became interaction-dominated later than for other SNe Ia-CSM such as SNe 1997cy, 1999E, and SN 2012ca (SN Ia-CSM/IIn, for which a clear type has not been established). Inserra et al. (2014) argues for a core-collapse origin for SN 2012ca given this low amount of [Fe III] along with the detection of blueshifted Carbon and Oxygen lines (which however, were later argued to be [Fe II] lines by Fox et al. 2015). S13 instead argues in favor of a thermonuclear origin given the presence of this blue quasi-continuum, despite [Fe III] being weaker. Fox et al. (2015) points out that a similarly suppressed ratio of [Fe III]/[Fe II] is observed in some SNe Ia, particularly the super-Chandra candidate SN 2009dc, for which the explanation was suggested to be a low ionization nebular phase owing to high central ejecta density and low expansion velocities (Taubenberger et al. 2013). Fox et al. (2015) argue that in the case of SNe Ia-CSM, a lower ionization state could arise owing to the deceleration of ejecta by the dense CSM, explaining the Fe line ratio suppression. Since Ca has lower first and second ionization potentials than Fe, the detection of [Ca II]  $\lambda\lambda 7291, 7324$  would be consistent with this low ionization, which Fox et al. (2015) confirms for SNe 2012ca and 2013dn. Indeed, we find clear evidence of [Ca II] emission

for 8 out of 12 SNe in our sample and a moderate to weak signal for the remaining 4. Although this does favor the argument for a thermonuclear origin, a similar blue quasi-continuum is also observed in other interacting SN types like SNe Ibn (SN 2006jc, Foley et al. 2007) and SNe IIn (SNe 2005ip and 2009ip), making Fe an incomplete indicator of the progenitor nature (see detailed discussion in Fox et al. 2015).

We do not find strong evidence of O I  $\lambda\lambda 7774$  or [O I]  $\lambda\lambda 6300, 6364$  emission in our sample, although they might be present at very weak levels in some SNe (e.g., SN 2020uem). SN 2020uem has strong emission lines at 6248, 7155, and 7720 Å which are consistent with being iron lines and were also observed in SNe 2012ca, 2013dn, and 2008J. S13 note that the very broad emission around 7400 Å can be due to a blend of [Ca II]  $\lambda\lambda 7291, 7324$  and [O II]  $\lambda\lambda 7319, 7330$ , however we note that this broad emission is likely to be from calcium as O II is harder to excite than O I which is either very weak or absent in our spectra. The broad Ca NIR triplet feature resulting from electron scattering is the next strongest feature after the Balmer emission and is present in all mid to late-time spectra of the SNe in our sample, where the wavelength coverage is available. We observe it increasing in relative strength with phase, at least for a year, after which we no longer have spectral coverage.

The bottom panel of Figure 2.7 shows the line profile of H $\alpha$ , with the blue side reflected over the red side at the maximum flux after continuum removal. We do see evidence of diminished flux in the red wing of H $\alpha$  at late phases in some SNe (most notably in SNe 2018evt and 2020uem), which can indicate formation of new dust in the post-shock CSM. S13 claim to observe this for all non-PTF SNe Ia-CSM in their sample starting at  $\sim 75$ –100 days, while for the PTF SNe Ia-CSM, they do not have spectra available post that phase range. For some BTS SNe Ia-CSM, we also do not have spectra available post 100 days, which limits any analysis of this phenomenon for a large enough sample.

The spectra were reduced and processed as outlined in §2.2 for the emission line analysis, the results of which are described in the next section. We used only good SNR SEDM spectra and intermediate resolution spectra for line identification and analysis.

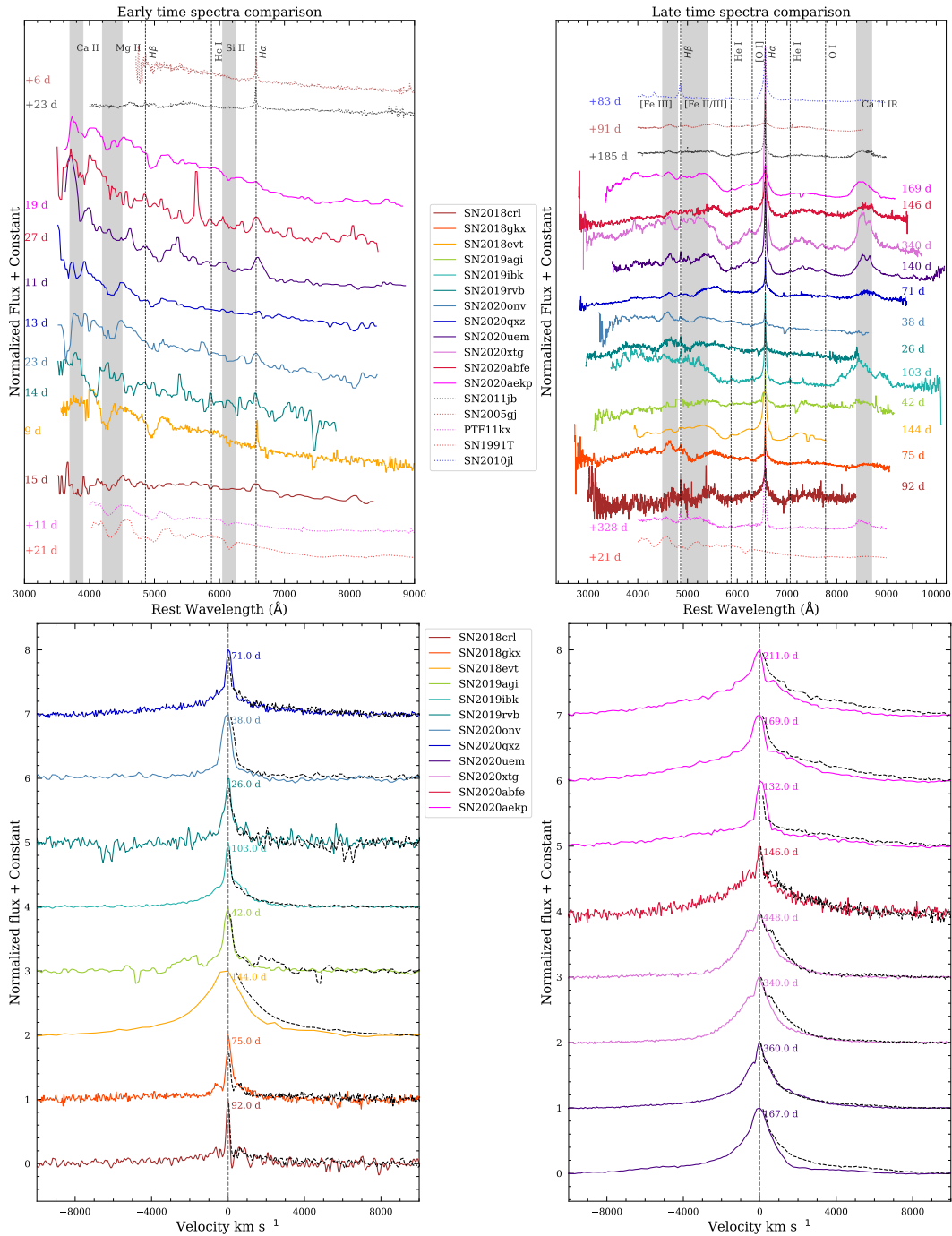


Figure 2.7: *Top left:* Early-time spectra of BTS SNe Ia-CSM with phases between 0 and 30 days since explosion compared to spectra of SNe 2011jb, 2005gj, 1991T, and PTF11kx (phases in days since discovery). *Top right:* Late-time spectra of BTS SNe Ia-CSM (phases ranging from 40 to 370 days since explosion) compared to spectra of SNe 2011jb, 2005gj, 2010jl, and PTF11kx (phases in days since discovery). *Bottom left and right:* H $\alpha$  line profiles (post continuum removal) with the blue side reflected across the peak flux, marked by dashed lines. SNe 2020aekp, 2020abfe, 2020xtg, and 2020uem in the right panel, and SNe 2018crl, 2018gkx, 2018evt, 2019agi, 2019ibk, 2019rvb, 2020onv, and 2020qzx in left panel.

### **H $\alpha$ , H $\beta$ , and He I emission lines**

To analyze the H $\alpha$  line emission, we first fit the continuum level using the `fit_continuum` function of the `specutils` Python package, where the continuum is estimated by a cubic function fitted on regions on each side of the line. We remove this continuum level and then fit the H $\alpha$  line with a broad and a narrow component Gaussian function using the `fit_lines` function of `specutils`, which returns the best fit Gaussian model and the  $1\sigma$  uncertainty on the model parameters. We generate 1000 sample models within  $1\sigma$  uncertainties of the parameters centered around the best-fit values and calculate the intensity, flux, and velocity (FWHM) of the broad and narrow components for each model. Then we take the median and standard deviation of the intensity, flux, and velocity FWHM distributions to get their final best value and  $1\sigma$  uncertainty. The equivalent width was also calculated for the H $\alpha$  line using the model fit as well as directly from the data, and the difference between the values derived from the model and data is reported as the error on the EW. All values are reported in Table 2.5. For 3 SNe in our sample, we have a series of intermediate resolution spectra through which we can trace the evolution of the H $\alpha$  line with phase. Figure 2.8 shows this trend of the H $\alpha$  line parameters (integrated flux in the top panel and equivalent width in the bottom panel) versus phase for all SNe in our sample. The unfilled markers represent the narrow emission, while the filled markers represent the broad emission. For SNe where this analysis could be done on multiple spectra, we see that the H $\alpha$  equivalent width generally increases over time, with some SNe showing fluctuations up to 100 days, possibly due to interaction of ejecta with multiple CSM shells of varying density. For SN 2018evt, Yang et al. (2022) analyzed H $\alpha$  line properties from a comprehensive spectral series data, which are plotted in Figure 2.8 in gray circles and seem to agree well with our analysis at comparable epochs.

From the Gaussian profile line fitting analysis of the H $\alpha$  emission line, we found that the broader component has velocities ranging from  $\sim 1000$  to  $\sim 4000$  km s $^{-1}$  (intermediate width) and the narrow component has velocities of about  $\sim 200$  km s $^{-1}$  to  $\sim 1000$  km s $^{-1}$  (see Figure 2.9). The narrow component could only be resolved down to  $\sim 300$  km s $^{-1}$  limited by the mediocre resolution of the spectrographs used (KeckI/LRIS R $\sim 800$ , P200/DBSP R $\sim 1000$ , NOT/ALFOSC has R $\sim 360$ ). While we know that the narrow lines originate in the unshocked ionized CSM, the exact origin of the intermediate components is uncertain. They could arise from the post-shock gas behind the forward shock or from the shocked dense clumps in the CSM (Chugai

et al. 1994).

The luminosities of the  $H\alpha$  line measured from the BTS SNe Ia-CSM lie in the range  $2.5\text{--}37\times 10^{40}$  erg s $^{-1}$  which are comparable to the values from S13 who reported most of their SNe in the  $1\text{--}10\times 10^{40}$  erg s $^{-1}$  range except one object that had a luminosity of  $39\times 10^{40}$  erg s $^{-1}$ . From the broad  $H\alpha$  luminosity, we did a simple estimate of the mass-loss rate assuming spherically symmetric CSM deposited by a stationary wind  $\rho \propto r^{-2}$  having velocity  $v_w$  (Chugai 1991; Salamanca et al. 1998). The mass-loss rate  $\dot{M}$  can be related to the broad  $H\alpha$  luminosity  $L_{H\alpha}^{Broad}$  as (Salamanca et al. 1998, their Eq. 2)

$$L_{H\alpha}^{Broad} = \frac{1}{4} \epsilon_{H\alpha} \frac{\dot{M}}{v_w} v_s^3$$

where  $v_s$  is the shock velocity (obtained from the broad component velocity of the  $H\alpha$  line). We used a value of  $100$  km s $^{-1}$  considering previous high resolution spectral studies of SNe Ia-CSM (Kotak et al. 2005; Aldering et al. 2006; Dilday et al. 2012) for  $v_w$  as we cannot fully resolve the narrow component and a maximum value of  $0.1$  for the efficiency factor  $\epsilon_{H\alpha}$  (Salamanca et al. 1998). The mass-loss rates were estimated from the available spectra and are shown in Figure 2.10 as a function of years before explosion ( $t_w = \frac{v_s t}{v_w}$ , where  $t$  is the phase of the spectra). For most SNe in the sample, the mass-loss rates lie between  $0.001\text{--}0.02 M_{\odot} \text{ yr}^{-1}$ , except for SN 2019rvb, which has  $\sim 0.07 M_{\odot} \text{ yr}^{-1}$  lost within 2 years prior to the explosion. These rates are much higher than what could be attained from a red giant superwind ( $\sim 3 \times 10^{-4} M_{\odot} \text{ yr}^{-1}$ ) but are comparable to previous estimates (calculated through multiple methods) for SNe Ia-CSM and require some unusual mechanism to reach such persistently higher mass-loss rates in the decades prior to explosion. Also to consider is that the simplistic assumption of spherical symmetry likely does not apply for SNe Ia-CSM. Evidence of multiple thin shells and asymmetric CSM was observed for PTF11kx (Dilday et al. 2012), and light curve modeling of SNe 1997cy and 2002ic suggested a better fit to a flat density profile rather than a stationary wind (Chugai et al. 2004b). An asymmetric or clumpy CSM might be the norm for SNe Ia-CSM (and some SNe IIn) rather than the exception.

The same analysis as for the  $H\alpha$  line was also carried out for  $H\beta$  and He I  $\lambda 5876$  with a one-component Gaussian fit. For cases where a Gaussian model could not fit the data, we integrate the flux value in a  $100 \text{ \AA}$  region centered at  $5876 \text{ \AA}$  for He I. The Na ID absorption lines are also prevalent in some spectra and blend with the He I line, resulting in positive EWs for some SNe. The cumulative distributions of  $H\beta$

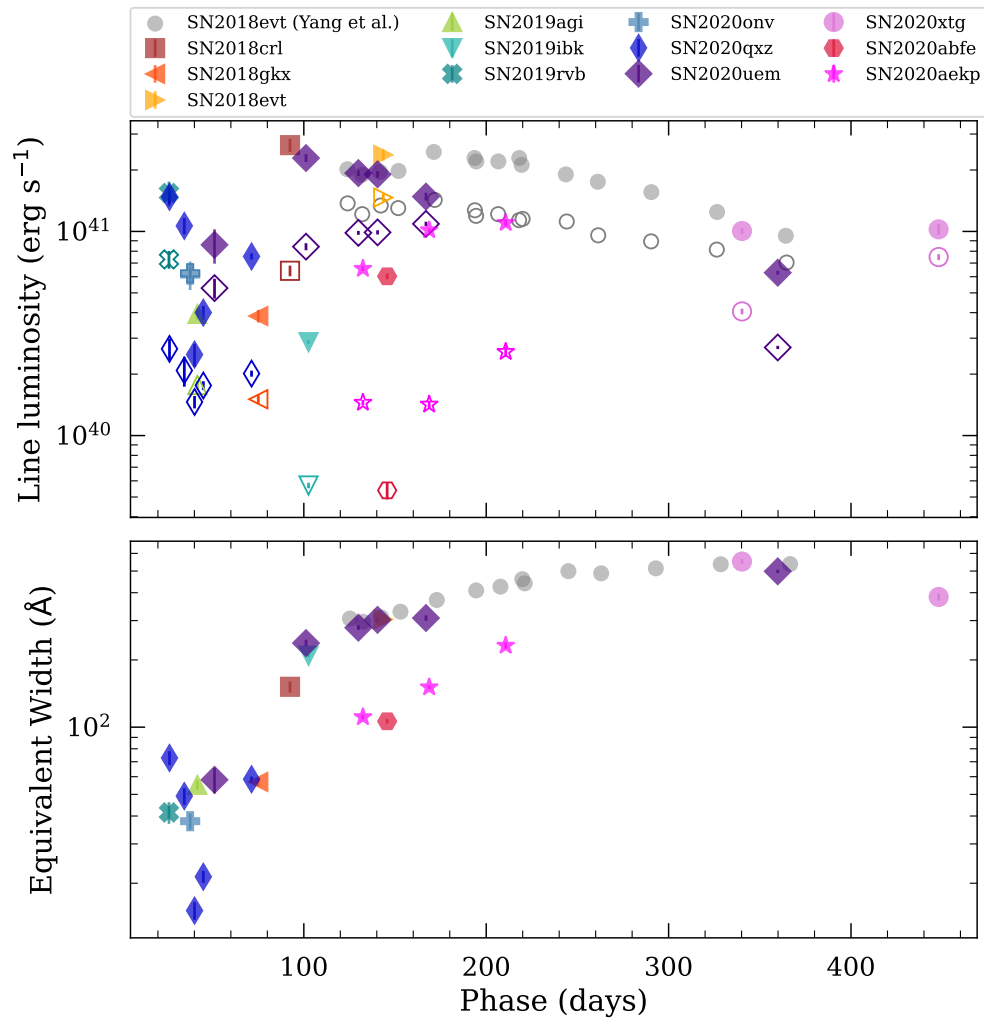


Figure 2.8: Integrated fluxes and equivalent widths of  $H\alpha$  emission line with respect to SN phases for the BTS SN Ia-CSM sample. Broad component values are shown with filled markers and narrow component values with unfilled markers. SN 2018evt  $H\alpha$  luminosities and EWs presented in Yang et al. (2022) are also shown in gray circles.

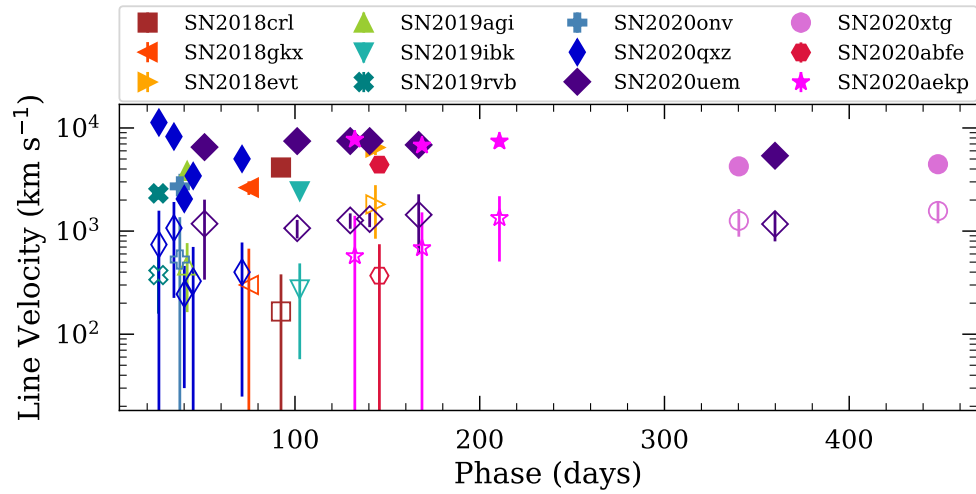


Figure 2.9: Velocity of H $\alpha$  emission line with respect to SN phases for the BTS SN Ia-CSM sample. Broad component values are shown with filled markers and narrow component values with unfilled markers.

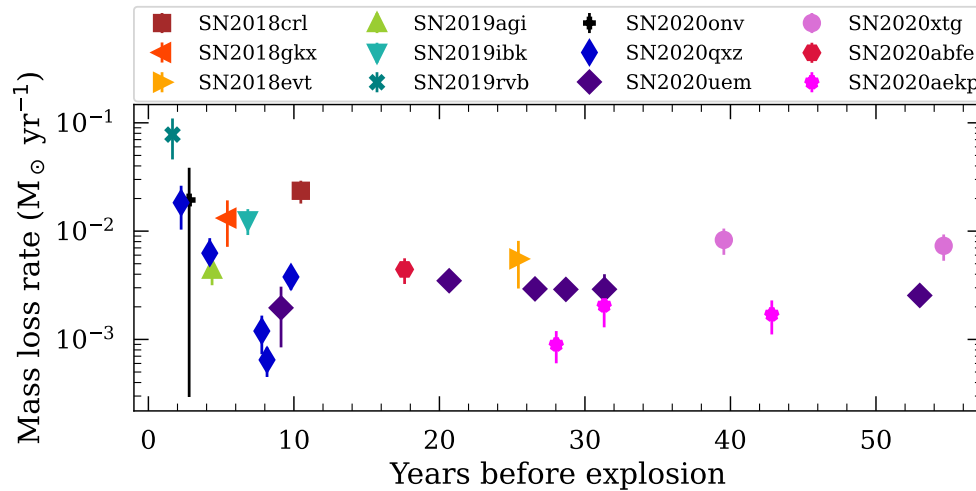


Figure 2.10: Mass-loss rates estimated from the luminosity of the broad component of H $\alpha$  for the BTS SNe Ia-CSM. A value of 100 km s $^{-1}$  was assumed for the wind velocity.

Table 2.5: Summary of H $\alpha$  line properties obtained from two-component Gaussian fitting.

SN Name	Phase (days)	Broad Flux ( $10^{-16}$ erg s $^{-1}$ cm $^{-2}$ )	Narrow Flux ( $10^{-16}$ erg s $^{-1}$ cm $^{-2}$ )	Total Flux ( $10^{-16}$ erg s $^{-1}$ cm $^{-2}$ )	Broad Velocity FWHM (km s $^{-1}$ )	Narrow Velocity FWHM (km s $^{-1}$ )
SN 2018crl	92	135.4 $\pm$ 10.0	32.8 $\pm$ 2.0	168.2 $\pm$ 12.0	4137 $\pm$ 312	< 214
SN 2018gkx	75	9.9 $\pm$ 0.7	3.9 $\pm$ 0.2	13.7 $\pm$ 0.9	2640 $\pm$ 398	< 375
SN 2018evt	144	2020.3 $\pm$ 128.5	1247.4 $\pm$ 52.8	3267.7 $\pm$ 181.3	6465 $\pm$ 997	1816 $\pm$ 973
SN 2019agi	42	52.7 $\pm$ 3.6	23.7 $\pm$ 1.1	76.4 $\pm$ 4.7	3836 $\pm$ 349	464 $\pm$ 301
SN 2019ibk	103	85.6 $\pm$ 1.7	17.0 $\pm$ 0.5	102.6 $\pm$ 2.3	2431 $\pm$ 217	272 $\pm$ 214
SN 2019rvb	26	22.0 $\pm$ 3.0	10.4 $\pm$ 1.0	32.5 $\pm$ 4.1	2321 $\pm$ 298	374 $\pm$ 216
SN 2020onv	38	32.8 $\pm$ 5.2	33.3 $\pm$ 2.0	66.1 $\pm$ 7.2	2714 $\pm$ 879	<834
SN 2020qxz	26	76.6 $\pm$ 6.2	13.8 $\pm$ 1.7	90.4 $\pm$ 7.9	11294 $\pm$ 1106	< 836
SN 2020qxz	34	55.1 $\pm$ 5.0	10.8 $\pm$ 1.8	65.9 $\pm$ 6.8	8252 $\pm$ 1039	1070 $\pm$ 845
SN 2020qxz	40	12.9 $\pm$ 1.7	7.6 $\pm$ 0.5	20.5 $\pm$ 2.2	2049 $\pm$ 284	245 $\pm$ 215
SN 2020qxz	45	20.7 $\pm$ 1.6	9.1 $\pm$ 0.4	29.8 $\pm$ 2.1	3429 $\pm$ 419	< 375
SN 2020qxz	71	39.1 $\pm$ 1.3	10.4 $\pm$ 0.4	49.5 $\pm$ 1.7	5013 $\pm$ 395	400 $\pm$ 375
SN 2020uem	51	246.3 $\pm$ 47.2	151.1 $\pm$ 16.8	397.4 $\pm$ 64.0	6520 $\pm$ 1163	1178 $\pm$ 840
SN 2020uem	101	655.2 $\pm$ 28.9	241.2 $\pm$ 9.6	896.4 $\pm$ 38.4	7456 $\pm$ 309	1066 $\pm$ 217
SN 2020uem	130	552.9 $\pm$ 17.6	281.8 $\pm$ 6.2	834.8 $\pm$ 23.8	7465 $\pm$ 265	1269 $\pm$ 215
SN 2020uem	140	545.4 $\pm$ 20.0	283.4 $\pm$ 6.8	828.8 $\pm$ 26.7	7457 $\pm$ 275	1308 $\pm$ 216
SN 2020uem	167	424.3 $\pm$ 19.0	312.0 $\pm$ 7.7	736.3 $\pm$ 26.6	6852 $\pm$ 854	1439 $\pm$ 834
SN 2020uem	360	179.8 $\pm$ 4.0	77.4 $\pm$ 1.4	257.2 $\pm$ 5.4	5377 $\pm$ 382	1170 $\pm$ 375
SN 2020xtg	340	129.2 $\pm$ 4.2	52.1 $\pm$ 1.6	181.3 $\pm$ 5.8	4242 $\pm$ 382	1258 $\pm$ 376
SN 2020xtg	448	131.7 $\pm$ 7.7	96.3 $\pm$ 3.2	228.0 $\pm$ 10.9	4452 $\pm$ 395	1566 $\pm$ 377
SN 2020abfe	146	33.6 $\pm$ 1.1	3.0 $\pm$ 0.3	36.6 $\pm$ 1.4	4411 $\pm$ 389	< 376
SN 2020aekp	132	149.5 $\pm$ 4.0	33.0 $\pm$ 1.0	182.5 $\pm$ 5.0	7728 $\pm$ 846	< 833
SN 2020aekp	169	231.0 $\pm$ 4.5	32.3 $\pm$ 1.3	263.3 $\pm$ 5.8	6775 $\pm$ 839	< 834
SN 2020aekp	211	251.0 $\pm$ 9.5	58.6 $\pm$ 3.4	309.6 $\pm$ 12.8	7422 $\pm$ 852	1342 $\pm$ 836

and He I equivalent widths are shown in the top and bottom panels of Figure 2.11, respectively.

The H $\beta$  median EW measured from the BTS SN Ia-CSM sample is 7.1 Å, close to the S13 value of  $\sim$ 6 Å and quite weak compared to what S13 measured for SNe IIn ( $\sim$ 13 Å). The overall cumulative distribution of H $\beta$  EW is also comparable to the S13 SNe Ia-CSM rather than to the S13 SNe IIn. For the He I  $\lambda$ 5876 line, the median EW measured for our BTS SN Ia-CSM sample, considering only significant emission features, is 2.4 Å. This is close to the value of  $\sim$ 2 Å reported in S13, and again significantly different from their SN IIn value of  $\sim$ 6 Å ( $\sim$ 4 Å with upper limits), however the overall distribution seems to be closer to the S13 SNe IIn (but still weaker) rather than to the S13 SNe Ia-CSM. This indicates that perhaps He I is not as good a discriminant between the populations compared to H $\beta$ . Among the most He-rich SNe in our sample are SNe 2019ibk, 2020uem, 2020xtg, 2020aekp, and 2018evt, and these SNe also have the higher H $\alpha$  equivalent widths in the sample.

Figure 2.12 plots the cumulative distribution of the Balmer decrements ( $\frac{F_{H\alpha}}{F_{H\beta}}$ ) measured for our sample SNe. The higher Balmer decrement values ( $>$ 15) have large errors associated with them because of the low SNR of the spectra from which they were derived, particularly near the H $\beta$  line. Consistent with the results of S13, the

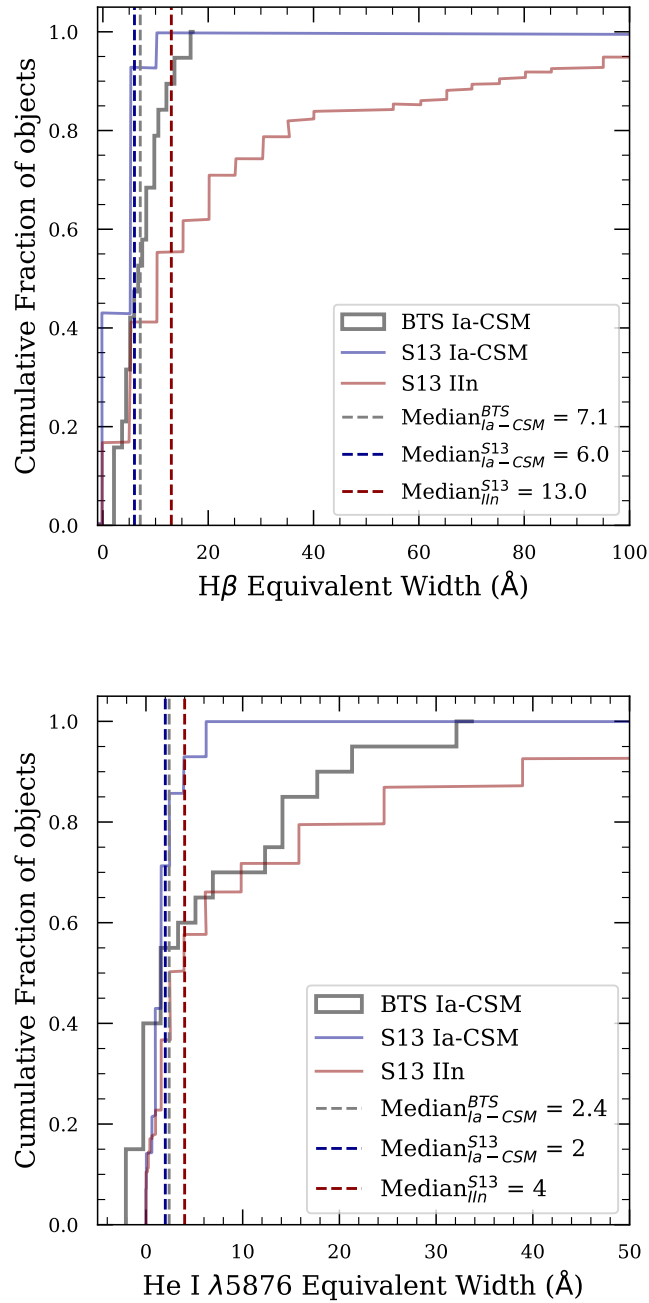


Figure 2.11: Cumulative distributions of equivalent width of  $H\beta$  and He I  $\lambda 5876$  emission lines calculated from the BTS SNe Ia-CSM (in grey) compared with the respective distributions presented in S13 for SNe Ia-CSM (blue) and SNe IIIn (red). Vertical dashed lines mark the median EW of the distributions.

SNe Ia-CSM from this sample also have a high median Balmer decrement value of  $\sim 7$  ( $\sim 5$  in S13), indicating that the emission line mechanism is probably collisional excitation or self-absorption rather than recombination, from which the expected Balmer decrement value is  $\sim 3$ . In the case of SNe Ia-CSM, if the CSM distribution consists of multiple shells as suggested for PTF11kx, moderately high densities could be created when fast moving ejecta overtake slowly moving thin dense CSM shells, creating large enough optical depth in the  $H\alpha$  line which results in the  $H\beta$  transition decaying as  $P\alpha + H\alpha$  (Xu et al. 1992). For some individual SNe where multiple spectra are available, the Balmer decrement is observed to first increase and later decrease with phase.

### Host galaxies

We retrieved science-ready co-added images from the *Galaxy Evolution Explorer* (GALEX) general release 6/7 (Martin et al. 2005), the Sloan Digital Sky Survey DR 9 (SDSS; Ahn et al. 2012), the Panoramic Survey Telescope and Rapid Response System (Pan-STARRS, PS1) DR1 (Chambers et al. 2016), the Two Micron All Sky Survey (2MASS; Skrutskie et al. 2006), and preprocessed WISE images (Wright et al. 2010) from the unWISE archive (Lang 2014)<sup>10</sup>.

We used the software package LAMBDA (Lambda Adaptive Multi-Band Deblending Algorithm in R) (Wright et al. 2016) and tools presented in Schulze et al. (2021) to measure the brightness of the host galaxy. The spectral energy distribution (SED) was modelled with the software package Prospector<sup>11</sup> (Johnson et al. 2021). We assumed a linear-exponential star-formation history, the Chabrier (2003) initial mass function, the Calzetti et al. (2000) attenuation model, and the Byler et al. (2017) model for the ionized gas contribution. The priors were set as described in Schulze et al. (2021).

Figure 2.13 shows the log of star formation rate (SFR) as a function of stellar mass for hosts of BTS SNe Ia-CSM. We also use a Galaxy-zoo (Lintott et al. 2011) sample of elliptical and spiral galaxies (randomly sampled in the redshift range  $z = 0.015 - 0.05$ ), and BTS SN Ia hosts as comparison samples collected by and used for comparison in Irani et al. (2022). We find the SN Ia-CSM host galaxy population to be consistent with late-type spirals and irregulars with recent star formation history. Four out of twelve SNe have clearly spiral hosts, 3 have edge-on host galaxies, 4 seem to have irregulars as hosts, and 1 has an unclear host type.

<sup>10</sup><http://unwise.me>

<sup>11</sup><https://github.com/bd-j/prospector> version 0.3

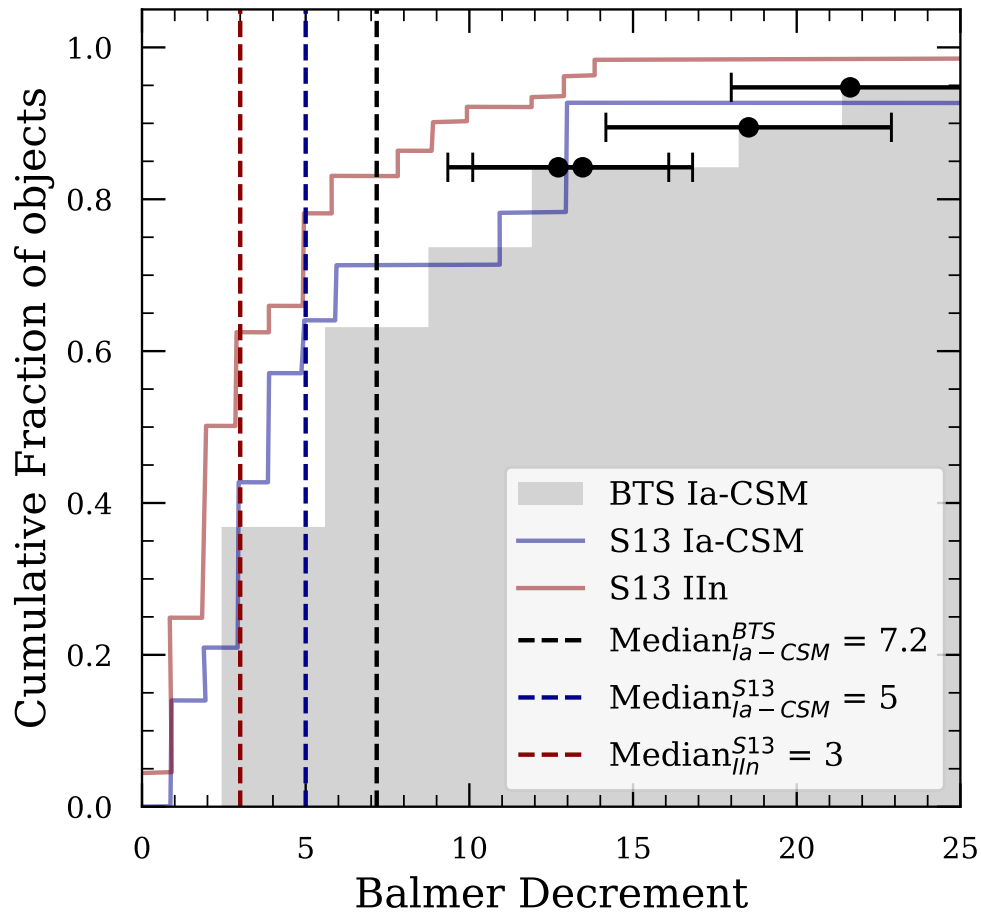


Figure 2.12: Cumulative distribution of  $H\alpha/H\beta$  intensity ratio (Balmer decrement) calculated from intermediate resolution spectra of the BTS SN Ia-CSM sample (grey shaded region). The red line is the distribution of Balmer decrement of SNe IIn measured in S13, and the blue line is the SN Ia-CSM Balmer decrement distribution from S13. The black circles are a few representative points indicating the high Balmer decrement values and the uncertainties on them. The vertical dashed line is the median Balmer decrement measured from BTS SNe Ia-CSM.

Host galaxies of 10 out of 12 SNe have  $w2 - w3$  measurements available which are all  $> 1$  mag, putting them in late-type category (Irani et al. 2022), 1 (SN 2019rvb) does not have W3 measurement but has  $NUV - PS1_r \sim 1$  mag again putting it towards late-type and 1 (SN 2020abfe) does not have any of the above information available except the  $PS1_r$  band magnitude of 20.766, which is the faintest host galaxy (absolute SDSS  $r$ -band magnitude of  $-17.4$ ) in our BTS SN Ia-CSM sample. As noted in S13, the SN Ia-CSM hosts of their sample had generally low luminosities ( $-19.1 < M_r < -17.6$ ) except MW-like spiral hosts. Our BTS SN Ia-CSM host luminosities lie in the range of  $-21.8 < M_r < -17.4$ , covering low to MW-like luminosities.

### Rates

Following the methodology for calculating the volumetric rate of transients found in the Bright Transient Survey from Perley et al. (2020), we use their equation 2 to calculate the SN Ia-CSM rate:

$$R = \frac{1}{T} \sum_{i=1}^N \frac{1}{\left(\frac{4\pi}{3} D_{max,i}^3\right) f_{sky} f_{ext} f_{rec} f_{cl,i}}$$

where  $T$  is the duration of the survey,  $N$  is the number of transients that pass the quality cut,  $D_{max,i}$  is the distance out to which the  $i^{th}$  transient with peak absolute magnitude  $M_i$  can be detected above the survey magnitude limit  $m_{lim}$  ( $=19$  mag for BTS SNe Ia-CSM) at peak light without any extinction,  $f_{sky}$  is the average active survey coverage as a fraction of full sky,  $f_{ext}$  is average reduction in effective survey volume due to Galactic extinction,  $f_{rec}$  is the average recovery efficiency for a detectable transient within the survey coverage area, and  $f_{cl,i}$  is the classification efficiency dependent on apparent magnitude.

The duration of the survey in which these 12 SNe Ia-CSM were detected is from 2018-05-01 to 2021-05-01, i.e.,  $T = 3$  years. We calculate  $f_{sky}$  during this time period by averaging the sky area coverage of the public MSIP survey considering 3-day cadence for ZTF Phase I (2018-05-01 to 2020-10-31) and 2-day cadence for ZTF Phase II (since 2020-11-01), which turns out to be  $12505 \text{ deg}^2$  for Phase I and  $14831 \text{ deg}^2$  for Phase II, giving a mean  $f_{sky} = 0.32$ . We use the same value of 0.82 for  $f_{ext}$  as calculated in Perley et al. (2020), given there has not been any change in the number and positions of ZTF fields.

To estimate  $f_{rec}$ , we consider SNe Ia-CSM brighter than  $-18.5$  peak absolute magnitude and brighter than 18 apparent magnitude (a total of 5) of which 4 pass

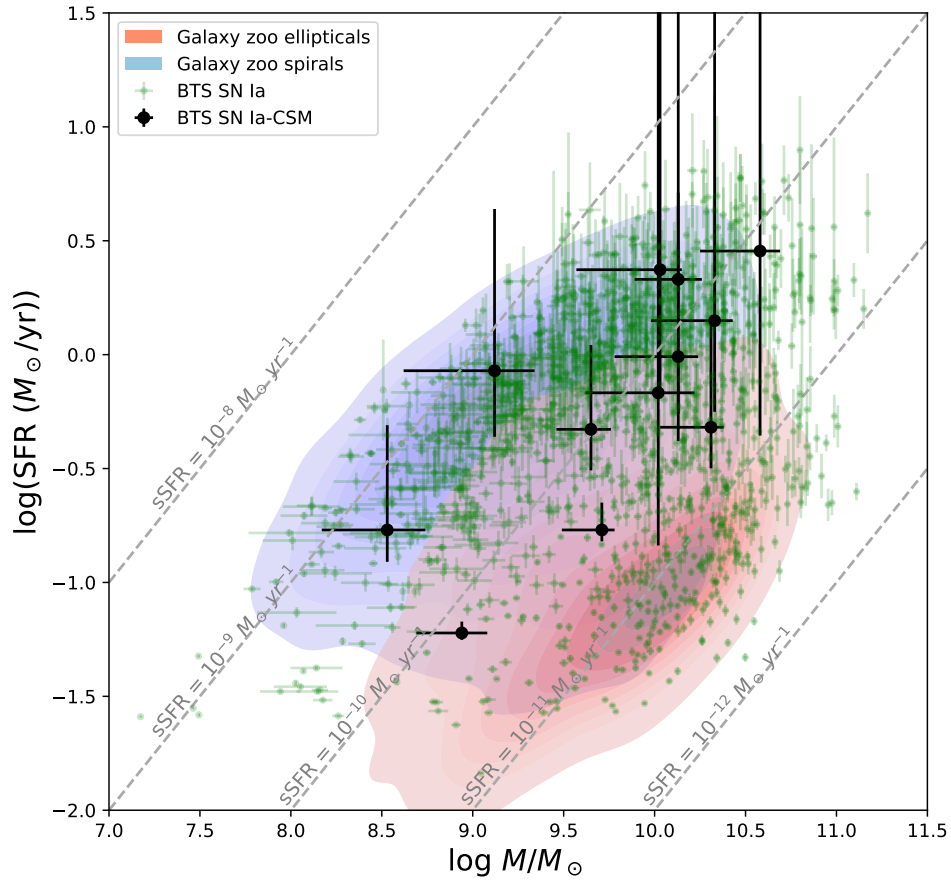


Figure 2.13: Host galaxies of BTS SN Ia-CSM (black circles) on SFR vs stellar mass plot with Galaxy-zoo spiral (blue contours) and elliptical (red contours) galaxies for comparison. BTS SN Ia hosts are also shown for comparison in green circles. Equal sSFR lines are marked with grey dashed lines.

the quality cut, giving an  $f_{rec}$  of 0.8. We take classification completeness of 0.75 at 19 mag, 0.9 at 18.5 mag, and 1 at 17.2 mag, and linearly interpolate in between these values to get  $f_{cl,i}$ .

Then using  $H_0 = 70 \text{ km s}^{-1} \text{ Mpc}^{-1}$ , ignoring cosmological effects<sup>12</sup> as in Perley et al. (2020) and applying a uniform K-correction ( $K = 2.5 \times \log_{10}(1 + z)$ ), we get a rate of  $29.35^{+27.53}_{-21.37} \text{ Gpc}^{-3} \text{ yr}^{-1}$  for SNe Ia-CSM. We also calculate a SN Ia rate of  $2.88^{+0.28}_{-0.25} \times 10^4 \text{ Gpc}^{-3} \text{ yr}^{-1}$  from SNe Ia observed in the same period following the same method, which is close to the value of  $2.35 \times 10^4 \text{ Gpc}^{-3} \text{ yr}^{-1}$  calculated in Perley et al. (2020). This puts SNe Ia-CSM to be 0.02–0.2% of SNe Ia. However, this rate estimate should be considered a lower limit given various caveats in the correct identification of SNe Ia-CSM (see discussion §2.4). If the ambiguous classification cases outlined in Appendix 2.7 are considered to be SN Ia-CSM and included in the rate calculation, we obtain a rate upper limit of  $97.7^{+135.8}_{-77.3} \text{ Gpc}^{-3} \text{ yr}^{-1}$ , which is 0.07–0.8% of SNe Ia.

### Precursor rates

The ZTF precursor rates were calculated following the method in Strotjohann et al. (2021a) which studied the frequency of precursors in interacting SNe found in ZTF. Strotjohann et al. (2021a) included 6 of the SNe Ia-CSM presented in this paper in addition to 4 other SNe Ia-CSM not in this paper (see Appendix 2.7 for details) for their search but did not find any robust  $5\sigma$  precursor detections. This non-detection was concluded to be due to the small sample size of SNe Ia-CSM (or that they are more distant) compared to the SN IIn sample, so even if the precursors were as bright or frequent as for SNe IIn, it would be difficult to detect them.

The same search was carried out here for our larger sample by taking the ZTF forced photometry multi-band ( $g, r, i$ ) light curves generated by the pipeline outlined in Masci et al. (2019) and stacking them in 1, 3, and 7-day long bins to search for faint outbursts. There were 7389 total available pre-explosion epochs for BTS SNe Ia-CSM, the earliest epoch being 1012 days prior to the explosion and the median phase 340 days prior. Hence, the results are valid for typical SN Ia-CSM progenitors at about  $\sim 1$  year before the SN. We did not find any robust  $5\sigma$  precursor detections. The upper limits for the precursor rates in different bands are shown in Figure 2.14, where the solid lines indicate up to what fraction of the time a precursor of a given brightness could have been detected while being consistent with the ZTF

<sup>12</sup>Contraction of control time window approximately compensated by increase in the star-formation rate density in the low redshift regime for redshift dependent SN rates.

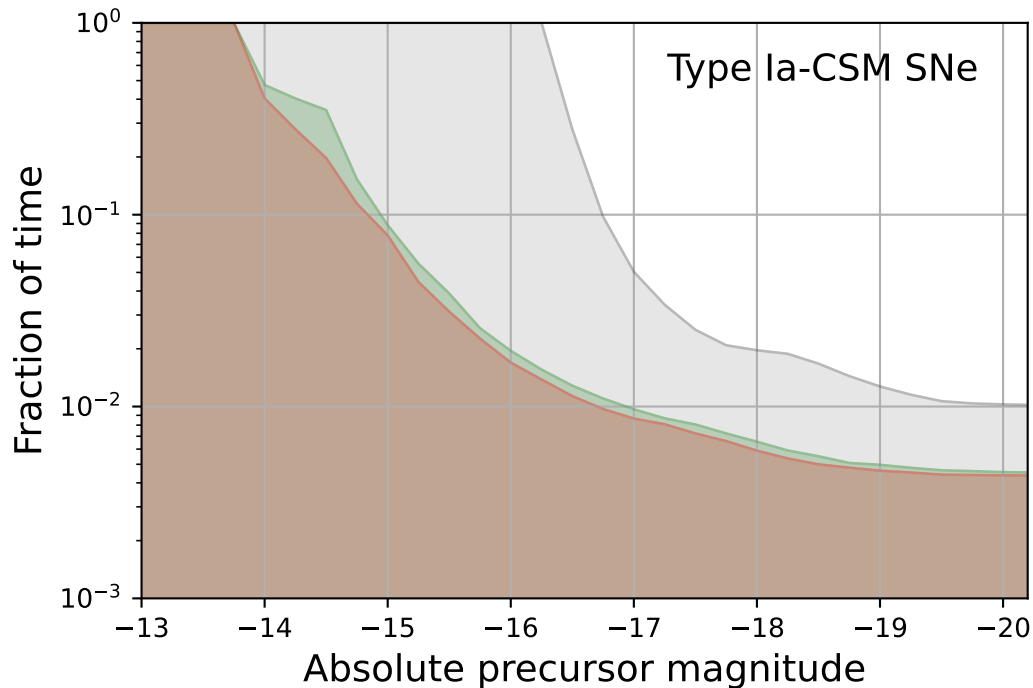


Figure 2.14: Precursor rate as a function of magnitude calculated from BTS SN Ia-CSM pre-explosion ZTF forced photometry stacked in 7-day bins. The different colored shaded regions correspond to different ZTF bands (*r*-red, *g*-green, *i*-grey). The solid lines depict the upper limits on the fraction of the time a precursor of the corresponding magnitude would have been detected, which is consistent with the ZTF non-detections.

non-detections. A precursor of  $-15$  magnitude could occur as frequently as  $\sim 10\%$  of the time given the ZTF non-detections. A continuous search for the precursors as more SNe Ia-CSM are found and classified, and their sample size increases, could yield a detection if the precursors are as frequent and bright as for SNe IIn. The dense and massive CSM around these objects is close enough to have been deposited within decades prior to the SN, but the lack of precursors within 1 year indicates that there is likely no violent event that ejects a lot of mass in that period. Probing for precursors could potentially constrain the progenitor in at least some cases. For example, Soker et al. (2013b) predicts for their core degenerate (CD) model for PTF11kx-like SNe release of significant energy ( $\sim 10^{49}$  erg) before explosion over timescale of several years, implying a precursor 3–7 magnitudes fainter than the SN explosion spread over several years, peaking in the near-IR.

## 2.4 Discussion

### Fraction of SNe Ia-CSM with delayed interaction

The fastest declining SNe in our sample (SNe 2018crl, 2020qxz, and 2020aekp) are also the ones that develop a plateau and show relatively stronger SN Ia-like absorption features in their early spectra. They seem to have a delayed start for the interaction like PTF11kx but not as fast a decline, and thus bridge the gap between PTF11kx and the rest of the strongly interacting SNe Ia-CSM. It remains to be seen how many SNe Ia are weakly interacting where the CSM interaction starts in earnest at timescales of  $\sim$ year or more after the explosion. Dubay et al. (2022) constrained the rate of late-onset CSM interaction (similar to that of PTF11kx) to be  $\leq 5.1\%$  between 0 and 500 days after discovery by searching for late-time UV excess in GALEX data of 1080 SNe Ia. A similar study in optical with ZTF data, currently undertaken by Terwel et al. (in prep), is searching for faint detections in carefully calibrated forced photometry light curves (stacked to go fainter). From the current sample, it appears that in addition to SNe Ia-CSM being intrinsically rare, delayed interaction SNe Ia-CSM are even rarer and only constitute about a quarter of all SNe Ia-CSM. This delayed interaction behaviour could also be an effect of asymmetric or clumpy CSM, wherein part of the SN ejecta shines through depending on the viewing angle. Observational campaigns that capture the inner boundary of the CSM and the geometry robustly could shed light on the distribution of the inner CSM radius and reveal if it is a continuous distribution or if there are multiple progenitor scenarios within the SN Ia-CSM class.

### Implications for progenitor based on observed mass loss

From Figure 2.10, the estimated mass-loss rates from a simple spherical treatment of the CSM and a stationary wind lie between  $\sim 10^{-3}$  to  $10^{-1} M_{\odot} \text{ yr}^{-1}$  over a period of less than  $\sim 60$  years before explosion. That gives a total mass loss of  $\sim 0.1$  to  $\sim 1 M_{\odot}$ . Dilday et al. (2012) estimated  $\sim 5 M_{\odot}$  of CSM around PTF11kx while Graham et al. (2017) revised it to be  $\sim 0.06 M_{\odot}$ . Light curve modeling of SN 1997cy and SN 2002ic by Chugai et al. (2004b) resulted in  $\sim 5 M_{\odot}$  estimates for both SNe. Inserra et al. (2016) also fit analytical models to some SNe Ia-CSM and found the CSM mass to lie between  $0.4$  and  $4.4 M_{\odot}$ . From Figure 2.5, the pseudo-bolometric luminosities of our SNe Ia-CSM lie somewhere between PTF11kx and SNe 1997cy, 2002ic, and 2005gj, with SN 1999E somewhere in the middle. We can say that the total CSM mass in our sample of SN Ia-CSM should also be several solar masses. A WD+AGB star system has typically been suggested for historical SNe Ia-CSM

to explain this massive CSM. The WD could either gain mass through Roche Lobe overflow (RLOF) from the companion that drives an optically thick wind (OTW) or merge with the core of the AGB star that then explodes in or soon after the common envelope phase. Meng et al. (2019) model WD+MS systems for their common envelope wind (CEW) model and find  $\sim 1 M_{\odot}$  CSM around SNe Ia-CSM. Thus, given the large observed CSM mass range, the nature of the companion cannot be solely determined from total mass lost. High-resolution spectroscopy that can resolve the narrow unshocked CSM wind velocity is also needed to determine the compactness of the companion.

### **Implications for progenitor based on observed volumetric rate**

Robust observed rate estimates for SNe Ia-CSM have been few and far between. Dilday et al. (2010) found 1 interacting SN Ia (SN 2005gj) in a sample of 79 SNe Ia at  $z < 0.15$  in the SDSS-II SN survey, giving a rate of  $\sim 1\%$ . After the PTF11kx discovery in the Palomar Transient Factory (PTF) survey, the SN Ia-CSM rate was estimated to be  $\sim 0.1\%$  (1 in 1000 classified SNe Ia; Dilday et al. 2012) but without spectroscopic completeness determination. S13 identified 7 more SNe Ia-CSM from the PTF SN IIn sample, bumping up the estimate to  $\sim 0.8\%$ . With this sample, we have improved the rate estimate, providing a robust value (along with an uncertainty estimate on that value) from an unbiased survey with high spectroscopic completeness up to 18.5 magnitude. However, this rate is quite possibly still underestimating the true value for two reasons: the first being possible thermonuclear SNe that are enshrouded so completely by CSM interaction that they are misclassified as SNe IIn in the absence of good early time data. In the BTS SN IIn sample, we found 6 SNe IIn to have ambiguous classifications, which could possibly be SNe Ia-CSM, and these are described in Appendix 2.7. Including these ambiguous cases in rate estimation results in a rate upper limit of 0.07–0.8% for strongly interacting thermonuclear SNe, while excluding them gives an underestimated rate of 0.02–0.2%.

The second issue with the rates is if there is indeed a continuum of delayed interaction SNe Ia-CSM like PTF11kx, interaction in SNe Ia may present itself hundreds of days later at magnitudes fainter than ZTF's limit ( $\sim 20.5$ ), resulting in those SNe not being counted when they may be sharing the same progenitor as the rest of the interacting SNe Ia-CSM. Lastly in some rare cases, the SN might appear normal in its light curve shape and duration (and thus would be missed by the selection criteria used in this paper) but seem to have peculiar narrow  $H\alpha$  in its spectrum or bright

mid-IR flux (like in the case of SN 2020aaym; Thévenot et al. 2021).

Han et al. (2006) predicted a rate of 0.1–1% for 02ic-like events for their delayed dynamical instability SD model, but could not naturally explain the delayed interaction and multiple CSM shells in PTF11kx (which is relevant for some SNe in our sample). A symbiotic nova-like progenitor was suggested by Dilday et al. (2012) for PTF11kx, and they quoted the theoretical rates for the same to lie between 1–30%; however, the model could not explain the massive CSM. Soker et al. (2013b) suggested a core degenerate (CD) scenario in which the explosion is set by the violent prompt merger of the core of the giant companion onto the WD and could naturally explain the massive CSM of PTF11kx (Livio et al. 2003). Soker et al. (2013b) estimated the occurrence of such SNe ( $M_{core} + M_{WD} \gtrsim 2 M_{\odot}$  and  $M_{env} \gtrsim 4 M_{\odot}$ ) through population synthesis and found it to be 0.002 per 1000  $M_{\odot}$  stars formed. Assuming  $\sim 1$ – $2$  SNe Ia occur per 1000  $M_{\odot}$  stars formed (Maoz et al. 2012), this corresponds to 0.1–0.2%, which compares well with our observed rate estimate.

The CEW model by Meng et al. (2019) predicts that the SNe Ia-CSM like objects could arise in the SD CEE scenario when CONe White Dwarfs (WD) steadily accrete material at the base of the CE without quickly spiraling in due to the driving of a CEW wind ( $10$ – $100 \text{ km s}^{-1}$ ). The WD explodes when it reaches the Chandrasekhar mass ( $1.38 M_{\odot}$ ) and could possibly explode within the CE before it is ejected. The CEW model predicts that 25–40% of the SNe Ia from CONe WD in Common envelope evolution with a Main Sequence (MS) companion will show SN Ia-CSM-like properties. Meng et al. (2019) also gives the ratio of SNe Ia from CONe WDs to normal SNe Ia from CO WDs to be between 1/9 and 1/5 (considering normal SNe Ia only come from CO WD + MS systems). Combining that with the estimate that roughly 10–20% of all SNe Ia may come from the SD scenario (Hayden et al. 2010; Bianco et al. 2011), SNe Ia-CSM from CONe WD according to the CEW model should be 0.28% to 1.6% of all SNe Ia. A spin-down before the explosion of the WD (Justham 2011; Di Stefano et al. 2012) could also explain the time delay between the explosion and interaction.

Soker (2022) estimated the common envelope to explosion delay time distribution (CEEDTD) shortly after the CEE ( $t_{CEED} < 10^4 \text{ yr}$ ) from SN in planetary nebula rates and SN Ia-CSM observed rates to be roughly constant rather than having a  $t^{-1}$  dependence, that is the SN explosion could occur very soon after the CEE as well. Our observed rates are on the lower side compared to these theoretical model estimates, but compare well within the observational uncertainties, though the CEW

model seems to best account for the overall SNe Ia-CSM properties.

## 2.5 Summary

In this paper, we have presented optical and mid-IR photometry, optical spectra, and detailed analysis of 12 new SNe Ia-CSM identified in the Zwicky Transient Facility Bright Transient Survey, nearly doubling the total number of such objects discussed previously by Silverman et al. (2013b). The properties of the sample extracted in this paper agree very well with similar analysis conducted in S13, particularly the median EW of  $H\beta$  is found to be significantly weaker in SNe Ia-CSM compared with SNe IIn, and consequently, the Balmer decrements are ubiquitously higher in SNe Ia-CSM. The brightness of SNe Ia-CSM in mid-IR is comparable to SNe IIn, and observations of reduced flux in the red side of the  $H\alpha$  wing, together with the mid-IR brightness, point to the formation of new dust in the cooling post-shock gas. The host galaxies of SNe Ia-CSM lie towards late-type galaxies with recent star formation. Unlike SNe IIn, no precursors were found within  $\sim 1000$  days before explosion for SNe Ia-CSM, which could be an observational bias (less number of SNe Ia-CSM compared to SNe IIn). We provide a robust rate estimate of 0.02–0.2% of all SNe Ia for SNe Ia-CSM on account of the BTS survey being unbiased and spectroscopically highly complete. The simple mass-loss rate estimates from the broad  $H\alpha$  luminosity of  $\sim 10^{-2} M_{\odot} \text{yr}^{-1}$  are similar to previous estimates from various methods and indicate several solar masses of CSM around these SNe. The observed rate agrees well within the observational uncertainties with the CEW model by Meng et al. (2019), which can also explain the interaction delay and massive CSM.

There are still many unanswered questions about the nature of the progenitors and whether we are accurately identifying all potential members of this class. As ZTF Phase II continues, we are identifying more and more SNe Ia-CSM (interacting with hydrogen-rich and helium-rich CSM) and looking further to the future, if ZTF continues for a Phase III and when LSST survey operations begin, a larger sample would further improve upon the observed rate calculation. However, individual object studies are as important, and detailed spectroscopic and multi-wavelength follow-up is essential to capture the CSM configuration and mass.

## 2.6 Acknowledgment

Based on observations obtained with the Samuel Oschin Telescope 48-inch and the 60-inch Telescope at the Palomar Observatory as part of the Zwicky Transient

Facility project. ZTF is supported by the National Science Foundation under Grants No. AST-1440341 and AST-2034437 and a collaboration including current partners Caltech, IPAC, the Weizmann Institute of Science, the Oskar Klein Center at Stockholm University, the University of Maryland, Deutsches Elektronen-Synchrotron and Humboldt University, the TANGO Consortium of Taiwan, the University of Wisconsin at Milwaukee, Trinity College Dublin, Lawrence Livermore National Laboratories, IN2P3, University of Warwick, Ruhr University Bochum, Northwestern University and former partners the University of Washington, Los Alamos National Laboratories, and Lawrence Berkeley National Laboratories. Operations are conducted by COO, IPAC, and UW. The ZTF forced-photometry service was funded under the Heising-Simons Foundation grant #12540303 (PI: Graham). This work was supported by the GROWTH project (Kasliwal et al. 2019) funded by the National Science Foundation under PIRE Grant No 1545949. The Oskar Klein Centre was funded by the Swedish Research Council. Partially based on observations made with the Nordic Optical Telescope, operated by the Nordic Optical Telescope Scientific Association at the Observatorio del Roque de los Muchachos, La Palma, Spain, of the Instituto de Astrofísica de Canarias. Some of the data presented here were obtained with ALFOSC. Some of the data presented herein were obtained at the W. M. Keck Observatory, which is operated as a scientific partnership among the California Institute of Technology, the University of California, and NASA; the observatory was made possible by the generous financial support of the W. M. Keck Foundation. The SED Machine is based upon work supported by the National Science Foundation under Grant No. 1106171. This work has made use of data from the Asteroid Terrestrial-impact Last Alert System (ATLAS) project. The Asteroid Terrestrial-impact Last Alert System (ATLAS) project is primarily funded to search for near earth asteroids through NASA grants NN12AR55G, 80NSSC18K0284, and 80NSSC18K1575; byproducts of the NEO search include images and catalogs from the survey area. The ATLAS science products have been made possible through the contributions of the University of Hawaii Institute for Astronomy, the Queen's University Belfast, the Space Telescope Science Institute, the South African Astronomical Observatory, and The Millennium Institute of Astrophysics (MAS), Chile. This research has made use of the NASA/IPAC Infrared Science Archive, which is funded by the National Aeronautics and Space Administration and operated by the California Institute of Technology. The Liverpool Telescope is operated on the island of La Palma by Liverpool John Moores University in the Spanish Observatorio del Roque de los Muchachos of the Instituto de Astrofísica de Canarias with

financial support from the UK Science and Technology Facilities Council.

Y. Sharma thanks the LSSTC Data Science Fellowship Program, which is funded by LSSTC, NSF Cybertraining Grant #1829740, the Brinson Foundation, and the Moore Foundation; her participation in the program has benefited this work.

S. Schulze acknowledges support from the G.R.E.A.T research environment, funded by *Vetenskapsrådet*, the Swedish Research Council, project number 2016-06012.

This work has been supported by the research project grant “Understanding the Dynamic Universe” funded by the Knut and Alice Wallenberg Foundation under Dnr KAW 2018.0067,

The research of Y. Yang is supported through a Bengier-Winslow-Robertson Fellowship.

Fritz (Walt et al. 2019; Duev et al. 2019) and GROWTH marshal (Kasliwal et al. 2019) (dynamic collaborative platforms for time-domain astronomy) were used in this work.

*Software:* LAMBDA (Wright et al. 2016), Prospector (Johnson et al. 2021), pySEDM (Rigault et al. 2019), IRAF (Tody 1986; Tody 1993), pyNOT (<https://github.com/jkrogager/PyNOT>), LPipe (Perley 2019), pypeit (Prochaska et al. 2020), extinction (Barbary 2016), pyraf-dbsp (Bellm et al. 2016), FPipe (Fremling et al. 2016), DBSP\_DRP (*DBSP DRP* 2021), ztfquery (Rigault 2018), astropy (Astropy Collaboration et al. 2013; Astropy Collaboration et al. 2018; Astropy Collaboration et al. 2022a), matplotlib (Hunter 2007a).

## 2.7 Appendix A: Ambiguous SN Ia-CSM/II<sub>n</sub> in BTS

To identify potential SNe Ia-CSM hiding in the SN II<sub>n</sub> sample classified by BTS, we rechecked all SNe II<sub>n</sub> classifications (total 142) using SuperNova IDentification (SNID; Blondin et al. 2007) software. SNe II<sub>n</sub> spectra were processed through SNID, and any SN having  $\geq 3$  matches to a SN Ia-CSM in the top 10 matches were manually checked. The SNe having ambiguous classifications are described below.

### SN 2019smj

Discovered by ZTF and reported to TNS by ALeRCE (Förster et al. 2021) on 2019-10-13 11:28:42.000, SN 2019smj (ZTF19aceqlxc) was classified as a Type II<sub>n</sub> by BTS at  $z = 0.06$ . It peaked at apparent magnitude 17.1 in the  $r$  band ( $\sim -20.1$ ) and then developed a weaker but broader bump. The spectra showed very weak  $H\beta$ ,

barely any He I  $\lambda 5876$ , no O I  $\lambda 7774$  or [O I] lines but showed some iron group lines, Ca NIR emission and [Ca II]. SNID best matches were to SNe 1997cy and 2005gj. The early spectra from P60/SEDM have some matches to SN 2005gj but are too noisy and of ultra-low resolution to conclusively provide a Ia-CSM classification. From these observations, SN 2019smj is most likely a Type Ia-CSM, but given the lack of confirmation, we have excluded it from the main sample.

### **SN 2018dfa**

Discovered and reported to TNS by ATLAS on 2018-07-05 08:51:21.000, SN 2018dfa was classified initially as a Type IIP by BTS but later spectra revealed it to be a Type IIn at  $z = 0.128$ . It peaked at an apparent magnitude of 17.5 in the  $r$  band ( $-20.2$ ) and showed a minor bump before the main peak in the light curve. The spectra showed weak  $H\beta$  and He I  $\lambda 5876$ , no O I  $\lambda 7774$  or [O I] lines. SNID best matches were to SNe 2002ic and 2005gj, along with SNe Ia-norm/91T. The earliest spectra with good SNR from P200/DBSP had one match to SN 2005gj but could not provide a robust Ia-CSM classification. From these observations, SN 2018dfa is most likely a Type Ia-CSM, but given the lack of confirmation, we have excluded it from the main sample.

### **SN 2019vpk**

Discovered by ZTF and reported to TNS by ALERCE on 2019-11-25 06:33:38.000, SN 2019vpk was classified as a Type IIn by BTS at  $z = 0.1$ . It peaked at apparent magnitude of  $\sim 18$  in the  $r$  band ( $\sim -20.5$ ). The early spectra were too noisy and the only spectrum with good SNR was obtained with P200/DBSP nearly 6 weeks after discovery which showed weak  $H\beta$ , no clear He I emission but possibly Si II  $\lambda 5958$  emission (which is unlike any other SN Ia-CSM). SNID top matches were to SN 2005gj, but visually did not look entirely convincing, and some matches were also to Type IIn. We conclude SN 2019vpk does not have enough data for a robust Ia-CSM classification.

### **SN 2019wma**

Discovered by ZTF and reported to TNS by ALERCE on 2019-12-13 13:35:26.000, SN 2019wma was classified as a Type IIn by BTS at  $z = 0.088$ . It peaked at an apparent magnitude of  $\sim 18.5$  in the  $r$  band ( $\sim -19.5$ ). The spectra obtained were either from P60/SEDM or LT/SPRAT, hence of low resolution and showed weak  $H\beta$  and He I emission. SNID top matches to the earliest SEDM spectrum were to SN

2005gj at the correct redshift, but given the lack of intermediate resolution spectra and absence of late time follow-up, we did not assign a Type Ia-CSM classification to SN 2019wma and excluded it from the main sample.

### **SN 2019kep**

Discovered and reported to TNS by ATLAS on 2019-07-02 14:13:55.000, SN 2019kep was classified as a Type II<sub>n</sub> by BTS at  $z = 0.02388$ . It peaked at an apparent magnitude of 18.2 in the  $r$  band ( $-17$ ). Most early spectra were too noisy for classification but matched SN 2005gj. A good SNR P200/DBSP spectrum showed narrow P-Cygni  $H\alpha$  with absorption minimum at  $\sim 2500 \text{ km s}^{-1}$  but overall matched to a Type II SN. From these observations, we could not determine a robust classification for SN 2019kep and excluded it from the main sample.

### **SN 2018ctj**

Discovered and reported to TNS by ZTF on 2018-04-21 08:36:57.000, SN 2018ctj was classified as a Type II<sub>n</sub> by BTS at  $z = 0.0378$ . It peaked at an apparent magnitude of 18.4 in the  $r$  band ( $-17.8$ ) and was also detected in unWISE data. Only one P60/SEDM spectrum was obtained that matched well to SNe 1997cy and 2005gj. Given the lack of intermediate resolution spectra, this SN remains classified as Type II<sub>n</sub> and excluded from the main sample.

*Chapter 3*

**DRAMATIC REBRIGHTENING OF THE TYPE-CHANGING  
STRIPPED-ENVELOPE SUPERNOVA SN 2023AEW**

Sharma, Y. et al. (May 2024). “Dramatic Rebrightening of the Type-changing Stripped-envelope Supernova SN 2023aew”. In: *ApJ* 966.2, 199, p. 199. DOI: 10.3847/1538-4357/ad3758.

Yashvi Sharma<sup>1</sup>, Jesper Sollerman<sup>2</sup>, Shrinivas R. Kulkarni<sup>1</sup>, Takashi J. Moriya<sup>3,4,5</sup>, Steve Schulze<sup>6</sup>, Stan Barmenloo<sup>2</sup>, Michael Fausnaugh<sup>7</sup>, Avishay Gal-Yam<sup>8</sup>, Anders Jerkstrand<sup>2</sup>, Tomás Ahumada<sup>1</sup>, Eric C. Bellm<sup>9</sup>, Kaustav K. Das<sup>1</sup>, Andrew Drake<sup>1</sup>, Christoffer Fremling<sup>1</sup>, David Hale<sup>10</sup>, Saarah Hall<sup>6</sup>, K. R. Hinds<sup>11</sup>, Theophile Jegou du Laz<sup>1</sup>, Viraj Karambelkar<sup>1</sup>, Mansi M. Kasliwal<sup>1</sup>, Frank J. Masci<sup>12</sup>, Adam A. Miller<sup>6</sup>, Guy Nir<sup>13</sup>, Daniel A. Perley<sup>11</sup>, Josiah N. Purdum<sup>10</sup>, Yu-Jing Qin<sup>1</sup>, Nabeel Rehemtulla<sup>6,14</sup>, R. Michael Rich<sup>15</sup>, Reed L. Riddle<sup>10</sup>, Antonio C. Rodriguez<sup>1</sup>, Sam Rose<sup>1</sup>, Jean Somalwar<sup>1</sup>, Jacob L. Wise<sup>11</sup>, Avery Wold<sup>12</sup>, Lin Yan<sup>1</sup>, and Yuhan Yao<sup>16,17</sup>

<sup>1</sup>Division of Physics, Mathematics and Astronomy, California Institute of Technology, Pasadena, CA 91125, USA

<sup>2</sup>Department of Astronomy, The Oskar Klein Center, Stockholm University, AlbaNova, 10691 Stockholm, Sweden

<sup>3</sup>National Astronomical Observatory of Japan, National Institutes of Natural Sciences, 2-21-1 Osawa, Mitaka, Tokyo 181-8588, Japan

<sup>4</sup>Graduate Institute for Advanced Studies, SOKENDAI, 2-21-1 Osawa, Mitaka, Tokyo 181-8588, Japan

<sup>5</sup>School of Physics and Astronomy, Monash University, Clayton, Victoria 3800, Australia

<sup>6</sup>Center for Interdisciplinary Exploration and Research in Astrophysics (CIERA), Northwestern University, 1800 Sherman Avenue, Evanston, IL 60201, USA

<sup>7</sup>Department of Physics & Astronomy, Texas Tech University, Lubbock, TX 79410-1051, USA

<sup>8</sup>Department of Particle Physics and Astrophysics, Weizmann Institute of Science, 234 Herzl Street, 76100 Rehovot, Israel

<sup>9</sup>DIRAC Institute, Department of Astronomy, University of Washington, 3910 15th Avenue NE, Seattle, WA 98195, USA

<sup>10</sup> Caltech Optical Observatories, California Institute of Technology, Pasadena, CA 91125, USA

<sup>11</sup> Astrophysics Research Institute, Liverpool John Moores University, Liverpool Science Park, 146 Brownlow Hill, Liverpool L3 5RF, UK

<sup>12</sup> IPAC, California Institute of Technology, 1200 E. California Boulevard, Pasadena, CA 91125, USA

<sup>13</sup> Department of Astronomy, University of California, Berkeley, CA 94720-3411, USA

<sup>14</sup> Department of Physics and Astronomy, Northwestern University, 2145 Sheridan Road, Evanston, IL 60208, USA

<sup>15</sup> UCLA Dept of Physics and Astronomy, PAB 430 Portola Plaza, Box 951547, Los Angeles, CA 90095-1547, USA

<sup>16</sup> Miller Institute for Basic Research in Science, 468 Donner Lab, Berkeley, CA 94720, USA

<sup>17</sup> Department of Astronomy, University of California, Berkeley, CA 94720, USA

## Abstract

Multi-peaked supernovae with precursors, dramatic light-curve rebrightenings, and spectral transformation are rare, but are being discovered in increasing numbers by modern night-sky transient surveys like the Zwicky Transient Facility (ZTF). Here, we present the observations and analysis of SN 2023aew, which showed a dramatic increase in brightness following an initial luminous ( $-17.4$  mag) and long ( $\sim 100$  days) unusual first peak (possibly precursor). SN 2023aew was classified as a Type IIb supernova during the first peak but changed its type to resemble a stripped-envelope supernova (SESN) after the marked rebrightening. We present comparisons of SN 2023aew’s spectral evolution with SESN subtypes and argue that it is similar to SNe Ibc during its main peak. P-Cygni Balmer lines are present during the first peak, but vanish during the second peak’s photospheric phase, before  $H\alpha$  resurfaces again during the nebular phase. The nebular lines ([O I], [Ca II], Mg I],  $H\alpha$ ) exhibit a double-peaked structure which hints towards a clumpy or non-spherical ejecta. We analyze the second peak in the light curve of SN 2023aew and find it to be broader than normal SESNe as well as requiring a very high  $^{56}\text{Ni}$  mass to power the peak luminosity. We discuss the possible origins of SN 2023aew, including an eruption scenario where a part of the envelope is ejected during the first peak, which also powers the second peak of the light curve through SN-CSM interaction.

## 3.1 Introduction

Core-collapse (CC) supernovae (SNe) mark the final explosions of massive stars ( $\gtrsim 8 M_{\odot}$ ), and stripped-envelope SNe (SESN) represent CC in stars that have lost most—or all—of their envelopes prior to explosion. This includes Type IIb SNe (some H left), SNe Ib (no H, some He), and SNe Ic (neither H nor He, Gal-Yam 2017).

Even though we now have hundreds of well-observed SESNe, there are still several open questions regarding their nature, both when it comes to their progenitor stars and their powering mechanism. Binarity seems to be a key component for stripping their envelopes, with arguments supported by relatively low ejecta masses, large relative rates (Smith 2011), and direct evidence of a binary system after the SESN 2022jli (Chen et al. 2024). These deduced ejecta masses often come from comparisons with simple analytical models, e.g., Arnett 1982; Yang et al. 2023; Barbarino et al. 2021, that match reasonably well with the observed light curves assuming powering by radioactive  $^{56}\text{Ni}$ . However, modern explosion models are unable to produce the amount of radioactive nickel required for the brighter Type Ibc SNe (Sollerman et al. 2022), and some SESNe show light-curve features that are not compatible with the standard scenario. Such unusual SESNe have emerged from the large samples of SNe now available, and include double bump light curves (LCs), for example, for SN 2019cad (Gutiérrez et al. 2021), SN 2022xxf (Kuncarayakti et al. 2023), and SN 2022jli (Chen et al. 2024), where different powering mechanisms were suggested in each of these cases for explaining the second LC bump.

In this paper, we present the unusual stripped-envelope SN 2023aew (ZTF23aaawbsc) discovered as part of the Zwicky Transient Facility Bright Transient Survey (BTS; Fremling et al. 2020; Perley et al. 2020; Rehemtulla et al. 2024). This supernova shows an unprecedented first peak with a broad light curve and a slight plateau, followed by another unusually broad second peak light curve. Spectrally, this object is clearly a SESN, but unlike any previous such objects.

The paper is organized as follows. In §3.2 we present the discovery and the observations of our SN, as well as details about the data reductions and calibrations. Section §3.3 presents an analysis of the photometric and spectroscopic data as well as comparisons to a number of similar SNe from the literature. In §3.4 we discuss in particular the mechanisms that could power the main light curve peak of SN 2023aew, and in this connection we also present a few other objects with relevant observations. Finally, §3.5 presents our conclusions and a short discussion where we put our results in context.

### 3.2 Observations

In this section, we present our observations of SN 2023aew obtained over 300 days with multiple instruments and describe the data processing methods.

## Discovery

SN 2023aew was detected in Zwicky Transient Facility (ZTF; Bellm et al. 2019; Graham et al. 2019; Dekany et al. 2020) data obtained with the Palomar Schmidt 48-inch Samuel Oschin telescope (P48), on 2023-01-23 (MJD 59967.511) and the discovery was reported to the Transient Name Server (TNS<sup>1</sup>) by ALeRCE (Förster et al. 2021; Munoz-Arancibia et al. 2023). This first ZTF detection magnitude was 18.05 in the  $r$  band at the J2000.0 coordinates  $\alpha = 17^h40^m51.395^s$ ,  $\delta = +66^\circ12'22''.62$ . The transient is apparently positioned on the outskirts of the spiral host galaxy SDSS J174050.55+661220.7. The transient was subsequently reported to TNS by Gaia (Hodgkin et al. 2021) in February, ATLAS (Tonry et al. 2018) in March, and by MASTER (Lipunov et al. 2019) in May when it began to brighten again. Gaia reported an 18.16 mag detection in  $G$ -Gaia band two days before the ZTF discovery (i.e., at MJD 59965.284). The last  $3\sigma$  upper limit is  $\sim 200$  days before first detection in ATLAS  $o$  band and  $\sim 500$  days before first detection in ZTF  $r$  band. However, the Transiting Exoplanet Survey Satellite (TESS; Ricker 2014) had a serendipitous two months of coverage of SN 2023aew right before the ZTF discovery (from MJD 59910 to 59962). TESS captured a slow, 30-day rise of this SN where ground-based telescopes only caught the tail of this transient at its ZTF discovery (see Figure 3.1). We derive an explosion epoch of MJD  $59936.18 \pm 1.4$  days by fitting a power law to an 8-hour binned TESS-Red band light curve (details in §3.2, Fausnaugh et al. 2021). Therefore, all phases throughout this paper will be reported with respect to this explosion epoch estimate.

The transient was spectroscopically classified as a SN I Ib by ZTF (Wise et al. 2023) on 2023-01-27 (four days after ZTF discovery) with a spectrum obtained using the Spectral Energy Distribution Machine (SEDM; Ben-Ami et al. 2012; Blagorodnova et al. 2018) on the Palomar 60-inch telescope (P60; Cenko et al. 2006) and its `superfit` (Howell et al. 2005) match to SN I Ib templates at a redshift of  $z = 0.025$ . This is consistent with the redshift of  $z = 0.0255 \pm 0.0001$  obtained from the narrowest lines in our late high signal-to-noise ratio Keck2/ESI spectrum (§2.3). Using a flat cosmology with  $H_0 = 70 \text{ km s}^{-1}$  and  $\Omega_m = 0.3$ , this redshift corresponds to a luminosity distance of 111 Mpc. The transient, initially classified as SN I Ib was observed to have a smooth initial light-curve decline for  $\sim 25$  days, which then turned into a slow plateau for another  $\sim 50$  days in ground-based optical data. The great surprise came with the rapid rebrightening of SN 2023aew, which

---

<sup>1</sup><https://www.wis-tns.org>.

started around 2023-04-11 (MJD 60045), wherein the SN rose by  $\sim 2$  magnitudes in  $\sim 10$  days. As spectroscopic campaigns began in earnest, Frohmaier et al. (2023) reported their spectrum taken on 2023-04-20 with SPRAT (Pascik et al. 2014) on the Liverpool Telescope (Steele et al. 2004) to be consistent with SN Ib templates, albeit at a slightly higher redshift using SNID (Blondin et al. 2007). Hoogendam et al. (2023) reported three more spectra taken with SNIFS on the University of Hawaii 2.2m telescope on 2023-04-23, 2023-04-25, and 2023-04-29, which were more consistent with late-time SN Ic templates.

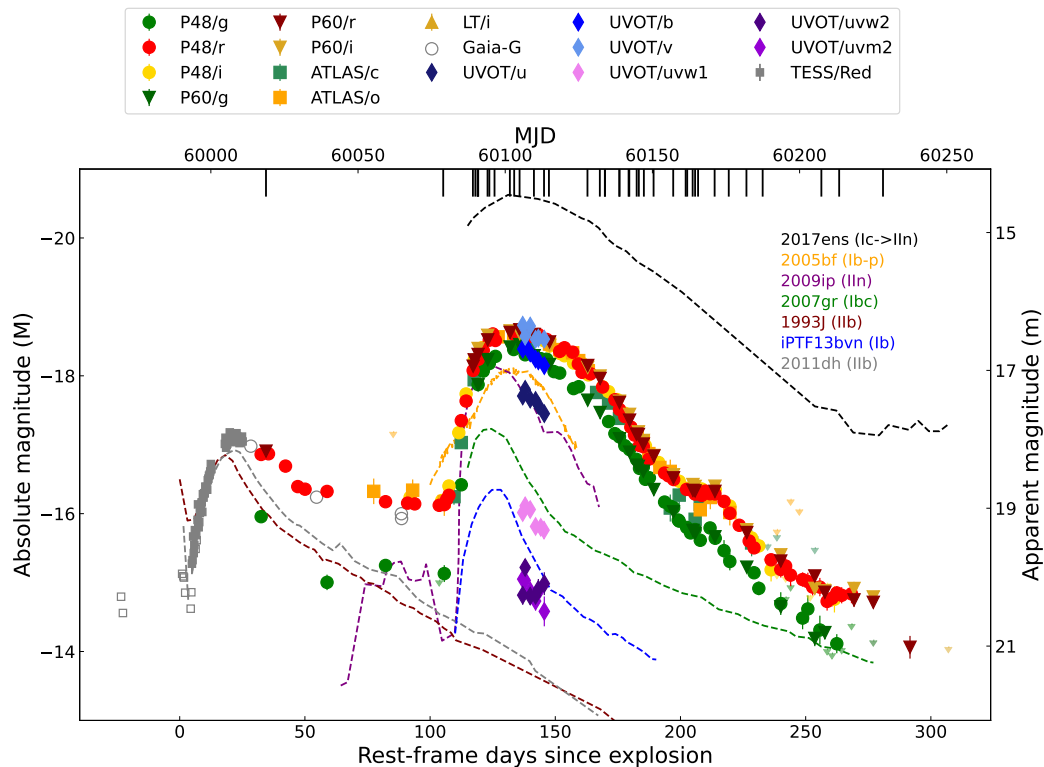


Figure 3.1: Light curve of SN 2023aew. The TESS observations cover the rise of the first peak and are shown in gray squares, with  $5\sigma$  significance denoted with full markers and  $3\sigma$  with empty markers. The spectroscopic epochs are marked with black lines at the top. Also shown for comparison are absolute magnitude  $r$ -band light curves of SNe 1993J (IIb), 2011dh (IIb), 2005bf (Ib-pec), 2007gr (Ic), 2009ip (IIIn), iPTF13bvn (Ib), and the type-changing 2017ens (Ic to IIIn). SNe 1993J and 2011dh are shifted to match their first detection with the SN 2023aew explosion epoch. Other comparison SNe are shifted by  $\sim 100$  days to match the start of the second peak. The overall light curve shape is somewhat similar to that of SN 2009ip but is broader, with the second peak having similar broadness as SN 2017ens.

### Optical photometry

We obtained forced PSF photometry via the ZTF forced photometry service (Masci et al. 2019; IRSA 2022; Masci et al. 2023) in  $g$ ,  $r$ , and  $i$  bands and via ATLAS forced photometry service (Tonry et al. 2018; Smith et al. 2020) in  $c$  and  $o$  bands. Additional photometry was obtained with the Rainbow camera on P60 and processed with the automatic image subtraction pipeline FPipe (Fremling et al. 2016). The Gaia-G band photometry was obtained from the Gaia Alerts service<sup>2</sup>. All photometry is corrected for Milky Way extinction using the Python package `extinction` (Barbary 2016), the dust extinction law from Fitzpatrick (1999), the Schlafly et al. (2011) dust map,  $E(B - V) = 0.0386$  mag, and an  $R_V$  of 3.1. All measurements are converted into flux units for the analysis. We do not account for the host reddening, given that the transient is at the outskirts of the host galaxy.

### TESS photometry

SN 2023aew had serendipitous coverage from TESS observations of Sector 59 and 60 from MJD 59910 to 59962—two months before the first ZTF detection. The TESS-Red<sup>3</sup> filter extends from 5802.57 Å to 11171.45 Å with a reference wavelength of 7697.60 Å. Image subtraction and forced photometry at SN 2023aew’s location were carried out according to the methodology in Fausnaugh et al. (2021). The differential flux has a cadence of 200 seconds but was binned into 6-hour bins and converted into Vega magnitudes. These were further converted to the AB system and corrected for MW extinction following the method in the previous section and using the TESS-Red reference wavelength. The binned TESS photometry is included in Table 3.3.

### Swift Ultraviolet/Optical telescope photometry

The field was observed with the Ultraviolet/Optical Telescope (Roming et al. 2005) (UVOT) aboard the *Swift* satellite (Gehrels et al. 2004) between MJD=60076.47 and 60085.44 in  $w2$ ,  $m2$ ,  $w1$ ,  $u$ ,  $b$ , and  $v$ . The science-ready data were retrieved from the *Swift* archive<sup>4</sup>. In December 2023, deep template images were obtained in all filters to remove the host contamination from the transient photometry. Then all-sky exposures for a given epoch and filter were co-added to boost the signal-to-noise

<sup>2</sup><http://gsaweb.ast.cam.ac.uk/alerts/home>.

<sup>3</sup><http://svo2.cab.inta-csic.es/theory/fps/index.php?mode=browse&gname=TESS&asttype=>.

<sup>4</sup>[https://www.swift.ac.uk/swift\\_portal](https://www.swift.ac.uk/swift_portal).

ratio using `uvotimsum` in HEASoft<sup>5</sup> version 6.31.1. Afterwards, the brightness of the SN was measured with the *Swift* tool `uvotsource`. The source aperture had a radius of  $5''$ , while the background region had a significantly larger radius. We measured the host contribution from the December 2023 templates using the same source and background apertures and subtracted this contribution from the transient flux measurements. All measurements were calibrated with the latest calibration files from November 2021 and converted to the AB system following Breeveld et al. (2011). Table 3.4 summarizes all measurements (not corrected for reddening).

### ***Swift* X-ray telescope measurements**

While monitoring SN 2023aew with UVOT between MJD=60076.47 and 60085.44, *Swift* also observed the field with its onboard X-ray telescope XRT between 0.3 and 10 keV in photon-counting mode (Burrows et al. 2005). This data was analyzed with the online tools of the UK *Swift* team<sup>6</sup> that use the software package HEASoft version 6.32 and methods described in Evans et al. (2007) and Evans et al. (2009).

SN 2023aew evaded detection in all epochs. The median  $3\sigma$  count-rate limit of each observing block is  $8 \times 10^{-3} \text{ s}^{-1}$  (0.3–10 keV). Coadding all data pushes the  $3\sigma$  count-rate limits to  $1.4 \times 10^{-3} \text{ s}^{-1}$ . A list of the limits from the stacking analysis is shown in Table 3.5. To convert the count-rate limits into a flux, a power-law spectrum was assumed with a photon index<sup>7</sup> of  $\Gamma = 2$  and a Galactic neutral hydrogen column density of  $3.4 \times 10^{20} \text{ cm}^{-2}$  (HI4PI Collaboration et al. 2016). The co-added count-rate limit corresponds to an unabsorbed flux of  $< 5.5 \times 10^{-14} \text{ erg cm}^{-2} \text{ s}^{-1}$  between 0.3–10 keV and luminosity of  $< 7.8 \times 10^{40} \text{ erg s}^{-1}$ . The flux and luminosity limits of the individual bins are shown in Table 3.5.

### **Optical spectroscopy**

We obtained a comprehensive spectroscopic follow-up dataset from many facilities at a variety of spectral resolutions (e.g., KeckI/LRIS  $R \sim 800$ –1400, P200/DBSP  $R \sim 1000$ , NOT/ALFOSC  $R \sim 360$ , P60/SEDM  $R \sim 100$ ) to study the evolution of this SN. In total, we have 41 spectra covering epochs from 34 days to 281 days since the explosion. Table 3.1 lists the facilities, instruments, and data processing software references. The spectral sequence is listed in Table 3.2 and shown in Figure 3.2. All the spectra were corrected for Milky Way extinction using the same

<sup>5</sup><https://heasarc.gsfc.nasa.gov/docs/software/heasoft/>.

<sup>6</sup>[https://www.swift.ac.uk/user\\_objects](https://www.swift.ac.uk/user_objects).

<sup>7</sup>The photon index is defined as the power-law index of the photon flux density ( $N(E) \propto E^{-\Gamma}$ ).

Table 3.1: Description of spectrographs used for follow-up and the corresponding data reduction pipelines.

Instrument	Telescope	Software
SEDM <sup>1</sup>	Palomar 60-inch	pySEDM <sup>2</sup>
ALFOSC <sup>3</sup>	Nordic Optical Telescope	PyNOT <sup>4</sup> PyPeIt
DBSP <sup>5</sup>	Palomar 200-inch	DBSP_DRP <sup>6</sup>
KAST <sup>7</sup>	Shane 3-m	IRAF <sup>8</sup>
LRIS <sup>9</sup>	Keck1	LPipe <sup>10</sup>
SPRAT <sup>11</sup>	Liverpool Telescope	PyPeIt
NIRES <sup>12</sup>	Keck2	Wilson et al. 2004
ESI <sup>13</sup>	Keck2	makee <sup>14</sup>

<sup>1</sup> Spectral Energy Distribution Machine (Blagorodnova et al. 2018).

<sup>2</sup> Rigault et al. (2019) and Kim et al. (2022)

<sup>3</sup> Andalucia Faint Object Spectrograph and Camera

<sup>4</sup> <https://github.com/jkrogager/PyNOT>

<sup>5</sup> Double Beam Spectrograph (Oke et al. 1982)

<sup>6</sup> pypeit (Prochaska et al. 2020) based pipeline ([https://github.com/finagle29/dbsp\\_drp](https://github.com/finagle29/dbsp_drp))

<sup>7</sup> Kast Double Spectrograph (Miller et al. 1987)

<sup>8</sup> Tody (1986) and Tody (1993)

<sup>9</sup> Low Resolution Imaging Spectrometer (Oke et al. 1995)

<sup>10</sup> IDL based automatic reduction pipeline (Perley 2019; <https://sites.astro.caltech.edu/~dperley/programs/lpipe.html>)

<sup>11</sup> Spectrograph for the Rapid Acquisition of Transients (Piascik et al. 2014)

<sup>12</sup> Near-Infrared Echellette Spectrometer (Wilson et al. 2004)

<sup>13</sup> Echellette Spectrograph and Imager (Sheinis et al. 2002)

<sup>14</sup> <https://www2.keck.hawaii.edu/inst/esi/makee.html>

procedure as for the photometry, then scaled to match the synthetic photometry from the spectra with the contemporaneous host-subtracted ZTF  $r$ -band data. The SN redshift ( $z = 0.0255 \pm 0.0001$ ) was obtained from the narrowest lines in our highest resolution Keck2/ESI spectrum in the absence of a pre-existing host redshift measurement. The spectra will be made available on WISeREP<sup>8</sup> (Yaron et al. 2012).

### 3.3 Analysis

#### Light curve

SN 2023aew had a rise of about 2.5 mag over the first 25 days ( $\sim 11 \text{ mag } 100\text{d}^{-1}$ ) to a first peak in TESS data, with a peak magnitude of 17.88 mag in TESS-Red band ( $-17.2$ ; see Figure 3.1). It then proceeded to decline with an initial decline

<sup>8</sup><https://www.wiserep.org/>.

Table 3.2: Summary of optical and NIR spectra.

<b>MJD</b>	<b>Phase</b> (day)	<b>Telescope/Instrument</b>	<b>Int</b> (sec)
59972	34	P60/SEDM	2250
60044	105	LT/SPRAT	2200
60056	117	P60/SEDM	1800
60057	118	P60/SEDM	1800
60058	119	NOT/ALFOSC	1800
60058	119	P60/SEDM	1800
60058	119	Lick-3m/KAST	1200
60062	123	P60/SEDM	1800
60063	124	Keck2/NIRES	520
60065	126	LT/SPRAT	2200
60071	132	P60/SEDM	1800
60073	134	NOT/ALFOSC	600
60075	136	P60/SEDM	1800
60081	141	P60/SEDM	1800
60085	146	Keck1/LRIS	300
60087	147	P60/SEDM	1800
60103	163	P60/SEDM	1800
60108	168	P60/SEDM	1800
60110	170	Keck1/LRIS	180
60110	170	Keck1/LRIS	1200
60116	176	P60/SEDM	1800
60116	176	P200/DBSP	600
60120	179	NOT/ALFOSC	1800
60120	180	P60/SEDM	1800
60123	183	P60/SEDM	2250
60124	183	P60/SEDM	1800
60126	185	P60/SEDM	1800
60130	189	P60/SEDM	1800
60138	197	P60/SEDM	1800
60143	202	Keck1/LRIS	300
60144	203	NOT/ALFOSC	2400
60146	205	P60/SEDM	2250
60147	206	P60/SEDM	2250
60148	207	Keck1/LRIS	600
60155	214	P60/SEDM	2250
60161	219	NOT/ALFOSC	2400
60168	226	P60/SEDM	2250
60175	233	NOT/ALFOSC	4400
60199	256	NOT/ALFOSC	1100
60206	263	Keck2/ESI	2700
60224	281	Keck1/LRIS	900

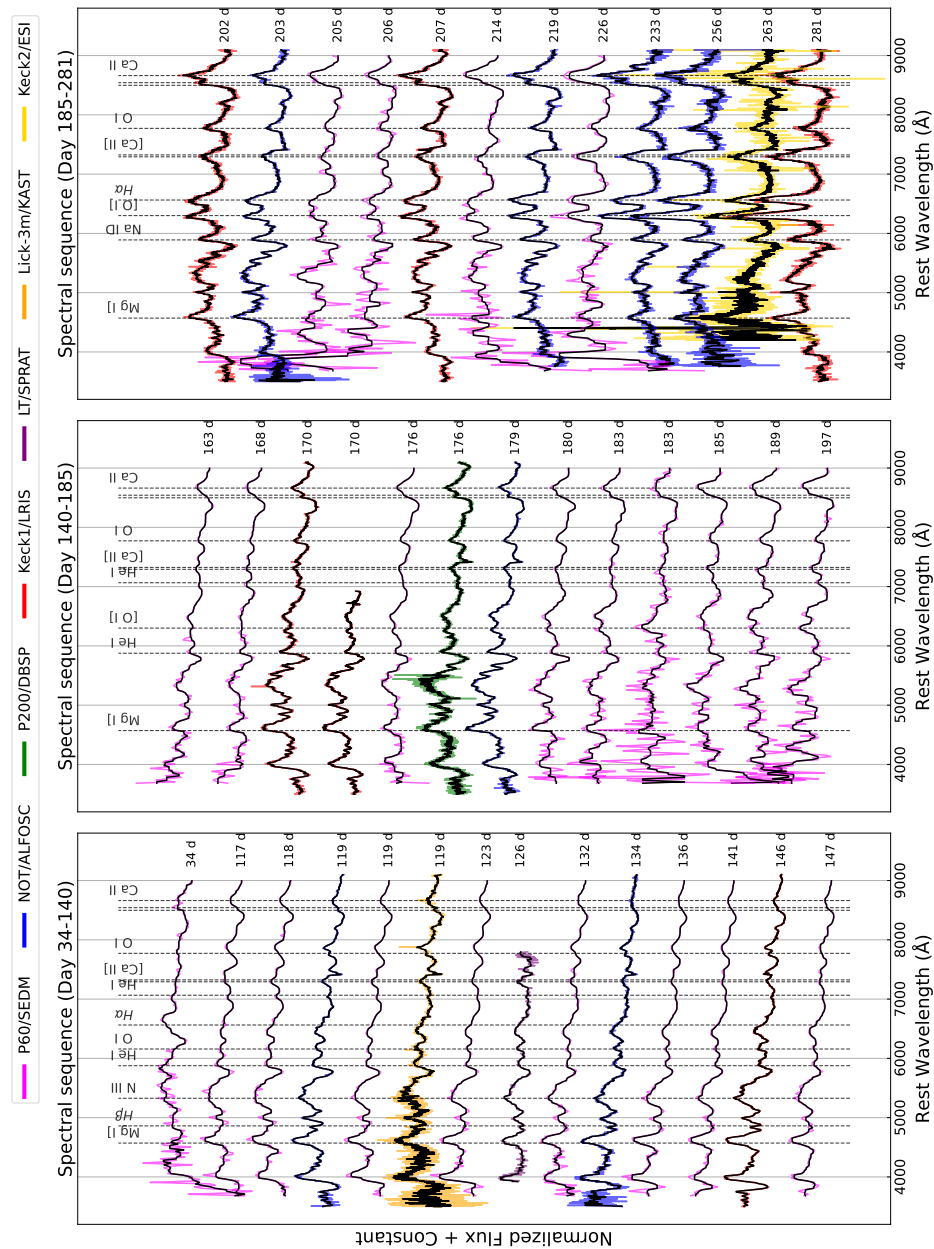


Figure 3.2: Spectral sequence of SN 2023aew from day 34 to day 281. The black lines are smoothed spectra (using a median filter), and the colored lines are original spectra, with different colors depicting different instruments. Some important spectral lines are marked with gray dashed lines. In the left panel, the Balmer lines are visible in the first spectrum at 34 days, then H $\alpha$  seemingly shows up again in the nebular phase spectra in the third panel.

rate of  $2.6 \text{ mag } 100\text{d}^{-1}$  in the  $r$  band for the next 30 days (rest-frame) and settled onto a slowly declining plateau with only  $0.2 \text{ mag } 100\text{d}^{-1}$  in the  $r$  band between day 60 to 105, reaching a minimum brightness of  $18.93 \text{ mag}$  ( $-16.5$ ). After day 105, SN 2023aew suddenly started brightening again and rose at a rate of  $13.5 \text{ mag } 100\text{d}^{-1}$  in the  $r$  band and reached a second peak brightness of  $16.45 \text{ mag}$  ( $-18.8$ ) at day 132 after which it started turning over to decline at a rate of  $\sim 4 \text{ mag } 100\text{d}^{-1}$  ( $r$  band). Around day  $\sim 205$ , the SN developed a smaller bump in the light curve for  $\sim 25$  days, before coming back to its previous decline rate. Our last detection of  $21.2 \text{ mag}$  in the  $i$  band was obtained on day 315, and the last limit of  $> 22.1 \text{ mag}$  in the  $r$  band was obtained on day 323. Figure 3.1 also shows the light curves of some peculiar SESNe from the literature for comparison. The light curves of comparison SNe were obtained from the Open Supernova Catalog (Guillochon et al. 2017) for SNe 1993J (van Driel et al. 1993; Benson et al. 1994; Richmond et al. 1994; Barbon et al. 1995; Richmond et al. 1996), 1998bw (Galama et al. 1998; Sollerman et al. 2000; Patat et al. 2001; Sollerman et al. 2002), 2005bf (Tominaga et al. 2005; Stritzinger et al. 2018), 2007gr (Valenti et al. 2008b; Bianco et al. 2014; Chen et al. 2014), 2009ip (Mauerhan et al. 2013; Margutti et al. 2014), 2011dh (Arcavi et al. 2011; Ergon et al. 2015) and iPTF13bvn (Fremming et al. 2016; Modjaz et al. 2016; Shivvers et al. 2019), and from ATLAS forced photometry service (Tonry et al. 2018; Smith et al. 2020; Shingles et al. 2021) for SN 2017ens (Chen et al. 2018).

Figure 3.3 depicts the  $g-r$  and  $r-i$  color evolution of SN 2023aew and the comparison SNe. During the declining phase of the first peak, the color of SN 2023aew is red and constant. During the rapid rebrightening, the color gets rapidly bluer, then slowly turns red again, similar to the comparison SNe.

The UV colors obtained with *Swift* just after the second peak (see Figure 3.1) do not seem particularly bluer than other SESNe at those epochs. However, as there are only a few SESNe observed in UV, and they show a wide variety of behavior in their UV colors, no inferences can be made with certainty (Brown et al. 2009; Brown et al. 2015).

### **Bolometric luminosity**

SN 2023aew has good coverage in only the TESS-Red band for the first 30 days and then only in the  $r$  band for the rest of the first peak duration, after which there is decent coverage in all ZTF and ATLAS optical bands. However, as there is no coverage in the UV or the infrared, it is difficult to produce a full bolometric light

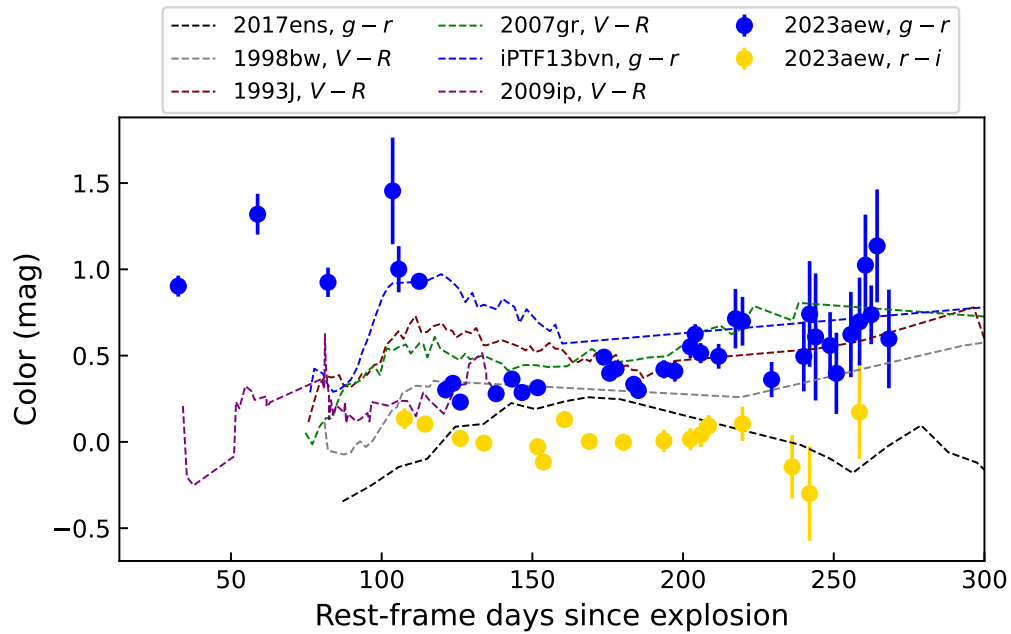


Figure 3.3:  $g - r$  and  $r - i$  color curves of SN 2023aew. Shown for comparison are  $V - R$  color curves of SNe 1993J, 1998bw, 2007gr, and 2009ip, and  $g - r$  color curves of SN 2017ens and iPTF13bvn.

curve.

The TESS-Red band fluxes were converted into luminosities by multiplying them with the effective filter width (integrated area under the TESS-Red filter transmission curve; Rodrigo et al. 2012; Rodrigo et al. 2020) and the luminosity distance factor. This estimate was used as an approximate pseudo-bolometric luminosity.

We used Superbol (Nicholl 2018a) with ZTF  $gri$  bands and ATLAS  $co$  bands to get pseudo-bolometric and bolometric light curves. Superbol interpolates all bands to the  $r$ -band epochs, calculates pseudo-bolometric luminosity by integrating the observed fluxes over the available bandpasses, and estimates the bolometric luminosity by adding blackbody corrections (absorbed UV and NIR) to the pseudo-bolometric light curve. Additionally, HAFJET (Yang et al. 2023) was also used to obtain another bolometric light curve estimate by applying bolometric corrections to  $g$ -band data following Lyman et al. (2014).

Figure 3.4 shows both the bolometric luminosity and the pseudo-bolometric luminosity for SN 2023aew along with luminosities of SNe 1998bw (pseudo-bolometric light curve from their figure 18, Patat et al. 2001), 2005bf (bolometric light curve

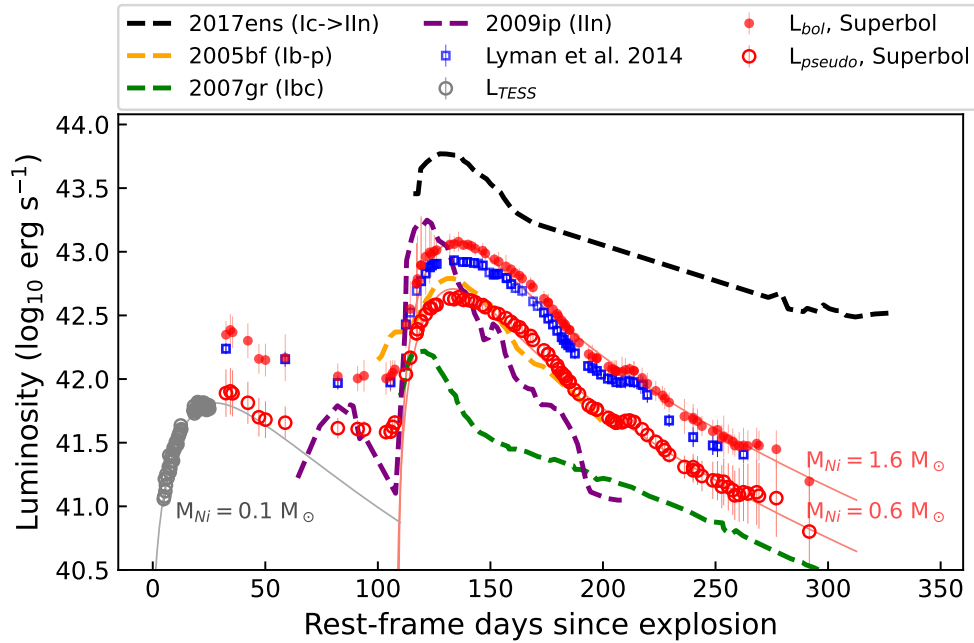


Figure 3.4: Bolometric (filled red circles) and pseudo-bolometric (open red circles) light curves of SN 2023aew along with some comparison SNe. Gray open circles denote the pseudo-bolometric luminosity approximation from TESS observations. Also shown (blue squares) is an alternative estimate of the bolometric light curve obtained by applying bolometric corrections to  $g$ -band data following Lyman et al. (2014). The  $^{56}\text{Ni}$  radioactivity power fits to the bolometric and pseudo-bolometric light curves following the Arnett method are plotted in light-red color for the second peak and gray color for the first peak.

from their figure 8, Folatelli et al. 2006), 2007gr (pseudo-bolometric light curve from their figure 6, Chen et al. 2014), 2009ip (bolometric light curve from their figure 11, Margutti et al. 2014), and 2017ens (pseudo-bolometric light curve from their figure 1, Chen et al. 2018). The pseudo-bolometric luminosity of the first peak reached a maximum of  $6.6 \pm 0.2 \times 10^{41} \text{ erg s}^{-1}$ , while the second peak reached a maximum of  $4.4 \pm 0.6 \times 10^{42} \text{ erg s}^{-1}$ . The maximum bolometric luminosity of the second peak is  $1.2 \pm 0.2 \times 10^{43} \text{ erg s}^{-1}$ .

The pseudo-bolometric light curve from TESS data was integrated to obtain the radiated energy output over its duration, and it came out to be  $8.0 \pm 0.6 \times 10^{47} \text{ erg}$ . The bolometric light curve was integrated for the rest of the first peak (until day 100), which came out to be  $8.8 \pm 0.4 \times 10^{48} \text{ erg}$ . Hence, a lower limit of  $9.6 \pm 0.5 \times 10^{48} \text{ erg}$  can be placed on the total radiated energy during the first peak. For the second peak

(from rebrightening until our last photometry point at 294 days since explosion), the radiated energy is  $5.60 \pm 0.13 \times 10^{49}$  erg. Thus, the total energy radiated by SN 2023aew from the explosion until our last detection is  $6.56 \pm 0.18 \times 10^{49}$  erg. Comparison of this radiated energy with other similar events is further discussed in §3.4.

Assuming the two peaks are separate SESNe, we fit  $^{56}\text{Ni}$  power luminosity models using the Arnett (Arnett 1982; Valenti et al. 2008a) method separately to both peaks. For the first peak, we use the pseudo-bolometric luminosity from TESS observations and from Superbol (see above), covering days 0 to 50 since the explosion, to fit the Arnett radioactivity model. We obtain a lower limit on nickel mass,  $M_{\text{Ni}} = 0.11_{-0.06}^{+0.02} M_{\odot}$  and ejecta mass,  $M_{\text{ej}} = 27.6_{-19.0}^{+4.1} M_{\odot}$  assuming a photospheric velocity of  $11,800 \text{ km s}^{-1}$  (see §3.3).

Next, assuming that the second brightening is also powered by  $^{56}\text{Ni}$  decay, *gri* data during the rise of the second peak were fitted with power laws using HAFET to obtain an “explosion” epoch, which came out to be  $\sim 115$  days after the explosion epoch from TESS. Using this explosion epoch as a reference, models were fitted to the bolometric and pseudo-bolometric light curves, respectively, which seem to agree well except around the bump at 210 days from the explosion. The radioactivity power fit to  $L_{\text{bol}}$  requires a nickel mass,  $M_{\text{Ni}} = 1.59_{-0.40}^{+0.62} M_{\odot}$  and an ejecta mass,  $M_{\text{ej}} = 8.52 \pm 2.40 M_{\odot}$  assuming a photospheric velocity of  $6,000 \text{ km s}^{-1}$  (see Figure 3.11). A fit to the pseudo-bolometric luminosity provides a lower limit of  $M_{\text{Ni}} = 0.59_{-0.19}^{+0.31} M_{\odot}$  and  $M_{\text{ej}} = 7.62 \pm 3.16 M_{\odot}$ . Clearly, this nickel mass estimate is unreasonably high compared to what is observed in other SESNe and what is predicted from models, and thus must be hinting at an additional power source for the second peak.

Also, the radioactivity models for the “two SESNe” combined cannot explain the luminosity of the plateau that bridges the two peaks (see Figure 3.4), thus making the two separate SESNe scenario less likely.

### **First peak of SN 2023aew**

Serendipitous coverage from TESS revealed the explosion epoch, the rise, and the peak of the first bump, which were not detected in any other data. The overall light curve shape of SN 2023aew resembles SN 2009ip but is much broader in both peaks (see Figure 3.1). Figure 3.1 also compares the first peak with Type IIb SNe 1993J and 2011dh, which have a faster decline than SN 2023aew and narrower light curves. The rise time of the first peak from the explosion epoch to peak is 20 rest-frame

days, and from half-peak flux to peak flux is  $\sim 9$  rest-frame days. The decline time from peak to half-peak is  $\sim 27$  rest-frame days, but is likely affected by the plateau that the first peak develops at 50 days. The half-peak to peak rise and decline times of the first peak are compared with a sample of bright supernovae obtained from the ZTF Sample Explorer<sup>9</sup> (Perley et al. 2020; Fremling et al. 2020; classified since the start of ZTF and having pre- and post-peak coverage) in Figure 3.5. The first peak rise seems consistent with the BTS sample SNe, but the decline time is slightly higher than for the SESN sample and more towards the SN II population.

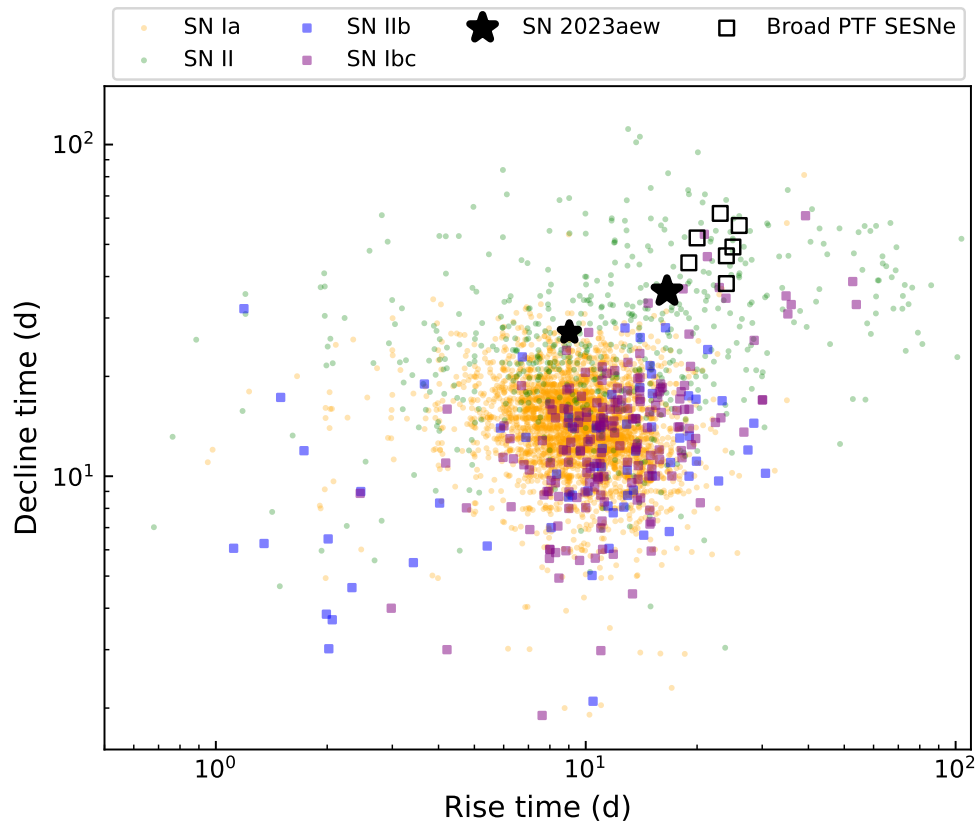


Figure 3.5: Rise time versus decline time (peak to half-peak in the  $r$  band) of the Bright Transient Survey sample of supernovae (colored points) and broad light-curve SESNe from Karamehmetoglu et al. (2023) (empty black squares). The first peak of SN 2023aew is marked with the smaller black star (rise time from TESS data), and the second peak is marked with the larger black star ( $r$  band data).

After the ZTF discovery, an initial spectrum at the first peak was obtained through the usual spectroscopic efforts of the Bright Transient Survey which showed a P-

<sup>9</sup><https://sites.astro.caltech.edu/ztf/bts/explorer.php>.

Cygni  $H\alpha$  profile of with a velocity of  $\sim 11,800 \text{ km s}^{-1}$ . Using the Python version of template matching supernova classification software *Superfit* (Howell et al. 2005; Goldwasser et al. 2022), a match to the Type IIb SN 2001ig was obtained, and SN 2023aew was classified as a SN IIb (§3.1). Panel (a) of Figure 3.6 shows that this earliest spectrum of SN 2023aew (+34 days from explosion) is a good match with the early time spectra of Type IIb SNe 1993J (+28 days) and 2011dh (+5 days). The broad component of  $H\alpha$  is similar in velocity to the broad component of the precursor spectra of Type IIc SN 2009ip; however, any narrow components, if present, cannot be discerned in our SEDM spectrum. The deviation from 09ip-like behavior occurs during the second peak, where SN 2023aew transforms into a SN Ibc and does not show any narrow lines in the spectra.

### Second peak of SN 2023aew

For the second peak resulting from the rapid rebrightening, the rise time from half of the peak luminosity to peak luminosity is  $\sim 17.5$  rest-frame days, and the decline time from the peak to half of the peak luminosity is  $\sim 36.1$  rest-frame days. The light curve width at half-max is  $\sim 53.5$  rest-frame days. These values are higher than what has typically been observed for normal SESNe (Prentice et al. 2016; Taddia et al. 2018b). In Figure 3.5, the half-peak to peak rise and decline times of the second peak of SN 2023aew are compared with the BTS sample and with the sample of broad light-curve SESNe from Palomar Transient Factory (PTF) presented in Karamehmetoglu et al. (2023). The second peak of SN 2023aew is indeed broader than what is the case for most ZTF SESNe and consistent with those in the broad Karamehmetoglu et al. (2023) sample. Though none of the SESNe in Karamehmetoglu et al. (2023) had a long precursor-like first peak as SN 2023aew, some of them do display similar undulations in the light curve. Karamehmetoglu et al. (2023) favor ejecta from massive stars ( $> 20 - 25 M_{\odot}$ ) as the cause behind the broad light curves, but do not rule out hidden CSM interaction or additional powering mechanisms.

Figure 3.6 panel (b) compares spectra taken around the second peak maximum of SN 2023aew to the mean spectra of SNe IIb, SNe Ib, and SNe Ic at peak ( $0 \pm 2$  days) as constructed in Liu et al. (2016). The absorption feature at He I  $\lambda 5876$  appears to be closer in strength to a SN Ib rather than a SN Ic, with perhaps a weak helium feature present also at  $7065 \text{ \AA}$ . On the other hand, with He I  $\lambda \lambda 6678$  and  $7065$  being weak or absent, the  $5876 \text{ \AA}$  feature could be due to Na ID instead, making a stronger case for a spectral similarity to SNe Ic. The presence of trace helium in SNe Ic is

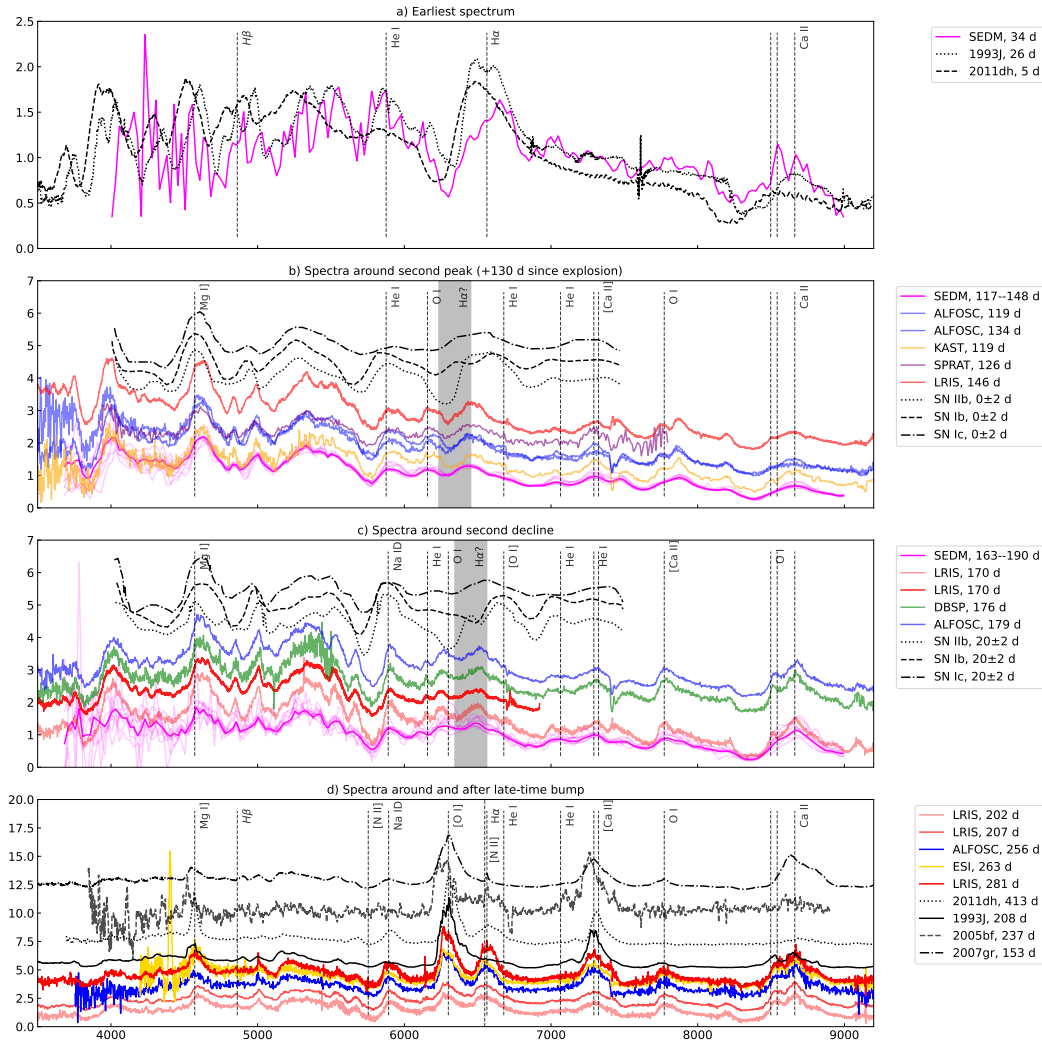


Figure 3.6: SN 2023aew spectral comparison at different phases compared to mean spectra of SNe Iib, SNe Ib, and SNe Ic from Liu et al. (2016).

also highly debated (Branch et al. 2002; Elmhamdi et al. 2006), however, Liu et al. (2016) suggests that for a true SN Ib classification either the  $5876 \text{ \AA}$  line should be strongly identified before maximum or all three He I lines ( $5876, 6678, 7065 \text{ \AA}$ ) should be present post maximum and at  $< 40$  days. Considering the phase of SN 2023aew to be near maximum (and second brightening to be the main peak) and given that the  $5876 \text{ \AA}$  line is clearly present, we suggest that SN 2023aew resembles more a SN Ib at this phase. There is an absorption line around  $\sim 6200 \text{ \AA}$  that matches the  $H\alpha$  absorption from the earliest spectrum, however, the corresponding emission peak is blueshifted from the  $H\alpha$  rest wavelength and redshifted from Si II  $\lambda 6355$ . Several studies (Matheson et al. 2001; Branch et al. 2002; Elmhamdi et al. 2006;

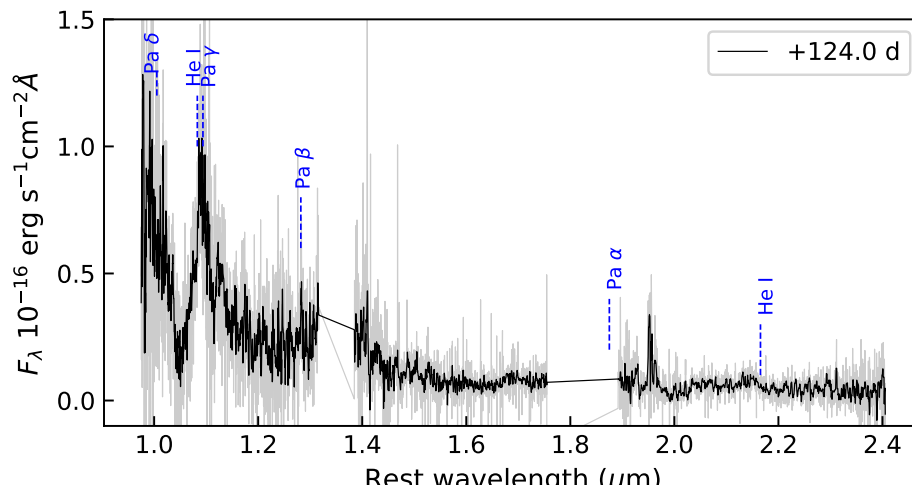


Figure 3.7: A near-infrared spectrum of SN 2023aew obtained with Keck2/NIRES, smoothed using a median filter of kernel size of 9 pixels (in black). Tentative line identifications are marked with blue dashed lines.

Yoon et al. 2010; Liu et al. 2016; Parrent et al. 2016) have indicated the presence of trace hydrogen in SNe Ib and that the origin of similar features around 6000–6400 Å in SNe Ib could be blueshifted emission of H $\alpha$  (their §3.1, Gal-Yam 2017).

Figure 3.6 panel (c) compares post-second peak decline spectra of SN 2023aew with Liu et al. (2016) SESN mean spectra at  $20 \pm 2$  days past maximum. The spectral evolution of SN 2023aew is slow, but at this stage it has started developing [O I]  $\lambda$ 6300 and strong Ca II NIR emission. Absorption near He I  $\lambda$ 5876 is strong but likely Na ID at this stage, and the other He I lines are much weaker compared to the SN Ib mean spectrum. The overall spectra at this stage appear more similar to the SN Ic than to the SN Ib template, which is also supported by SNID matches to SN Ic templates (Hoogendam et al. 2023).

A near-infrared spectrum was also obtained with Keck2/NIRES covering a wavelength range from 1.0–2.4  $\mu$ m, but unfortunately, the data has a poor signal-to-noise ratio. Figure 3.7 shows the NIR spectrum along with some possible line identifications. The Paschen series is marked, as well as He I around 1.085  $\mu$ m. Pa $\alpha$  falls in a no-coverage zone, and Pa $\beta$  and Pa $\delta$  fall in high noise regions, hence are not clearly discernible in the spectrum. The feature near 1.1  $\mu$ m could be either Pa $\gamma$  or He I, but the helium line at 2.2  $\mu$ m is not detected.

### Nebular spectra and emergence of $H\alpha$

Figure 3.6 panel (d) compares spectra taken around the late-time bump at  $\sim 200$  days from explosion to nebular spectra of SESNe 1993J (IIb; Barbon et al. 1995; Matheson et al. 2000), 2011dh (IIb; Ergon et al. 2015; Yaron et al. 2012), 2005bf (Ib-pec; Shivvers et al. 2019) and 2007gr (Ic; Shivvers et al. 2019) obtained from the Open SN catalog. The strongest features present at this stage are Ca II NIR, [Ca II]  $\lambda\lambda 7292, 7324$ , O I  $\lambda 7774$ , [O I]  $\lambda\lambda 6300, 6364$ , Na ID  $\lambda 5890$  and an emission feature centered around  $H\alpha$ . [N II]  $\lambda\lambda 6548, 6583$  is also a major contributor of flux around the  $H\alpha$  wavelength at the nebular phases in the low mass end of SESNe (low mass Type IIb, Jerkstrand et al. 2015), but is almost absent for the high mass SESNe. The same is reflected in the spectra of comparison SESNe in Figure 3.6 panel (d), with SN 2011dh (IIb) having the most flux in the [N II] line and SN 2007gr (Ic) barely having any. However, SN 2023aew seems to have a larger flux in that line compared to the others, possibly due to the contribution from  $H\alpha$ .  $H\beta$  is almost non-existent, but is also similarly weak in the day 208 spectrum of SN 1993J.

To further explore the nature of SN 2023aew, flux ratios of nebular diagnostic lines are compared with the analysis of SESNe presented in Fang et al. (2019) and Fang et al. (2022). The line fluxes of [O I]  $\lambda\lambda 6300, 6364$ , [Ca II]  $\lambda\lambda 7292, 7324$  and [N II]/ $H\alpha$  complex, and the width of the [O I] line are calculated for SN 2023aew following similar procedures as in Fang et al. (2019) and Fang et al. (2022). Figure 3.8 top panel plots the correlation of the [O I]/[Ca II] ratio versus the [O I] width for SN 2023aew along with data obtained from figure 7a of Fang et al. (2022). Figure 3.8 bottom panel plots the line ratio of [N II]/[O I] versus the line ratio of [O I]/[Ca II] for SN 2023aew along with data obtained from figure 3 of Fang et al. (2019). The [O I] fluxes were calculated by fitting and subtracting a pseudo-continuum to the oxygen-nitrogen complex, then fitting and subtracting a Gaussian profile centered at  $6563 \text{ \AA}$  to remove the [N II]/ $H\alpha$  contribution, and finally integrating the remaining flux in the complex over a suitable wavelength range. The [N II] fluxes were similarly calculated by subtracting a Gaussian profile fit centered at  $6300 \text{ \AA}$  to remove the [O I] contribution after continuum removal. The [Ca II] fluxes were calculated after subtracting a pseudo-continuum and integrating over the line. The uncertainties were calculated using the Monte-Carlo method as described in Appendix 3.7. In both panels, the measurements for SN 2023aew are marked with purple stars having decreasing transparency with increasing phase.

Fang et al. (2022) discerned that oxygen-rich ejecta expand faster, and the SESN

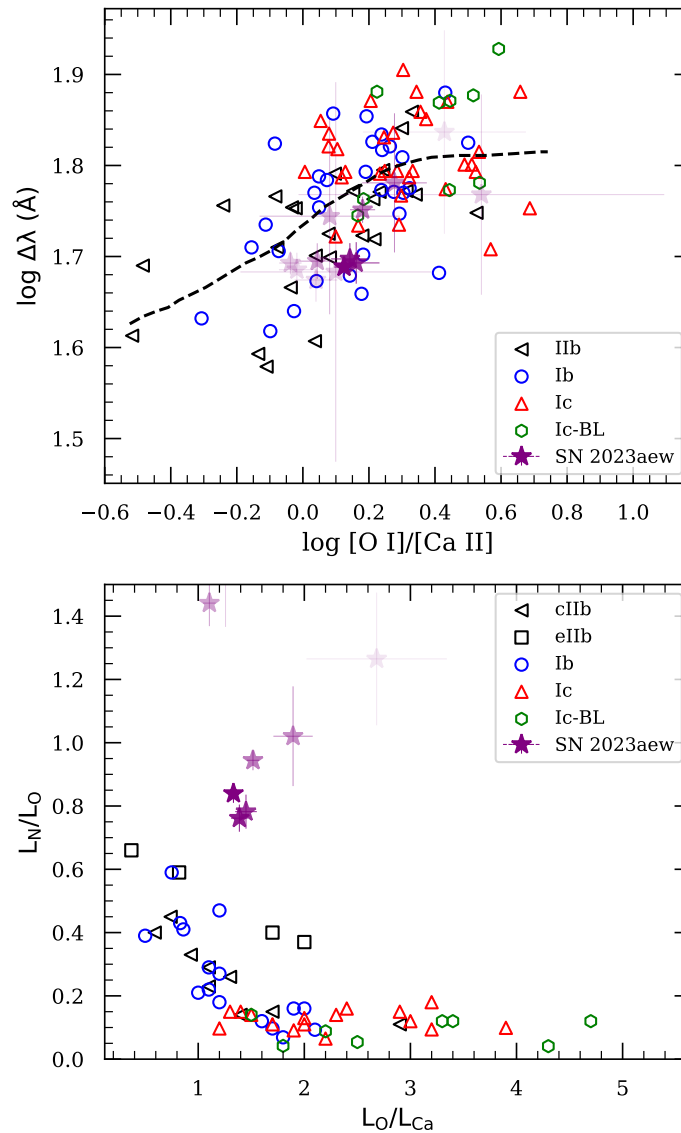


Figure 3.8: *Upper panel:* SN 2023aew in the logarithmic phase-space of [O I] width versus [O I]/[Ca II] flux ratio for SESNe published in Fang et al. (2022, their fig. 7a). *Lower panel:*  $L_N/L_O$  versus  $L_O/L_{Ca}$  for SESNe published in Fang et al. (2019, their fig. 3). ‘cIIb’ and ‘eIIb’ refer to compact and extended SNe IIb, respectively. Values for SN 2023aew are shown in purple stars and derived from late-time spectra (phases ranging from 200 to 281 days from explosion) with the transparency decreasing with increasing phase. The SN nebular spectra used in Fang et al. (2019) range from 150 to 300 days after the peak, while for SN 2023aew they range from 75 to 150 days after the second peak. SN 2023aew consistently shows higher values on the [N II]/[O I] axis, which suggest the presence of H $\alpha$  contaminating (or rather dominating) the [N II] lines at these phases.

subtype distribution showed that SNe I Ib/Ic are more steeply correlated than SNe I c/Ic-BL (see their figure 7a and top panel of our figure 3.8). SN 2023aew has a  $\log_{10}([\text{O I}]/[\text{Ca II}]) \sim 0.1$ , before the correlation curve in Figure 3.8 (top panel) starts to flatten, but has slower velocities, again more towards the phase space that SNe I Ib/Ic occupy. The luminosity ratio of  $[\text{N II}]/[\text{O I}]$  in Figure 3.8 (bottom panel) is considerably higher than the corresponding values Fang et al. (2019) measured for SESNe at that  $L_O/L_{Ca}$ , once again suggesting the presence of hydrogen in the nebular phase.

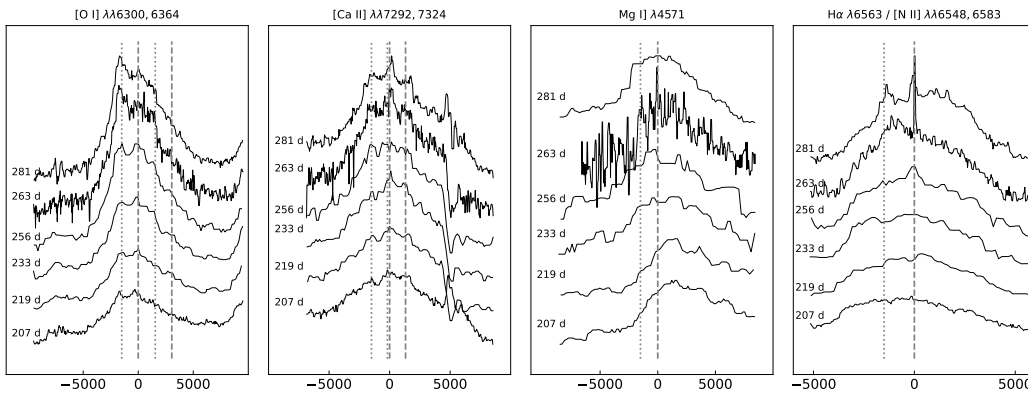


Figure 3.9: Line profiles of nebular  $[\text{O I}]$ ,  $[\text{Ca II}]$ ,  $\text{Mg I}]$ , and  $\text{H}\alpha/[\text{N II}]$  complex from 207 days to 281 days. Dashed vertical lines mark the rest wavelengths and dotted vertical lines mark the blueshifted ( $\sim 1500 \text{ km s}^{-1}$ ) components. The blueshifted component in all lines appears to be increasing in strength with phase.

Further arguments for the  $6500 \text{ \AA}$  feature consisting mostly of hydrogen are found when comparing to Barmantloo et al. (2024, in preparation). In this work, the authors compare  $[\text{N II}]$  emission from a set of nebular model spectra to a sample of observed SESNe. They find that up until  $\sim 200\text{--}250$  days post-explosion, the contribution of  $[\text{N II}]$  in this region is below 50% for all progenitor models, with the feature being almost non-existent for  $M_{\text{preSN}} \gtrsim 4.5 M_{\odot}$ . Perhaps more importantly, it is found that the line widths for the  $[\text{N II}]$  feature in their sample have a lower limit FWHM of  $170 \text{ \AA}$ , with the median around  $\sim 200\text{--}220 \text{ \AA}$ . Performing the same analysis for SN 2023aew, we find FWHM values between  $115\text{--}135 \text{ \AA}$ . This means that if the feature were mostly  $[\text{N II}]$ , SN 2023aew would be a significant outlier (as when comparing with Fang et al. 2022). Finally, calculating the  $f_{[\text{NII}]}$  diagnostic from Barmantloo et al. (2024) for our spectral series, the resulting values would indicate a  $M_{\text{preSN}} \lesssim 3 M_{\odot}$ , which does not match with any of our earlier estimates. All in all, the above findings suggest that any presence of  $[\text{N II}]$  could only be very

minor, with the majority of the emission in this region due to other elements, most probably hydrogen.

A final inference that can be derived from the nebular spectra comes from the line profiles of [O I]  $\lambda\lambda 6300, 6364$ , [Ca II]  $\lambda\lambda 7292, 7324$  and Mg I]  $\lambda 4571$ . Figure 3.9 shows the nebular line profiles with dashed vertical lines marking the rest line wavelengths and dotted vertical lines marking blueshifted (by  $1500 \text{ km s}^{-1}$ ) wavelengths. The [O I] profile clearly has blueshifted components for both the 6300 and 6364 Å lines, creating a double-peaked profile. [Ca II] also has hints of double-peaked structure with peaks blueshifted by  $1500 \text{ km s}^{-1}$ , though not as clear as for [O I]. The Mg I] peak is redshifted at earlier epochs, but a blueshifted component seems to develop at later times. The blueshifted peak in all three lines seems to get stronger with time. The double-peaked shape can also be discerned in O I  $\lambda 7774$  and in the  $\text{H}\alpha$ /[N II] complex for some epochs. Double-peaked structure in [O I] lines has been observed in nebular spectra of many SESNe (Modjaz et al. 2006; Modjaz 2007; Maeda et al. 2007; Modjaz et al. 2008), and in most cases, the two peaks are symmetric around the rest wavelength (for example see Modjaz et al. 2008, their figure 2). SN 2005bf (Folatelli et al. 2006; Maeda et al. 2007), a peculiar Type Ib SN, was an exception with a highly blueshifted ( $\sim 2000 \text{ km s}^{-1}$ ) trough, similar to what is seen here for SN 2023aew. An aspherical explosion in the shape of a torus could give rise to a double-peaked feature in the case of optically thin ejecta at nebular times, but does not explain the blueshift. For SN 2005bf, a unipolar blob of low mass, accelerated by a pulsar kick, was suggested by Maeda et al. (2007). On the other hand, less extreme blueshifts can be explained by residual opacity effects as described in Taubenberger et al. (2009). More recently, Fang et al. (2023) analyzed a sample of nebular spectra of SESNe and found that roughly half of the SESNe had either a double-peaked [O I] or [Ca II], but none had double-peaked structure in both lines. Fang et al. (2023) theorize an axisymmetric model for their observations, where the oxygen-burning ash (Ca-rich region) is distributed in bipolar bubbles with unburnt oxygen outside it, and depending on the viewing angle, leads to a double-peaked profile in one of the lines. However, applying this prescription to SN 2023aew is difficult due to the structure present in the calcium line and the blueshifted trough. More advanced 3D models are just beginning to be explored, e.g., van Baal et al. 2023.

### 3.4 Discussion

#### Two distinct supernovae or a single peculiar one?

To determine whether the light curve of SN 2023aew is due to a single transient or potentially due to two separate events, like two SNe that just happened to explode very close in time and space (along the line-of-sight), we imaged SN 2023aew with WaSP (Wafer-Scale Imager for Prime) on the Palomar 200-inch telescope (P200) in  $g$ ,  $r$ , and  $i$  bands 144 days after explosion, right around the second peak. The exposure time used per band was 300 seconds, which corresponds to a  $5\sigma$  limiting magnitude of  $\sim 22.5$  mag for WaSP in good seeing conditions. The SN was observed at an average seeing of  $1.4''$ . On the same night, a confirmed sibling SN Ia pair, SN 2023egs, with peaks separated by  $\sim 20$  days and on-sky separation of  $\sim 1.6''$  was also observed with WaSP. The first SN Ia of this pair was  $\sim 50$  days past maximum at the time of observation and thus would be at least 3 magnitudes fainter than peak (18.4 mag) if it were a normal SN Ia (Phillips et al. 2017), making it  $\gtrsim 21$  mag. The second SN was  $\sim 19$  mag at the time of observation, and both SNe Ia in SN 2023egs were clearly detected in the WaSP image. Considering the initial decline of the first peak of SN 2023aew ( $2.6 \text{ mag } 100\text{d}^{-1}$ ), the “first” SN in SN 2023aew at 144 days from explosion would be  $\sim 21.1$  mag, while the second SN was  $\sim 16.7$  mag and thus both would still be separately detected in WaSP data if they were  $\sim 2''$  apart. Upon analyzing the WaSP observations of SN 2023aew, there did not seem to be two sources present at the location of SN 2023aew within the seeing limit.

Graham et al. (2022b) analyzed sibling SNe (SNe sharing the same host galaxy) in the ZTF Bright Transient Survey sample of 2 years and found 5 sibling pairs (10 SNe) brighter than 18.5 mag, corresponding to a rate of only  $\sim 1\%$  of total SNe in BTS in that same period. Out of these, only two were SESNe, i.e., about one per year. The lowest on-sky separation of these siblings was  $3.7''$ . Thus, the chances of SN 2023aew being a SESN sibling pair with coincident location ( $< 2''$ ) and also exploding within  $\sim 115$  days (4 months) of each other are extremely small.

Post-facto statistics are difficult, but another crude estimate of the rarity of SN 2023aew being a sibling pair might be calculated as follows. Assuming a SN rate of 1 per 100 years per galaxy, the Poisson probability of two SNe exploding within half a year is  $P_1 \sim 1 \times 10^{-5}$ . As SN 2023aew is roughly 7 kpc from the center of its host, the probability of the siblings occurring at that radius also needs to be taken into account. This probability can be estimated by taking the radial distribution of CCSNe in a galaxy from Wang et al. (1997, their fig. 2), then calculating the ratio of

the integrated distribution over a radius span of 6–8 kpc with integrated distribution over the galaxy span (assuming  $\sim 20$  kpc), which comes out to be  $P_2 \sim 0.14$ . From the P200/WaSP image, the on-sky separation is known to be within  $2''$ , which translates to  $\sim 1$  kpc at the distance of SN 2023aew. Thus, the fraction of volume of the 6–8 kpc disc that the siblings are expected in would be at most  $P_3 \sim 0.01$ . The exact off-centre distance to the host is, of course, not important, but the fact that the SN exploded in the outskirts of a resolved galaxy where the star formation rate is limited makes the probability for two unrelated SNe much more unlikely. Thus, the total probability of two SESNe exploding within half a year in the same galaxy at  $\sim 7$  kpc from the galaxy center and within  $2''$  on-sky separation is  $P \sim 1.7 \times 10^{-8}$  per galaxy. Next, the maximum distance out to which SN 2023aew ( $M_{\text{abs}}^{\text{peak}} \sim -18.7$ ) would be detected and classified by the BTS survey (flux limit of 18.5 mag) is  $\sim 275$  Mpc. Taking the density of galaxies in this volume (assuming MW-like) to be  $\sim 0.006$   $\text{Mpc}^{-3}$ , assuming a uniform distribution and accounting for the fact that ZTF can only observe  $\sim 0.75$  of the sky, the number of galaxies ZTF will observe in 275 Mpc volume is  $\sim 392000$ . Multiplying that by the per galaxy probability, the expected number of siblings like SN 2023aew is  $\sim 0.007$ , and hence the Poisson probability of detecting one event is 0.7%. Even more unlikely is that both of these events are SESNe, and in particular, the unusual properties of the second peak in terms of lower-than-average line velocities and broader-than-average and more luminous peak make it very unlikely that the events are not linked. We also do not know of any mechanism that would make one SN trigger the other in a common system on such short timescales.

### **Rebrightening or precursor?**

The usual interpretation for supernova rebrightening is that it is caused by interaction with a CSM shell ejected during the final moments of the progenitor. This is most frequently observed in SNe IIn, where the light curves have multiple undulations and late-time emission; see, for example, Nyholm et al. (2017). SN 2021qqp (Hiramatsu et al. 2023) had a long, slow-rising precursor before the first peak as well as a late-time brightening after about a year, with both first and second peaks showing spectral similarity. Late-time emission due to CSM interaction has also been observed in spectrally normal SESNe that develop narrow emission lines and secondary light-curve plateaus or peaks, some examples being SNe 2017ens (Chen et al. 2018) and 2019oys (Sollerman et al. 2020). In the case of SN 2023aew, the second peak is spectrally different (Ibc-like) from the first (IIb-like), unlike SN 2021qqp, and

even though the SN light curve shows undulations, it does not evolve into having interaction-dominated spectra with narrow lines like SNe 2017ens and 2019oys. Hydrogen is present during the first peak but not during the second one, and then comes back again in the nebular phase but has broader velocities than strongly interacting SNe IIn. If CSM interaction is indeed the cause of the rebrightening, the corresponding spectral signs are hidden. The horned and blueshifted [O I] and [Ca II] emission line profiles (see Figure 3.9) which could arise due to asymmetric gas distribution (SN 2005bf; Tominaga et al. 2005; Maeda et al. 2007; Modjaz et al. 2008) also hint at unusual geometry that could possibly hide the spectral signatures of interaction. Sollerman et al. (2020) presented two interacting SESNe, one where the dramatic light curve transformation was accompanied by spectral interaction signatures, while the second only depicted slight undulations. Hence, it is less likely for such a dramatic rebrightening not to be associated with transformation into an interacting SN.

Other suggested causes of double peaks include double-peaked nickel distribution in the ejecta (SN 2005bf; Tominaga et al. 2005) and delayed magnetar energy injection (Maeda et al. 2007). However, the timescales from both of these scenarios are not consistent with the evolution of SN 2023aew (Kasen et al. 2016; Orellana et al. 2022).

Another possibility is the first peak being a precursor emission (Ofek et al. 2014; Strotjohann et al. 2021b) similar to SN 2009ip (Mauerhan et al. 2013; Pastorello et al. 2013; Margutti et al. 2014). Pre-cursors have also been seen in hydrogen-deficient SNe (Brennan et al. 2024). Figure 3.10 upper panel compares the light curves of SN 2023aew (circles) and SN 2009ip (dashed lines), and many similarities are apparent. While SN 2023aew has a more luminous and longer precursor than SN 2009ip, the following main peak is also more luminous and broader, and both SNe show undulations in their declining light curves. The main peak rise time is also similar in both SNe. However, the SN 2023aew precursor is much redder than the SN 2009ip precursor (see Figure 3.3). SN 2009ip also showed clear narrow, intermediate, and broad velocity features in the  $H\alpha$  emission line, and thus it was evident that circumstellar material was present and interacting with the SN ejecta; it was a clear Type IIn SN. However, for SN 2023aew, given that the only spectrum taken during the precursor event is from P60/SEDM, only the broad velocity feature can be resolved ( $11,800 \text{ km s}^{-1}$ ), which is similar to the broad velocity seen in SN 2009ip.

If we assume for a moment that SN 2023aew is similar to a 09ip-like event, with the first peak being due to an eruption (a precursor) and the second peak the actual supernova explosion. The longer and much more energetic precursor outburst could be generating energy when the SN ejecta later run into this material to power the second peak in addition to radioactive  $^{56}\text{Ni}$ . An eruption mechanism could be considered for the precursor following the models in Matsumoto et al. (2022), wherein the precursor light curve is recombination-driven, similar to Type IIP SNe. Though not observed in the first peak of SN 2023aew, perhaps due to inadequate spectral resolution, we assume a similar narrow line velocity as for SN 2009ip ( $\sim 1,500 \text{ km s}^{-1}$ ) in the following calculations.

Matsumoto et al. (2022) found that their semi-analytical models largely follow the Popov (1993) analytical scalings (eqs. 19,20 Matsumoto et al. 2022). For SN 2023aew, the “precursor” plateau duration ( $t_{\text{pl}}$ ) is 80 days (which is a lower limit considering possible interruption by the following SN explosion), and the precursor radiated energy is  $E_{\text{pl}} \approx 1.0 \times 10^{49} \text{ erg}$  which gives a precursor plateau luminosity ( $L_{\text{pl}} = \frac{E_{\text{pl}}}{t_{\text{pl}}}$ ) of  $1.5 \times 10^{42} \text{ erg s}^{-1}$ . Then, using the inverted Popov equations and an ejecta speed of  $v_{\text{ej}} \approx 1500 \text{ km s}^{-1}$ , we estimate an ejecta mass of  $M_{\text{ej}} \approx 0.61 M_{\odot}$  and an initial radius of  $R_0 \approx 9774 R_{\odot}$  for the precursor; both values are comparable to the SNe analyzed in Matsumoto et al. (2022). Then again from Matsumoto et al. (2022, eqs. 27, 28), we obtain an outer radius of the precursor ejecta  $R_{\text{CSM}} \sim 1 \times 10^{15} \text{ cm}$ , and density of the precursor ejecta  $\rho_{\text{CSM}} \sim 2.6 \times 10^{-13} \text{ g cm}^{-3}$ , which is a more extended and less dense CSM than for SN 2009ip (see fig. 8, Matsumoto et al. 2022). Such a CSM, coupled with asymmetric geometry (signatures of which are present in the form of double-peaked nebular lines), could potentially result in a SN-CSM interaction without narrow lines in the optical spectra. Estimating the luminosity from shock heating using Matsumoto et al. (2022, their eq. 29), we get  $L_{\text{sh}} \approx 2 \times 10^{43} \text{ erg s}^{-1}$  assuming a radiative efficiency of 0.1 and  $v_{\text{SN}} = 6000 \text{ km s}^{-1}$ , which broadly agrees with the observed main peak luminosity. We discuss the possible mechanisms that can cause such eruptive mass loss as well as other possible progenitor scenarios in §3.4.

Interestingly enough, there is a recent analogue of SN 2023aew, in terms of the precursor-like ZTF light curve (there is no TESS data to constrain the explosion in this case). SN 2023plg was discovered by ZTF and reported to TNS by ALeRCE on 2023-08-14 with a reported apparent magnitude of 18.7. The ZTF light curve of SN 2023plg tracks closely that of SN 2023aew, both being very red during the initial

decline, then brightening suddenly and maintaining a broad second peak. During the second peak, SN 2023plg was classified as a SN Ib on TNS by ePESSTO, but no spectroscopic data are available for the first peak. Close examination of more spectra suggests weak He I lines similar to what we see in SN 2023aew. The comparison is shown in Figure 3.10, with light curves in the upper panel and Keck1/LRIS spectra of both SNe in the lower panel. SN 2023plg is being followed up for future studies.

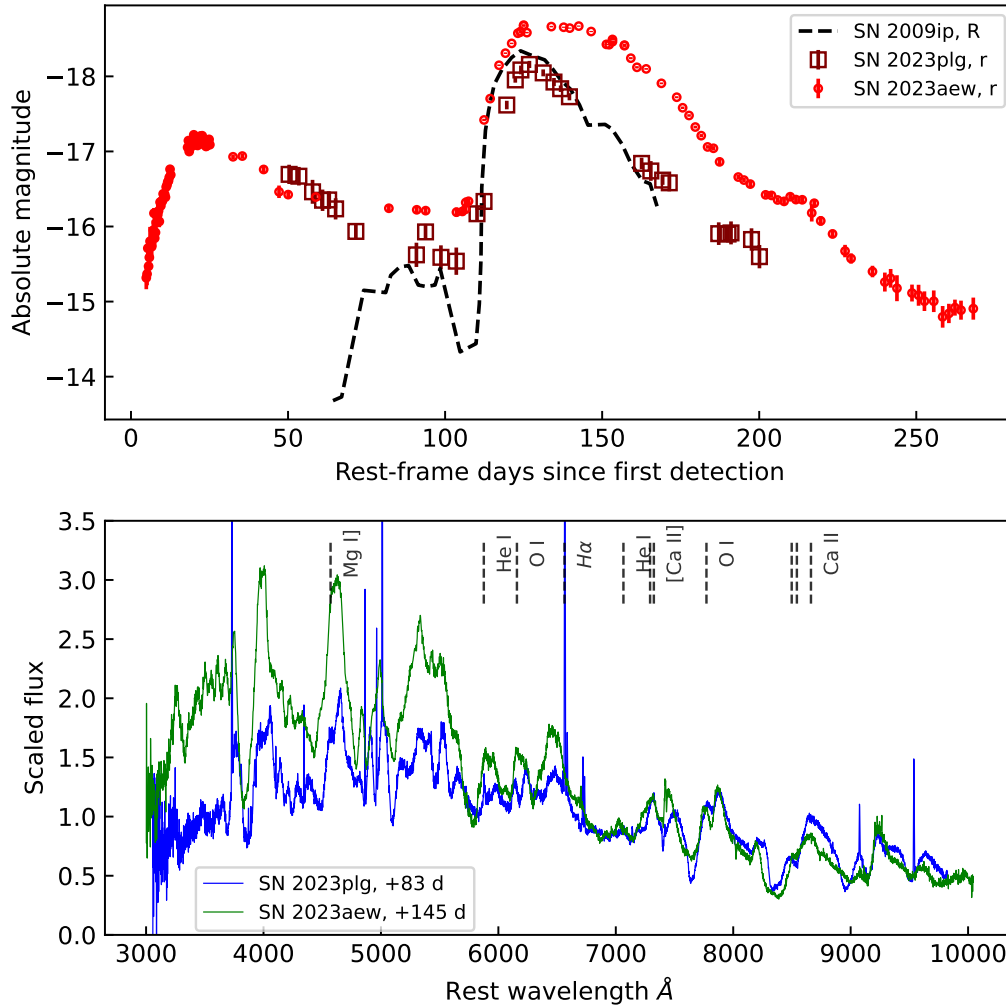


Figure 3.10: Comparison of SN 2023aew with the canonical precursor Type II SN 2009ip, but also with the analogous SESN SN 2023plg, showing both a similar luminous, long-lived declining precursor and a bright second peak. Light curves shifted to match the rise of the main peak. SN 2023plg also exhibits a Type Ibc SN spectrum.

### **Origin of SN 2023aew**

In this section, we discuss several scenarios that might explain the peculiar nature of SN 2023aew. We list several possibilities but leave a more detailed assessment and modeling of each scenario for a future study.

The precursor activities observed in SNe are often associated with mass ejection from their progenitors shortly before their explosions. One possible scenario to explain SN 2023aew is a mass ejection forming the precursor (first peak), followed by a SN explosion that shapes the major (second) light-curve peak. In the case of SN 2023aew, a hydrogen feature was observed during the precursor, which weakens during the following brighter phase. Thus, the pre-SN mass ejection may have resulted in the ejection of all the remaining hydrogen-rich envelope in the progenitor, and the following SN became a hydrogen-poor stripped envelope SN. Thus, the progenitor might have been similar to those of Type IIb SNe, retaining a small amount of hydrogen-rich envelope. Several stripped-envelope SNe are known to have a nearby hydrogen-rich CSM (e.g., SN 2014C, Milisavljevic et al. 2015; SN 2017ens, Chen et al. 2018). SN 2023aew could be an extreme case of a similar kind where the final ejection of the hydrogen-rich envelope occurred immediately before the explosion, forming the precursor, and the following SN is observed as hydrogen-poor.

There are several suggested mechanisms that can trigger the mass ejection shortly before the explosions of massive stars. For example, an explosive nuclear shell burning may occur in the final stages of massive star evolution, triggering a strong mass ejection, (e.g., Woosley et al. 2015). Mass ejection may also be triggered by an acoustic wave initiated by the strong convective motion in the core of massive stars shortly before explosion, (e.g., Quataert et al. 2012; Fuller et al. 2018). However, in both cases, the predicted energy that can be released is lower than the precursor energy estimated in SN 2023aew (see, e.g., Matsumoto et al. 2022; Wu et al. 2021; Leung et al. 2021). If the progenitor is in a close binary system with a compact companion, the accretion onto the companion may help provide additional energy to form the bright precursor (Tsunai et al. 2024).

Close passage of a massive star in an eccentric binary system could also result in precursor outbursts and was suggested for  $\eta$ Car (Damineli et al. 1997) by Soker (2001), Soker (2004), Kashi et al. (2010), and Smith (2011). Soker et al. (2013a) explored a merger-burst model (non-terminal) for SN 2009ip where the precursor outbursts were explained by close periastron passages of the massive stars, and

non-spherical CSM (torus-like) is naturally expected from these encounters.

Another possibility is a pulsational pair-instability SN (Woosley et al. 2007). Pulsational instability SNe are transients caused by a partial mass ejection of very massive stars triggered by the pair instability. A pulsational mass loss forming the precursor phase can occur several months before the final collapse of the massive stars. The final collapse may result in a SN explosion forming the major light curve peak as observed in SN 2023aew. For example, some pulsational pair-instability SN models presented in Woosley (2017) have a similar luminosity to the precursor of SN 2023aew. It is possible that the progenitor of SN 2023aew experienced pulsational pair-instability mass ejection followed by a SN explosion. Although the progenitors of pulsational pair-instability SNe are expected to be massive ( $\gtrsim 30 M_{\odot}$ , e.g., Renzo et al. 2020), a SN explosion with an ejecta mass of around  $10 M_{\odot}$  could be achieved if a part of the progenitor forms a black hole.

The “precursor” of SN 2023aew is as bright as a typical Type II SN. Thus, it is possible that the precursor itself is already a SN event, and the second peak is instead caused by a delayed energy injection at the center. If the hydrogen-rich layers in the ejecta are thin enough, the second peak caused by the delayed energy injection could be observed as a hydrogen-poor event. The delayed energy injection may be caused by a fallback accretion disk towards the central compact remnant (e.g., Moriya et al. 2019b; Chen et al. 2024). Depending on the initial angular momentum, the formation of the accretion disk that can provide the central energy injection could be delayed. The delayed energy input may also be caused by a delayed phase transition of neutron stars to quark stars (Ouyed et al. 2013).

### 3.5 Summary and conclusions

In summary, SN 2023aew shows an unprecedented double-bumped light curve with two bright peaks separated by as much as 112 days. The light curve shares some similarities with the light curves of 09ip-like SNe with their long-lived precursors, but SN 2023aew is spectrally a stripped-envelope supernova during its main peak. SN 2023aew has a luminous 100-day-long precursor, which has a 20-day rise and a spectrum similar to Type IIb SNe with a velocity of  $\sim 11,800 \text{ km s}^{-1}$ . Such a precursor is predicted by semi-analytical eruption models of Matsumoto et al. (2022) for 09ip-like SNe. After 100 days, SN 2023aew brightens rapidly to  $-18.8$  magnitude and exhibits a broader than typical (for SESNe) main peak with undulations in its decline. The bolometric light curves, when fitted with the Arnett model for

radioactivity power, result in unreasonably high  $^{56}\text{Ni}$  masses, indicating the need for an additional powering source to explain the luminosity and broadness. During the main peak phase, the SN is spectrally similar to a SN Ibc, although with weaker He I features and hydrogen, which emerges again in the nebular phase. Photospheric and nebular phase line strengths are more similar to those of SNe Ib than to SNe Ic. Line strength of the nebular  $\text{H}\alpha$ /[N II] complex is much higher and the line width is much smaller than expected for a normal hydrogen-free SN Ibc, strengthening the case for hydrogen being present in the late spectra. Additionally, the nebular lines ([O I], [Ca II], Mg I) and  $\text{H}\alpha$ ) show double-peaked or “horned” profiles with one peak at rest wavelength and the other blueshifted by  $\sim 1500 \text{ km s}^{-1}$ , indicating a non-spherical geometry.

We explored the possibility of SN 2023aew being two coincident SNe in the same host galaxy and found this to be highly unlikely. We then discussed the possible origins of SN 2023aew. Although the first peak has properties consistent with a SESN (SN Iib), the dramatic rebrightening would require either a strong delayed interaction with CSM (but no signs of this interaction are seen in the spectra) or a very delayed energy injection by a central engine. The first peak could instead be an eruptive precursor to the SN explosion (second peak), additionally powering the second peak through shock interaction, but with spectral signatures of interaction hidden due to asymmetric geometry. Ultimately, the powering mechanism(s) of this double-bumped supernova remain elusive. In any case, SN 2023aew and similar SNe provide a unique opportunity to study the final throes of a dying stripped massive star, and we encourage further studies with detailed theoretical modeling of the data to understand its progenitor scenario.

### 3.6 Acknowledgement

Based on observations obtained with the Samuel Oschin Telescope 48-inch and the 60-inch Telescope at the Palomar Observatory as part of the Zwicky Transient Facility project. ZTF is supported by the National Science Foundation under Grants No. AST-2034437 and a collaboration including current partners Caltech, IPAC, the Oskar Klein Center at Stockholm University, the University of Maryland, University of California, Berkeley, the University of Wisconsin at Milwaukee, University of Warwick, Ruhr University, Cornell University, Northwestern University, and Drexel University. Operations are conducted by COO, IPAC, and UW. The ZTF forced-photometry service was funded under the Heising-Simons Foundation grant #12540303 (PI: Graham). The Gordon and Betty Moore Foundation, through

both the Data-Driven Investigator Program and a dedicated grant, provided critical funding for SkyPortal. The Oskar Klein Centre was funded by the Swedish Research Council. Partially based on observations made with the Nordic Optical Telescope, operated by the Nordic Optical Telescope Scientific Association at the Observatorio del Roque de los Muchachos, La Palma, Spain, of the Instituto de Astrofísica de Canarias. Some of the data presented here were obtained with ALFOSC. Some of the data presented herein were obtained at the W. M. Keck Observatory, which is operated as a scientific partnership among the California Institute of Technology, the University of California, and NASA; the observatory was made possible by the generous financial support of the W. M. Keck Foundation. The SED Machine is based upon work supported by the National Science Foundation under Grant No. 1106171. This work has made use of data from the Asteroid Terrestrial-impact Last Alert System (ATLAS) project. The Asteroid Terrestrial-impact Last Alert System (ATLAS) project is primarily funded to search for near earth asteroids through NASA grants NN12AR55G, 80NSSC18K0284, and 80NSSC18K1575; byproducts of the NEO search include images and catalogs from the survey area. The ATLAS science products have been made possible through the contributions of the University of Hawaii Institute for Astronomy, the Queen's University Belfast, the Space Telescope Science Institute, the South African Astronomical Observatory, and The Millennium Institute of Astrophysics (MAS), Chile. This research has made use of the NASA/IPAC Infrared Science Archive, which is funded by the National Aeronautics and Space Administration and operated by the California Institute of Technology. The Liverpool Telescope is operated on the island of La Palma by Liverpool John Moores University in the Spanish Observatorio del Roque de los Muchachos of the Instituto de Astrofísica de Canarias with financial support from the UK Science and Technology Facilities Council. We acknowledge ESA Gaia, DPAC and the Photometric Science Alerts Team (<http://gsaweb.ast.cam.ac.uk/alerts>). Funding for the TESS mission is provided by NASA's Science Mission directorate. This paper includes data collected by the TESS mission, which are publicly available from the Mikulski Archive for Space Telescopes (MAST). This research has made use of the Spanish Virtual Observatory (<https://svo.cab.inta-csic.es>) project funded by MCIN/AEI/10.13039/501100011033/ through grant PID2020-112949GB-I00.

Y. Sharma thanks the LSSTC Data Science Fellowship Program, which is funded by LSSTC, NSF Cybertraining Grant #1829740, the Brinson Foundation, and the Moore Foundation; her participation in the program has benefited this work.

S. Schulze, N. Rehemtulla and A. A. Miller are supported by LBNL Subcon-

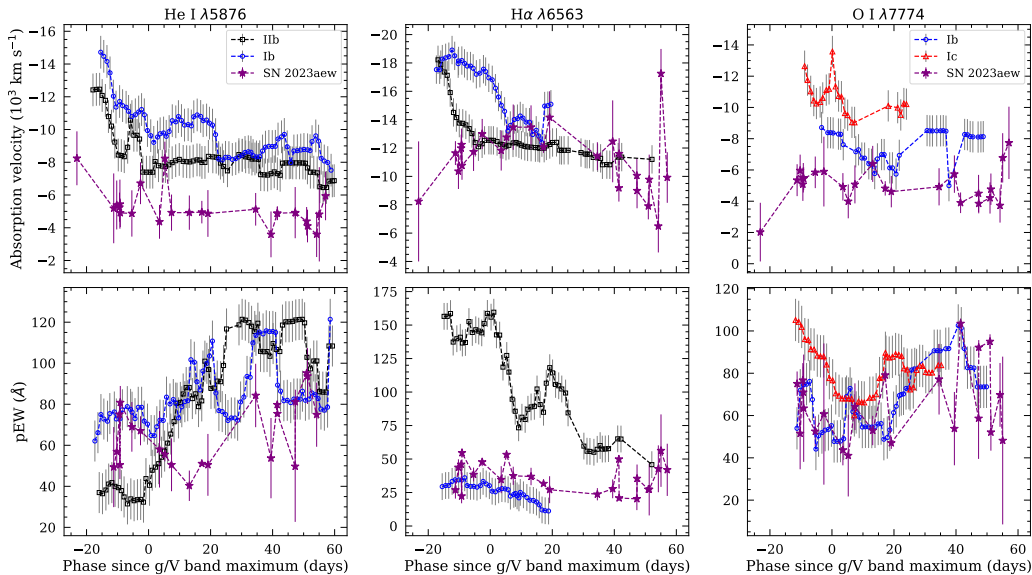


Figure 3.11: Absorption velocity and pseudo-equivalent width (pEW) evolution with phase for He I  $\lambda 5876$ , H $\alpha$  and O I  $\lambda 7774$ . Shown for comparison are running weighted averages of velocities and pEWs for SNe I Ib, Ib, and Ic with error bars of  $1000 \text{ km s}^{-1}$  and  $10 \text{ \AA}$  respectively from Liu et al. (2016).

tract NO. 7707915. The material contained in this document is based upon work supported by a National Aeronautics and Space Administration (NASA) grant or cooperative agreement. Any opinions, findings, conclusions, or recommendations expressed in this material are those of the author and do not necessarily reflect the views of NASA. This work was supported through a NASA grant awarded to the Illinois/NASA Space Grant Consortium.

Fritz (Walt et al. 2019; Duev et al. 2019; Coughlin et al. 2023) (a dynamic collaborative platform for time-domain astronomy) was used in this work.

### 3.7 Appendix A: Photospheric phase line strengths and velocities

In an attempt to quantitatively compare spectral features of SN 2023aew with different SESN subtypes, the evolution of the absorption velocity and the pseudo-equivalent width (pEW) with phase were measured, and these are plotted for SN 2023aew along with mean values of these quantities for Type I Ib, Ib, and Ic SNe as obtained from Liu et al. (2016). Running means of the absorption velocity and pEW during the photospheric phase ( $-20$  to  $60$  days) for He I  $\lambda 5876$  and H $\alpha$  for a sample of SNe I Ib and Ib, and for O I  $\lambda 7774$  for SNe Ib and Ic are shown in Figure 3.11 with values for SN 2023aew (assuming the  $5876 \text{ \AA}$  feature is from helium) marked in purple stars. An average error of  $1000 \text{ km s}^{-1}$  for velocities and

10 Å for pEW is shown instead of the exact errors from Liu et al. (2016). Similar to Liu et al. (2016), absorption velocities were estimated by fitting a smooth curve to the line absorption to find the minimum flux. For the pEWs, a local (pseudo-)continuum was estimated by fitting a low-order polynomial curve to points around maxima on either side of the absorption line, which was then used to estimate the equivalent width. To estimate the uncertainty on the velocity and pEW, a median filter was applied to each spectrum, and the smoothed spectrum was subtracted from the original to get residuals, then the standard deviation of these residuals was taken as the flux uncertainty at each wavelength bin of the spectrum. Assuming the flux uncertainty as the  $1\sigma$  noise, which obeys a Gaussian distribution centered around the smoothed spectrum, 10000 samples were drawn to generate synthetic spectra, and the line parameters were calculated on these spectra, the standard deviations of which were taken as the  $1\sigma$  errors. The phases plotted for SN 2023aew (Figure 3.11) are not with respect to the explosion epoch but with respect to the second peak maximum (132 days from explosion) to match with the Liu et al. (2016) data.

Looking at the He I  $\lambda 5876$  and the H $\alpha$ -“feature” (as marked in Figure 3.6) absorption velocities with respect to phase in the upper left and middle panels of Figure 3.11, SN 2023aew has lower velocities at all phases than both SNe Ib and IIb. The helium velocity is roughly constant with phase at  $5000 \text{ km s}^{-1}$ . The trend observed in pEW (lower left and middle panels in Figure 3.11) is more indicative of SN 2023aew being similar to SNe Ib rather than to SNe IIb for both lines. The H $\alpha$  strength is slightly more than visible in a SN Ib but much lower than for an average SN IIb, making SN 2023aew an intermediate, somewhat peculiar object between the two classes in this regard. The helium pEW is higher in SNe Ib before maximum and thereafter similar in both SNe Ib and IIb (Fremming et al. 2018; Liu et al. 2016), and SN 2023aew aligns more closely with SNe Ib in Figure 3.11. Looking at the rightmost upper and lower panels, both the O I  $\lambda 7774$  velocity and pEW are more similar to those of SNe Ib than to SNe Ic at all epochs. Even though SN template matching programs estimate SN 2023aew to be a Type Ic at these epochs, the oxygen line strength for this SN is closer to those seen in SNe IIb/Ib, and velocities are slower than for a typical SN Ic.

### 3.8 Appendix B: Note added in proofs

At the submission of this paper, another investigation of the same object was submitted to arXiv. Kangas et al. (2024) also presents a comprehensive observational campaign on SN 2023aew, and although we do not agree on all details in the analy-

sis, there is overall agreement that this is an enigmatic, unique object for which it is very difficult to determine the powering mechanism of the two peaks.

### 3.9 Appendix C: Photometry tables

Table 3.3: Log of TESS-Red band observations of  $3\sigma$  significance (full table available online).

MJD	Brightness (mag)
59941.177	$19.78 \pm 0.15$
...	

Table 3.4: Log of UVOT observations of  $3\sigma$  significance (full table available online).

MJD	Filter	Brightness (mag)
60076.47	uvw2	$20.96 \pm 0.24$
...		

Table 3.5: Log of XRT observations.

MJD	Count rate ( $10^{-3} \text{ s}^{-1}$ )	$F$ (0.3 – 10 keV) ( $10^{-13} \text{ erg s}^{-1} \text{ cm}^{-2}$ )	$L$ (0.3 – 10 keV) ( $10^{42} \text{ erg s}^{-1} \text{ cm}^{-2}$ )
Individual epochs			
$60076.47 \pm 0.01$	< 5.5	< 2.10	< 0.30
$60077.67 \pm 0.33$	< 22.0	< 8.41	< 1.20
$60079.71 \pm 0.27$	< 4.4	< 1.67	< 0.24
$60081.85 \pm 0.04$	< 5.4	< 2.08	< 0.30
$60083.61 \pm 0.60$	< 10.5	< 4.01	< 0.57
$60085.34 \pm 0.14$	< 16.4	< 6.25	< 0.89
Stacking			
$60080.97 \pm 4.51$	< 1.4	< 0.55	< 0.08

The time of reference is MJD=60076.465219. The time reports the mid-time of the observation, and its error indicates the extent of the time bin.

Table 3.6: Log of optical photometry of  $5\sigma$  significance (full table available online).

MJD	Filter	Telescope	Brightness (mag)
59969.51	g	P48:ZTF	$19.1 \pm 0.05$
...			

*Chapter 4*

TWIN PEAKS: SN 2021UVY AND SN 2022HGK IN THE  
 LANDSCAPE OF DOUBLE-PEAKED STRIPPED ENVELOPE  
 SUPERNOVAE

Paper in preparation, to be submitted in Publications of the Astronomical Society  
 of the Pacific (PASP) in May 2025

Yashvi Sharma<sup>1</sup>, Jesper Sollerman<sup>2</sup>, William Meynardie<sup>3</sup>, Christoffer Fremling<sup>4</sup>,  
 Kaustav K. Das<sup>1</sup>, Gene Yun<sup>5</sup>, Shrinivas R. Kulkarni<sup>1</sup>, Steve Schulze<sup>6</sup>, Jacob  
 Wise<sup>7</sup>, Sean. J. Brennan<sup>2</sup>, Thomas G. Brink<sup>8</sup>, Michael W. Coughlin<sup>9</sup>, Richard  
 Dekany<sup>4</sup>, Matthew J. Graham<sup>1</sup>, K. R. Hinds<sup>7</sup>, Viraj Karambelkar<sup>1</sup>, Mansi M.  
 Kasliwal<sup>1</sup>, Maggie L. Li<sup>1</sup>, Kira Nolan<sup>1</sup>, Daniel A. Perley<sup>7</sup>, Josiah N. Purdum<sup>4</sup>,  
 Sam Rose<sup>1</sup>, Ben Rusholme<sup>10</sup>, Tawny Sit<sup>11</sup>, Anastasios Tzanidakis<sup>12</sup>, Avery  
 Wold<sup>10</sup>, Lin Yan<sup>4</sup>, and Yuhan Yao<sup>13,8</sup>

<sup>1</sup>Division of Physics, Mathematics and Astronomy, California Institute of Technology, Pasadena,  
 CA 91125, USA

<sup>2</sup>Department of Astronomy, The Oskar Klein Center, Stockholm University, AlbaNova, 10691  
 Stockholm, Sweden

<sup>3</sup>Department of Astronomy, University of Michigan, 1085 S. University Ave., Ann Arbor, MI  
 48109, USA

<sup>4</sup>Caltech Optical Observatories, California Institute of Technology, Pasadena, CA 91125, USA

<sup>5</sup>Loomis Laboratory of Physics, University of Illinois at Urbana-Champaign, 1110 W Green St  
 Loomis Laboratory, Urbana, IL, 61801, USA

<sup>6</sup>Center for Interdisciplinary Exploration and Research in Astrophysics (CIERA), Northwestern  
 University, 1800 Sherman Ave., Evanston, IL 60201, USA

<sup>7</sup>Astrophysics Research Institute, Liverpool John Moores University, 146 Brownlow Hill, Liverpool  
 L3 5RF, UK

<sup>8</sup>Department of Astronomy, University of California, Berkeley, CA 94720-3411, USA

<sup>9</sup>School of Physics and Astronomy, University of Minnesota, Minneapolis, MN 55455, USA

<sup>10</sup>IPAC, California Institute of Technology, 1200 E. California Blvd, Pasadena, CA 91125, USA

<sup>11</sup>Department of Astronomy and Center of Cosmology and AstroParticle Physics, The Ohio State  
 University, Columbus, OH 43210, USA

<sup>12</sup>Department of Astronomy and the DiRAC Institute, University of Washington, 3910 15th Avenue  
 NE, Seattle, WA 98195, USA

<sup>13</sup>Miller Institute for Basic Research in Science, 468 Donner Lab, Berkeley, CA 94720, USA

**Abstract**

In recent years, a class of stripped-envelope supernovae (SESNe) has emerged that show two distinct peaks in their light curves, where the first peak cannot be attributed to shock cooling emission. Such peculiar supernovae are often studied individually, explained by invoking some combination of powering mechanisms. However, they have seldom been discussed in the broader context of double-peaked SESNe. In this paper, we attempt to form a picture of the landscape of double-peaked SESNe and their powering mechanisms by adding two more objects—SN 2021uvy and SN 2022hgk. SN 2021uvy is a broad and luminous SN Ib with an unusually long rise of the first peak and constant color evolution with rising photospheric temperature during the second peak. Although its first peak is similar to that of SN 2019stc, the properties of SN 2021uvy differ during the second peak, making it unique among double-peaked objects. SN 2022hgk, on the other hand, shows striking photometric similarity to SN 2019cad and spectroscopic similarity to SN 2005bf, both of which have been suggested to be powered by a double-nickel distribution in their ejecta. We analyze their light curves and colors, compare them with a sample of other double-peaked published supernovae for which we have additional data, and analyze the light curve parameters of the sample. We observe a correlation (p-value  $\sim 0.025$ ) between the peak absolute magnitudes of the first and second peaks. The sample shows variety in the photometric and spectroscopic properties, and thus no single definitive powering mechanism applies to the whole sample. However, sub-groups of similarity exist that can be explained by mechanisms like the double-nickel distribution, magnetar central engine, interaction, and fallback accretion. We also map out the duration between the peaks ( $\Delta t^{21}$ ) vs the difference between peak absolute magnitudes ( $\Delta M^{21}$ ) as a phase-space that could potentially delineate the most promising powering mechanisms for the double-peaked SESNe.

#### 4.1 Introduction

The number of observed stripped-envelope supernovae (SESNe) showing two distinct light-curve peaks has been increasing in recent years with the advent of wide-field dynamic all-sky surveys. This emerging class of SESNe does not seem to form a homogeneous group, instead, there might be subgroups of objects that share observational similarities and powering mechanisms. A common subgroup is SESNe that show a fast initial decline ( $t_{1/2} \lesssim 5$  days) and then develop a second (i.e. the main) peak that appears like a normal SESN. Such a rapidly declining first peak is often associated with the shock-cooling phase from the extended envelope of the progenitor (Nakar et al. 2014; Piro 2015; Piro et al. 2021) or very nearby circumstellar material

(CSM, e.g., Jin et al. 2021; Khatami et al. 2024), and is commonly observed in Type IIb SNe (Morales-Garoffolo et al. 2015; Pellegrino et al. 2023; Crawford et al. 2025) but also some Type Ibc SNe (Taddia et al. 2016; Das et al. 2024). SESNe with early shock-cooling peaks also appear to show a strong correlation between the first and second peak absolute magnitudes, likely because both peak luminosities are related to the explosion energy (see fig. 1 of Das et al. 2024).

However, the rest of the double-peaked SESNe show large heterogeneity in light curve shapes, luminosities, and spectral properties, sometimes varying between the two peaks of the same supernova. Such objects have often been studied individually and compared to a few similar, previously known SNe, and various combinations of powering mechanisms have been invoked. The commonly used powering mechanisms include (see §4.4 for specific examples, references and discussion): i) double-nickel distribution, ii) delayed magnetar energy injection, iii) interaction with circumstellar material (CSM), iv) energy injection due to fallback accretion, v) eruptive precursor powering the initial peak, and vi) pulsational pair-instability eruptions. For a few SNe, tell-tale signs of the powering mechanism are present in the observations, such as narrow emission lines in the optical spectra (indicating CSM interaction). However, for many double-peaked SESNe, a number of these scenarios, or combinations thereof, can reasonably fit the light curve data well. More seldom have these supernovae been analyzed as a photometric class, but doing so might reveal pockets of homogeneity in this dispersed group of objects that perhaps correlate to a particular powering mechanism. Several of the invoked powering mechanisms also have their own limitations on the brightness of the peaks they can produce, the duration between the two peaks, or other observables that can help differentiate between the mechanisms (see §4.4).

Gathering more observations of such peculiar supernovae can be particularly important given the rarity of the objects themselves and the exceptional nature of some of the proposed models. Collecting a larger sample also improves our ability to group these objects systematically based on light-curve similarity. In this paper, we present an extensive analysis of SN 2021lvy—a bright, slowly evolving double-peaked SN Ib, and SN 2022hgk—a moderate luminosity and duration double-peaked SN Ib, which we have followed as part of the Zwicky Transient Facility (ZTF) survey and were previously mentioned in the sample study by Das et al. (2024). We compare these two supernovae with a sample of clearly double-peaked, published SNe Ibc, mainly from the ZTF archive (see §4.3). For this double-peaked SESNe

sample, we estimate several light-curve parameters and attempt to infer whether any phase space mapped out by these parameters can be useful for discerning the possible powering mechanisms of these objects.

This paper is organized as follows. In §4.2, we present the observations of the two SNe and data processing methods. In §4.3, we compare the light curves, colors, bolometric luminosities, and spectra of the two SNe with other similar double-peaked SESNe from the literature. We define a sample of clearly double-peaked SESNe from the ZTF archive in §4.3, analyze their light curve parameters in §4.4, and discuss the landscape of powering mechanisms for this sample in §4.4. Finally, we summarize our results in §4.5.

## 4.2 Observations

### Discovery

#### SN 2021uvy

SN 2021uvy (a.k.a. ZTF21abmldj) is located at J2000.0 coordinates  $\alpha = 00^h29^m30.88^s$  and  $\delta = +12^\circ06'21''.01$  in a faint host galaxy (SDSS  $r$  band 22.2 mag). The redshift is determined to be  $z = 0.0944$  from one of our intermediate resolution spectra at late times (§4.2). SN 2021uvy was first detected in the ZTF survey (Bellm et al. 2019; Graham et al. 2019; Dekany et al. 2020) data on 2021 August 4 (MJD 59403.424) at a host-subtracted magnitude of 20.64 in the ZTF  $r$  band and was reported (Fremling 2021) to the Transient Name Server (TNS<sup>1</sup>) by the Bright Transient Survey (BTS; Fremling et al. 2020; Perley et al. 2020; Rehemtulla et al. 2024) team. The SN was caught at an early stage and has good photometric coverage before and during the rise. It was initially reported as a superluminous supernova (SLSN) candidate (Lunnan et al. 2021) and initially classified as a SLSN-I at  $z \sim 0.255$  (Poidevin et al. 2021) based on the top SNID (Blondin et al. 2007) match of a spectrum obtained on 2021 August 13 with SPRAT (Piascik et al. 2014) on the Liverpool Telescope (LT; Steele et al. 2004). It was reclassified as SN Ibc at  $z = 0.1$  (Ridley et al. 2021) by the ePESSTO team (Smartt et al. 2015; Chen 2019) using a higher resolution spectrum obtained also on 2021 August 13 with EFOSC2 (Buzzoni et al. 1984) on ESO’s New Technology Telescope, which removed its superluminous candidacy. Finally, it was classified as a SN Ib-pec (peculiar) by the BTS team (Chu et al. 2021) based on a spectrum obtained with the LRIS (Oke et al. 1995; Perley 2019) spectrograph on the Keck-I telescope on 2021 September 9. SN 2021uvy was inter-

---

<sup>1</sup><https://www.wis-tns.org>

esting as a luminous Type Ib supernova with an unusually long  $\sim 50$  days rise to the peak ( $M_{pk}^1 \approx -19.8$ ). It became even more peculiar when it brightened again after declining for  $\sim 25$  days post-peak. The rise of the second peak was also slow ( $\sim 30$  days) and attained a similar luminosity as the first peak ( $M_{pk}^2 \approx -19.3$ ). We obtained follow-up optical imaging and spectroscopic observations until the SN faded below apparent magnitude  $m_r = 22.7$ .

### **SN 2022hgw**

SN 2022hgw (a.k.a. ZTF22aaezyos) is located at J2000.0 coordinates  $\alpha = 14^h 10^m 23.70^s$  and  $\delta = +44^\circ 14' 01''.21$  in the host galaxy SDSS J141023.70+441401.8. The redshift is determined to be  $z = 0.0335$  from a host-galaxy spectrum obtained after the SN faded. SN 2022hgw was first detected in ZTF data on 2022 April 6 (MJD 59675.344) at a host-subtracted  $r$ -band magnitude of 20.76 and reported to TNS (Fremling 2022). The transient remained fainter than 19 magnitude for the next  $\sim 25$  days and, thus, was not assigned for follow-up under the BTS survey criteria. Spectroscopic follow-up was triggered only once the transient started brightening again and developed a second peak, and SN 2022hgw was subsequently classified as a SN Ib by the BTS team (Perley et al. 2022a) based on a spectrum obtained with the SEDM spectrograph (Ben-Ami et al. 2012; Blagorodnova et al. 2018) on the Palomar 60-inch telescope on 2022 May 20. We continued follow-up optical imaging and spectroscopy until the SN faded below 21 magnitude.

### **Optical photometry**

For both of these SNe, we obtained forced point-spread function photometry from the ZTF forced photometry service (Masci et al. 2019; Masci et al. 2023) in  $g$ ,  $r$ , and  $i$  bands and from the ATLAS forced photometry service (Tonry et al. 2018; Smith et al. 2020) in  $c$  and  $o$  bands. Additional optical photometry was obtained with the Rainbow camera on the Palomar 60-inch telescope (Cenko et al. 2006), the Optical wide-field camera (IO:O) on LT, ALFOSC on the Nordic Optical Telescope (NOT), and the imaging camera on the Katzman Automatic Imaging Telescope (KAIT) at Lick Observatory. The data from P60 and KAIT were processed with the automatic image subtraction pipeline FPipe (Fremling et al. 2016). The data from LT was processed with custom image subtraction and analysis software (K. Hinds and K. Taggart et al., in prep.), and the photometry was measured using PSF fitting techniques from Fremling et al. (2016). The data from NOT was reduced

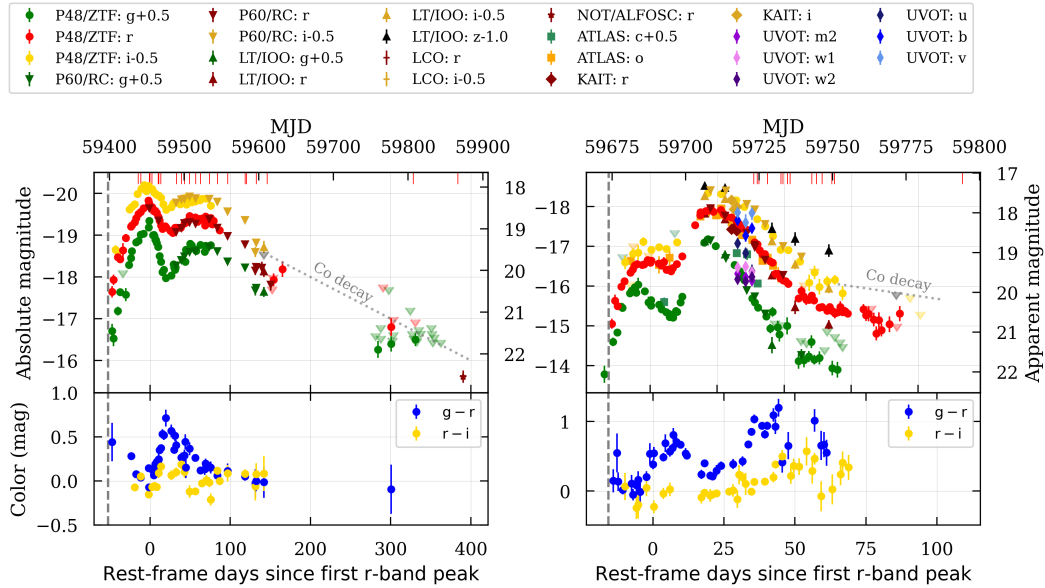


Figure 4.1: Light (top) and color (bottom) curves of SN 2021uvy (left) and SN 2022hgk (right). The  $5\sigma$  detections are shown with solid markers and  $3\sigma$  upper limits with transparent markers. All photometry is corrected for MW extinction. Absolute magnitudes are K-corrected (by adding  $-2.5\log_{10}(1+z)$ ) and obtained using Planck Collaboration et al. (2020) cosmology. The  $^{56}\text{Co}$  decay rate (radioactive power) is shown with a dotted gray line. The spectral phases are marked on the top axis with red vertical lines. The explosion epochs are shown with gray dashed lines.

with PyNOT<sup>2</sup> data reduction pipeline, image subtraction to remove host contribution was performed with HOTPANTS version 5.11 (Becker 2015) using a pre-supernova  $r$  band image from the DESI Legacy Imaging Surveys (LS; Dey et al. 2019), and the aperture photometry was calibrated against a set of stars from the DESI Legacy Imaging Surveys.

All photometry presented in this paper is corrected for Milky Way extinction using the Python package extinction (Barbary 2016), the dust extinction law from Fitzpatrick (1999), the Schlafly et al. (2011) dust map,  $E(B - V) = 0.067$  mag for SN 2021uvy,  $E(B - V) = 0.005$  mag for SN 2022hgk, and  $R_V = 3.1$  for both SNe. All measurements are converted into flux units for the analysis. The luminosity distances (and in turn, distance moduli and absolute magnitudes) are calculated using the cosmology parameters from Planck Collaboration et al. (2020) ( $H_0 = 67.7$ ,  $\Omega_m = 0.31$ ,  $\Omega = 1$ ). The absolute magnitudes are calculated using a distance modu-

<sup>2</sup><https://github.com/jkrogager/PyNOT>

lus (DM) of 38.254 for SN 2021uvy and 35.879 for SN 2022hgk and are K-corrected. Given the absence of Na ID narrow absorption in spectra of both SNe and the faint host galaxy of SN 2021uvy, we do not account for any host reddening. The optical photometry data are included in Appendix 4.7 and shown in Figure 4.1.

### ***Swift* Ultraviolet/Optical telescope photometry**

The field of SN 2022hgk was observed with the Ultraviolet/Optical Telescope (Romling et al. 2005) (UVOT) aboard the *Swift* satellite (Gehrels et al. 2004) between MJD = 59720.72 and 59732.38 in bands  $w2$ ,  $m2$ ,  $w1$ ,  $u$ ,  $b$ , and  $v$ . We retrieved science-ready data from the *Swift* archive<sup>3</sup>. The all-sky exposures for a given epoch and filter were co-added to boost the signal-to-noise ratio using `uvotimsum` in HEASoft<sup>4</sup> version 6.31.1. We measured the brightness of the SN with the *Swift* tool `uvotsource`, setting the source aperture radius of  $5''$  and a significantly larger background region. All measurements were calibrated with the latest calibration files and converted to the AB system following Breeveld et al. (2011). The UV photometry (not corrected for reddening and not host-subtracted) is included in Appendix 4.7. Since the UV photometry is not corrected for host contribution, we do not use it to construct the bolometric light curves.

### **Optical spectroscopy**

We obtained spectroscopic follow-up for SN 2021uvy between 2021 August 16 and 2023 July 23 and for SN 2022hgk between 2022 May 8 and 2022 July 27 with the following instruments:

- Spectral Energy Distribution Machine (SEDM,  $R \sim 100$ , Blagorodnova et al. 2018) on P60, data processed using `pysedm` (Rigault et al. 2019; Kim et al. 2022).
- Low Resolution Imaging Spectrometer (LRIS,  $R \sim 800 \sim 1400$ , Oke et al. 1995) on the Keck-I telescope, data processed using `LPipe` (Perley 2019).
- Double Beam Spectrograph (DBSP,  $R \sim 1000$ , Oke et al. 1982) on the Palomar 200-inch telescope (P200), data processed using `DBSP-DRP` (Roberson et al. 2022; Prochaska et al. 2020).

<sup>3</sup>[https://www.swift.ac.uk/swift\\_portal](https://www.swift.ac.uk/swift_portal)

<sup>4</sup><https://heasarc.gsfc.nasa.gov/docs/software/heasoft/>

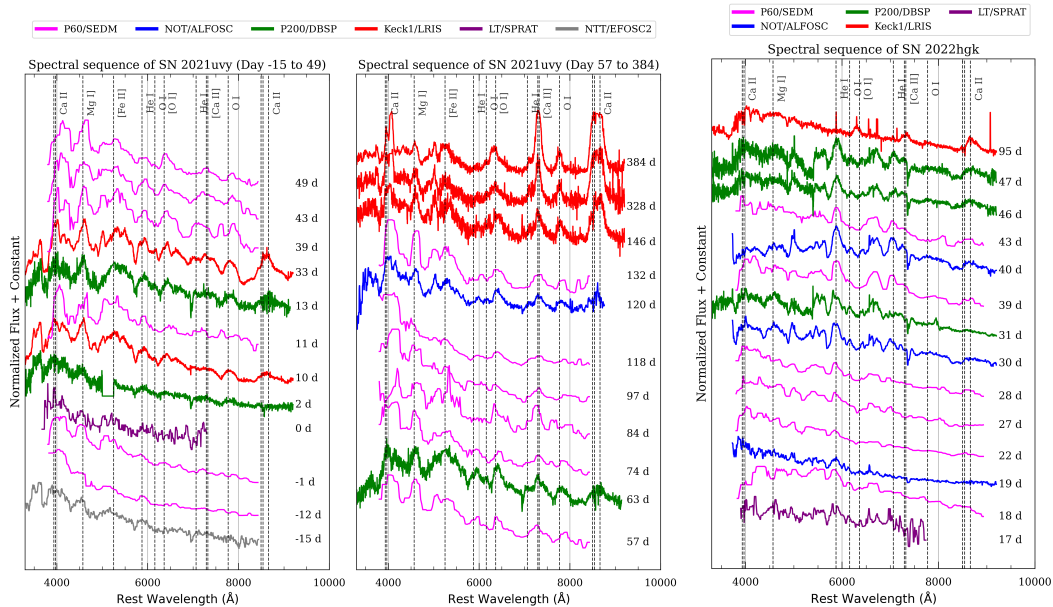


Figure 4.2: Spectral sequences of SN 2021uvy (left and center) covering epochs from  $-15$  to 384 rest-frame days since its first peak and of SN 2022hgk (right) covering epochs from 17 to 95 rest-frame days since its first peak. Some characteristic spectral lines are marked with vertical gray dashed lines. Spectra are smoothed with a median filter of window size 5.

- Alhambra Faint Object Spectrograph and Camera (ALFOSC,  $R \sim 360$ ), on the Nordic Optical Telescope (NOT), data processed using PypeIt (Prochaska et al. 2020).
- Spectrograph for the Rapid Acquisition of Transients (SPRAT,  $R \sim 360$ , Piascik et al. 2014) on the Liverpool Telescope (LT, Steele et al. 2004). Data processed using a custom Python pipeline utilizing the packages Astropy (Astropy Collaboration et al. 2022b), NumPy (Harris et al. 2020), SciPy (Virtanen et al. 2020), and Matplotlib (Hunter 2007b).

We present 23 spectra of SN 2021uvy in this paper (22 from the ZTF group, 1 from TNS, Ridley et al. 2021) covering epochs from  $-15$  to 384 rest-frame days from its first peak in the  $r$  band and 14 spectra of SN 2022hgk covering epochs from 17 to 95 rest-frame days from its first peak in the  $r$  band. The spectral sequences are listed in Appendix 4.8 and shown in Figure 4.2. We also present spectra obtained as part of the ZTF follow-up campaigns of double-peaked SESNe in our sample (see §4.3 for details) that have not been published previously in Appendix 4.8, namely SN 2020acct (11 spectra,  $-1$  to 149 rest-frame days), SN 2021pkd (4 spectra,  $-7$  to

7 days), and SN 2023plg (22 spectra, 70 to 147 days). All spectra were corrected for Milky Way extinction using the same procedure as the photometry, then calibrated using contemporaneous host-subtracted ZTF data in the  $r$  band. All spectra will be made available on WISeREP (Yaron et al. 2012).

### 4.3 Analysis

#### The double-peaked SESN sample

Table 4.1: Sample of published double-peaked SESNe in the ZTF archive.

IAU Name	ZTF Name	Redshift	Type	$E(B - V)_{MW}$ (mag)	$E(B - V)_{host}$ (mag)	Reference
SN 2018ijp	ZTF18aceqrrs	0.0848	Ic	0.03	0.0	Tartaglia et al. (2021)
SN 2019cad	ZTF19aamsetj	0.02751	Ic	0.02	0.5 <sup>a</sup>	Gutiérrez et al. (2021)
SN 2019oys	ZTF19abucwzt	0.0162	Ib	0.09	0.0	Sollerman et al. (2020)
SN 2019stc	ZTF19acbonaa	0.1178	Ic/SLSN-I	0.08	0.18 <sup>b</sup>	Gomez et al. (2021)
SN 2020acct	ZTF20acwobku	0.0347	Ibc	0.03	0.0	Angus et al. (2024)
SN 2021pkd	ZTF21abfjlxk	0.0398	Ib	0.04	0.0	Soraisam et al. (2022)
SN 2021uvy	ZTF21abmlldj	0.0944	Ib	0.07	0.0	Das et al. (2024)
SN 2022hgk	ZTF22aaezyos	0.0335	Ib	0.01	0.0	Das et al. (2024)
SN 2022jli	ZTF22aapubuy	0.0055	Ic	0.04	0.25 <sup>c</sup>	Chen et al. (2024)
SN 2022xxf	ZTF22abnvurz	0.0034	Ic-BL	0.04	0.8 <sup>d</sup>	Kuncarayakti et al. (2023)
SN 2023aew	ZTF23aaawbsc	0.025	Ibc	0.04	0.0	Kangas et al. (2024) <sup>e</sup>
SN 2023plg	ZTF23aaxuvkn	0.027	Ibc	0.06	0.0	Sharma et al. (2024)

<sup>a</sup> From Gutiérrez et al. (2021)

<sup>b</sup> From Chen et al. (2023a)

<sup>c</sup> From Chen et al. (2024)

<sup>d</sup> From Kuncarayakti et al. (2023)

<sup>e</sup> Also Sharma et al. (2024)

To collect the sample of previously published double-peaked SESNe in ZTF, we looked at ZTF light curves of all unambiguously classified SESNe (Type Ib, Ic, Ic-BL, Ib/c, Ib-pec) in the ZTF archive (a total of 501 objects). We obtained the light curves from Fritz (Walt et al. 2019; Coughlin et al. 2023) and interpolated them using Gaussian process regression. We then used `scipy.signal.find_peaks` functionality to search for prominent peaks in the  $r$ -band light curves (and  $g$ -band light curves in cases where  $r$ -band data was not available). We visually vetted the light curves that were identified to have  $>1$  peak (46 out of 501) and rejected objects that: i) had incorrect identification of multiple peaks due to missing coverage (and consequently incorrect interpolation), ii) had more than two bumps/peaks (for example, SN 2021efd identified as a bumpy SN in Soraisam et al. 2022), or iii) had non-prominent bumps and plateaus. We also rejected one object that fits the double-peak criteria but has not yet been published. SN 2022jli did not get filtered out with this methodology, as its first peak was not covered in ZTF, but we added it to our sample since it is a known peculiar double-peaked supernova. The resulting sample (12 SNe) is summarized in Table 4.1, and includes SNe 2021uvy and 2022hgk. We

note that SN 2019stc is classified as a luminous SN Ic in Gomez et al. (2021), but if host extinction is considered, it reaches superluminous status and is classified as a SLSN-I in Chen et al. (2023a). Thus, the observed fraction of clearly double-peaked Type Ibc SNe is  $\sim 2.5\%$  of all Type Ibc SNe. In the following sections, we compare the photometric and spectroscopic properties of our two key objects, SNe 2021uvy and 2022hgk, with supernovae from this collected sample.

### Light curves

We fit the rise of SN 2021uvy in ZTF data with an exponential curve to constrain the explosion epoch, as the rise time is unusually long, but for SN 2022hgk, we fit the rise with a power-law curve. We converted the  $r$ ,  $g$ , and  $i$ -band magnitudes into linear flux densities (in  $\mu\text{J}$ ), then used the Markov Chain Monte Carlo (MCMC) technique with the following equation to fit the exponential rise in the bands separately:

$$f = f_{max} \left( 1 - e^{-\frac{(t_{exp}-t)}{t_c}} \right) \quad (4.1)$$

where  $f$  is the flux in  $\mu\text{Jy}$ ,  $t_{exp}$  is the explosion epoch,  $f_{max}$  is the maximum flux, and  $t_c$  is the characteristic rise-time. We then calculate the mean and standard deviation of the best-fit values of  $t_{exp}$  obtained from the three ZTF bands to get the final explosion epoch at  $\text{MJD } 59398.21 \pm 2.50$  for SN 2021uvy and  $\text{MJD } 59673.80 \pm 4.60$  for SN 2022hgk.

Figure 4.1 shows the light- (top panel) and color- (bottom panel) curves of SN 2021uvy (left) and SN 2022hgk (right). Both objects show very conspicuous double-peaked light curves, which is highly unusual for SESNe. There are also obvious differences in luminosities and timescales. SN 2021uvy's first peak is broad and has a very slow rise of 52 rest-frame days from explosion to a peak absolute magnitude of  $M_{pk,r}^1 = -19.8$  in the  $r$  band. It then declines for 25 rest-frame days at a rate of  $0.030 \pm 0.002 \text{ mag d}^{-1}$  in the  $r$  band, faster than the radioactive Co-decay rate ( $\approx 0.01 \text{ mag d}^{-1}$ ). After a clear minimum at around  $\text{MJD } 59480$ , SN 2021uvy brightens again for  $\sim 28$  rest-frame days to an absolute magnitude of  $M_{pk,r}^2 = -19.3$  (slightly fainter than the first peak), then slowly declines at a rate of  $0.011 \pm 0.001 \text{ mag d}^{-1}$ , very close to the decay rate of  $^{56}\text{Co}$ , shown by the gray dotted line in Figure 4.1 (left).

On the other hand, SN 2022hgk is nearly two magnitudes fainter at maximum luminosity than SN 2021uvy, and has an overall shorter duration and a more luminous second peak compared to the first peak, unlike SN 2021uvy. SN 2022hgk has a first rise time of  $\sim 16$  rest-frame days from explosion to a peak absolute magnitude of

$M_{pk,r}^1 = -16.6$ , after which it slightly declines for only  $\sim 7$  rest-frame days before brightening again to a peak absolute magnitude of  $M_{pk,r}^2 = -17.9$ . The peak-to-peak duration ( $\Delta t^{21}$ , more details in §4.4) in the  $r$  band for SN 2022hgk is  $\sim 22$  rest-frame days compared to  $\sim 66$  days for SN 2021uvy. The final decline of SN 2022hgk proceeds at a rate of  $0.078 \pm 0.002$  mag d $^{-1}$  in the  $r$  band until around MJD 59750, after which the decline appears to become slower and similar to the Co decay rate.

In Figure 4.3, we show the absolute  $r$ -band light curves of our double-peaked sample, along with the  $r$ -band light curves of peculiar double-peaked SNe like SN 2005bf (Type Ib; Anupama et al. 2005; Folatelli et al. 2006; Maeda et al. 2007) and PTF11mnb (Type Ic; Taddia et al. 2018a). We obtained the light curves of SNe in our sample following §4.2 and binned them into 3-day bins. The absolute magnitudes of all SNe shown were calculated using the same cosmology (see §4.2), and host-galaxy extinction was taken into account wherever available. The light curves have been shifted horizontally to align their first peaks and shifted vertically for clarity.

Table 4.2: Light curve parameters of our double-peaked SESN sample. The rise and fade times are calculated between peak flux and half-of-peak flux. The superscripts ‘1’ and ‘2’ denote the first and second peak parameters, respectively. The rise times, fade times, and duration between the two peaks ( $\Delta t^{21}$ ) are reported in rest-frame days.

SN	Band	$t_{rise,1/2}^1$ (days)	$M_{pk}^1$ (mag)	MJD $_{pk}^1$	$t_{fade,1/2}^1$ (days)	$t_{rise,1/2}^2$ (days)	$M_{pk}^2$ (mag)	MJD $_{pk}^2$	$t_{fade,1/2}^2$ (days)	$\Delta t^{21}$ (days)	$\Delta M^{21}$ (mag)
2018ijp	$r$	$8.1 \pm 0.3$	$-19.16 \pm 0.13$	58438	$> 9.2$	$> 18.4$	$-18.67 \pm 0.08$	58481	$33.7 \pm 1.0$	39.6	0.49
2019cad	$r$	$> 7.8$	$-17.87 \pm 0.09$	58567	$> 7.8$	$7.7 \pm 0.2$	$-19.17 \pm 0.03$	58593	$13.2 \pm 0.5$	25.3	-1.30
2019oys	$r$	-	$-16.35 \pm 0.05$	58723	$22.7 \pm 0.9$	$111.6 \pm 1.4$	$-15.74 \pm 0.02$	58982	$277.5 \pm 12.7$	254.9	$> 0.6$
2019stc	$r$	$34.0 \pm 0.7$	$-20.52 \pm 0.05$	58799	$29.3 \pm 1.0$	$> 20.6$	$-19.60 \pm 0.06$	58876	$> 17.0$	68.9	0.92
2020acct	$r$	$> 2.9$	$-18.06 \pm 0.03$	59196	$6.6 \pm 0.4$	$3.9 \pm 0.1$	$-17.21 \pm 0.01$	59253	$13.7 \pm 0.4$	55.1	0.85
2021pkd	$r$	$12.0 \pm 0.6$	$-17.84 \pm 0.06$	59394	$> 6.7$	$> 10.6$	$-17.80 \pm 0.05$	59414	$> 12.5$	19.2	0.04
2021uvy	$g$	$22.6 \pm 1.0$	$-19.80 \pm 0.09$	59455	$10.8 \pm 0.9$	$43.9 \pm 0.1$	$-19.24 \pm 0.02$	59531	$56.1 \pm 0.6$	69.4	0.56
	$r$	$25.6 \pm 1.9$	$-19.77 \pm 0.08$	59455	$20.0 \pm 0.7$	$> 41.1$	$-19.37 \pm 0.01$	59528	$55.6 \pm 0.4$	66.7	0.40
2022hgk	$g$	$5.5 \pm 0.4$	$-16.44 \pm 0.05$	59684	$11.9 \pm 0.4$	$6.4 \pm 0.4$	$-17.63 \pm 0.02$	59712	$10.7 \pm 0.3$	27.1	-1.20
	$r$	$11.8 \pm 0.7$	$-16.61 \pm 0.13$	59691	$> 5.8$	$7.7 \pm 0.1$	$-17.92 \pm 0.01$	59713	$14.8 \pm 0.5$	21.3	-1.31
2022jli	$g$	-	$-16.37 \pm 0.01$	59708	$> 17.9$	$12.6 \pm 0.7$	$-16.54 \pm 0.04$	59750	$73.0 \pm 3.9$	41.8	$> -0.2$
2022xxf	$r$	$> 8.0$	$-18.47 \pm 0.01$	59880	$> 24.9$	$33.9 \pm 2.1$	$-18.66 \pm 0.02$	59950	$9.0 \pm 0.1$	69.8	-0.19
2023aew	$r$	$11.7 \pm 0.1^a$	$-17.28 \pm 0.01$	59959	$34.6 \pm 0.5$	$19.5 \pm 0.1$	$-18.84 \pm 0.01$	60075	$32.2 \pm 0.1$	113.2	-1.50
2023plg	$r$	-	$-16.83 \pm 0.02$	60170	$> 22.1$	$7.8 \pm 0.1$	$-18.30 \pm 0.02$	60249	$23.1 \pm 0.6$	76.9	$> -1.5$

<sup>a</sup> Derived from TESS-Red band data

Immediately, we can deduce from Figure 4.3 that there is significant diversity across the sample, but also sub-groups that share some light curve properties. The slow rise, peak luminosity, and first decline of SN 2021uvy are similar to what is seen for SN 2019stc, a luminous SESN (Gomez et al. 2021; Chen et al. 2023a). Gomez et al. (2022) mentions that the first peaks of both SNe 2019stc and 2021uvy fit well to a combined magnetar central engine and  $^{56}\text{Ni}$  radioactive decay power model, but have

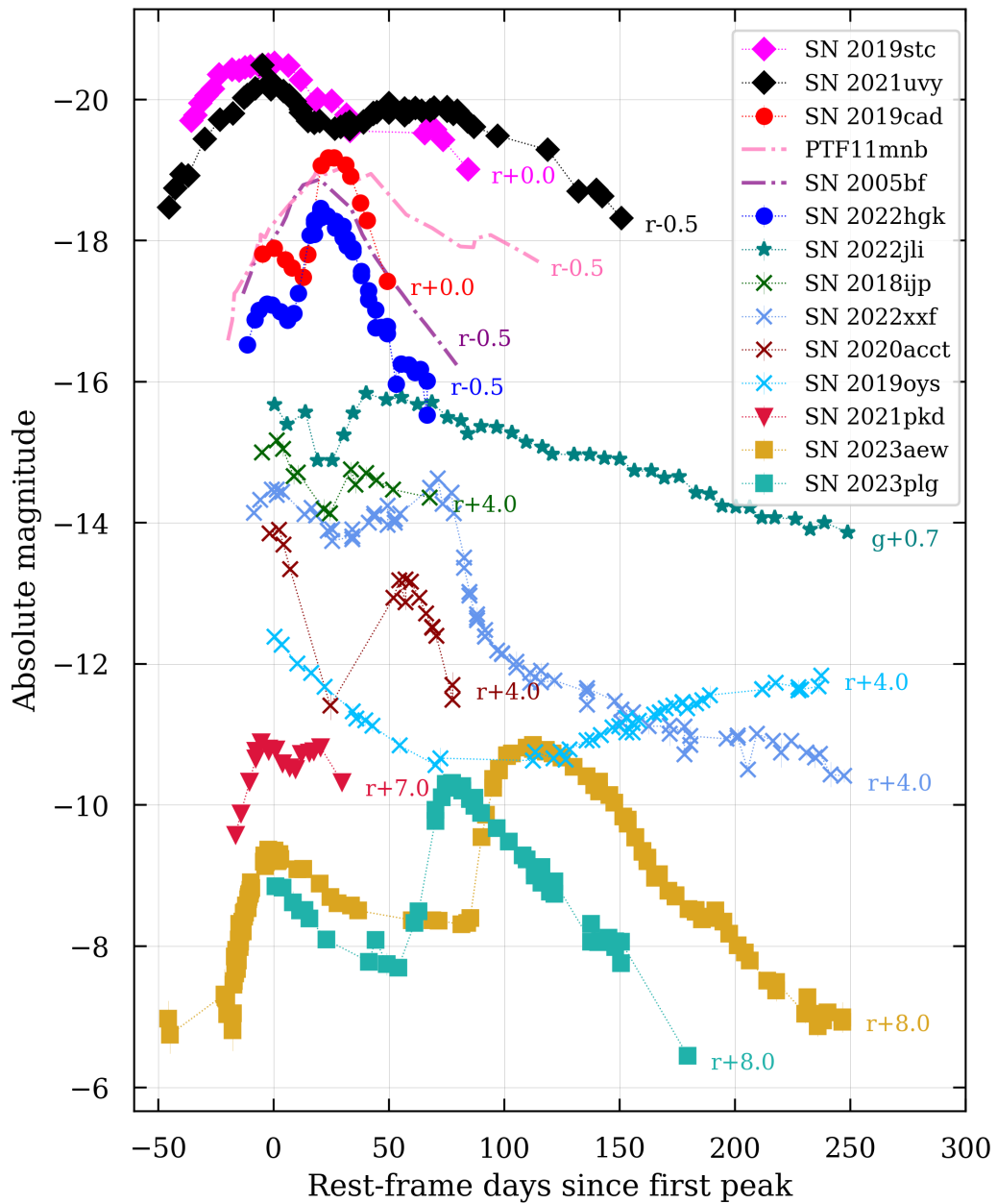


Figure 4.3: Light curves ( $r$ -band) of our sample of double-peaked SESNe, shifted vertically for clarity and with their first peaks aligned. Also shown for comparison are SN 2005bf and PTF11mnb (dashdot lines). All absolute magnitudes have been calculated using the same cosmology.

weaker magnetar engines than typical SLSNe. They posit that this could explain the SLSNe-like light curve but normal SESNe-like spectra of SN 2019stc. However, this combined model does not account for the rebrightening and cannot explain the second peaks of these two SNe. SN 2022hkg’s *r*-band light curve and color curve are remarkably similar to those of SN 2019cad, also considered analogous to SN 2005bf and PTF11mnb. The luminosities and timescales of the two peaks of this group of objects, especially the initial rise before the first peak, which is  $>10$  days from the explosion, fit the double-nickel distribution scenario (Folatelli et al. 2006; Bersten et al. 2013; Orellana et al. 2022) well. The final declines of these objects have some variation, with PTF11mnb and SN 2022hkg possibly showing a bump toward the end. The group of SESNe with confirmed CSM interaction signatures (SN 2018ijp—hydrogen-rich dense shell, SN 2019oys—hydrogen-rich CSM and high-ionization coronal lines, SN 2020acct—narrow emission lines during first peak, and SN 2022xxf—late-time narrow emission lines) are shown with crosses in Figure 4.3 and display the most variety in their light curve evolution, with some having ultra-long durations than others. The accretion-powered SN 2022jli is entirely unique, showing periodic undulations in its long decline. SN 2023aew and 2023plg both have widely separated peaks with a plateau connecting the two peaks and appear unlike any of the other SNe in the sample. Finally, SN 2021pkd does not share a strong similarity with any of the other SNe.

Table 4.2 shows the light-curve parameters (luminosities at both peaks, rise and decline times in different filters measured from peak flux to half of the peak flux) for the double-peaked SESN sample. These parameters were all consistently estimated from interpolated ZTF light curves of the listed SNe when available (TESS-Red band data from Sharma et al. 2024 was used for the first-peak of SN 2023aew, and ASAS-SN *g*-band data from Chen et al. 2024 was used for the first-peak of SN 2022jli). The interpolation was performed using Gaussian process regression with the help of the HAFRET Python package (Yang et al. 2023). We are collecting all these parameters in order to map out the landscape of double-peaked SESNe in terms of observable properties, and the ranges and distributions of these properties might later be valuable to constrain the viable powering mechanisms for their light curves. The grouping seen in Figure 4.3 is also apparent from this table, with some groups (e.g., SNe 2019stc, 2021uvy) having long rest-frame duration between the two peaks ( $\Delta t^{21}$ ) and a fainter second peak ( $\Delta M^{21} = M_{pk}^2 - M_{pk}^1 > 0$ ), while others (e.g., SNe 2019cad, 2022hkg) having shorter  $\Delta t^{21}$  and brighter second peak ( $\Delta M^{21} < 0$ ). SNe 2023aew and 2023plg sit independently in this phase space, with

a longer duration like the first group and a brighter second peak like the second.

### **Bolometric luminosities**

We used `Superbol` (Nicholl 2018b) to calculate the pseudo-bolometric luminosity and bolometric luminosity for SN 2021uvy using its ZTF *gri* data and for SN 2022hgk using its ZTF *gri* and ATLAS *co* data. The other bands are first interpolated to *r*-band epochs, and then the pseudo-bolometric luminosity is calculated by integrating the fluxes over the bandpasses at each epoch. The bolometric luminosity is estimated from the pseudo-bolometric luminosity by adding blackbody corrections (absorbed UV and near-infrared). Figure 4.4 shows the bolometric luminosity (top panel), estimated blackbody temperature (second panel), estimated blackbody radius (third panel), and  $g - r$  color (bottom panel) for SNe 2019cad, 2019stc, 2021uvy, and 2022hgk, along with the regular Type Ic-BL SN 1998bw, and a slow-evolving single-peaked SLSN-I PS1-14bj (chosen for comparison as it also shows no color evolution during its decline). The data for SN 1998bw was obtained with `Superbol` using its UBVRI light curves (Galama et al. 1998; Patat et al. 2001; Sollerman et al. 2002). For SN 2019cad, only bolometric luminosity has been presented in Gutiérrez et al. (2021) and not temperature or radius; therefore, we use the *groiz* light curves from Gutiérrez et al. (2021) and `Superbol` to calculate the shown data (we did not correct for host-extinction due to its high uncertainty). The data for SN 2019stc were obtained from Gomez et al. (2021, their fig. 5) (they did not correct for host-extinction, although it is estimated in Chen et al. (2023a) for SN 2019stc), and the data for PS1-14bj were obtained from Lunnan et al. (2016, their figs. 7 and 8).

Figure 4.4 shows that the first peaks of SN 2019stc and SN 2021uvy follow each other closely in bolometric luminosity, blackbody temperature, radius, and color. From the explosion until the end of the first decline (minima between the two peaks), both SNe show a consistent decrease in temperature (from  $\sim 10000$  K to  $\sim 5000$  K), an increase in radius, getting bluer during the rise and becoming redder during the first decline (which is typical of stripped-envelope supernovae powered by  $^{56}\text{Ni}$ , see SN 1998bw in gray). The similarity between SN 2019stc and SN 2021uvy stops at this point. For SN 2019stc, the temperature plateaus (like for SN 1998bw), and the radius follows the second brightening bump. However, for SN 2021uvy, the temperature starts rising rapidly along with no color evolution (like for PS1-14bj), staying around  $g - r \approx 0$  mag until very late times (indicating some new energy injection). At the same time, its radius declines at a similar rate as for PS1-14bj and

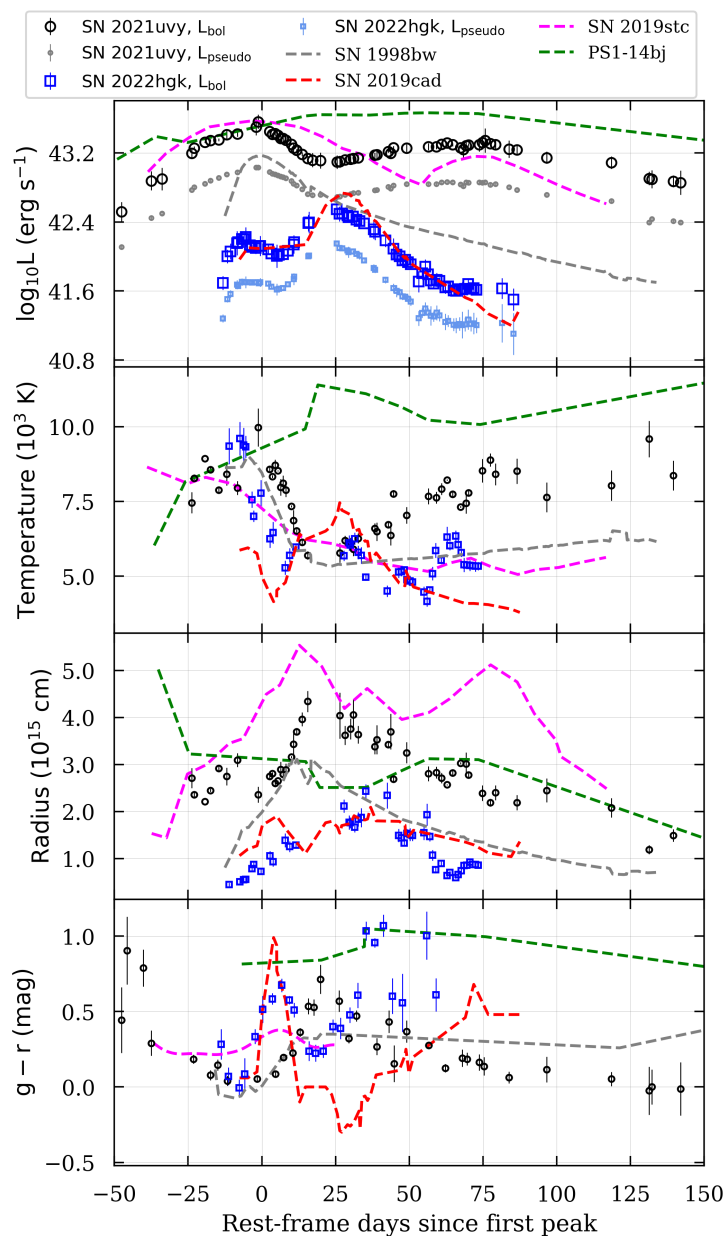


Figure 4.4: Evolution of the bolometric luminosity (top), blackbody temperature (second), blackbody radius (third), and  $g - r$  color (bottom) with time of SN 2021uvy (black circles) and SN 2022hgk (blue squares). Shown for comparison are SN 2019cad (red), SN 2019stc (magenta), PS1-14bj (green), and SN 1998bw (gray). SN 2021uvy and SN 2019stc show similar evolution during their first light-curve peaks but diverge in behavior during the second peaks. SN 2021uvy develops a gradual rise in temperature during the second peak, similar to PS1-14bj, which also correlates with the lack of color evolution for both these SNe. The properties of SN 2022hgk closely resemble those of SN 2019cad.

SN 1998bw. This might indicate that the powering mechanisms of the second peaks of SN 2019stc and SN 2021uvy are different. For SN 2019stc, both radioactive decay and delayed magnetar engine are disfavored according to Gomez et al. (2021), and an aspherical CSM, which could result in a lack of narrow lines, was instead favored for the second peak by those authors. We roughly estimate the  $^{56}\text{Ni}$  mass ( $M_{\text{Ni}}$ ) and ejecta mass ( $M_{\text{ej}}$ ) assuming that the first peaks of SNe 2019stc and 2021uvy are powered by radioactivity using the analytical expressions from Khatami et al. (2019). This gives  $M_{\text{Ni}}^{2019stc} \approx 1.9 M_{\odot}$ ,  $M_{\text{Ni}}^{2019uvy} \approx 2.3 M_{\odot}$ ,  $M_{\text{ej}}^{2019stc} \approx 10 M_{\odot}$ , and  $M_{\text{ej}}^{2019uvy} \approx 17 M_{\odot}$ , which, as expected, are much too large compared to typical SESNe (and inconsistent with neutrino-driven core-collapse models), and thus make radioactivity as the only powering mechanism unfeasible.

Table 4.3: Peak bolometric and pseudo-bolometric luminosities and estimated radiated energies in the two peaks of our double-peaked SESN sample. The superscripts ‘1’ and ‘2’ denote the first and second peaks, respectively. SN 2021uvy has  $\sim 32\times$  more energy radiated than SN 2022hgk.

SN	Lightcurve	$L_{pk}^1$ ( $10^{43}\text{erg s}^{-1}$ )	$L_{pk}^2$ ( $10^{43}\text{erg s}^{-1}$ )	$E_{rad}^1$ ( $10^{50}\text{erg}$ )	$E_{rad}^2$ ( $10^{50}\text{erg}$ )	$E_{rad}^{total}$ ( $10^{50}\text{erg}$ )
2018ijp	Bolometric	$\sim 1.5$	$\sim 0.6$	$\sim 0.3$	$\sim 0.7$	$\sim 1.1$
2019cad	Bolometric	$0.13 \pm 0.02$	$0.59 \pm 0.07$	$0.008 \pm 0.001$	$0.114 \pm 0.005$	$0.139 \pm 0.006$
2019oys	Bolometric	$> 0.12$	$0.10 \pm 0.39$	$> 0.03$	$0.405 \pm 0.296$	$0.436 \pm 0.294$
2019stc	Bolometric	$\sim 3.7$	$\sim 1.4$	$\sim 1.82$	$\sim 0.52$	$\sim 2.38$
2020acct	Bolometric	$0.96 \pm 0.06$	$0.35 \pm 0.01$	$\sim 0.07$	$\sim 0.04$	$\sim 0.15$
2021pkd	Bolometric	$0.85 \pm 1.13$	$0.34 \pm 0.09$	$0.092 \pm 0.018$	$0.059 \pm 0.007$	$0.154 \pm 0.019$
<b>2021uvy</b>	Pseudo-bolometric	$1.08 \pm 0.03$	$0.72 \pm 0.04$	$0.371 \pm 0.004$	$0.764 \pm 0.015$	$1.160 \pm 0.016$
	Bolometric	$3.88 \pm 0.77$	$2.30 \pm 0.76$	$1.070 \pm 0.037$	$2.244 \pm 0.181$	<b><math>3.367 \pm 0.183</math></b>
<b>2022hgk</b>	Pseudo-bolometric	$0.05 \pm 0.01$	$0.14 \pm 0.01$	$0.007 \pm 0.001$	$0.037 \pm 0.001$	$0.045 \pm 0.001$
	Bolometric	$0.18 \pm 0.05$	$0.35 \pm 0.10$	$0.021 \pm 0.001$	$0.095 \pm 0.006$	<b><math>0.117 \pm 0.006</math></b>
2022jli	Pseudo-bolometric	$\sim 0.3$	$\sim 0.4$	$\sim 0.05$	$\sim 0.29$	$\sim 0.35$
2022xxf	Bolometric	$\sim 0.9$	$\sim 1.3$	$\sim 0.22$	$\sim 0.42$	$\sim 0.67$
2023aew	Bolometric	$0.07 \pm 0.00$	$1.20 \pm 0.20$	$0.096 \pm 0.005$	$0.560 \pm 0.013$	$0.656 \pm 0.018$
2023plg	Bolometric	$> 0.19$	$0.67 \pm 0.04$	$> 0.04$	$0.218 \pm 0.004$	$0.258 \pm 0.008$

On the other hand, SN 2022hgk’s bolometric light curve almost exactly matches that of SN 2019cad (if not corrected for host extinction), except towards the very end, when SN 2022hgk shows a little bump before fading completely. The temperature mirrors the luminosity and decreases sharply during the first decline (same as SNe 1998bw, 2019cad, 2019stc, 2021uvy), shows a small rise during the second brightening (like SN 2019cad, SN 2021uvy), decreases again during the second decline (like SN 2019cad), and rises at the very end (coincident with the final luminosity bump). SN 2022hgk’s radius only shows a rise and a decline, peaking around the second (and brightest) luminosity maximum. SN 2022hgk’s  $g - r$  color becomes progressively redder during the second decline, as expected, and has a

similar evolution to the  $g - r$  color of SN 2019cad.

In Table 4.3, we have collected bolometric (and in some cases pseudo-bolometric when the bolometric estimate is not provided) luminosities at the two light-curve peaks and the estimated total radiated energies ( $E_{rad}$ ) to crudely compare the energetics across the sample. We integrate bolometric light curves of SNe 2019cad, 2019oys, 2021pkd, 2021uvy, 2022hgk, and 2023plg obtained using Superbo1 and ZTF light curves to estimate the radiated energies and use the Monte-Carlo method to estimate the uncertainties on radiated energies as follows. We sample 1000 random points per epoch from a normal distribution that has the epoch luminosity as the mean and the uncertainty on the luminosity as the  $\sigma$ . We integrate the sampled light curves over the rest-frame days and take the mean and standard deviation of the resulting energy estimates. For SN 2023aew, we list the values reported in Sharma et al. (2024) that have been estimated using the same process described above. For SNe 2018ijp, 2019stc, 2020acct, 2022jli, and 2022xxf we integrate the bolometric (or pseudo-bolometric) light curves obtained from Tartaglia et al. (2021, their fig. 2), Gomez et al. (2021, their fig. 5), Angus et al. (2024, their fig. 9), Chen et al. (2024, fig. 4), and Kuncarayakti et al. (2023, their fig. A.1) respectively. We simply consider points from the first detection to the local minimum between the two peaks for calculating the energy radiated in the first peak and from the local minimum to the last detection for calculating the energy radiated in the second peak. This provides the simplest lower limits for the radiated energies, as we are not fitting any specific powering mechanisms to the light curves.

### Spectral comparison

Figure 4.5 compares the spectra obtained near the first (left panel) and second (right panel) peaks of SNe 2021uvy and 2022hgk with the most similar double-peaked SESNe from the sample. The first-peak spectra of SN 2021uvy have normal SESN features and look similar to those of SN 2019stc and PS1-14bj. SN 2021uvy shows He I  $\lambda 5876$  signatures from the pre-peak epochs (Figure 4.2, left) which classifies it as a Type Ib. From the absorption minima of O I  $\lambda 7774$  in the day 10 spectrum, we estimate an ejecta velocity of  $\sim 8000 \text{ km s}^{-1}$ , which is also consistent with the He I absorption minimum. The lines of Ca II  $\lambda\lambda 3934, 3969$ , Mg I]  $\lambda 4571$ , and O I  $\lambda 7774$  appear to be of similar strength in these three SNe. The Fe II complex between  $5000 \text{ \AA}$  and  $5600 \text{ \AA}$  has more flux on the blue side and appears broader in SN 2021uvy than for SN 2019stc and PS1-14bj. SN 2021uvy and PS1-14bj also appear to have a slightly bluer continuum than SN 2019stc past the first peak.

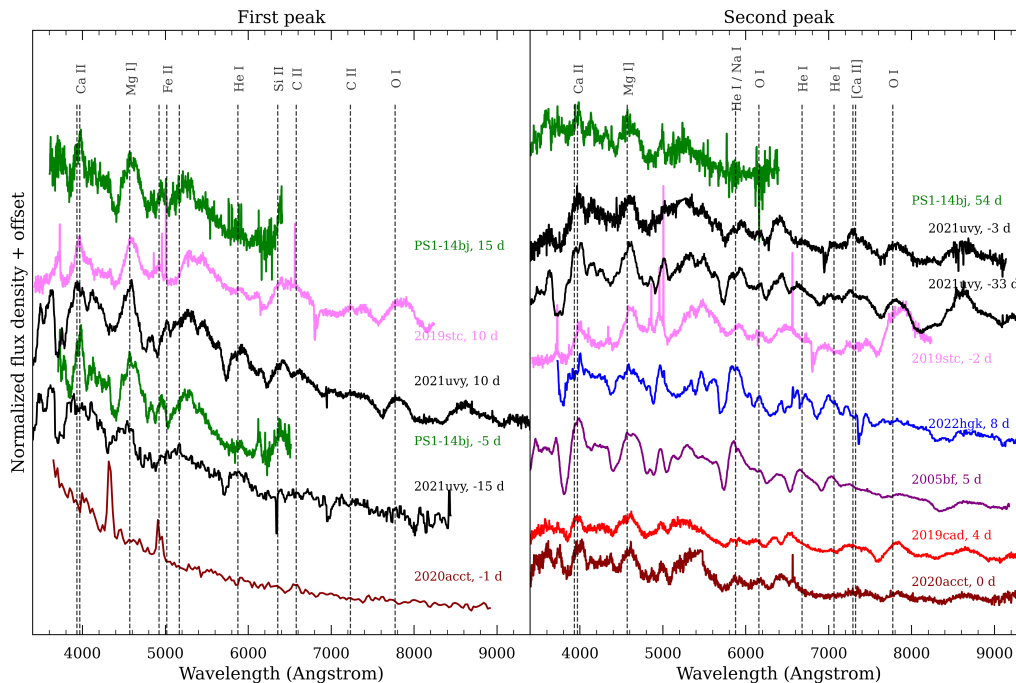


Figure 4.5: *Left*: First-peak spectra of SN 2021uvy (black) compared with those of SNe 2019stc (magenta), 2020acct (brown), and PS1-14bj (green), with phases reported with respect to the first peak. Similar to normal SESNe, the first-peak spectra of SNe 2019stc, 2021uvy and PS1-14bj are dominated by Ca II, Mg I], Fe II and O I. SN 2020acct, on the other hand, shows signs of CSM interaction at this phase. *Right*: Second-peak spectra of SNe 2021uvy (black) and 2022hgw (blue) compared with those of SNe 2005bf (purple), 2019cad (red), 2019stc (magenta), 2020acct (brown), and PS1-14bj (green), with phases reported with respect to the second peak (except for PS1-14bj). SN 2022hgw shows a close spectroscopic resemblance to the peculiar Type Ib SN 2005bf around their main (second) peaks. All spectra are smoothed with a median filter of window size 5 (except for SN 2020acct).

Overall, SN 2021uvy’s first peak exhibits Type Ib nature spectrally but with a slow-evolving SLSN-like light curve that hints towards a mixed powering mechanism (radioactivity + magnetar) as suggested by Gomez et al. (2021) and Gomez et al. (2022).

Other double-peaked SESNe that exhibit normal SESN spectra during the first peak include SNe 2019cad, 2022jli, and 2022xxf. However, SN 2022jli evolved into having accretion-powered second peak (Chen et al. 2024), and SN 2022xxf developed subtle H/He-free signs of CSM interaction (Kuncarayakti et al. 2023). SN 2023aew changed its type from SN II during the first peak to SN Ic during its second peak and then to having hydrogen reappear during the nebular phase,

which could be due to hidden CSM interaction with a complex geometry (Sharma et al. 2024). SN 2020acct showed some early flash-ionization features, a sign of brief CSM interaction during the first peak (Angus et al. 2024), confirming its power source. This is to say that the sample of double-peaked SESNe show as much variety in their spectral nature as they do in their light curves and intermediate resolution spectra taken at crucial epochs in the light-curve evolution (early rise, peak, minima between peaks, second peak, and nebular) are necessary to enable the identification of the powering mechanism. Unfortunately, for SN 2022hgk, no first-peak spectra were taken as it remained below the threshold for triggering follow-up as part of the BTS survey.

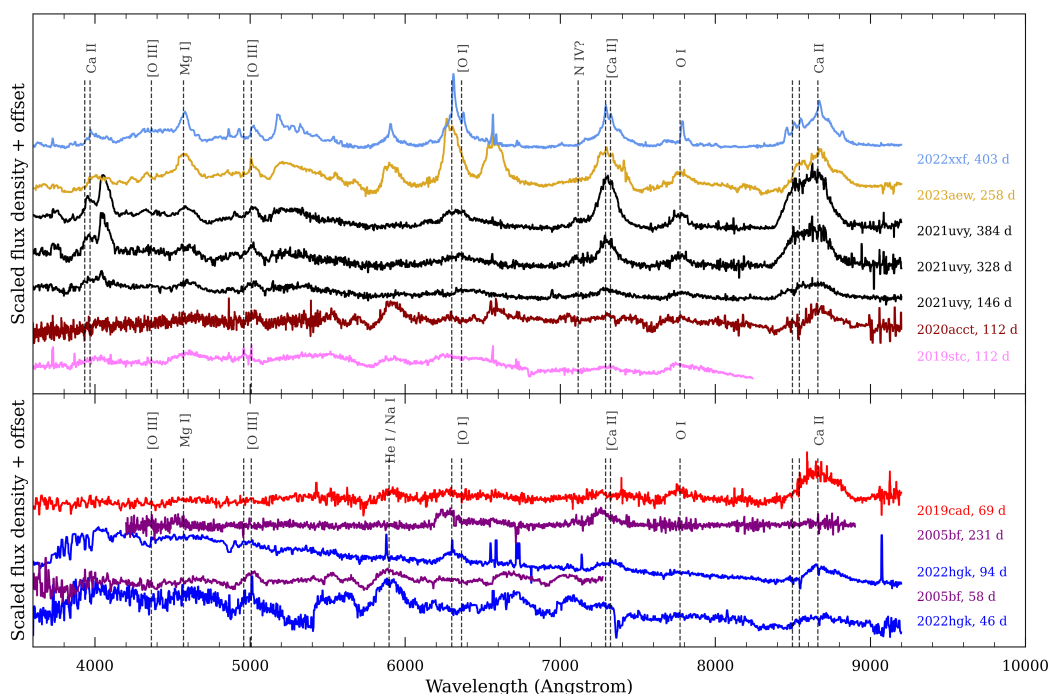


Figure 4.6: *Top:* Comparison of nebular spectra of SN 2021uvy (black) with SNe 2019stc (magenta), 2020acct (brown), 2022xxf (cornflowerblue) and 2023aew (gold). *Bottom:* Comparison of nebular spectra of SN 2022hgk (blue) with SNe 2005bf (purple) and 2019cad (red). All spectral phases are reported with respect to the first peak.

Looking at the right panel of Figure 4.5, around the second peak, the broad features of SNe 2019cad, 2019stc, 2020acct, and 2021uvy are similar and post-peak SESN-like but redder than PS1-14bj. The Ca NIR bumps also become prominent in SNe 2019cad, 2020acct, and 2021uvy. SN 2021uvy also has emission around  $7300 \text{ \AA}$  which could possibly be  $[\text{Ca II}] + [\text{O II}]$ , which is unusual for typical SESNe

in photospheric phase, but has been observed in SNe 2019stc, 2020acct, 2023aew, and also 2018ibb (Schulze et al. 2024a) as noted in Angus et al. (2024). Angus et al. (2024) also noted the striking similarity of the second-peak spectra of SNe 2020acct and 2023aew. SN 2022hgk shows strong He I lines at this epoch ( $\sim 10000 \text{ km s}^{-1}$ ) and a blue continuum. The SN 2022hgk spectrum at 7 days after the second peak closely resembles SN 2005bf's spectrum at 5 days past the second peak (Shivvers et al. 2019), with both showing He I lines and a lack of O I  $\lambda 7774$ . None of these SNe show obvious signs of interaction in their second peak spectra.

Figure 4.6 shows nebular (and near-nebular) spectra of some double-peaked SESNe, with the common nebular lines marked and some tentative line identifications. The phases shown are from the estimated time of the explosion. The final spectra available of SNe 2019stc and 2020acct are shown in the top panel and though they are not fully nebular, we can see [O I]  $\lambda\lambda 6300, 6364$  and [Ca II]  $\lambda\lambda 7292, 7324$  starting to appear. The spectra of SNe 2022xxy, 2023aew, and 2021uvy in the top panel have slight differences that could allude to their origin. Narrow lines become discernible in the nebular spectra of SN 2022xxf, revealing the H/He-free CSM interaction. SN 2023aew shows strong emission at the location of  $H\alpha$ , which appears to be too strong to be the [N II] nebular emission seen in many Type IIb/Ib (Sharma et al. 2024; Barmantloo et al. 2024) and instead could be re-emerged  $H\alpha$ , revealing the hidden CSM powering the supernova. However, the [Ca II]/[O I] flux ratio in these SNe (2021uvy  $\sim 1.18$ , 2022xxf  $\sim 1.16$ , 2023aew  $\sim 0.8$ , 2022hgk  $\sim 0.92$ , 2005bf  $\sim 0.90$ ) are similar, indicating similar oxygen core masses and in turn similar progenitors. SN 2021uvy shows strong emission lines around  $\sim 4000 \text{ \AA}$  which could be Ca II H&K lines but appear to be redshifted. The [Ca II] line in SN 2021uvy maintains a Gaussian profile with time, but [O I] seems to become flat-topped (similar to the case of Type Ib iPTF13bvn; Kuncarayakti et al. 2015), especially in the 384-day spectrum. This could be due to some asphericity in the ejecta (clumps or torus-like oxygen distribution as suggested in Taubenberger et al. 2009), or it could be due to absorption in the interior (Milisavljevic et al. 2010).

The bottom panel of Figure 4.6 compares SNe 2019cad and 2022hgk with SN 2005bf. The 46, 58, and 69-day spectra of SNe 2022hgk, 2005bf, and 2019cad, respectively, show hints of nebular emission lines but are not fully nebular. SN 2019cad differs from the other two SNe and shows stronger O I emission. SN 2022hgk at 46 days matches SN 2005bf at 58 days, maintaining the spectral similarities since their peaks. The 231-day spectrum of SN 2005bf shows its characteristic blueshifted

nebular lines, but the 94-day spectrum of SN 2022hgk does not, which is where SN 2022hgk finally differs from SN 2005bf. The blue continuum in SN 2022hgk at this phase is likely contamination from the host galaxy.

#### 4.4 Discussion

##### Trends in the double-peaked light curve properties

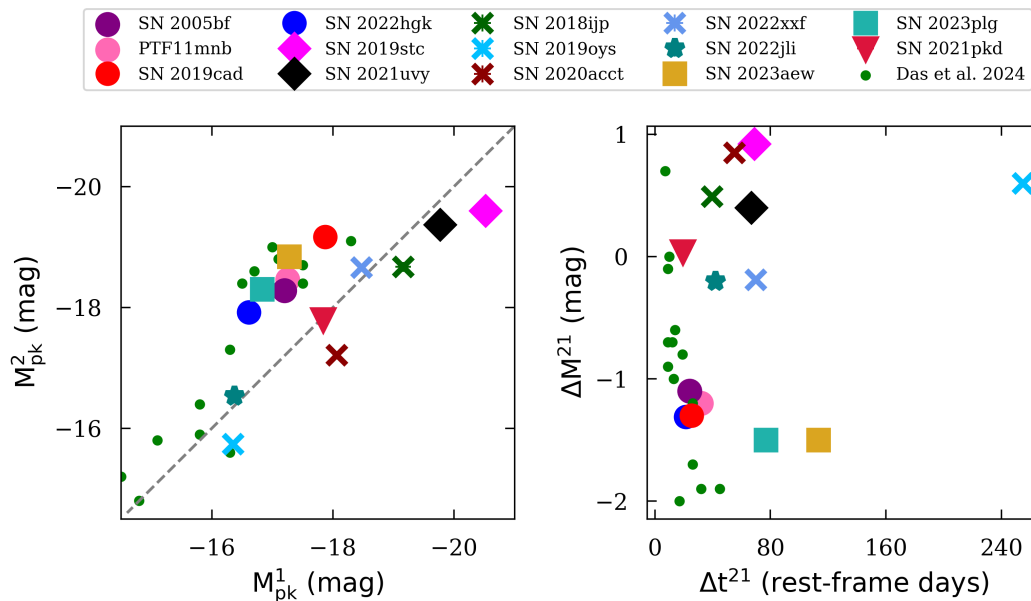


Figure 4.7: *Left*: Peak absolute magnitudes of the second peak vs. the first peak for the double-peaked SESN sample, and the shock-cooling powered double-peaked SESNe presented in Das et al. (2024). There appears to be a correlation between the peak magnitudes, which is strongest for the Das et al. (2024) SESNe (p-value  $< 10^{-5}$ ) but also significant for our double-peaked SESN sample (p-value = 0.005). *Right*: Magnitude difference vs. rest-frame duration between the two peaks. Again, the potentially double-nickel powered SESNe form a tight group in this phase space.

The left panel of Figure 4.7 shows the  $r$ -band ( $g$ -band for SN 2022jli) absolute magnitudes of the second peak against those of the first peak ( $M_{pk}^2$  vs  $M_{pk}^1$ ), the right panel depicts the difference between the peak magnitudes against rest-frame duration between the peaks ( $\Delta M^{21}$  vs  $\Delta t^{21}$ ) for the double-peaked SESN sample discussed in this paper and for the sample of double-peaked Type Ibc SNe presented in Das et al. (2024). There appears to be a correlation between the absolute magnitudes of the first and second peaks (p-value = 0.005). The absolute magnitude correlation was observed by Das et al. (2024) for double-peaked SESNe that have the first peak attributed to cooling after the shock passes the extended envelope (or nearby CSM) of the progenitor. The mechanism behind such a correlation remains unclear.

One possibility that Das et al. (2024) put forth is that SESNe with shock-cooling first peaks have He-star progenitors that shed their envelopes in binary interactions shortly before exploding. For such progenitors, the first peak depends on the progenitor radius and the second peak on the  $^{56}\text{Ni}$  mass. In both panels of Figure 4.7, SNe 2005bf, PTF11mnb, 2019cad, and 2022hgk (all potentially powered by double-nickel distributions, marked with circles) seem to form a group and lie in the same phase-space as the SESNe with shock-cooling peaks. The correlation in shock-cooling powered and double-nickel powered cases could also stem from both peaks being positively correlated with the explosion energy. SESNe with at least one of the peaks potentially powered by CSM interaction (marked with crosses) and the accretion-powered SN 2022jli (marked with a star) follow the correlation in the left panel but do not seem to form a group. Finally, SNe 2019stc and 2021uvy form a close duo in all panels.

It is apparent from Figure 4.7 that the location these supernovae occupy in the different phase spaces created by the light curve properties ( $M_{pk}^2 - M_{pk}^1$ ,  $\Delta M^{21} - \Delta t^{21}$ , etc.) can help unveil the possible powering mechanisms, especially for models that have quantifiable restrictions on these light curve properties.

### Powering Mechanisms

The double-peaked stripped-envelope supernovae discussed so far exemplify the uncertainty about the powering mechanism of the light curves of this class. Normal SNe Ibc can be relatively well explained as being powered by the decay of radioactive  $^{56}\text{Ni}$  that diffuses out of the initially optically thick ejecta. This self-contained explanation follows the simple model by Arnett 1982. It should be mentioned, however, that even this picture has been questioned in the literature. The ejecta masses deduced from some light curve analysis studies indicate values lower than anticipated from massive single stars (e.g., Taddia et al. 2015; Prentice et al. 2019) and the  $^{56}\text{Ni}$  masses are too high to be explained by contemporary neutrino-driven core collapse models (Sollerman et al. 2022), spurring discussion on the need for other powering mechanisms even for the normal objects (e.g., Rodríguez et al. 2024; Karamehmetoglu et al. 2023). Analysis of the relationship between nebular line flux ratios ( $[\text{Ca II}]/[\text{O I}]$ ) and ejecta masses estimated from light curve modeling (with Arnett 1982) of SESNe also revealed no connection between the two, meaning both low and high ejecta mass objects have similar progenitors, implying the presence of other powering mechanisms responsible for the light-curve behavior (Prentice et al. 2022). Studying the rarer family of double-peaked objects has provided a plethora

of suggestions, including the most common scenarios for powering the emission of supernovae. Often, different mechanisms or a combination thereof are invoked to explain each peak in such supernovae, although some modeling studies exist that try to explain the double-peaked light curve with a single mechanism. In the following sections, we briefly discuss the suggested powering mechanisms and attempt to form a picture of their diversity.

### **Double-Nickel distribution**

An early suggestion for double-peaked SESNe was the notion of double nickel distributions. A jet-like structure that brings some radioactive material closer to the surface was proposed for the double-peaked peculiar Type Ib SN 2005bf (Folatelli et al. 2006), which would produce an early light curve peak before the central Ni power diffuses out on a longer time scale. SN 2019cad (analog of SN 2005bf) was proposed to have such a structure (Gutiérrez et al. 2021; Taddia et al. 2018a, see also PTF11mnb), and the scenario was further explored e.g., Orellana et al. 2022. This mechanism fits well given SN 2022hgk’s striking photometric similarity with SN 2019cad and spectral similarity with SN 2005bf. It is clear from these models, however, that they have limited ability to match light-curve peaks that are well separated (large  $\Delta t^{21}$  and in turn delayed second peak that would be inconsistent with radioactive power diffusion timescale, like SNe 2019stc, 2020acct, 2021lvy, 2023aew), or with high luminosities (that require unreasonable nickel mass like SN 2019stc and SN 2021lvy), or that have more than two peaks, and the model is thus not generic enough to explain the full double peaked sample of SESNe.

### **Magnetar**

The magnetar model has become popular for long-lived transients where the Arnett model yields unphysical  $^{56}\text{Ni}$  masses, and is often invoked for peculiar SESNe (like SN 2005bf; Maeda et al. 2007), luminous SNe (Gomez et al. 2022) and superluminous supernovae SLSNe, e.g., Chen et al. 2023b. The model offers a lot of flexibility in terms of rise times, peak luminosities, and duration—but does not naturally allow for double-peaked light curves or undulations. Chugai et al. (2022) opposed the CSM-interaction scenario for the second peak of the luminous SN 2019stc as put forth in Gomez et al. (2021), and instead suggested a magnetar engine by invoking a less-understood dipole-field enhancement to allow for the second peak. Other similar suggestions, like magnetar flare activity, have been

proposed in the context of wiggly light curves of SLSNe (Dong et al. 2023; Zhu et al. 2024), and Moriya et al. (2022) suggested that variations in the thermal energy injection from magnetar spin-down cause the light-curve bumps. However, Chugai et al. (2022) only explains a single bump and does not identify any specific smoking-gun observables that could support the model. Moriya et al. (2022), on the other hand, predicts an increase in photospheric temperature coincident with the bumps and notes that SN 2019stc does not show such an increase. The only supernova in our sample that shows an increase in photospheric temperature for the second peak is SN 2021uvy, and therefore, could be an example of the magnetar thermal energy injection scenario. However, our temperature measurements only use *gri* bands, but UV data is required for a more accurate temperature estimate, and thus, this observation of temperature rise is tentative. The temperature rise in SN 2021uvy also appears to last throughout the entire duration of the second peak, implying that the increase in thermal energy injection would also need to be maintained for  $>100$  days.

## CSM

While some double-peaked SESNe have shown strong signs of interaction after the first peak that completely transform their spectra—for example, hydrogen-rich CSM interaction in SNe 2018ijp (Tartaglia et al. 2021) and 2019oys (Sollerman et al. 2020); others have shown much more subtle but revealing signs of CSM interaction. One example of such a case is SN 2022xxf (Kuncarayakti et al. 2023), where the evidence for CSM interaction became obvious only at later times when narrow emission lines became more apparent in the optical spectra. The CSM must, in this case, be poor in both hydrogen and helium, which makes the configuration highly unusual (a detached CSM model was suggested for SN 2022xxf by Takei et al. 2024). The analytical modeling by Chiba et al. (2024) explicitly mentions the possibility of modeling both of the peaks in the light curves of SNe 2005bf and 2022xxf using a flat density profile for the CSM. However, the model comes with the caveat that the duration between the two peaks ( $\Delta t^{21}$ ) can be at most  $\lesssim 100$  days, otherwise, the ejecta mass requirements become unphysical. Another caveat is that if the two peaks are too temporally separated (large  $\Delta t^{21}$ ), the breakout luminosity (first peak) cannot be comparable to the luminosity of the second peak and thus the model has difficulty in explaining cases where first peak is brighter than the second peak (e.g., SN 2019stc). Khatami et al. (2024) explore different theoretical scenarios enabling a large variety of light curves from the CSM interaction powering

only, including double-peaked light curves which in their modeling occur when the shock breaks out just outside the CSM edge (so that there is no continued interaction phase, see Khatami et al. 2024, their fig. 3) and the CSM is “heavy” (CSM mass  $\gtrsim$  ejecta mass, making the shock cooling phase more prominent). However, spectral signatures of such heavy CSM might be difficult to hide, thus making this scenario less likely for SESNe without any narrow line signatures. In the case of SN 2023aew (Kangas et al. 2024; Sharma et al. 2024), the  $H\alpha$  P-Cygni feature seen during the first peak vanished at the time of the second peak and appeared again at later times, and the nebular lines showed a “horned” structure. These features, combined with the double-peaked light curve with large  $\Delta t^{21}$ , could be evidence that an aspherical or clumpy CSM powers the second peak of the supernova along with radioactive nickel decay, with the first peak being an eruptive precursor. SN 2023plg (Sharma et al. 2024) follows the light-curve behavior of SN 2023aew, and its second peak spectra share strong similarities with SN 2023aew’s second peak spectra (Sharma et al. 2024, their fig. 10), and could share the same powering mechanism.

### **Accretion**

Another potential powering mechanism is accretion onto a compact object, where an accretion disk might form and efficiently convert energy to radiation. SN 2022jli (Chen et al. 2024)—the double-peaked SESN showing periodic undulations in its light curve during the second decline, was potentially powered by such a scenario. Chen et al. 2024 advocated that the first peak might have been powered by a normal radioactive decay, whereas the second peak would be powered by mass accretion from the companion onto the newly formed compact object remnant. The second peak of this supernova was instead suggested to be powered by a magnetar (§4.4) by Cartier et al. 2024. In general, the different powering scenarios mentioned in these sections have been combined in a variety of different ways to explain double-peaked SESNe.

### **Pulsational Pair Instability mechanism**

Finally, we mention the suggestion put forward by Angus et al. 2024 for SN 2020acct, that the double-peaked light curve could have been powered by CSM interaction with a configuration from a pulsational pair instability supernova (PPISN; Barkat et al. 1967; Rakavy et al. 1967). PPI events cause extreme mass loss, and thus their ejecta CSM interactions can be quite luminous. The timing of the different events can

vary depending on the specific evolution of the system and therefore provide models that can fit multiple well-separated peaks, explain precursors, and also bumpy light curves (Woosley 2017; Leung et al. 2019). However, clear identification of PPISNe is difficult as other powering mechanisms (and their combinations) could also fit the observations of peculiar multi-peaked SNe, and the surrounding CSM could also come from various mass-loss mechanisms (LBV eruptions, winds, etc.). The unique properties of SN 2020acct—hydrogen-poor interaction signatures during the first peak and a second peak showing terminal explosion SESN-like properties, together with an unfeasible nickel fraction ( $f_{Ni} \sim 0.91$ ) from fitting radioactive decay power to the second peak, made it a possible PPISN candidate (Angus et al. 2024).

#### 4.5 Summary

In this paper, we have presented optical photometry and spectroscopy of two double-peaked stripped envelope supernovae discovered by the Zwicky Transient Facility. We discuss the comprehensive dataset in conjunction with a sample of previously reported, clearly double-peaked stripped-envelope supernovae from the ZTF archive, and for several of these, we also provide previously unpublished data. With data from one homogeneous survey, we can quantify some of the key properties of the double-peaked light curves, analyze correlations between these properties, and contextualize them with some of the common powering mechanisms that we review from the literature.

SN 2021uvy is a luminous and slowly evolving Type Ib supernova with both peaks reaching roughly the same brightness. Although it shows many similarities to SN 2019stc, with both having their first peaks fitting a combination of radioactive nickel power and magnetar central engine input, their second peaks diverge significantly in behavior. SN 2021uvy shows a lack of color evolution during the second decline and a rise in photospheric temperature, which is a prediction in the case of variable thermal energy injection from magnetar spin-down (Moriya et al. 2022).

SN 2022hgk, on the other hand, is an average-luminosity Type Ib supernova with a much brighter second peak. Its light curve is very similar to the light curve of SN 2019cad, which is considered an analog of SN 2005bf (and also to PTF11mnb). The spectra of SN 2022hgk, however, show a significant similarity with those of SN 2005bf (strong helium absorption features) rather than with those of SN 2019cad. Overall, these four supernovae (SNe 2005bf, PTF11mnb, 2019cad, and 2022hgk) have similar light-curve parameters and form a tight group in the phase space of

absolute peak magnitudes of the second peak vs. that of the first peak and in the magnitude difference between the peaks vs. the duration between the peaks. The double-nickel distribution powering mechanism might well fit this group of supernovae (see e.g., Orellana et al. 2022).

With a sample of double-peaked SESNe coming together (being  $\sim 2.5\%$  of all Type Ibc SNe), it becomes clear that this is a phenomenon that requires a more holistic approach. There have been good arguments in the literature as to why some of these events should not be just random alignments of two distinct SNe, or even two separate stars exploding in a binary system, and with the expanding sample, such probability estimates gain more weight. At the same time, fine-tuned models to explain individual and very rare systems become less probable once it is realized that more of these systems exist. Upcoming facilities like the Rubin Observatory will increase the sample size of double-peaked and multi-peaked SESNe and also provide more light curve properties to help uncover their powering mechanisms with the depth of the Legacy Survey of Space and Time (LSST; Ivezić et al. 2019).

#### **4.6 Acknowledgement**

Based on observations obtained with the Samuel Oschin Telescope 48-inch and the 60-inch Telescope at the Palomar Observatory as part of the Zwicky Transient Facility project. ZTF is supported by the National Science Foundation under Grants No. AST-1440341 and AST-2034437 and a collaboration including current partners Caltech, IPAC, the Weizmann Institute of Science, the Oskar Klein Center at Stockholm University, the University of Maryland, Deutsches Elektronen-Synchrotron and Humboldt University, the TANGO Consortium of Taiwan, the University of Wisconsin at Milwaukee, Trinity College Dublin, Lawrence Livermore National Laboratories, IN2P3, University of Warwick, Ruhr University Bochum, Northwestern University and former partners the University of Washington, Los Alamos National Laboratories, and Lawrence Berkeley National Laboratories. Operations are conducted by COO, IPAC, and UW. The ZTF forced-photometry service was funded under the Heising-Simons Foundation grant #12540303 (PI: Graham). This work was supported by the GROWTH project (Kasliwal et al. 2019) funded by the National Science Foundation under PIRE Grant No 1545949. The Oskar Klein Centre was funded by the Swedish Research Council. Partially based on observations made with the Nordic Optical Telescope, operated by the Nordic Optical Telescope Scientific Association at the Observatorio del Roque de los Muchachos, La Palma, Spain, of the Instituto de Astrofísica de Canarias. Some of the data presented here

were obtained with ALFOSC, which is provided by the Instituto de Astrofísica de Andalucía (IAA) under a joint agreement with the University of Copenhagen and NOT. Some of the data presented herein were obtained at the W. M. Keck Observatory, which is operated as a scientific partnership among the California Institute of Technology, the University of California, and NASA; the observatory was made possible by the generous financial support of the W. M. Keck Foundation. The SED Machine is based upon work supported by the National Science Foundation under Grant No. 1106171. This work has made use of data from the Asteroid Terrestrial-impact Last Alert System (ATLAS) project. The Asteroid Terrestrial-impact Last Alert System (ATLAS) project is primarily funded to search for near earth asteroids through NASA grants NN12AR55G, 80NSSC18K0284, and 80NSSC18K1575; byproducts of the NEO search include images and catalogs from the survey area. The ATLAS science products have been made possible through the contributions of the University of Hawaii Institute for Astronomy, the Queen's University Belfast, the Space Telescope Science Institute, the South African Astronomical Observatory, and The Millennium Institute of Astrophysics (MAS), Chile. This research has made use of the NASA/IPAC Infrared Science Archive, which is funded by the National Aeronautics and Space Administration and operated by the California Institute of Technology. The Liverpool Telescope is operated on the island of La Palma by Liverpool John Moores University in the Spanish Observatorio del Roque de los Muchachos of the Instituto de Astrofísica de Canarias with financial support from the UK Science and Technology Facilities Council.

Y. Sharma thanks the LSSTC Data Science Fellowship Program, which is funded by LSSTC, NSF Cybertraining Grant #1829740, the Brinson Foundation, and the Moore Foundation; her participation in the program has benefited this work.

M.W.C. acknowledges support from the National Science Foundation with grant numbers PHY-2308862 and PHY-2117997.

Fritz (Walt et al. 2019; Coughlin et al. 2023) and GROWTH marshal (Kasliwal et al. 2019) (dynamic collaborative platforms for time-domain astronomy) were used in this work.

#### 4.7 Appendix A: Photometry Data

Table 4.4: Log of optical photometry of SN 2021uvy and SN 2022hgk of  $>5\sigma$  significance (full table available online).

IAU Name	MJD	Filter	Telescope	Brightness (mag)
SN 2021uvy	59401.44	<i>r</i>	P48:ZTF	$20.85 \pm 0.24$
...				
SN 2022hgk	59672.32	<i>g</i>	P48:ZTF	$21.58 \pm 0.22$
...				

Table 4.5: Log of UVOT observations of SN 2022hgk of  $>3\sigma$  significance (full table available online).

MJD	Filter	Brightness (mag)
59720.72	uvw2	$19.677 \pm 0.075$
...		

#### 4.8 Appendix B: Spectroscopy Data

Table 4.6: Summary of optical spectra of SNe 2021uvy, 2022hgk, and 2020acct. We report phases (in rest-frame days) calculated with respect to both the first peak of the light curve and the estimated explosion epoch (inside parentheses).

IAU Name	MJD	Phase (day)	Telescope /Instrument	Exposure (s)	IAU Name	MJD	Phase (day)	Telescope /Instrument	Exposure (s)
SN 2020acct	59195	-1 (1)	P60/SEDM	2700	SN 2022hgk	59708	17 (33)	LT/SPRAT	600
	59253	55 (58)	P200/DBSP	450		59709	18 (34)	P60/SEDM	2700
	59254	56 (59)	P60/SEDM	2700		59710	19 (35)	NOT/ALFOSC	3600
	59255	57 (60)	NOT/ALFOSC	1350		59713	22 (38)	P60/SEDM	2700
	59256	58 (61)	P60/SEDM	2700		59718	27 (43)	P60/SEDM	2700
	59260	62 (65)	NOT/ALFOSC	900		59719	28 (44)	P60/SEDM	2700
	59260	62 (65)	P60/SEDM	2700		59721	30 (46)	NOT/ALFOSC	1800
	59263	64 (67)	Keck1/LRIS	1275		59722	31 (47)	P200/DBSP	1200
	59277	78 (81)	NOT/ALFOSC	1800		59730	39 (55)	P60/SEDM	2700
	59311	112 (114)	Keck1/LRIS	2312		59732	40 (56)	NOT/ALFOSC	2400
59350	149 (152)	Keck1/LRIS	2705	59734	43 (59)	P60/SEDM	2700		
SN 2021pkd	59386	-7 (12)	P60/SEDM	2700	59738	46 (62)	P200/DBSP	1500	
	59389	-4 (15)	P60/SEDM	2700	59739	47 (63)	P200/DBSP	900	
	59391	-3 (17)	P60/SEDM	2700	59788	95 (111)	Keck1/LRIS	900	
	59401	7 (26)	Keck1/LRIS	300	SN 2023plg	60242	70 (70)	P60/SEDM	2700
SN 2021uvy	59439	-15 (38)	NTT/EFOSC2	900		60246	74 (74)	LT/SPRAT	750
	59442	-12 (40)	P60/SEDM	2700		60246	74 (74)	P60/SEDM	2160
	59454	-1 (51)	P60/SEDM	2700		60249	77 (77)	P60/SEDM	2160
	59455	0 (52)	LT/SPRAT	750		60254	82 (82)	P60/SEDM	2160
	59458	2 (55)	P200/DBSP	600		60256	84 (84)	Keck1/LRIS	300
	59467	10 (62)	Keck1/LRIS	600		60259	87 (87)	P60/SEDM	2160
	59467	11 (63)	P60/SEDM	2700		60269	97 (97)	P60/SEDM	2700
	59470	13 (66)	P200/DBSP	900		60274	102 (102)	P60/SEDM	2700
	59491	33 (85)	Keck1/LRIS	600		60275	102 (102)	NOT/ALFOSC	2400
	59498	39 (91)	P60/SEDM	2700		60280	107 (107)	P60/SEDM	2760
59502	43 (95)	P60/SEDM	2700	60281		108 (108)	P60/SEDM	2760	
59509	49 (101)	P60/SEDM	2700	60281		108 (108)	P200/DBSP	1200	
59517	57 (109)	P60/SEDM	2700	60282		109 (109)	P60/SEDM	3624	
59524	63 (115)	P200/DBSP	900	60283	110 (110)	P60/SEDM	396		
59536	74 (126)	P60/SEDM	2700	60285	112 (112)	P60/SEDM	2700		
59547	84 (136)	P60/SEDM	2700	60285	112 (112)	P60/SEDM	3840		
59561	97 (149)	P60/SEDM	2700	60286	113 (113)	NOT/ALFOSC	2400		
59585	118 (171)	P60/SEDM	2700	60288	115 (115)	P60/SEDM	2700		
59587	120 (172)	NOT/ALFOSC	2700	60296	123 (123)	P60/SEDM	2700		
59600	132 (185)	P60/SEDM	2700	60299	126 (126)	NOT/ALFOSC	1200		
59615	146 (198)	Keck1/LRIS	300	60321	147 (147)	NOT/ALFOSC	2400		
59815	328 (380)	Keck1/LRIS	1800						
59875	384 (436)	Keck1/LRIS	2700						

*Chapter 5*COMMISSIONING THE SPECTRAL ENERGY DISTRIBUTION  
MACHINE AT KITT PEAK 2.1-M TELESCOPE

Yashvi Sharma<sup>1</sup>, S. R. Kulkarni<sup>1</sup>, Michael W. Coughlin<sup>2</sup>, James D. Neill<sup>3</sup>, Daniel L. McKenna<sup>3</sup>, Lauren Fahey<sup>3</sup>, Michael Feeney<sup>3</sup>, Jason Fucik<sup>3</sup>, Larry Lingvay<sup>3</sup>, Reed R. Riddle<sup>3</sup>, Saarah Hall<sup>4</sup>, Mitchell Karmen<sup>5</sup>, Alexander Criswell<sup>2</sup>, Brendan King<sup>2</sup>, Cristina Andrade<sup>2</sup>, Benjamin Roulston<sup>6</sup>, Adam A. Miller<sup>4</sup>, Suvi Gezari<sup>5,7</sup>, S. Bradley Cenko<sup>8,9</sup>

<sup>1</sup>Division of Physics, Mathematics and Astronomy, California Institute of Technology, Pasadena, CA, 91125, USA

<sup>2</sup>School of Physics and Astronomy, University of Minnesota, Minneapolis, MN 55455, USA

<sup>3</sup>Caltech Optical Observatories, California Institute of Technology, Pasadena, CA 91125, USA

<sup>4</sup>Center for Interdisciplinary Exploration and Research in Astrophysics (CIERA), Northwestern University, 1800 Sherman Ave., Evanston, IL 60201, USA

<sup>5</sup>Department of Physics and Astronomy, Johns Hopkins University, 3400 N. Charles Street, Baltimore, MD 21218, USA

<sup>6</sup>Coulter School of Engineering and Applied Sciences, Clarkson University, 8 Clarkson Ave, Potsdam, NY 13699, USA

<sup>7</sup>Space Telescope Science Institute, Baltimore, MD 21218, USA

<sup>8</sup>Astrophysics Science Division, NASA Goddard Space Flight Center, Greenbelt, MD 20771, USA

<sup>9</sup>Joint Space-Science Institute, University of Maryland, College Park, MD 20742, USA

**Abstract**

The discovery of optical transients is at an all-time high because of the current time domain surveys and will be unprecedented once the Vera C. Rubin Observatory is operational. However, discovery does not mean confirmation of the transient, for which spectroscopic data is required. As spectroscopic resources are limited, there is a severe “follow-up drought” in the classification completeness, limiting the depth to which systematic samples can be collected. This problem has been tackled for bright transients by the Spectral Energy Distribution Machine (SEDM) on the Palomar 60-inch telescope and other dedicated classification efforts, with the SEDM being the top classifier on the Transient Name Server (TNS). Here we present SEDM-KP, an upgraded version of SEDM mounted on the Kitt Peak 2.1-m telescope. The ultra-low spectral resolution ( $R \sim 100$ ) IFU spectrograph channel is combined with an EMCCD guide camera capable of fast-cadenced imaging in

Sloan *ugriz* bands. The telescope and instrument robotic operations are optimized for observing efficiency and include completely automated data reduction pipelines. SEDM-KP spectrograph has an efficiency of  $\sim 40\%$  in the redder wavelengths, which is over  $\sim 2\times$  that of SEDM, and has better efficiency than SEDM over the whole wavelength range. Its imaging capabilities are on par with the Kitt Peak EMCCD Demonstrator (KPED), reaching a depth of  $\sim 23$  magnitude in *r* band in a 300-s exposure for single-frame observations, and achieving  $> 1$  Hz frame rates for rapid read-out mode observations. SEDM-KP will be used for spectroscopic classification, follow-up imaging of rare and fast transients, and rapid imaging of periodic sources discovered by ZTF and the Rubin Observatory.

## 5.1 Introduction

Time-domain astronomy (TDA) is undergoing a big-data revolution. Current all-sky optical surveys (like the Zwicky Transient Facility, a.k.a. ZTF) are already discovering transients by the thousands (Bellm et al. 2019; Graham et al. 2019; Dekany et al. 2020; Tonry et al. 2018; Shappee et al. 2014; Chambers et al. 2016). With the upcoming Vera C. Rubin observatory equipped with a  $10\text{-deg}^2$  field-of-view camera capable of reaching deep limiting magnitudes (i.e.,  $r = 24.7$  mag) in just 30 s and its dynamic all-sky survey—the Legacy Survey of Space and Time (LSST), the field is at the precipice of an explosion in the number of transients (Ivezić et al. 2019). With ZTF’s fast cadence and LSST’s depth, probes on the hour-to-day timescale for faint transients will be possible. However, discovery does not mean identification, and identification does not mean understanding. Some of these explosive events can be observed across the electromagnetic spectrum as well as through their gravitational waves (GW; Abbott et al. 2017) and neutrino emission (Stein et al. 2021). Thus, multiwavelength and multimessenger classification and characterization are necessary for maximizing science in this TDA era.

A quick initial classification of the discovered transients is essential to determine whether follow-up by larger telescopes (a scarce resource) is warranted. Some of the interesting transient classes fade on fast timescales (Andreoni et al. 2021) like gamma-ray burst (GRB) afterglows (van Paradijs et al. 2000; Cenko et al. 2013; Ho et al. 2020), fast blue optical transients (FBOT; Ho et al. 2019; Ho et al. 2023), and electromagnetic counterparts of gravitational wave sources (EMGW; Abbott et al. 2017; Kasliwal et al. 2017), which makes fast-turnaround follow-up of their candidates necessary. Supernovae (SN) that last for their typical timescales (a couple of months) could also benefit from early spectroscopic follow-up as some SN types

show early signatures of interaction (Miller et al. 2020a; Bruch et al. 2023) and multiple peaks (Kuncarayakti et al. 2023; Das et al. 2024; Sharma et al. 2024). Classifying large systematically collected samples to a high degree of spectroscopic completeness (Fremling et al. 2020) also allows for the discovery of rare transients (Gal-Yam et al. 2021; Perley et al. 2022b; Kool et al. 2022; Goobar et al. 2023; Chen et al. 2024), putting constraints on the observable rates of a variety of transients (Perley et al. 2020; Chen et al. 2023b; De et al. 2020b; Sharma et al. 2023), and creates large datasets for training machine/deep learning models (Fremling et al. 2021; Sharma et al. 2025).

ZTF’s workhorse classification instrument—the Spectral Energy Distribution Machine (SEDM; Ben-Ami et al. 2012; Blagorodnova et al. 2018) is a fully robotic ultra-low spectral resolution ( $R \sim 100$ ) spectrograph optimized for supernova classification and has been efficiently doing its job since 2018. It is the top classifier on the Transient Name Server (TNS) and has classified more than twice the number of transients than the next best instrument (Kulkarni 2020). SEDM has exemplified the power of dedicated classification instruments on 1–2 m class telescopes towards removing the follow-up bottleneck. This chapter presents the successfully commissioned SEDM-KP—an ultra-low resolution integral-field unit spectrograph with a fast framing imaging camera on a 2-m class robotic telescope. The system has a large field-of-view and is equipped with an Electron Multiplying CCD (EMCCD), whose exquisite cadenced (seconds) imaging is optimally suited for variable star and near-Earth asteroid science. The facility will be dedicated to classifying transients, vetting variable stars, and re-acquisition of near-earth asteroids. The proposed program will benefit not only the research groups part of the team (University of Minnesota, Northwestern University, Space Telescope Science Institute, University of Maryland / Goddard Space Flight Center, Caltech) but also the global astronomical community via public classifications as part of its core program.

The chapter is organized as follows. In §5.2, we provide an overview of the instrument; in §5.3, we describe the robotic operations code and the nightly observing routine; in §5.4, we detail the photometric and spectroscopic data reduction pipelines; in §5.5, we discuss the performance of the telescope and the instrument. We summarize the results and discuss future work in §5.6.

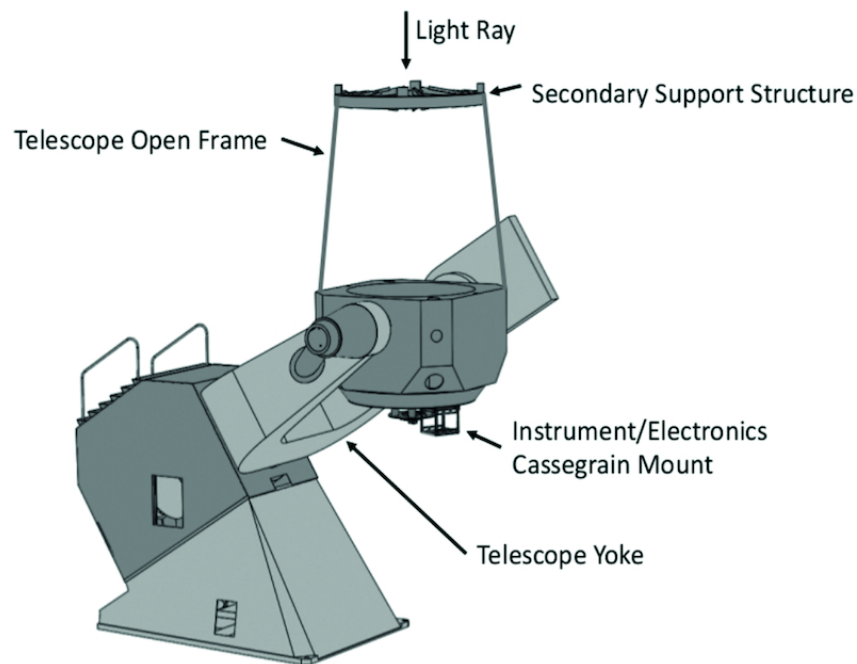


Figure 5.1: A schematic of the KP84 telescope showing where the instrument and electronics are mounted. *Image Credit:* Coughlin et al. (2019).

## 5.2 Instrument overview

The Kitt Peak 84-inch (2.1-m) telescope (henceforth KP84) has a Ritchey-Chrétien design with the instrument mounted at the Cassegrain focus ( $f/7.6$ ). Figure 5.1 shows a schematic of the telescope. A central obscuration of 34-inch diameter from the secondary results in the total collecting area being  $\sim 29,800 \text{ cm}^2$ , a factor of two more than P60. Figure 5.2 shows SEDM-KP mounted on the telescope. The standoff mount structure for SEDM-KP is mounted on the primary cell and 235.7 mm in height, and provides a rigid mounting surface for the instrument. The telescope focus position is 160.03 mm inside the instrument from the bottom face of the mounting plate that attaches the instrument to the standoff structure ( $\approx 0.4$  m from the primary cell). The adjacent electronics rack houses the control computer, power units, cables, and network power switch. Unlike SEDM, which has the guide camera sticking out of the spectrograph plane in a T-shape, SEDM-KP is designed to have both cameras in the same plane inside a sealed container, resulting in a more compact design ( $40 \times 31.5 \times 11.5$  in.) and reduced dust contamination<sup>1</sup>. The instrument, mounting plate, and standoff structure together weigh  $\sim 253$  kg, and the electronics rack  $\sim 44$  kg.

<sup>1</sup>No ash or dust was found inside the instrument after inspection post-2022 Contreras wildfire.

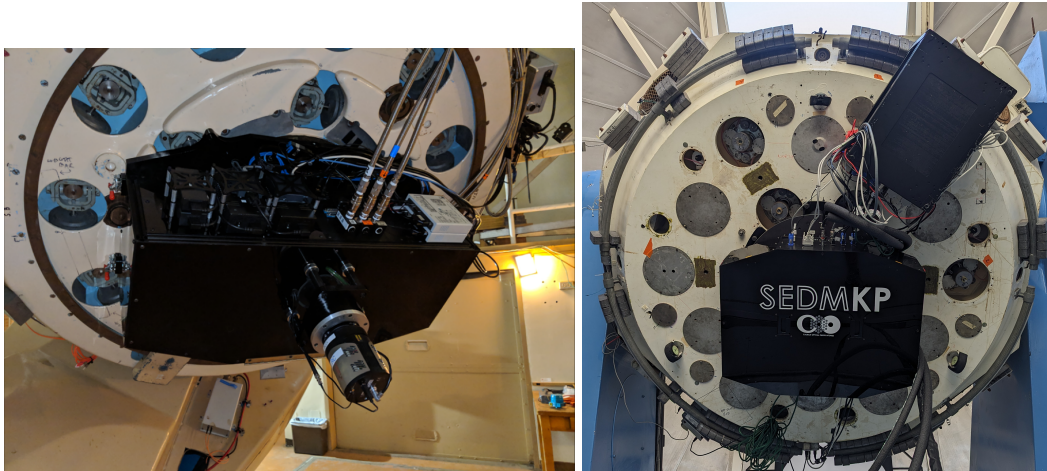


Figure 5.2: *Left:* A picture of SEDM on the Palomar 60-inch telescope. *Right:* A picture of SEDM-KP on the Kitt Peak 84-inch telescope. Note that the imaging/guide camera in SEDM is located out of the plane of the instrument, but in SEDM-KP is located inside the instrument in the same plane.

Figure 5.3 shows a schematic of the SEDM-KP instrument. Light enters the instrument through a small covered window of 2.53 in. radius. A central circular field-of-view (FoV) is picked off and sent to the spectrograph (IFU) channel while the rest goes to the imaging (EMCCD) channel, resulting in a central shadow of  $\sim 1'$  radius in the EMCCD images (see Figure 5.8).

The imaging channel beam is reflected through a fold mirror to the relay optics, which then goes through the filter wheel and is imaged on the EMCCD. The Finger Lakes Instruments (FLI) filter wheel is equipped with Sloan  $u$ ,  $g$ ,  $r$ ,  $i$ , and  $z$  filters, a clear filter, and a dark filter. In the IFU channel, the light beam goes through an expander lens that scales the 2.36 mm field width to 20 mm for the micro-lens array (MLA). The beam is then folded and sent to the MLA, which splits the field into smaller hexagonal pupil images of a corner-to-corner size of  $0.72''$  (a.k.a. spatial pixel or spaxel, see Figure 5.4). The light then goes through a collimator and onto a spectral triple-prism. As is the case for SEDM, the triple-prism ensures a constant resolution  $R \sim 100$  throughout the wavelength range of 330 nm to 1000 nm (see Figure 5.5). The dispersed micro-pupil beams go through CCD optics assembly and are imaged on the IFU camera. The dispersion length of the traces imaged on the CCD is  $\sim 300$  pix. The FoV of the imaging camera (EMCCD) is  $6' \times 6'$ , and the FoV of the IFU CCD is  $25'' \times 25''$ .

Both the IFU CCD and the EMCCD are mounted on linear motion stages manufac-

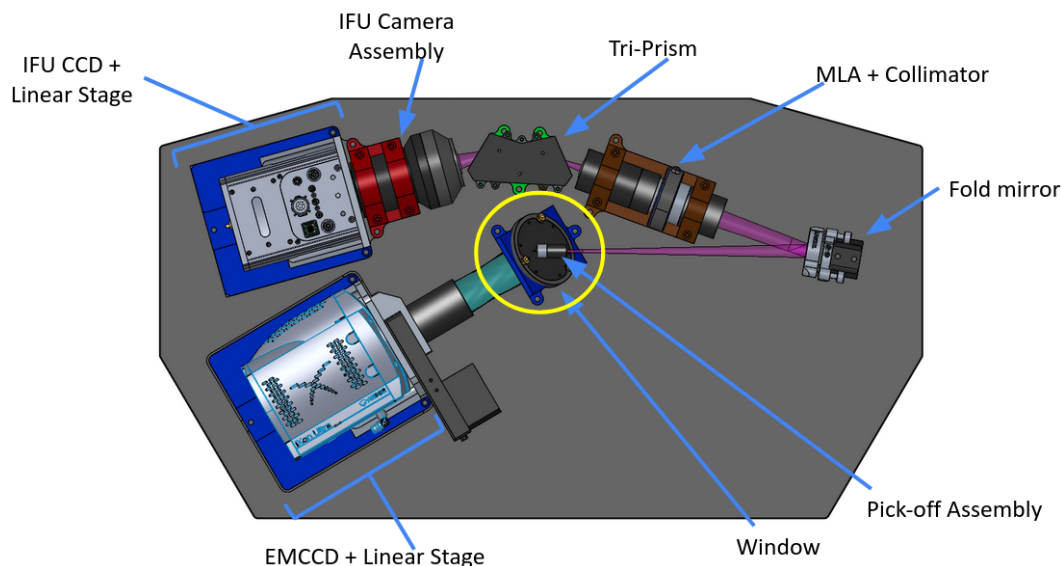


Figure 5.3: A schematic of the SEDM-KP design, showing the spectrograph channel and the imaging channel components. The light window is located under the pick-off assembly (inside the yellow circle). *Image Credit:* Lauren Fahey (Caltech Optical Observatories).

tured by Newport; the IFU stage is moved to focus the dispersed traces, while the EMCCD stage is moved to adjust focus in different filters. The secondary mirror is moved to focus point sources on the focal plane. To make the IFU and EMCCD channels parfocal, we pointed to a bright star, focused the star in the IFU CCD by measuring the full-width at half-maximum (FWHM) of the bright star in the IFU CCD as a function of the secondary mirror focus, set the secondary mirror position at the obtained best focus position, and then focused the field in the EMCCD for different filters by moving the EMCCD linear motion stage.

The IFU CCD is an Andor iKon-L-936 camera with  $2048 \times 2048$  pixels,  $13.5 \mu\text{m}$  pixel size, and a read noise of  $\sim 6e^-$  at 1 MHz read-out speed (which is our standard operating mode for this CCD). The EMCCD is an Andor iXon Ultra 888 camera with  $1024 \times 1024$  pixels,  $13.5 \mu\text{m}$  pixel size, read noise of  $\sim 6e^-$  in the conventional CCD (a.k.a. single-frame) mode, and read noise of  $< 1e^-$  with electron multiplication in the EMCCD (a.k.a. rapid read-out) mode. Both cameras can be thermo-electrically cooled and can easily reach  $-75^\circ\text{C}$  with the help of a chiller. The IFU CCD has a dark current of  $\sim 0.02 e^-/\text{pix}/\text{sec}$ , and the EMCCD has a dark current of  $\sim 0.0002 e^-/\text{pix}/\text{sec}$  at this temperature. A list of specifications for both CCDs can be found in Table 5.1.

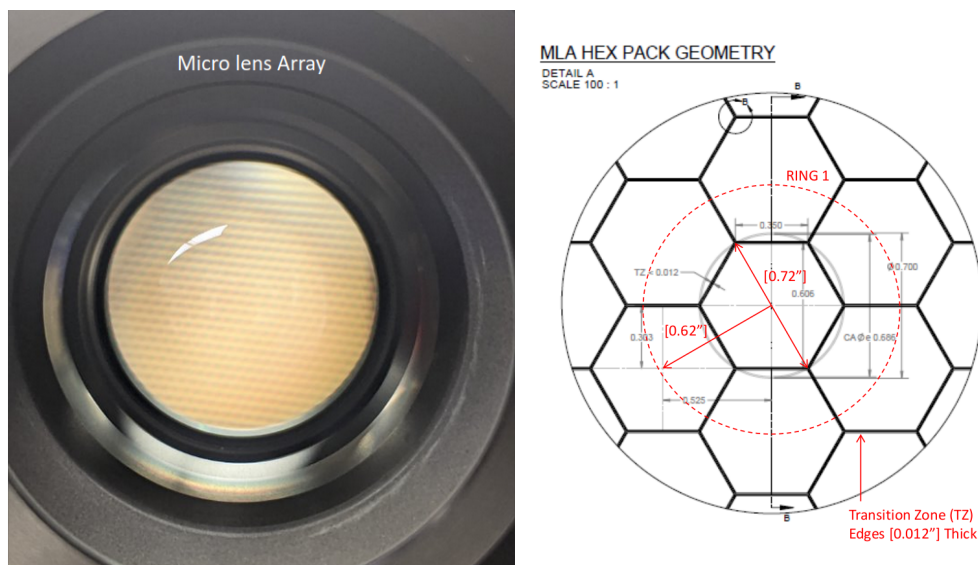


Figure 5.4: *Left:* A picture of the multi-lenslet array. *Right:* The geometry of the hexagonal micro-pupil images on the IFU CCD plane. Each micro-pupil image is 0.72" across, with 0.62" distance between centers of adjacent hexagons. *Image Credit:* Jason Fucik (Caltech Optical Observatories).

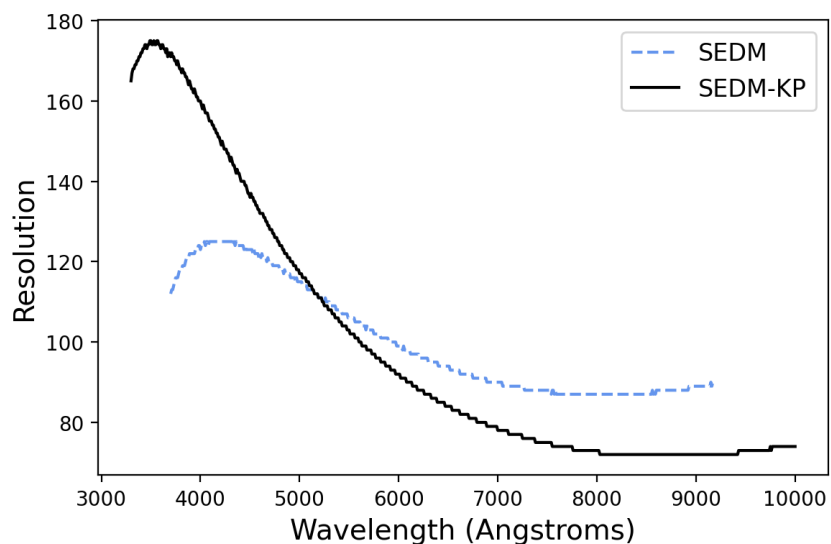


Figure 5.5: Comparison of the simulated resolutions as a function of wavelength for SEDM (blue) and SEDM-KP (black). SEDM-KP has a higher than SEDM resolution for  $\lambda \lesssim 5000 \text{ \AA}$  and lower than SEDM resolution for  $\lambda \gtrsim 5000 \text{ \AA}$ . Simulated data generated by Jason Fucik (Caltech Optical Observatories).

Table 5.1: Specifications of the EMCCD and the IFU CCD.

Parameter	EMCCD Specification	IFU Specification
Camera	iXon Ultra 888	iKon 1-936
Active pixels	$1024 \times 1024$	$2048 \times 2048$
Pixel size	$13.5 \mu\text{m}$	$13.5 \mu\text{m}$
Digitization	16-bit	16-bit
Read-out rate	1, 0.1 MHz (Conv. mode) 30, 20, 10, 1 MHz (EM mode)	5, 3, 1, 0.05 MHz
Dark current ( $-75^\circ\text{C}$ )	$\sim 0.0002 e^-/\text{pix}/\text{sec}$	$\sim 0.02 e^-/\text{pix}/\text{sec}$
Read noise	$\sim 6e^-$ (Conv. mode, 1 MHz) $< 1e^-$ (with EM gain)	$\sim 6e^-$ (1 MHz) $\sim 3e^-$ (0.05 MHz)
FoV	$6' \times 6'$	$25'' \times 25''$

Also, for calibration, there are three arc lamps (Xenon, Mercury, and Cadmium) mounted on the side of the secondary ring of the telescope for the purpose of wavelength calibration, and several white light lamps mounted on the front of the secondary ring for taking dome flat images.

### 5.3 Operations

#### Robotic operations software (ROS)

The control software for SEDM-KP (henceforth ROS) is derived from the control software of Robo-AO (Riddle et al. 2012; Jensen-Clem et al. 2018), KPED (Coughlin et al. 2019), and ZTF (Dekany et al. 2020), with added functionalities for the spectrograph channel, and is written in *C++*. ROS contains control modules for components of the telescope and instrument system (telescope, weather, cameras, filter wheel, linear motion stages, power, data, target queue) that interface with the respective hardware. The telescope and weather modules interface with the existing KP 2.1-m telescope control software (TCS), which controls the telescope, the dome, and reads weather station data. The camera module has code that uses the Andor Software Development Kit (SDK), the filter wheel module uses FLI's SDK, and the motion stage control module uses Newport's SDK. The power module interacts with the network power switch and controls the power to all instrument components, as well as the calibration lamps and the chiller. The data modules manage the images read out by the cameras and save them as FITS files, put the appropriate headers containing all the relevant image information in the FITS files, and manage the syncing of collected data to the analysis and storage computer. The queue module handles querying the target queue made by the Fritz (Walt et al. 2019; Coughlin

et al. 2023) scheduler and updating the status of observations. Finally, the robot module calls all of the subsystems to execute the nightly observing routine. The telemetry from the several subsystems of ROS is constantly updated in real time and displayed on a monitoring webpage. All user-controlled parameters are placed in configuration files and can be updated while ROS is running if needed. ROS also has an error manager module to detect and resolve known errors during operations so that the system runs smoothly without intervention.

### **Nightly observing routine**

During the afternoon, ROS creates a backup of and syncs the logs and data from the previous night to the analysis computer. The night start and end (or science start and end) times are configurable parameters controlled by the altitude of the Sun (degrees below horizon) and set to  $-9^\circ$  (halfway between civil and nautical twilight). ROS activates 2 hours before the night start time and initializes all subsystems. Once the system is initialized, the calibration loop is executed, in which a set of standard calibration images defined in the configuration file (bias and dome flat images for both cameras, dark images for EMCCD in various modes, and arc lamp images for IFU CCD) are taken one after the other. Once the calibration routine is complete, the telescope is stowed to zenith, and the dome is opened to stabilize its inside temperature with the outside temperature.

When the night starts, ROS runs an autofocus routine to obtain the best focus position for the secondary. In the autofocus routine, several test images are taken on both sides of the initial guess for the best focus position (the number of test images and focus position step size are configurable parameters in the configuration file). Then, on each image, ROS runs SExtractor (Bertin et al. 1996) to identify the bright point sources (stars), measure their FWHMs, and obtain the median FWHM. This provides the median FWHMs at the tested focus positions. The median FWHM is expected to be a quadratic function of the focus position (see Figure 5.6, left). We fit a quadratic curve to this data and find the position corresponding to its minimum to get the best focus position. It is crucial to start with a good initial guess for the best focus position, otherwise, the routine fails to sample both sides of the quadratic curve and ends up extrapolating. The best focus position also has a linear dependence on the dome temperature and fluctuates across nights and sometimes even during the night. From multiple autofocus loops conducted over many nights, we estimated this temperature dependence (see Figure 5.6, right). ROS uses this knowledge to set the initial guess for the best focus position, making sure that the autofocus routine

does not fail.

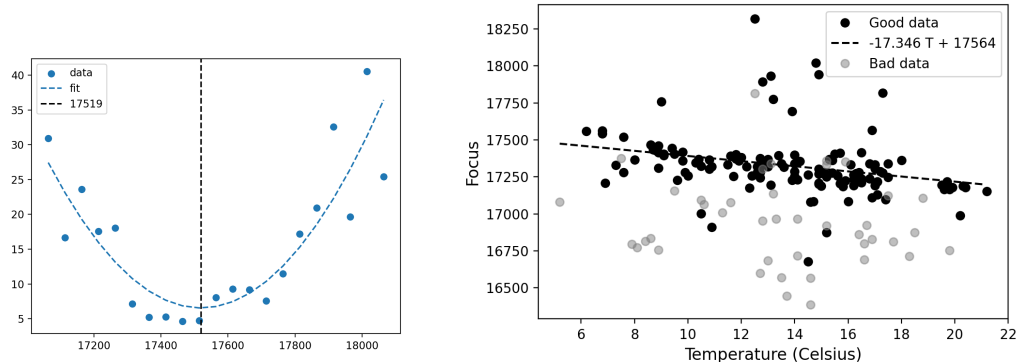


Figure 5.6: *Left:* Example of an autofocus loop routine showing the quadratic dependence of FWHM on telescope secondary focus position. *Right:* Plot showing best focus position as a function of dome temperature. The dark points are from good-quality quadratic fits on autofocus loops, gray points are from poor-quality quadratic fits (extrapolated, poor seeing, etc.). The linear relation is used to set the initial central position for autofocus loops.

After the autofocus routine, ROS begins queue observing by querying targets from the Fritz scheduler and observes them one after the other until the night ends. ROS executes the following steps for every queue target:

1. **Centering:** To get the target inside the field-of-view (at a designated location in the EMCCD FoV and the IFU CCD FoV for imaging and spectroscopy targets, respectively), ROS points to the requested target position, takes an image, solves the field using `Astrometry.net` (Lang et al. 2010), determines the coordinate offsets needed to center the target, and applies the offsets. This process is done iteratively up to 5 times and fails if ROS cannot get the target within  $5''$  of the designated position, which happens rarely.
2. **Science exposure and guiding:** Once the target is centered, ROS sets up the relevant observation parameters (filter, exposure time, exposure mode, FITS file name, etc.) and starts the science exposure. For spectroscopy targets, ROS also starts the guiding loop and sets up the EMCCD camera to take 1-s images in rapid read-out mode continuously while the IFU CCD exposure is in progress. Inside the guiding loop, ROS keeps track of the centroid positions of the detected stars in the guide images with respect to their centroid position in the first guide image and keeps calculating and applying the guiding offsets. We found the guide accuracy to be within  $\pm 0.2''$ .

3. Housekeeping: A few minutes before the exposure finishes, ROS queries for the next target from the scheduler to minimize overhead time. Once the science exposure is finished, ROS writes the image into a FITS file with all the necessary header information. It also sends the observation status (completed, failed, or skipped) to Fritz.

At the end of the night (science end time), ROS finishes up by taking any missing calibrations, shuts down the telescope and the instrument subsystems, and waits for the next night to begin.

### **Scheduler**

All of the follow-up requests for SEDM-KP are assigned through and handled by Fritz. Users submit the transient targets and provide the observation parameters for SEDM-KP requests through a form on the transient's Fritz source page. Then, using an API query, Fritz can be asked to generate a schedule for the night dynamically. Fritz employs the `astropplan` Python package to make this schedule that takes into account various constraints (e.g., telescope hour angle and altitude limits, minimum on-sky separation from the moon, and maximum airmass of the target).

To interface between Fritz and ROS, we developed two Python scripts that ROS can call to request the next queue target (`get_observation`) and mark the observation status of the current target (`observation_status`). The `get_observation` script queries the Fritz scheduler API endpoint, selects the first target in the schedule, checks that this target satisfies all constraints and will stay within the safe limits for the telescope during the exposure (if not it skips to the next target in the schedule), and saves the information of the target in a text file for ROS to read. This script also ensures that a spectroscopic standard star observation for the purpose of flux calibration is taken at the beginning and end of the night. The `observation_status` script receives the status of the current observation and posts it to Fritz via its API service. We also developed another housekeeping Python script that runs every morning and resets the Fritz status of follow-up requests marked as skipped or failed during the previous night; this way, users only have to reset their requests when the observation window of the assigned requests has passed.

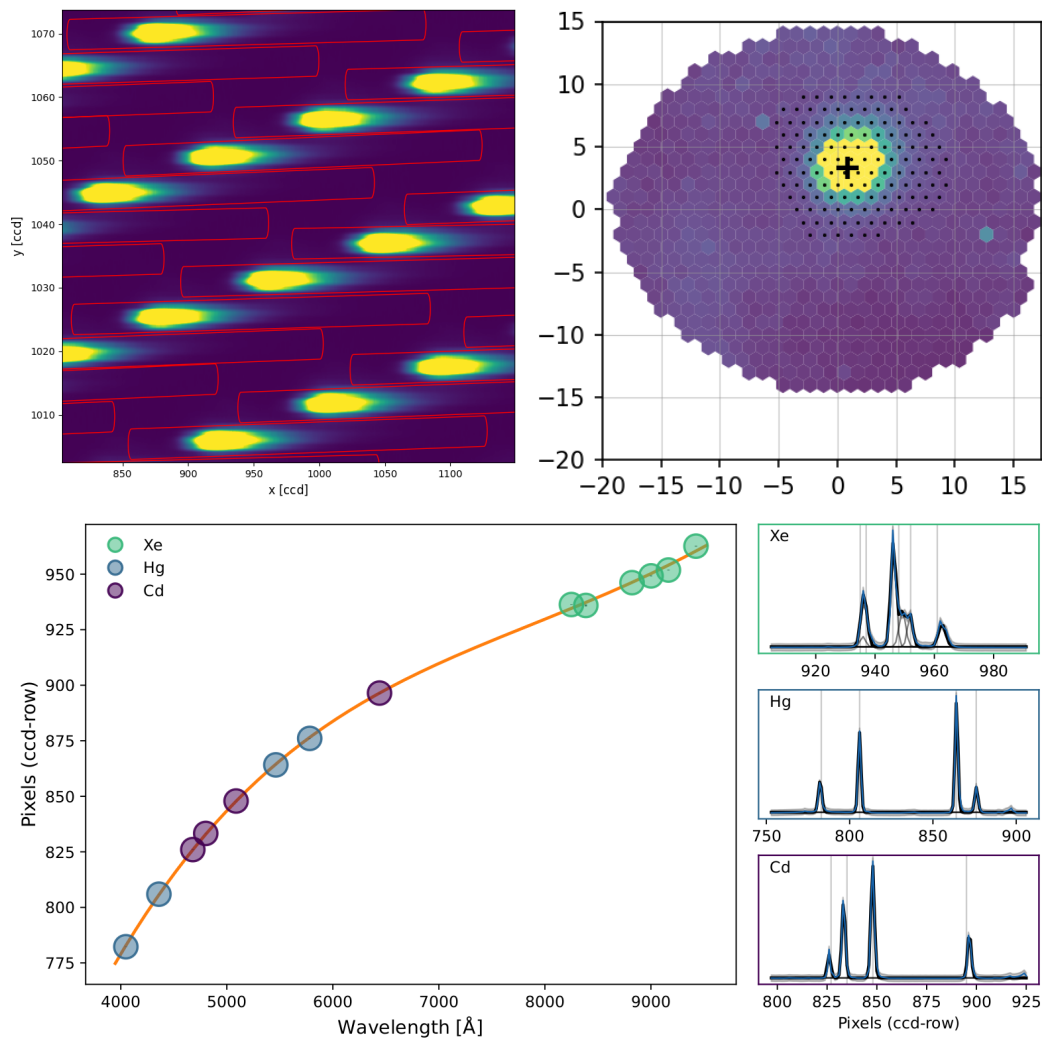


Figure 5.7: *Top left:* Spectral traces from micro-pupils on the IFU CCD for a dome flat image. The extracted trace boundaries are shown in red. *Top right:* The hexagonal grid formed by micro-pupil images on the IFU CCD plane, each micro-pupil image forms a spatial pixel or a “spaxel”. The bright target (in this case, a standard star) is clearly visible in the image, and the dotted area is used for PSF modeling. *Bottom:* Example of a wavelength solution for one spaxel using the arc lamps (Xe, Hg, Cd). The solution curve maps the pixels along the length of the trace to wavelengths.

## 5.4 Data Processing Software

### Spectroscopic data reduction

SEDM-KP is built upon SEDM’s legacy, so the automatic data reduction pipelines built for SEDM were also adapted for SEDM-KP. We modified `pysedm` (Rigault et al. 2019) and the wrapper script that calls `pysedm` to reduce data in real time to work on SEDM-KP’s IFU CCD images. The wrapper script processes the calibration files

to create master bias, flat, and arc lamps (Xe, Hg, Cd), subtracts the master bias, and removes cosmic rays from all images. Then `pysedm` identifies and extracts all the spaxel traces (dispersed light for each spaxel) from the master flat (see Figure 5.7, top left), maps their centroids onto a hexagonal grid (see Figure 5.7, top right), and creates a flat “cube” to be used for flat fielding the IFU data. From the master arcs, `pysedm` creates the wavelength solution for each spaxel by matching the observed line intensities with expected line intensities and generating the pixel to wavelength mapping (see Figure 5.7, bottom). Then, for each object image, `pysedm` creates a flat-corrected “cube”. To extract flux from all the spaxels that the observed target occupies, a point-spread function (PSF) is fit to the spatial axis of the cube at the target’s estimated position. This position of the observed target in the hexagonal grid is automatically deduced from the known positional mapping between the EMCCD and the IFU CCD. After the PSF fitting, the traces of all the spaxels inside the PSF are summed up to get an uncalibrated spectrum of the target. This spectrum is flux-calibrated using the standard star observations to get the final science-ready spectrum.

The wrapper script then runs transient classification programs, like SuperNova IDentification (SNID; Blondin et al. 2007), SuperFit (NGSF; Goldwasser et al. 2022), SNIascore (Fremling et al. 2021), and CCSNscore (Sharma et al. 2025), creates a summary report graphic for each spectrum, and uploads the spectra, the classification program results, and the summary graphic to `Fritz`.

### **Photometric data reduction**

The SEDM-KP photometric data reduction is implemented within the framework of MIRAR (Stein et al. 2025)—a Modular Image Reduction and Analysis Resource<sup>2</sup>. A flow chart of the various photometric data processing steps (bias subtraction, dark and flat correction, astrometric calibration, registration and stacking, photometric calibration, and aperture and PSF photometry) that are executed using MIRAR on SEDM-KP data are shown in Figure 5.8. For transients, MIRAR also implements template image subtraction based on the ZOGY algorithm (Zackay et al. 2016) to extract background-subtracted (a.k.a. differenced) photometry.

---

<sup>2</sup><https://github.com/winter-telescope/mirar>.

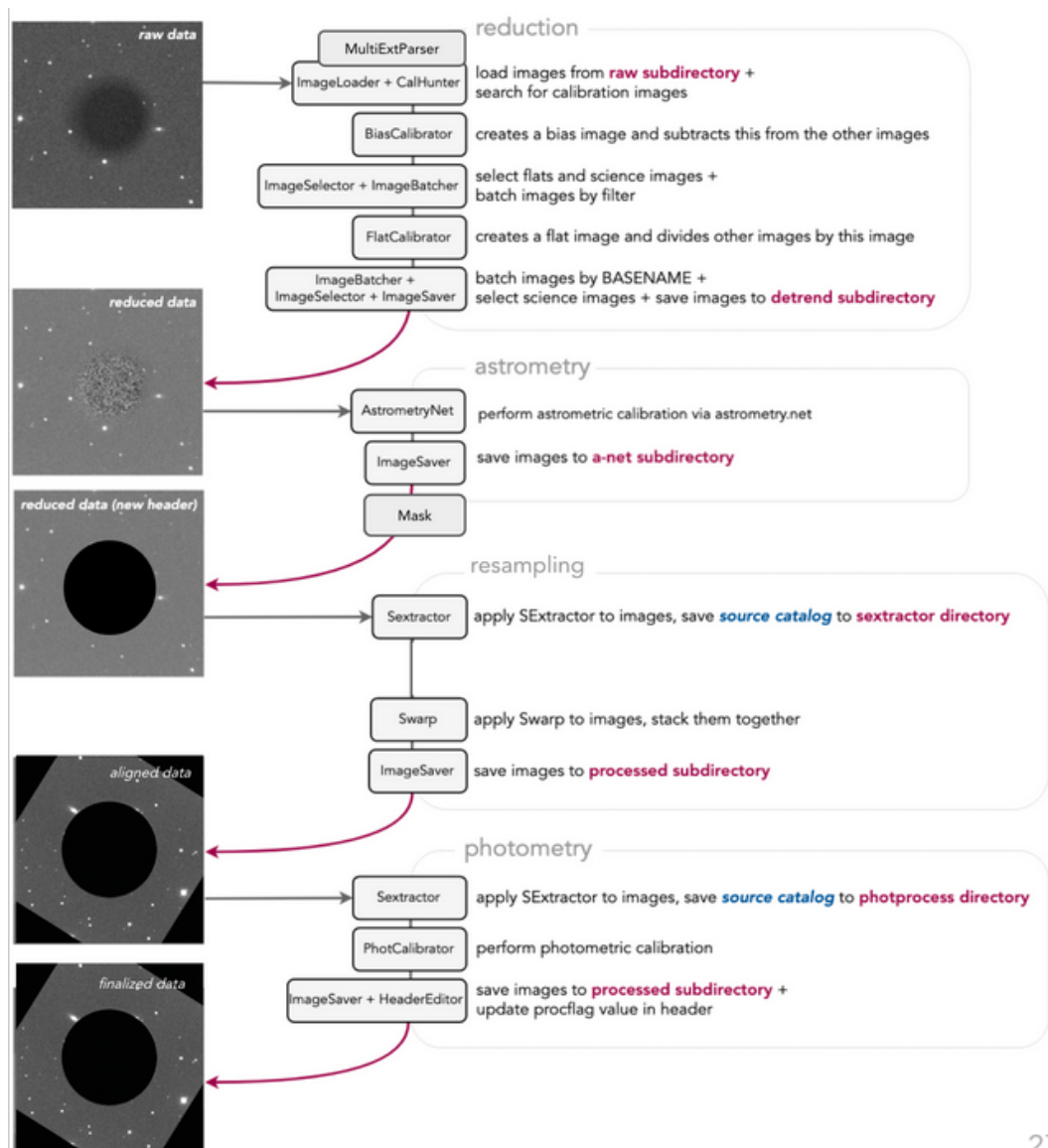


Figure 5.8: Flow chart of all the photometric data reduction steps that are executed using the MIRAR framework for SEDM-KP data. *Image Credit:* Saarah Hall (CIERA, Northwestern University).

## 5.5 Performance

### KP84 Telescope

The commissioning of SEDM-KP started in June 2022. In the KPED era, the KP84 telescope was remotely operable but not fully robotic. Therefore, the primary task for the commissioning period was to test and refine robotic operations. Unfortunately, Kitt Peak National Observatory (KPNO) was severely affected by the Contreras Fire in June 2022, and our commissioning plans were halted. Once the KPNO

infrastructure was repaired and KP84 was in operating condition by February 2023, we resumed SEDM-KP commissioning. However, our progress suffered multiple setbacks as mechanical and electrical issues with the old telescope and the dome (a consequence of fluctuating power supply following the fire) started surfacing.

We recorded motor current data for the hour angle (HA) and Declination (DEC) axes of the telescope during slewing and tracking operations and found that the telescope had oscillations (stick-slip) and a bumpy response in both axes (see Figure 5.9, left). We identified the likely cause of this behavior as a slight imbalance of the telescope and the fact that KP84 had not been serviced in many years (cleaning of hardened grease from the gears, re-lubrication, and other maintenance tasks that should be performed once every six months). After we fine-tuned the balance of the telescope, lubricated the axes gears, and tuned the preload current to an optimal value, the performance of the telescope showed a significant improvement (see Figure 5.9, right).

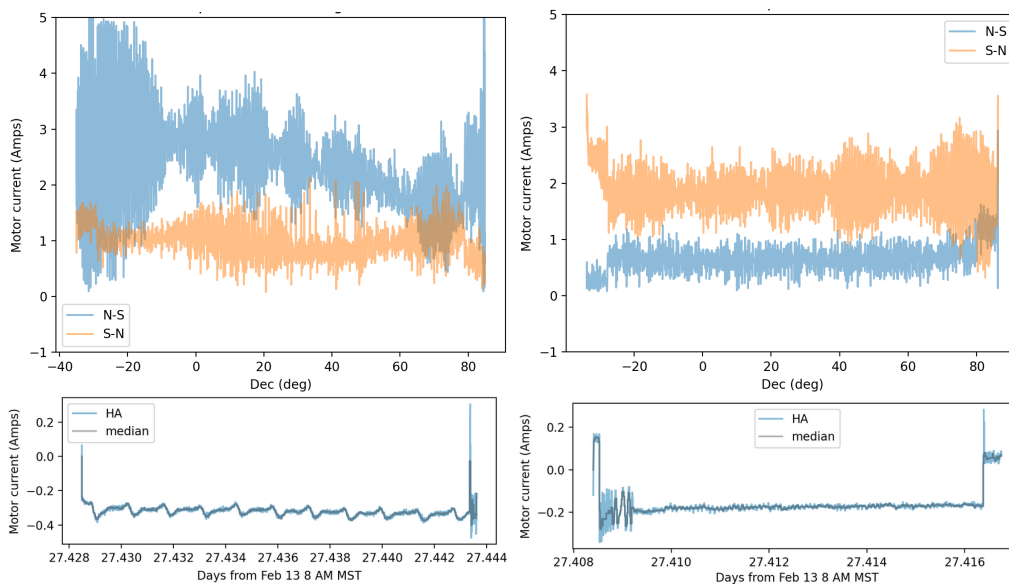


Figure 5.9: Motor current data collected for diagnosing the KP84 mechanical issues. *Top panels:* DEC axis motor current as a function of DEC encoder position during a long slew from North – South (blue) and South – North (orange) limits. *Bottom panels:* HA axis motor current as a function of time while the telescope is tracking. On the left are plots before servicing and tuning of the telescope mechanics, which show clear stick-slip oscillations. On the right are plots after the servicing, which show a much-improved performance of the telescope axes during slewing and tracking. Data collected with the help of Dan McKenna (COO).

The second major setback we faced was the failure of the dome drive and rotation

mechanism. Due to the heat from the fire, the dome structure had morphed such that there was no clearance left between the rotating and non-rotating structure in an area of the dome, which resulted in the overloading of the dome drive current that led to frequent switching off of the thermal overload protectors (hampering our remote testing capabilities during 2023). By the time this issue was correctly diagnosed, it led to a complete dome drive failure that prevented us from operating the telescope at all for nearly 5 months from mid-October 2023 to mid-March 2024.

After the dome drive was repaired, we started fully robotic operations without any observer intervention in April 2024 and had a brief period of stable operations for a month. That is when the HA encoder instability started to show up, where, due to faulty electrical connections and a failing HA encoder, the telescope started to “runaway”, i.e., make uncommanded moves unpredictably. During one of these runaway episodes, the safety limit switches failed to stop a rapid uncommanded slew, and the telescope declination ended up below the horizon by the time the telescope drive power cut off. This resulted in the primary mirror moving off its support slightly. Fortunately, we were able to recover the telescope from that position. The mirrors were sent for testing and re-aluminization, electrical connections were fixed, limit switches were repaired, and extra safety switches were installed. However, this recovery process took a whole year. KP84 is now back in operation in April 2025, but does not have the safety approval for allowing remote operations yet.

The raw pointing accuracy of KP84 currently is  $\pm 5'$ . This is because a new pointing model could not be implemented while the telescope and dome mechanical issues were ongoing. The tracking accuracy is similar to what was reported in Coughlin et al. (2019) ( $9.6''\text{hour}^{-1}$  in right ascension). The guiding accuracy is within  $\pm 0.2''$ .

### **EMCCD Imager**

Figure 5.10 (left) shows a quiver plot depicting the astrometric solution uncertainties in our observations of a short orbital period binary white dwarf system—SDSS J065133.33+284423.37 in rapid read-out mode (without EM gain) with frame exposure time of 10 s and total exposure time of 900 s, which contained 72 reference catalog-matched (with Pan-STARRS 1) sources. The astrometric uncertainties are consistent with what was found for KPED (Coughlin et al. 2019, their fig. 5) and within  $\pm 1''$ , with most being within  $\pm 0.5''$ . This implies that our astrometric solution is good in most of the field, but there are some distortions towards the edges. Figure 5.10 (right) depicts the photometric calibration quality of the same field.

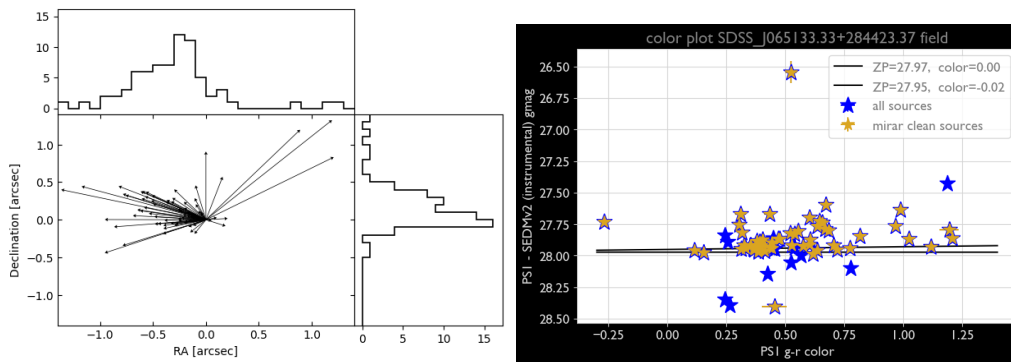


Figure 5.10: *Left*: Quiver plot showing astrometric solution uncertainties in RA and DEC derived from a field containing 72 reference catalog-matched stars. *Right*: Zero-point as a function of PS1  $g - r$  color for the same field in a  $g$ -band image. There is a negligible effect of color-term on our ZP fitting. *Image Credit*: Sarah Hall (CIERA, Northwestern University).

The difference between the Pan-STARRS 1 (PS1) catalog magnitude of the stars and SEDM-KP instrumental magnitude (zero-point) is plotted against the PS1  $g - r$  color, and as can be seen from the figure, the color-term effect in zero-point calculation is negligible. Figure 5.11 shows a false-color ( $gri$  bands) image of the Crab Nebula (M1) obtained with SEDM-KP to qualitatively depict the performance of the imager. The central obscuration area has been masked in this image.

### IFU Spectrograph

During the commissioning phase in 2023, we noticed a poor quality of wavelength solutions for the SEDM-KP IFU data. Upon investigation of the arc lamp images, we found that at the IFU motion stage position that gives the maximum counts in arc lines (a.k.a. the best focus position), all the arc lines had a diffused halo (or excess in the tails of the PSF) around them (see Figure 5.12, top left). This excess in the tail turned out to be caused by a birefringent material in the IFU optical path, which was focusing half of the unpolarized light at one position and the other half at a slightly farther position, resulting in poor FWHM of the traces. This effect caused some overlap in the adjacent traces, which resulted in large uncertainties in the wavelength solution (see nMAD value in Figure 5.12, bottom left), as well as reduced instrument throughput (a.k.a. efficiency). This uncertainty (nMAD) ideally should be  $< 20 \text{ \AA}$  (which it is for SEDM on P60). After the birefringent component was replaced, we saw an immediate improvement in the sharpness of the images (see Figure 5.12, top right) as well as the separation between adjacent traces (2-px



Figure 5.11: A false color image of Crab Nebula (M1) created using *gri*-band images taken with SEDM-KP. *Image Credit:* Mitchell Karmen (STScI).

wide). The wavelength solution also improved vastly (see Figure 5.12, bottom right) with  $< 20 \text{ \AA}$  uncertainty in the top half of the FoV (the high uncertainties towards the top and bottom edges is due to a slight misalignment of the tri-prism and will be corrected for in the future).

Figure 5.13 shows the instrument throughput or efficiency over time after key upgrades and compares it with SEDM on P60. The efficiency is calculated by comparing the expected (reference) standard star flux with the observed standard star flux. The reference standard star energy flux (in  $\text{erg s}^{-1} \text{cm}^{-2} \text{\AA}^{-1}$ ) is first converted to photon flux (in  $e^{-} \text{s}^{-1} \text{cm}^{-2} \text{\AA}^{-1}$ ). The observed photon flux is extracted from the uncalibrated cube and has the units of  $e^{-} \text{s}^{-1} \text{\AA}^{-1}$  (the native wavelength sampling as a function of wavelength is accounted for in this process). Finally, the observed photon flux is divided by the reference photon flux, resulting in the effective area of the instrument (in  $\text{cm}^2$ ) as a function of wavelength. To obtain the efficiency, the instrument's effective area is divided by the telescope's effective area, typically accounting for the telescope reflectance<sup>3</sup>. However, to show the effect on efficiency

<sup>3</sup>For more details, see <https://sites.astro.caltech.edu/sedm/Efficiency.html>.

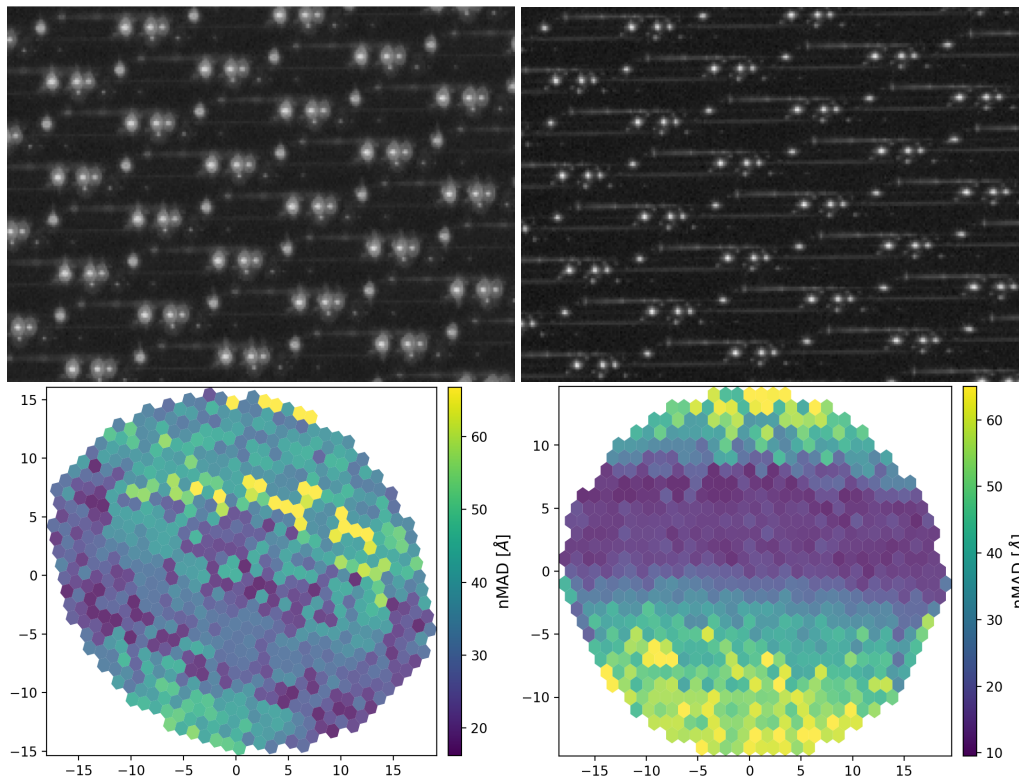


Figure 5.12: *Left panels:* A zoomed-in snapshot of the cadmium arc lamp calibration image (top) showing the halo effect around bright Cd lines caused by the birefringent component in the spectrograph optical path, and the corresponding wavelength solution uncertainties map (bottom). *Right panels:* The same images after the birefringent component was replaced. The Cd snapshot looks much sharper, with a darker background due to less scattered light and a clear 2-pix space between adjacent traces. The wavelength solution is improved and  $< 20 \text{ \AA}$  for the upper half spaxels but has higher uncertainties in the lower half due to minor misalignment of the tri-prism.

before and after aluminization, we do not divide the efficiency by the telescope's reflectance in Figure 5.13. The initial SEDM-KP efficiency (in red curve) has the expected improvement in throughput ( $\sim 10\%$  higher) over that of SEDM (light-blue dashed curve) in the redder wavelengths but is lower ( $\sim 5\%$  difference) in the bluer wavelengths. This is caused by the KP84 mirror not being re-aluminized in over 5 years and the throughput loss due to birefringence. After birefringence correction (the green curve), SEDM-KP's efficiency increases from  $\sim 25\%$  to  $\sim 30\%$  in the redder wavelengths and by a bit lower in the bluer wavelengths. The blue dashed curve shows SEDM (P60) efficiency after a camera upgrade, and although there is an increase in the efficiency from its previous value (light blue) in the redder bands,

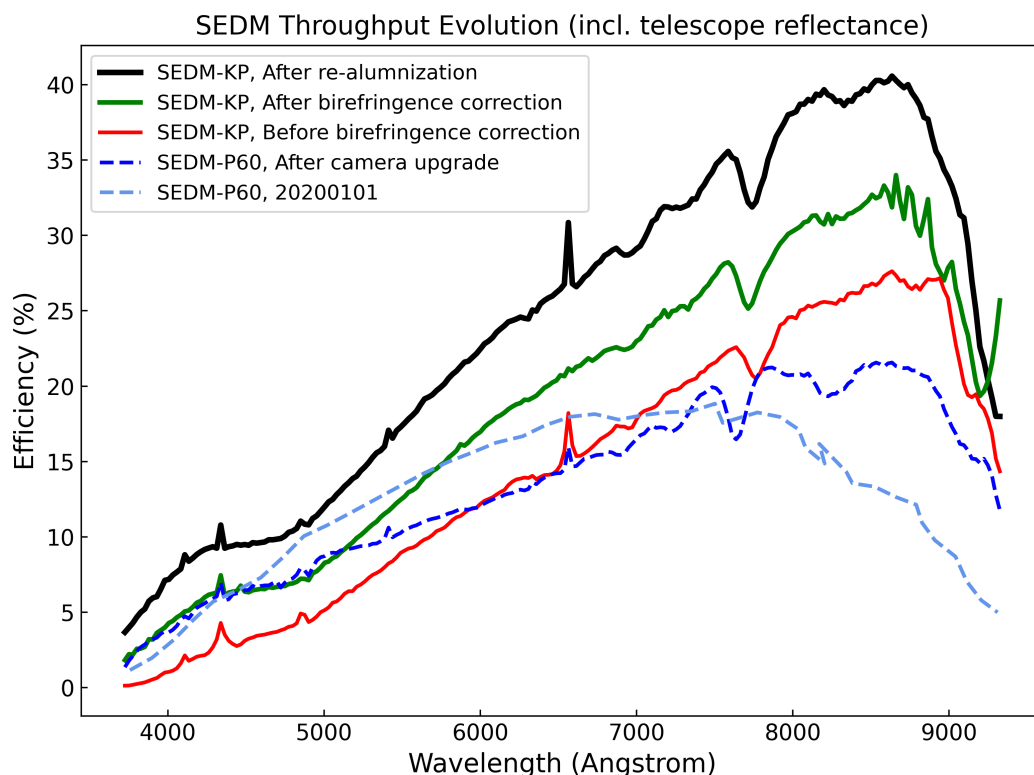


Figure 5.13: Evolution of SEDM and SEDM-KP's efficiency over time after key upgrades. SEDM-KP's final efficiency is  $1.6\times$  higher in the redder bands and  $4\times$  higher in the bluer bands compared to its initial efficiency and  $2\times$  higher than that of SEDM in redder bands. The efficiency number includes the effect of the telescope's primary and secondary mirror reflectances.

it is still  $\sim 10\%$  lower than SEDM-KP's (green). Finally, after re-aluminization, SEDM-KP efficiency in redder bands (black curve) is  $\sim 1.6\times$  more than its initial efficiency (red curve), and in bluer bands is  $\sim 4\times$  more than its initial efficiency.

Figure 5.14 shows an example of the summary report page that is created from `psyedm` data reduction quality metrics. The top left panel shows the position of the target in the hexagonal grid space. The remaining top panels show the PSF centroid as a function of wavelength and the PSF model subtraction residuals. The rightmost panels (middle and bottom) show the flexure correction. The extracted flux-calibrated spectrum flux and its uncertainty are shown in the bottom left panel. As evident from the booming P-Cygni  $H\alpha$  line, the target in this summary report figure is a Type II supernova.

In Figure 5.15, we show some of the data collected during the brief period of stable operations in April 2024, after the birefringent component in the instrument

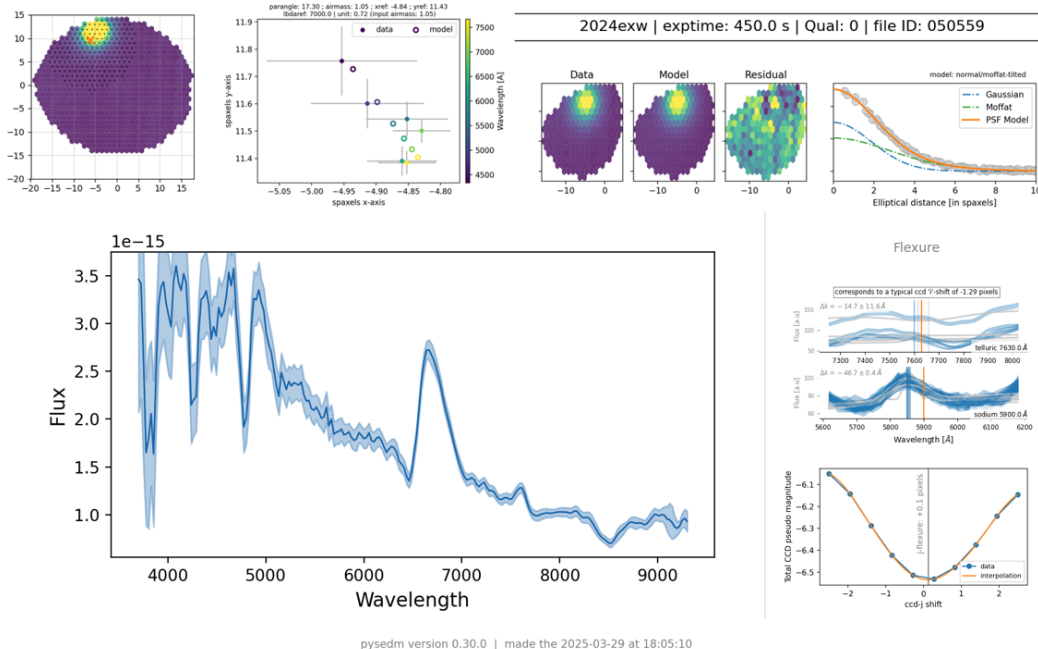


Figure 5.14: Example of a summary report page generated by `pysedm` for each observation taken. The plot shows PSF modeling quality, flexure correction fits, and the extracted spectrum (with uncertainties on the fluxes). This particular example is of a Type II supernova.

was replaced and before the catastrophic runaway incident. We obtained follow-up spectra of several bright supernovae from TNS (all Type II SNe). As is evident from the figure, the key identifying spectral features of SNe can be discerned from SEDM-KP spectra, making it suitable for its intended goal as a classification instrument.

Figure 5.16 shows the comparison of a SEDM spectrum and a SEDM-KP spectrum of the same supernova (SN 2024cld, Type II) taken around the same phase (1-day apart). The SEDM observation was exposed for 2160 s while the SEDM-KP observation was exposed for 900 s (0.42× lower). As KP84 has ~2× more effective telescope area than that of P60, ~0.5× reduction in exposure time for SEDM-KP should yield roughly the same signal-to-noise ratio (SNR) as SEDM. We can see that with ~0.4× lower exposure time on SEDM-KP (blue), we obtain a better SNR than the concurrent SEDM spectrum (orange), especially in the redder wavelengths (as expected from the efficiency curve in Figure 5.13).

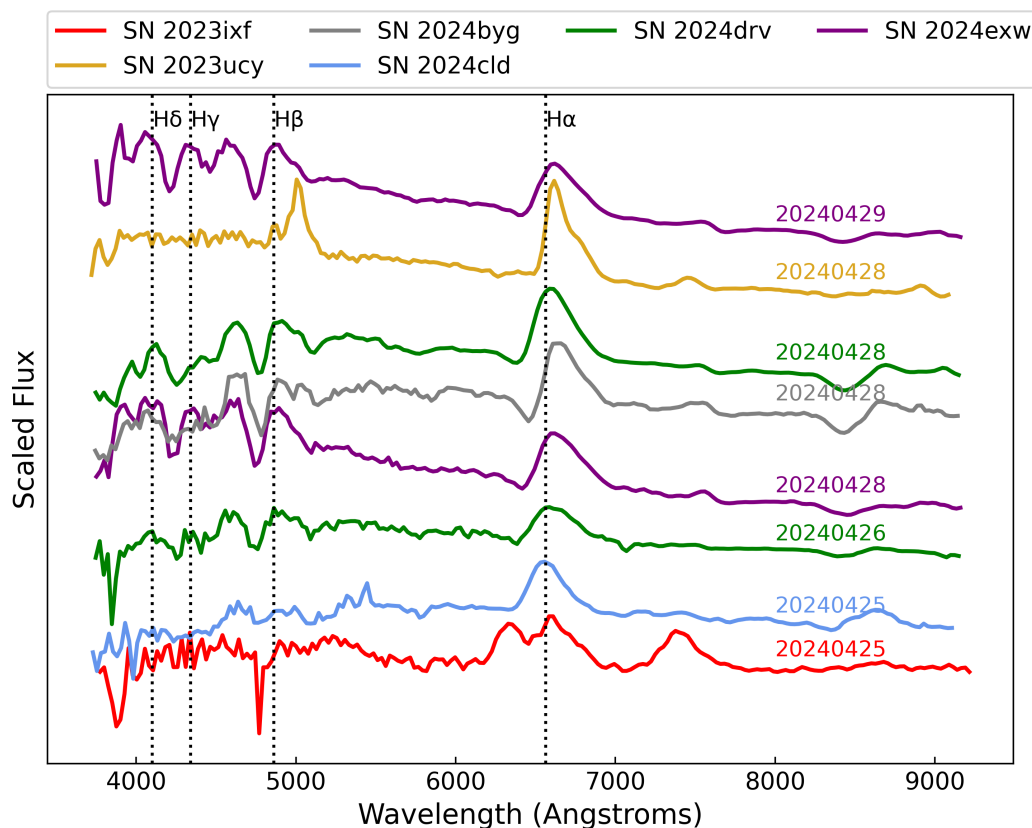


Figure 5.15: Spectra of some bright Type II SNe from TNS collected with SEDM-KP, with wavelengths transformed to the rest-frame, and with the hydrogen Balmer series marked with vertical dotted lines.

## 5.6 Summary

In this chapter, we presented SEDM-KP mounted on the Kitt Peak 84-inch telescope—an ultra-low resolution fully-robotic spectrograph with a similar but upgraded design as the SED-Machine on the Palomar 60-inch telescope. Motivated by the success of SEDM in dominating the classification of transients from the Zwicky Transient Facility, SEDM-KP was built to push the classification completeness deeper, and for fast-turnaround follow-up of critical fast-fading transients like GRB afterglows, fast blue optical transients, and electromagnetic counterparts of gravitational wave sources. Although faced with numerous unanticipated challenges (COVID delay, a wildfire, multiple critical telescope mechanical failures), we managed to complete the robotization of KP84 and SEDM-KP operations and collect scientific data, and demonstrated the superior performance of SEDM-KP over its predecessor SEDM. Table 5.2 lists the timeline of the project with the key milestones and setbacks.

There are still upgrades in progress to enable smooth robotic operations of the

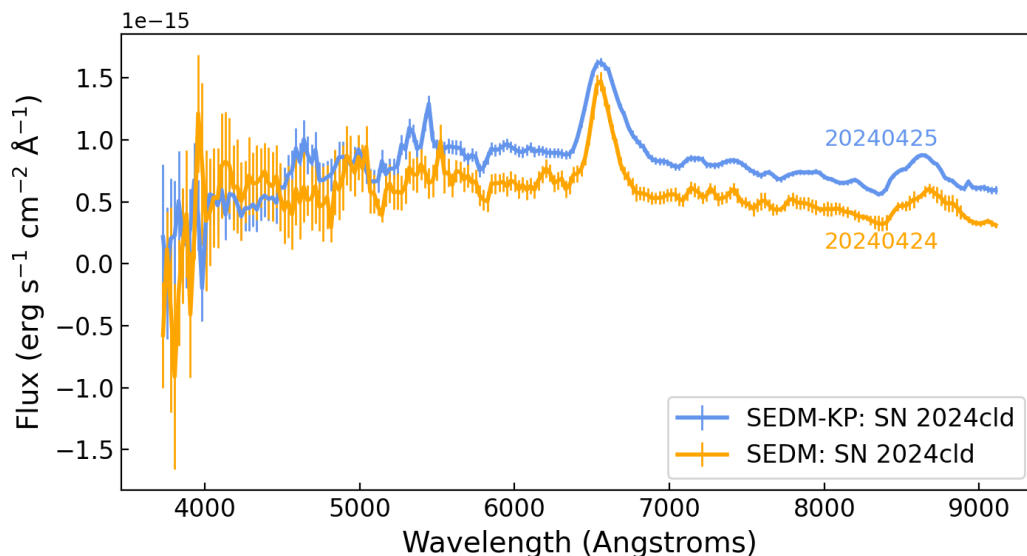


Figure 5.16: Comparison of a SEDM (2160 s exposure time) and a SEDM-KP (900 s exposure time) spectrum of the same supernova (SN 2024cld) taken around similar phase. Given that the KP84 effective area is  $2\times$  that of P60 and the SEDM-KP exposure time here is  $0.42\times$  that of SEDM, both spectra should have roughly the same SNR, but we see that SEDM-KP has a much better SNR than SEDM, especially in the redder bands.

instrument: complete replacement of the dome drive system with one having full remote capabilities (including resetting the thermal overload switches remotely if needed), motor and encoder upgrades for both of the telescope drives, creating a new pointing model for the telescope after the upgrades, and fixing the misalignment of tri-prism in the instrument to improve wavelength solution over the whole field-of-view. Then, SEDM-KP, together with SEDM, will vastly expand the number of transient classifications. Such dedicated facilities will become more valuable in the upcoming Rubin era.

Table 5.2: Timeline of the project.

Date	Event	Comment
January, 2020	Design review	Began fabrication immediately, aimed to commission in October, 2020.
March, 2020	COVID pandemic	Project paused .

*Continued on the next page*

Table 5.2: Timeline (continued)

Date	Event	Comment
December, 2020	KP84 lease approved	Caltech tenancy extended till December, 2025.
March, 2021	Fabrication begins	Delays due to COVID and supply chain issues.
June 5–8, 2022	Installation	Mounted the instrument with a stop-gap prism (triprism delivery delayed by vendor), obtained first light. Ready for remote operations and commissioning of the robotic system.
June 15, 2022	<b>Contreras fire</b>	KPNO evacuated, extensive damage to power and internet infrastructure from fire, road damage from fire and rock slides, damage to residences. All science buildings were kept safe with great effort.
September, 2022	Day visits allowed	Began recovery planning.
September 19–30, 2022	Multiple in-person trips	Post-fire cleaning, swapped stop-gap prism with the triprism.
October 18, 2022	Power restored	KPNO line power restored but was unstable, causing UPS failure.
October–December, 2022	Multiple in-person trips	Began testing and development of robotic operations. Multiple minor setbacks—oil pump failure, mirror cover failure, etc.
December, 2022	Internet restored	Remote access possible but not allowed without a working UPS.

*Continued on the next page*

Table 5.2: Timeline (continued)

Date	Event	Comment
January, 2023	Observed the “backlash” bug	Troubleshooting revealed that the backlash was a software bug, but also the poor performance of the telescope mechanics. Serviced the telescope to improve the performance.
February, 2023	UPS replaced	The new UPS failed after some months.
March, 2023	All robotic subsystems implemented	Spectrograph observations began.
March–September, 2023	Dome drive overloading failures	With regular operations, the dome rotation drive started failing more frequently (because of the structural issues discovered later). ROS error management was updated to work around the mechanical issues.
October, 2023	Complete dome drive failure	The dome rotation drive failed completely, took 5 months to repair, and the dome was operational again in mid-March 2024.
June, 2023–March, 2024	Discovered the birefringence issue	Birefringence in spectrograph optical path, causing poor instrument focus and throughput. Substitute optical components manufactured and replaced in April, 2024.
June, 2023–March, 2024	Telescope runaways	Runaways (uncommanded telescope moves) started happening often for unknown reasons, but limit switches kept the telescope safe.

*Continued on the next page*

Table 5.2: Timeline (continued)

Date	Event	Comment
April, 2024	Robotization complete	Despite the challenges, we took the operations from semi-robotic to fully robotic, and trained multiple students to monitor the robotic nightly operations.
April 29, 2024	Catastrophic runaway	Limit switch failure during a runaway resulted in the telescope moving to an unsafe position and pointing below the horizon. The primary mirror fell into the earthquake protection clips.
December, 2024	Recovery	NOIRLab managed the recovery effort. KP84 was stowed safely, the primary mirror was removed for inspection and re-aluminization, and was remounted in September, 2024. SEDM-KP team was requested for assistance with balancing and collimation. SEDM-KP team was also charged with investigating the runaways and the limit switches. We found bad electrical connections causing interference with the encoders and repaired them.
March, 2025	Operations resume	Only in-person observing allowed until the telescope's safety is ensured.
April, 2025	DLO oscillations	The catastrophic runaway resulted in damage to the declination axis, which is causing limit oscillations in the system. Repair ongoing (May, 2025).

## 5.7 Acknowledgment

SEDM-KP is a consortium of Caltech, the University of Minnesota, Goddard Space Flight Center, Northwestern University, and the Space Telescope Science Institute (STScI). SEDM-KP is based on work supported by the Heising-Simons Foundation (HSF) under grant #2021-2612, and by NASA under grant 80NSSC21K1505. We thank Larry Reddell (mountain facilities supervisor) and the KPNO staff for their continuous support and assistance. We thank John Henning (Palomar Observatory) and Richard Treffers (Starman Systems) for helpful discussions. We thank Josiah Purdum and Alex Reedeey for installation support. We thank Yu-Jing Qin, Tomas Ahumada, William Meynardie, and R. Weizmann Kiendrebeogo for support with nightly operations. We thank Viraj Karambelkar and Robert Stein for assisting with SEDM-KP's photometric data reductions through `mirar`.

Y. Sharma thanks the LSSTC Data Science Fellowship Program, which is funded by LSSTC, NSF Cybertraining Grant #1829740, the Brinson Foundation, and the Moore Foundation; her participation in the program has benefited this work.

*Chapter 6*

**CCSNSCORE: A MULTI-INPUT DEEP LEARNING TOOL FOR  
CLASSIFICATION OF CORE-COLLAPSE SUPERNOVAE  
USING SED-MACHINE SPECTRA**

Sharma, Y. et al. (2025). “CCSNscore: A Multi-input Deep Learning Tool for Classification of Core-collapse Supernovae Using SED-machine Spectra”. In: *PASP* 137.3, p. 034507. doi: 10.1088/1538-3873/adb4b.

Yashvi Sharma<sup>1</sup>, Ashish A. Mahabal<sup>1,2</sup>, Jesper Sollerman<sup>3</sup>, Christoffer Fremling<sup>4</sup>, S. R. Kulkarni<sup>1</sup>, Nabeel Rehemtulla<sup>5,6</sup>, Adam A. Miller<sup>5,6</sup>, Marie Aubert<sup>7</sup>, Tracy X. Chen<sup>8</sup>, Michael W. Coughlin<sup>9</sup>, Matthew J. Graham<sup>1</sup>, David Hale<sup>4</sup>, Mansi M. Kasliwal<sup>1</sup>, Young-Lo Kim<sup>10</sup>, James D. Neill<sup>4</sup>, Josiah N. Purdum<sup>4</sup>, Ben Rusholme<sup>8</sup>, Avinash Singh<sup>3</sup>, and Niharika Sravan<sup>11</sup>

<sup>1</sup>Division of Physics, Mathematics and Astronomy, California Institute of Technology, Pasadena, CA 91125, USA

<sup>2</sup>Center for Data Driven Discovery, California Institute of Technology, Pasadena, CA 91125, USA

<sup>3</sup>Department of Astronomy, The Oskar Klein Center, Stockholm University, AlbaNova, 10691 Stockholm, Sweden

<sup>4</sup>Caltech Optical Observatories, California Institute of Technology, Pasadena, CA 91125, USA

<sup>5</sup>Department of Physics and Astronomy, Northwestern University, 2145 Sheridan Road, Evanston, IL 60208, USA

<sup>6</sup>Center for Interdisciplinary Exploration and Research in Astrophysics (CIERA), Northwestern University, 1800 Sherman Ave, Evanston, IL 60201, USA

<sup>7</sup>Université Clermont Auvergne, CNRS/IN2P3, LPCA, F-63000 Clermont-Ferrand, France

<sup>8</sup>IPAC, California Institute of Technology, 1200 E. California Blvd, Pasadena, CA 91125, USA

<sup>9</sup>School of Physics and Astronomy, University of Minnesota, Minneapolis, MN 55455, USA

<sup>10</sup> Department of Physics, Lancaster University, Lancs LA1 4YB, UK

<sup>11</sup> Department of Physics, Drexel University, Philadelphia, PA 19104, USA

**Abstract**

Supernovae (SNe) come in various flavors and are classified into different types based on emission and absorption lines in their spectra. SN candidates are now abundant with the advent of large systematic sky surveys like the Zwicky Transient Facility (ZTF), however, the identification bottleneck lies in their spectroscopic confirmation and classification. Fully robotic telescopes with dedicated spectrographs optimized

for SN follow-up have eased the burden of data acquisition. However, the task of classifying the spectra still largely rests with the astronomers. Automating this classification step reduces human effort and can make the SN type available sooner to the public. For this purpose, we have developed a deep-learning based program for classifying core-collapse supernovae (CCSNe) with ultra-low resolution spectra from the SED-Machine spectrograph on the Palomar 60-inch telescope. The program consists of hierarchical classification task layers, with each layer composed of multiple binary classifiers running in parallel to produce a reliable classification. The binary classifiers utilize RNN and CNN architecture and are designed to take multiple inputs to supplement spectra with  $g$ - and  $r$ -band photometry from ZTF. On non-host-contaminated and good quality SEDM spectra (“gold” test set) of CCSNe, CCSNscore is  $\sim 94\%$  accurate in distinguishing between hydrogen-rich (Type II) and hydrogen-poor (Type Ibc) CCSNe. With light curve input, CCSNscore classifies  $\sim 83\%$  of the gold set with high confidence (score  $\geq 0.8$  and score-error  $< 0.05$ ), with  $\sim 98\%$  accuracy. Based on SNIAscore’s and CCSNscore’s real-time performance on bright transients ( $m_{pk} \leq 18.5$ ) and our reporting criteria, we expect  $\sim 0.5\%$  ( $\sim 4$ ) true SNe Ia to be misclassified as SNe Ibc and  $\sim 6\%$  ( $\sim 17$ ) of true CCSNe to be misclassified between Type II and Type Ibc annually on the Transient Name Server.

## 6.1 Introduction

Wide-field optical transient surveys are already finding supernova (SN) candidates in record numbers (Shappee et al. 2014, ASAS-SN; Chambers et al. 2016, PS1; Tonry et al. 2018, ATLAS; Bellm et al. 2019; Graham et al. 2019; Dekany et al. 2020, ZTF), which will increase tenfold in the era of the Rubin Observatory (Ivezić et al. 2019). A supernova candidate becoming a secure SN identification involves many steps. Taking the example of ZTF, the transient ‘alerts’ from ZTF (Patterson et al. 2019) are filtered by alert management frameworks (e.g. Fritz (Walt et al. 2019; Coughlin et al. 2023), AMPEL (Nordin et al. 2019), etc.) to obtain potential SN candidates from the slurry of transients, variable stars, moving solar system objects, and bogus artifacts. These candidates are visually inspected for spectroscopic follow-up candidates; however, this step can be automated depending on survey needs as demonstrated in Rehemtulla et al. (2024) (BTSbot). Finally, the selected candidates are assigned to various telescope facilities to obtain secure spectroscopic classifications, but as follow-up resources are limited, this step becomes the primary bottleneck. Still, dedicated SN classification instruments and programs (e.g., Ben-Ami et al. 2012; Blagorodnova et al. 2018, SEDM; Smartt et al.

2015, ePESSTO; Howell 2019, The Global Supernova Project) take spectra of a few thousand SNe per year, which are then analyzed by astronomers, assigned a classification, and then sent to the Transient Name Server (TNS<sup>1</sup>). Some programs exist that are meant to support astronomers in the manual SN classification task, such as SuperNova IDentification software (SNID; Blondin et al. 2007), Superfit (Howell et al. 2005), NGSF (Goldwasser et al. 2022), Gelato (Harutyunyan et al. 2008), all based on either template cross-correlation techniques (Tonry et al. 1979) or minimization algorithms. These programs often require user input (initial guesses for redshift, age, restriction of parameter search ranges, etc.) to obtain correct classifications. Still, they can be less effective because of host contamination (in SNID) or poor signal-to-noise ratio (SNR). Moreover, template-matching techniques are slow to run on thousands of spectra, suffer from type-attractor issues if one kind of template dominates the template bank, and are less accurate when automated (Kim et al. 2024). With the advent of deep learning techniques and the dedicated influx of spectral data, sophisticated deep learning-based models can be trained to automatically and reliably classify the most common SN types. Muthukrishna et al. (2019a) presented DASH (Deep Learning for the Automated Spectral Classification of Supernovae and their Hosts), trained on the SNID template dataset (which contains intermediate resolution spectra) and tested on the OzDES (Yuan et al. 2015; Childress et al. 2017) dataset, also from intermediate resolution ( $R \sim 1400$ ) spectrographs. Though DASH showed promising performance on the OzDES test set and is easy to install and use, it did not perform well on ultra-low resolution spectra ( $R \sim 100$ ) when tested in Fremling et al. (2021) and Kim et al. (2024).

Thus, *SNiascore* (Fremling et al. 2021)—a deep-learning based binary classifier was developed specifically for classifying SNe Ia using the spectra taken by SED-Machine (Ben-Ami et al. 2012; Blagorodnova et al. 2018; Rigault et al. 2019; Kim et al. 2022), an ultra-low resolution ( $R \sim 100$ ) IFU spectrograph operating in the optical wavelength range (3800 Å–9150 Å) on the fully robotic Palomar 60-in telescope (P60; Cenko et al. 2006). The need for *SNiascore* was motivated by the ZTF Bright Transient Survey (BTS; Fremling et al. 2020; Perley et al. 2020; Rehemtulla et al. 2024); a flux-limited survey to spectroscopically classify bright transients ( $m_{peak} < 18.5$ ) detected by ZTF with  $>90\%$  completeness. With SEDM’s resolution on the moderate aperture of P60, it is uniquely suited for bright transient classification and thus became the main workhorse instrument for BTS, as well as the top classifier on TNS. *SNiascore* was optimized to classify SNe Ia with

---

<sup>1</sup><https://www.wis-tns.org/>.

more than 90% accuracy at less than 0.6% false positive rate (FPR), and with this performance, automated half of the manual classification workload for BTS. *SNIascore* has allowed BTS to send robust SN Ia classifications to the TNS within  $\sim 11$  minutes of acquisition. Together, BTSbot and *SNIascore* enabled the first fully automatic end-to-end discovery and classification of an optical transient (Rehemtulla et al. 2023).

As (normal) SNe Ia are quite homogeneous in their spectral and photometric properties, it is a binary classification problem suited for deep learning. Also, SNe Ia are the most abundant type of supernova identified in flux-limited surveys like BTS, thus providing a large sample sufficient for training deep learning models. Core-collapse (CC) supernovae, however, are more heterogeneous, with some CCSNe even transitioning to a different spectral type over time or developing late-time interaction signatures (Milisavljevic et al. 2015; Chen et al. 2018; Sollerman et al. 2020; Sharma et al. 2024; Kangas et al. 2024). In BTS (Perley et al. 2020), the most abundant class among CCSNe is the hydrogen-rich Type II SNe ( $\sim 72\%$ ), followed by the hydrogen-poor Type I or stripped-envelope SNe (SESNe). Within the hydrogen-rich Type II class, the most common ( $\sim 76\%$ ) are the spectroscopically “normal” subtypes (SNe IIP/L) showing strong P-Cygni Balmer line profiles, with the rest (SNe IIb, IIc, and SLSN-II) contributing  $\sim 24\%$  combined. Within the Type I SESNe, SNe Ibc constitute  $\sim 59\%$ , SNe Ic-BL make up  $\sim 19\%$ , SLSN-I are  $\sim 13\%$  and the rest are the rare SNe Ibn and SNe Icn (SN subtype fractions referenced from Perley et al. 2020). This is a highly unbalanced dataset with the rarer subtypes only having a handful of examples, not nearly enough for training a deep-learning model. The problem is compounded by varying levels of noise in the spectra and the classification being inherently difficult for some subtypes with ultra-low resolution spectra (for example, the ‘n’ in IIc and Ibn refers to ‘narrow’ spectral lines of  $\sim 100 \text{ km s}^{-1}$ , impossible to resolve with a resolution of  $R \sim 100$ ). For these reasons, developing a high-performing and reliable automated spectral classifier for CCSNe using just the SEDM data is challenging.

This work attempts to face this challenge and presents a deep learning-based program—*CCSNscore*, designed specifically for CCSN classification, trained with SEDM spectral data, Open SN Catalog (Guillochon et al. 2017) spectral data, and ZTF photometry. The data preparation and preprocessing are described in §6.2, the application structure and model architecture are described in §6.3, the training and optimization process is outlined in §6.4, and the performance on the test set is

detailed in §6.5. We explore the limitations and caveats of this tool in §6.7. The CCSNscore software, trained models presented in this paper, and the metadata of training and test datasets are available on the GitHub repository of CCSNscore.

## 6.2 Dataset

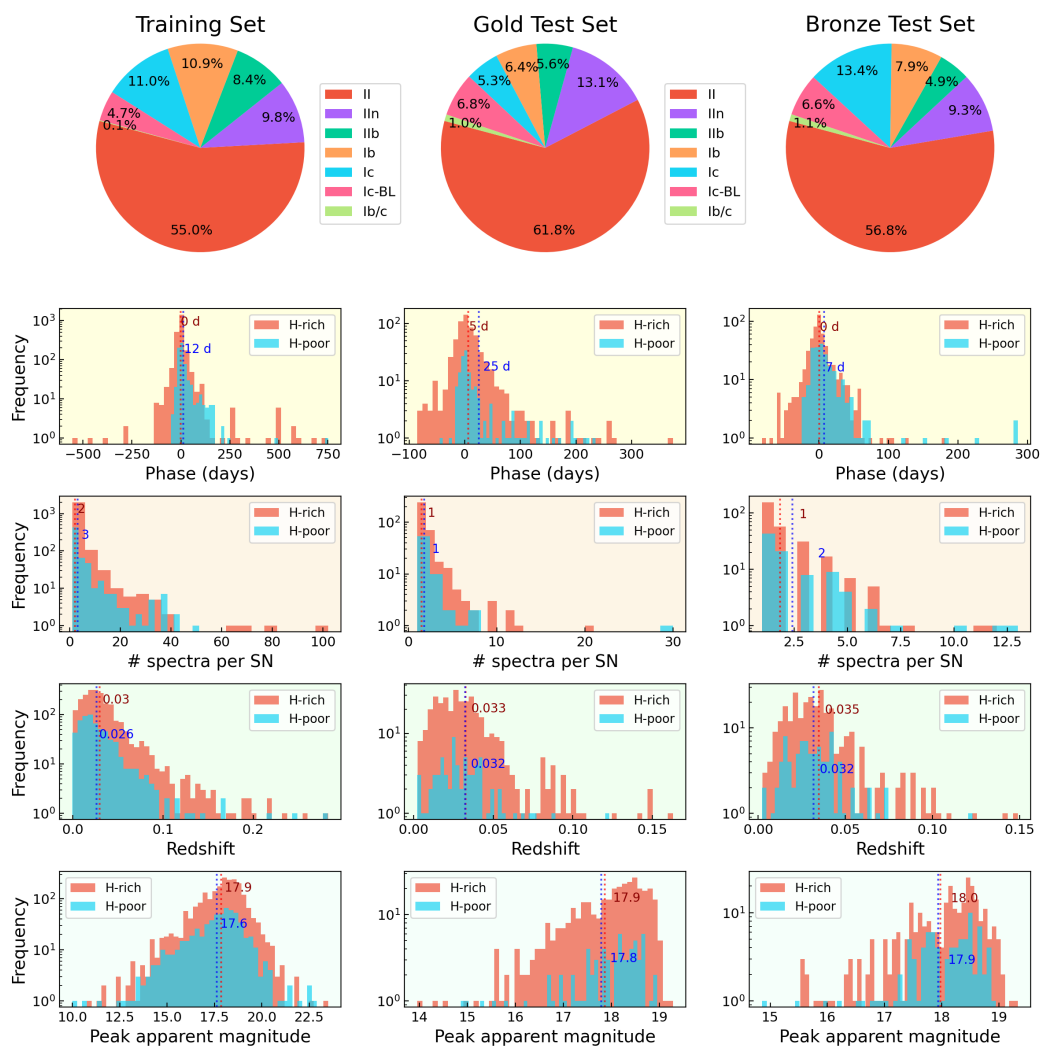


Figure 6.1: Distribution of properties of the training and test sets (gold and bronze). The first row contains pie charts depicting the highly imbalanced distribution of samples by CCSN subtype. The next four rows depict the property distribution for hydrogen-rich (Type II in blue) and hydrogen-poor (Type Ibc in red) SN samples separately, with the second row showing spectral phase distribution, the third row showing the distribution of the number of spectra per unique SN, the fourth row showing redshift distribution of the unique SNe and the fifth row showing the peak apparent magnitude distribution of unique SNe. The mean values of all distributions are marked with dotted vertical lines.

Initially, we started our study with the SEDM spectra of BTS transients used in Fremling et al. (2021) for SNIascore that are not SNe Ia (‘non-Ia’) and collected between March 2018 and August 2020. We kept the BTS sample spectra published in Fremling et al. (2020) in the test set, along with the spectra of a few peculiar CCSNe, and put the rest in the training set. We made sure that all spectra belonging to a transient were present in only one of the sets. We updated the dataset a few times as more spectra were collected through BTS, until March 2024. We also added optical spectra from the Open SN Catalog and resampled them to match the resolution of the SEDM spectra. Because we wanted to test the performance primarily on SEDM data, we put all of the Open SN Catalog spectra of SNe that had an unambiguous and non-peculiar classification in the training set. Then, we split the newer SEDM spectra of ZTF transients into training and test sets such that the final ratio of test samples to training samples per major subtype would be between 10% to 30%. We put most of the stripped-envelope SNe with ambiguous subtype (Type Ib/c) in the test set.

There are 8563 unique spectra in our training set, of which 3015 are SEDM spectra of 1222 unique ZTF transients and 5548 are Open SN Catalog spectra of 1546 unique transients. The training data consists of a broad range of spectral quality, from poor to great SNR (excluding extremely noisy cases), various levels of host galaxy contamination, and various strengths of the emission and absorption features (including completely featureless spectra), so that the models can learn to expect all kinds of observed data and do not overfit on only good quality of data. The test data, containing 1535 SEDM spectra, also shows this wide variety of spectral quality. To assess the model performance on good vs. bad (unclassifiable or difficult to classify) quality spectra, we split the test data into “gold” and “bronze” categories semi-automatically through a combination of parameter thresholding and visual inspection. The classifiability of a spectrum depends not just on the noise and SNR but also on the presence of broad supernova features (or similarity to SNe), which SNID encapsulates well. We found that the number of “good” SNID matches with an  ${}^2rlap > 4$  (referred to as *numSNID* henceforth) serves well as a discriminator for gold vs. bronze split. We found  $numSNID \geq 20$  appropriate for crudely separating spectra with clear supernova features and decent SNR. Next, we visually inspected all Type Ibc (hydrogen-poor) spectra in the test sample to identify spectra with severe host contamination. If the host galaxy has strong typical narrow emission lines ( $H\alpha$ , O III), they show up as blended emission lines in SEDM spectra due to the ultra-low

---

${}^2rlap$  is a SNID parameter indicating the goodness of a template fit.

resolution and appear just like the features of a SN II or SN IIn in SEDM spectra, making automatic identification of the host-contaminated Type Ibc SNe extremely difficult. We keep all of the visually identified host-contaminated samples in the bronze set. Finally, the gold (bronze) test set has a total of 780 (755) SEDM spectra of 431 (369) unique ZTF transients. The split comes out to be nearly 50%.

The properties of the (non-augmented) training and test set samples are shown in Figure 6.1. From the subtype distribution plots in Figure 6.1 (top row), it is immediately obvious that there is a significant imbalance between the subsamples of the hydrogen-rich (Type II) and the hydrogen-poor (Type Ibc) SNe. To correct this imbalance, we augment the data with fake spectra for each subtype by randomly choosing pairs of samples (of that subtype) around similar ages, transforming their wavelengths to rest-frame (deredshifting), and taking their weighted average (random weights). The number of fake samples to create per subtype can be chosen during the data preprocessing step. The fake samples are added to the real data to balance the distribution of training samples across categories for a given classification task. The second row of Figure 6.1 shows the spectral phase (days from maximum brightness at the time of spectral observation) distribution. The time of maximum brightness is not always equal to the peak brightness of the SN, as photometric coverage is sparse for many SNe in the dataset, often missing the rise and the peak. The mean (sigma-clipped) of the H-rich SNe phase distribution is around the maximum brightness, while it is after the maximum brightness for the H-poor SNe phase distribution for all three sets (training, gold test, bronze test). The standard deviation of the H-rich distribution is also higher than the H-poor distribution for all three sets, which reflects the naturally longer duration of H-rich SNe, resulting in more follow-up observations. The third row of Figure 6.1 depicts the distribution of the number of spectra per unique supernova, the mean of which is centered around 2–3 spectra per SN. The training set has more SNe with thorough spectral series data ( $>10$  spectra) owing to the dataset from the Open SN Catalog. The test sets, being exclusively SEDM, only have  $< 10$  SNe per set that have  $\geq 10$  spectra, not significant to affect the performance. These multiple spectra also probe various levels of noise, effects of varying sky background, and age of the SNe, and thus in a way are unique to the models. The fourth and fifth rows show the redshift and peak apparent magnitude distributions of the unique SNe. The redshifts are of the host galaxy of the SNe when available through the NED database or derived from the SNe classification spectra. The peak apparent magnitude distribution shown in the last row of Figure 6.1 is highly dependent on the photometric coverage quality

as mentioned earlier. The peak magnitudes were obtained from the BTS sample explorer page when available or derived from the interpolated light curves. The distributions center around 18 mag, and for the test data drop sharply around 19 mag, as that is the maximum depth attainable by SEDM for reasonable exposure times.

To further help with the classification task, we added the capability to use ZTF  $g$ - and  $r$ -band light curves (Masci et al. 2019) as additional input channels. The light curves can be supplied as fixed-length flux arrays where the fluxes are taken from the first detection of the transient in ZTF to a set number of days (200 days past first detection by default). The fixed length of arrays is a requirement of the model architecture. Both the SEDM spectra and ZTF light curves were queried from the dynamic user interfaces, the GROWTH Marshal (Kasliwal et al. 2019) and Fritz (Walt et al. 2019; Coughlin et al. 2023). No light curve information is currently supplied with the Open SN catalog spectra. We also added another method of providing the light curves by transforming them into “ $\delta m - \delta t$ ” phase space (Mahabal et al. 2017). The  $\delta m - \delta t$  representation takes all pairs of light curve points and maps them to a 2D space with the y-axis being the magnitude difference and the x-axis being the time difference (in days) between the two points. This 2D space can potentially capture the different rise and decline rates of various subtypes. The program offers optional usage of these additional channels for training. Further details on data preprocessing are described in the sections below. Figure 6.2 shows examples of input data samples for the various subtypes. A data “sample” in this study refers to one spectrum with its corresponding  $g, r$  light curves, and their  $\delta m - \delta t$  representations. Note that there can be multiple spectra of the same supernova, but each spectrum is counted as an individual sample. We have split the Type IIb class into ‘IIb-H’ (spectra at phases in which  $H\alpha$  P-Cygni dominates) and ‘IIb-noH’ (spectra at phases when the  $H\alpha$  feature has weakened and turned towards the nebular phase) to put in the H-rich and H-poor classes. Except for the IIc and IIb-noH examples, all shown examples are representative of spectra taken near peak-light and are good quality, not host-contaminated SEDM spectra that show strong and clear SN features. However, as mentioned earlier, the training samples span a wide range of SNR and SN feature strengths.

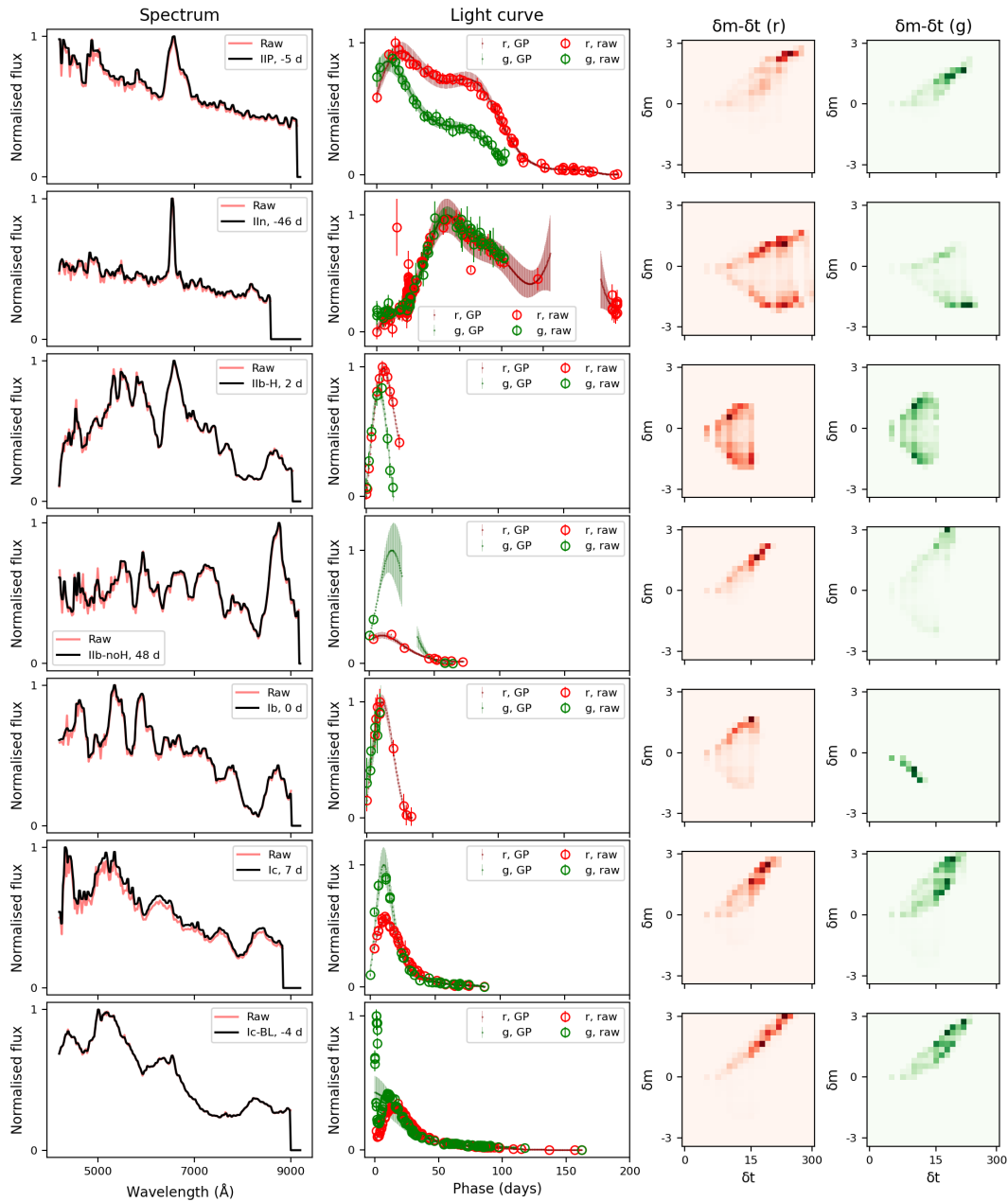


Figure 6.2: Training data samples representing the various transient types (rows). The first column shows the raw (red) and processed (black) normalized spectra, the second column shows the raw and GP-interpolated  $r$ - and  $g$ -band normalized light curves, and the third and fourth columns show  $\delta m - \delta t$  representations of the  $r$ - and  $g$ -band GP-interpolated light curves, respectively.

## Preprocessing

### Optical spectra

All spectra are deredshifted using the redshifts obtained from the GROWTH Marshal and Fritz for ZTF transients and the Open SN Catalog for the rest. Though SEDM spectra cover the wavelength range between 3700 Å and 9200 Å the bluest part of the spectra have been observed to be noisy. Therefore, we restrict the deredshifted wavelength range from 4200 Å to 9200 Å and interpolate the fluxes with a cubic spline function to get fluxes at a fixed space wavelength array of 256 points (to match the sampling across SEDM and Open SN catalog spectra) in the mentioned wavelength range. This flux array is then median filtered, normalized, and any ‘nan’ values are converted to zero. We do not divide the spectra by the continuum, as the continuum also contains information relevant to supernova classification.

### 1D light curves

We take the  $5\sigma$  detections from the ZTF  $g$ - and  $r$ -band light curves and fit them using Gaussian process (GP) regression with brightness as the dependent variable (in magnitudes) and phase from the first detection as the independent variable (in days). Interpolation is necessary as the cadence of the light curves is not constant and there are gaps in the data due to weather, sun occultation, and instrument downtime. We use a combination of a radial basis function (RBF, also known as “squared-exponential”) kernel with length scale bounds between (20,200) days, and a White Kernel to characterize the noise. We interpolate magnitudes and magnitude errors between the first and last detection in 1-day bins. Since all the input samples to the model need to be of fixed length, we pad the interpolated light curves with zeros if they are shorter than 200 days, and truncate if they are longer. These fixed-length magnitudes and magnitude error arrays are then converted to linear fluxes ( $\text{erg s}^{-1} \text{cm}^{-2} \text{Å}^{-1}$ ) and normalized. The light curves are not redshifted or K-corrected to limit preprocessing steps, especially the ones that rely on prior redshift being available. The final input that goes to the model is a stacked array with fluxes at the  $0^{\text{th}}$  index and flux errors at the  $1^{\text{st}}$  index, with a shape of (200,2) per sample.

### $\delta m - \delta t$ light curves

From the interpolated light curves, we compute the magnitude and time (in days) difference for all pairs of light curve points and create a 2D histogram with fixed but non-uniform bin sizes in magnitude and phase space. The bin intervals are decided

based on the magnitude ranges that our transients span and their typical duration timescales. The magnitude bin edges are  $[-4.5, -3, -2.5, -2, -1.5, -1.25, -0.75, -0.5, -0.3, -0.2, -0.1, -0.05, 0, 0.05, 0.1, 0.2, 0.3, 0.5, 0.75, 1.25, 1.5, 2, 2.5, 3, 4.5]$  mags, and the phase bin edges are  $[0, \frac{1}{24}, \frac{4}{24}, 0.25, 0.5, 0.75, 1, 2, 3, 6, 9, 12, 15, 24, 33, 48, 63, 72, 96, 126, 153, 180, 216, 255, 300]$  days. The shape of these 2D histogram inputs is (24,24) per sample. Examples of  $\delta m - \delta t$  histograms for the SN subtypes are shown in Figure 6.2.

### Simulated data for augmentation

The number of synthetic samples to create per subtype is specified during the preprocessing step. For a given subtype, we create two subsets from its training samples depending on the phase of the spectrum. The first subset (early-time phase) contains spectra taken before the light curve maximum, and the second subset (photospheric phase) has spectra taken after the light curve maximum till the SN becomes nebular. We use the early-time subset to create 30% of the total synthetic samples and the photospheric subset for the remaining 70%. To make a synthetic sample, we randomly choose pairs of samples from a subset without replacements and take the weighted average of their rest-frame (deredshifted) spectra with randomly chosen weights to generate the synthetic spectrum. We also set the synthetic sample’s redshift to the weighted average of the pair’s redshifts. Then, we pick one of the light curves from the pair, scale its flux to the new luminosity distance (redshift), and use it to generate the synthetic 1D interpolated light curves and their  $\delta m - \delta t$  representations for the synthetic sample.

### 6.3 Parallel binary classifiers

We used *Keras* (Chollet et al. 2015) Python library on top of TensorFlow (Martín Abadi et al. 2015) framework for this study. We initially started with a single multiclass model to classify all CCSN subtypes, similar to what is done in DASH (Muthukrishna et al. 2019a). During early training and validation, although the overall model accuracy was poor ( $\sim 50\%$ ), we recognized that the H-rich subtypes (Type II) formed a group, better separated from the H-poor subtypes (Type Ibc) group. Thus, we decided to make an application divided into two hierarchical layers based on the current core-collapse SN classification scheme and use parallel binary classifiers (also known as the One vs. Rest strategy) in each layer instead of a single multiclass model. Our application’s layer 1 has two binary classifiers, one trained for hydrogen-rich (H-rich) SNe and the second for hydrogen-poor (H-poor) SNe.

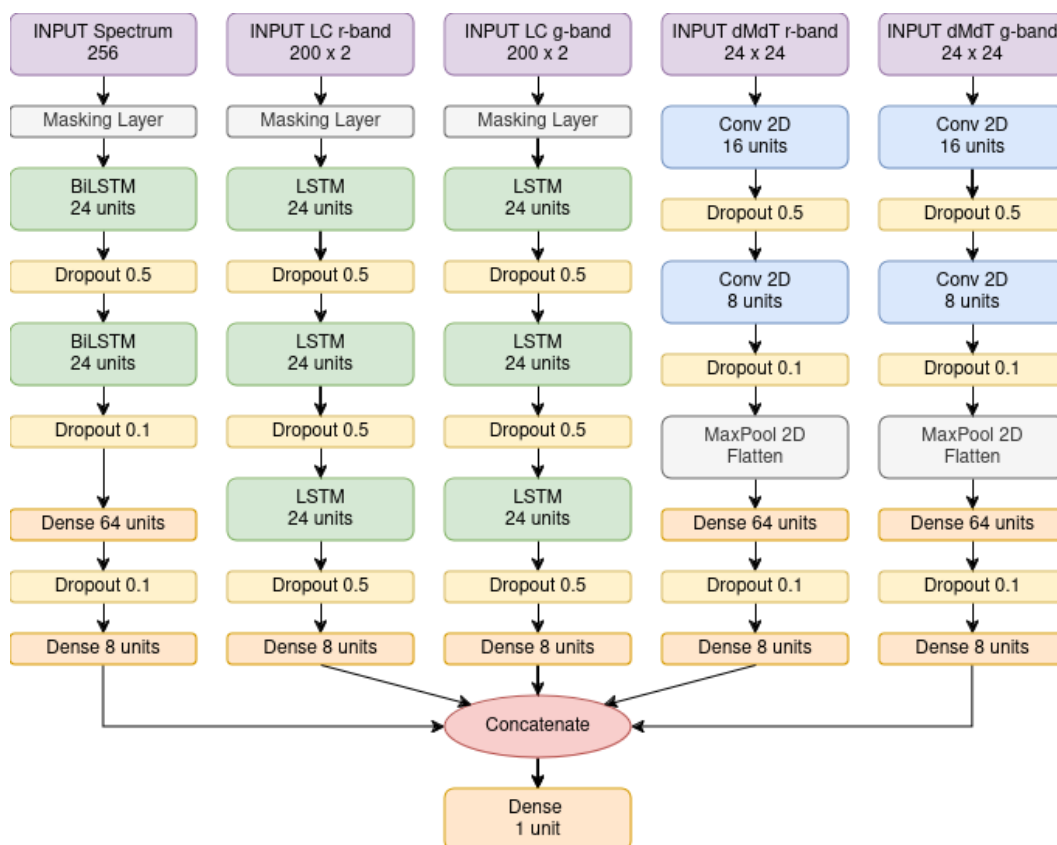


Figure 6.3: Multi-channel network architecture of CCSNscore. We found two bidirectional LSTM layers optimal for the spectrum channel, and three LSTM layers optimal for the light curve channels.

Though this could have been a single binary classifier task, we train two parallel classifiers for an added layer of robustness. Layer 2a has three binary classifiers for three major subtypes of H-rich SNe (II—normal Type II spectra, IIb-H—IIb spectra with hydrogen present, IIn—narrow lines from interaction), and layer 2b also has three models for major subtypes of H-poor SNe (Ib, Ic, Ic-BL). In total, we have eight binary classification tasks.

The number of samples in the training and test sets for each layer is outlined in Table 6.1. The number inside brackets in the ‘training samples’ column in Table 6.1 is the real number of training samples of that class, and the number outside brackets is the total training samples, including the augmented data. The number of augmented samples added to each class is such that the total number of samples is roughly balanced across all classes in that layer, making the training samples of the sub-layers 2a and 2b not add up to the respective layer 1 numbers. The gold vs. bronze test set evaluation is only done for layer 1.

Table 6.1: Total number of samples in the training and test sets per binary classifier. The total number of training samples (including augmented data) per class is listed outside brackets in the second column, while the real number of training samples is listed inside brackets. The number of samples in the gold test set is listed outside brackets in the third column, while the number of samples in the bronze set is listed inside brackets for Layer 1. The amount of augmented data added to each classifier in a layer is such that the samples per class are roughly balanced.

Classifier	# Training samples Total (real)	# Test samples Gold (bronze)
Layer 1		
H-rich	8478 (6025)	627 (536)
H-poor	8869 (2538)	153 (219)
Layer 2a		
II	6027 (4713)	911
IIb-H	5500 (471)	80
IIIn	5999 (841)	172
Layer 2b		
Ib	1761 (760)	110
Ic	1775 (774)	142
Ic-BL	1844 (343)	103

The architecture of a single binary classifier model that we arrived at after the optimization process described in Section 6.4 is shown in Figure 6.3. The models can be trained with up to five input channels, one for 1D optical spectra (the only required channel), two for 1D ZTF light curves (LC;  $r$  and  $g$  bands), and two for the  $\delta m - \delta t$  representations of the 1D light curves. The multiple inputs are processed through separate network paths concatenated at the end, and the output is passed through a final dense layer with a sigmoid activation function to generate the final output probabilities. We experimented with several configurations by varying the kind of neural network layers in the channels and the number of layers per channel to arrive at the base architecture and then optimized its hyperparameters.

#### 6.4 Optimization and training

For the first step of the optimization process, we kept the number of NN layers constant (two per channel) and trained several models varying just the NN layer type. For spectra and 1D light curves, we decided to test 1D convolutional neural

networks (CNN) and recurrent neural networks (RNN), specifically Gated Recurrent Unit (GRU), Long Short-Term Memory (LSTM), and bi-directional LSTM among the RNN layer types. For  $\delta m - \delta t$  we decided to use 2D CNN layers. We used a 10% dropout rate<sup>3</sup> in between NN layers to tackle overfitting of the data. These initial models were compiled with the Adam optimizer (initial learning rate,  $lr = 0.001$ ) and BinaryCrossentropy loss. The models were trained on H-rich and H-poor classification tasks with a batch size<sup>4</sup> of 32, a validation split<sup>5</sup> of 33%, and an early stopping criteria<sup>6</sup> (patience value of 7 on validation loss). Validation accuracy and precision were used to decide the best model. We found that bi-LSTM layers performed best for the spectral channel and LSTM layers performed best for the 1D light curve channel, as they captured the connections present within these serial data. We then optimized the number of NN layers in each channel by varying them in one channel at a time between 1 to 4 NN layers, keeping the other channels and dropouts unchanged. The models were compiled, trained, and evaluated in the same manner as before, and the optimal number of NN layers found per channel are shown in Figure 6.3. Next, with the help of `kerastuner`, we trained a grid of models varying the hyperparameter values within the ranges listed in Table 6.2 to find the best-performing values. This tuning was done separately for H-rich and H-poor binary classifiers (all input channels used), and both classifiers settled to the same optimal hyperparameters. We applied further manual tuning to arrive at the final hyperparameter values shown in Figure 6.3. Our best-performing model favors high dropout rates similar to SNIascore. We found that the initial learning rate of the Adam optimizer,  $lr = 0.001$ , and a mini-batch size of 64 performed well across all the binary classifiers.

For the final training of the binary classifiers, we set the training-validation split to 0.33, set training epochs to 100, and set an early stopping criterion with a patience value of 7 on the validation loss metric. For balanced training of the binary classifiers in case one class has more samples than the other, we take all samples of the smaller class and choose an equal number of samples from the larger class for the first round of training. Then, we repeat the training by redrawing samples from the larger class without substitution until enough samples are left in the larger class or the training has been repeated three times. After all the binary classifiers

---

<sup>3</sup>Percentage of nodes intentionally dropped from the neural network to prevent overfitting.

<sup>4</sup>The number of samples used in one training pass of the network.

<sup>5</sup>Percentage of training data to be used for validation.

<sup>6</sup>A conditional criteria to stop the training of a model early if the loss does not decrease for a certain number (patience value) of epochs.

Table 6.2: Hyperparameter ranges for tuning binary classifiers with kerastuner.

Layers	Range (units)	Step (units)
biLSTM	4–24	4
LSTM	4–24	4
Conv 2D (1)	16–64	16
Conv 2D (2)	8–32	8
Dense	8–64	8
Dropout	0.1–0.9	0.2

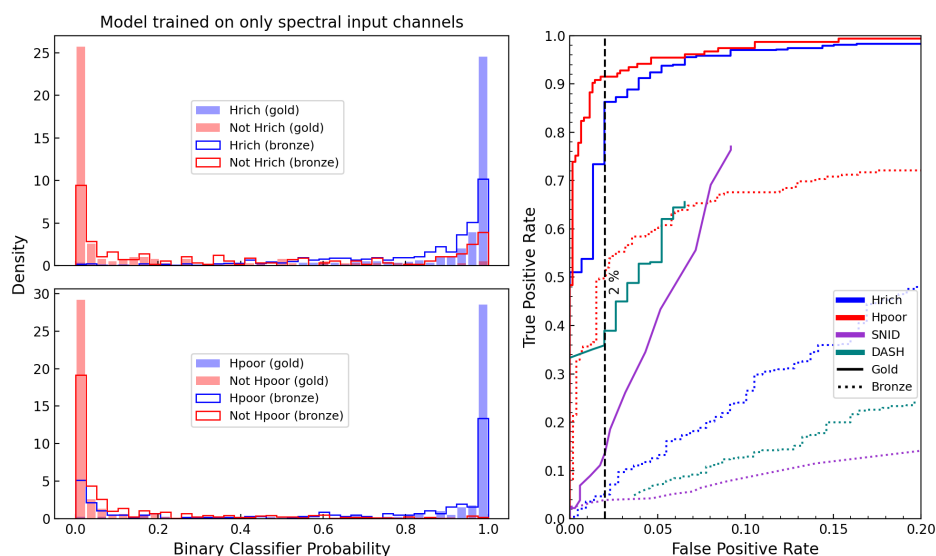
have been trained and saved, we predict the final classifications on the test sets. We generate 100 predictions per sample with dropout enabled in the trained model (Monte Carlo Dropout technique) and calculate the mean and standard deviation of the 100 predicted probabilities to get the final predicted probability and the uncertainty on it. This is done for each sample to get predictions from each binary classifier. We use the following scheme to get the final classifications based on the probabilities given by the parallel classifiers. The classifier that provides the maximum probability is chosen as the final class (and the max probability as the final score) if the difference between the highest and the second highest probabilities is more than the sum of their uncertainties. The remaining samples are assigned an ‘ambiguous’ classification and a score of zero.

We also train sets of models for different input channel combinations (input cases) for each binary classification task to compare the contribution of the light curve input in different forms. The input cases are as follows: ‘only spectra’, ‘spectra + 1D LC’, ‘spectra +  $\delta m - \delta t$ ’, and ‘spectra + 1D LC +  $\delta m - \delta t$ ’ (all channels). The results of this comparison are presented in §6.5.

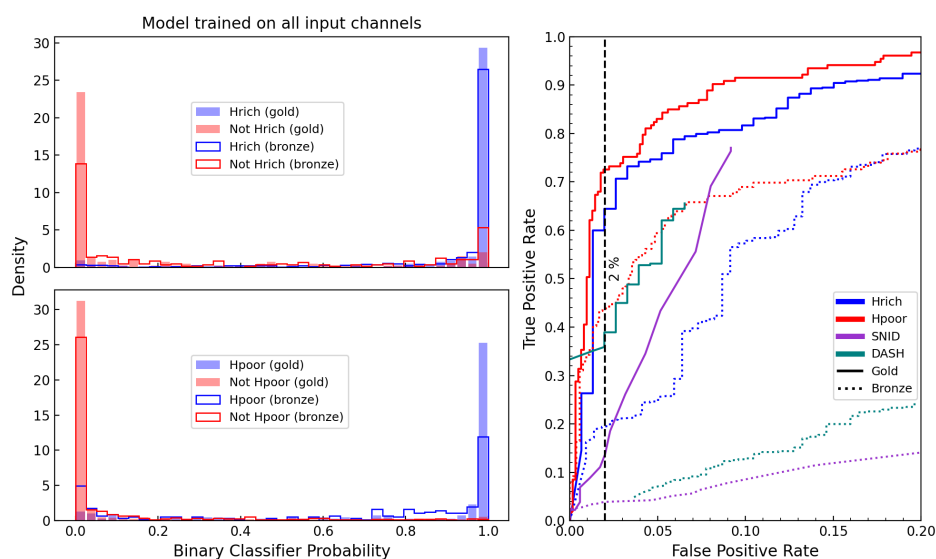
## 6.5 Performance

### Layer 1: H-rich vs. H-poor

Figures 6.4 and 6.5 show the performance of the layer 1 classification task, i.e., H-rich vs. H-poor. Figure 6.4a shows results for the “only spectra” input case models and Figure 6.4b for the “all channels” input case models. The left panel in both subfigures shows the distribution of probabilities predicted for the gold (filled bars) and bronze (not filled bars) test sets, with blue bars denoting samples that belong to the class (positive) and red bars for samples that do not (negative). For any good binary classifier, this distribution should be highly bimodal, with the positive



Results from binary classifiers trained only using the spectral input channel.



Results from binary classifiers trained using all input channels, i.e. spectra, light curves, and  $\delta m - \delta t$ .

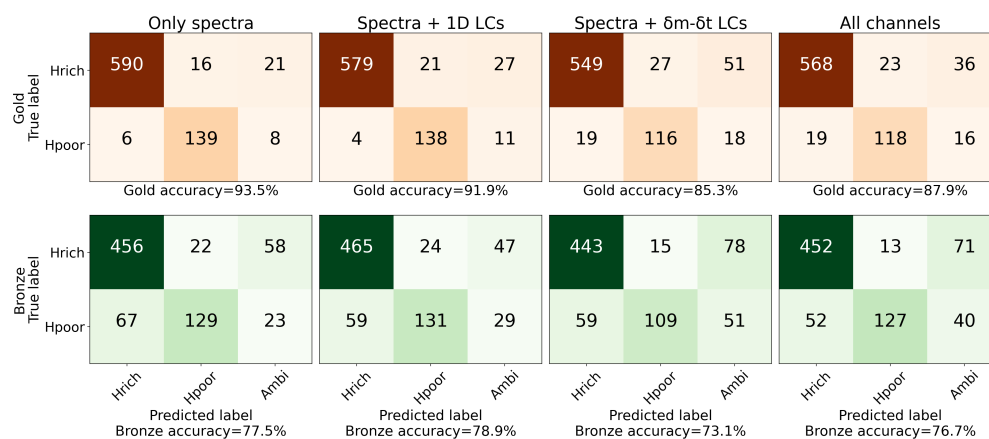
Figure 6.4: Performance of layer 1 binary classifiers on gold and bronze test sets. *Left:* Distribution of binary classifier predicted probabilities for positive class (blue) vs. negative class (red) for H-rich and H-poor classifiers. The gold test set distribution is depicted as filled bars, and the bronze set distribution as empty steps. *Right:* ROC curve from the two layer-1 binary classifiers (blue and red), with SNID (purple) and DASH (teal) for comparison. The gold set curves are depicted with solid lines and the bronze set curves with dotted lines. The black vertical dashed line marks a 2% false positive rate.

class getting the highest probability scores and the negative class getting the lowest. Models of both input cases show such bimodal distributions, but the distribution is less sharp for the “only spectra” input case than for the “all channels” case. Thus, adding the light curve inputs to model training results in generally higher predicted probabilities for the positive class and lower predicted probabilities for the negative class. However, it also increases the predicted probabilities of the false positive cases.

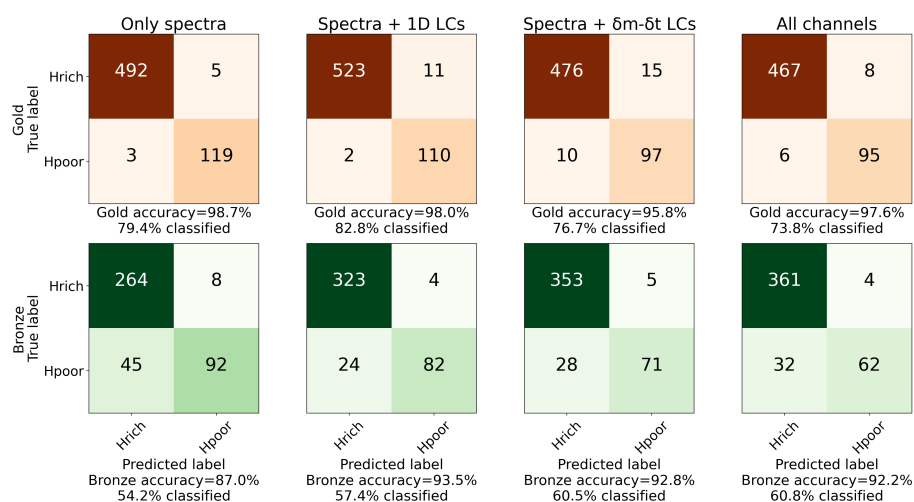
The right panel in both subfigures of Figure 6.4 shows the receiver operating characteristic (ROC) curve for the two layer 1 classifiers (in blue and red lines) on the gold and bronze test sets, along with the SNID (purple lines) and DASH (teal lines) ROC curves for comparison. A ROC curve depicts the true positive rate (TPR) vs. false positive rate (FPR) at all classification thresholds, which for our binary classifiers and DASH are the predicted probabilities, while for SNID are the r1ap scores (see Appendix A for the method used to construct SNID ROC curves). The SNID and DASH ROC curves are calculated considering H-rich as the positive class. Our best classifiers achieve  $\geq 90\%$  TPR compared to SNID’s  $\sim 75\%$  TPR at a FPR of 10% and DASH’s  $\sim 65\%$  TPR at a FPR of  $\sim 6\%$  on the gold set. Similar behavior is observed for the bronze set, with our best classifier achieving 30–60% TPR versus SNID’s and DASH’s  $\sim 10\%$  TPR at a FPR of 10%.

The addition of light curve inputs (both 1D LC and  $\delta m - \delta t$  together) ends up reducing the performance of both classifiers on the gold set but improves the performance on the bronze set, especially for the H-rich case with its area-under-the-curve (AUC) being larger for the model trained on all channels (see solid and dashed lines in right panels of Figures 6.4b and 6.4a respectively). This indicates that perhaps additional input is more suitable when the spectrum is of lesser quality, but can lead to more inaccuracies and model confusion otherwise. This could be due to how the multi-input channels are concatenated in the CCSNScore architecture (see Figure 6.3), with the spectral channel getting less weight as more channels are added.

For directly sending classifications to TNS without human intervention, a model with extremely low FPR is preferred, similar to SNIAscore (Fremling et al. 2021). If 2% FPR can be risked,  $\sim 80\text{--}90\%$  of both H-rich and H-poor gold quality SNe can be sent to TNS using the best-performing models. For SNID, this fraction is only  $\sim 10\%$ . However, programs like SNID, as well as Superfit (Howell et al. 2005) and Gelato (Harutyunyan et al. 2008), were always meant to assist with the classification process and thus perform best with manual user inputs, often



CMs constructed using all of the test samples' classifications. The 'Ambi' column contains samples for which H-rich and H-poor classifiers assigned probabilities within their uncertainties. The overall classification accuracy for the gold set is highest in the 'only spectra' case (without light curve addition), while for the bronze set is highest in the 'spectra + 1D LCs' case. The utility of light curve input is reflected better in Figure 6.5b when probability cuts are applied.



CMs derived using only the test samples that pass confidence and uncertainty cuts. All the ambiguous cases get filtered out with a strict probability cut. The fraction of the test set that qualifies for these cuts is printed under each confusion matrix. More bronze quality data gets reliable predictions when light curve inputs are used.

Figure 6.5: Results from the layer 1 (H-rich vs. H-poor) models. The four columns of confusion matrices (CM) are for the four input cases—'only spectra', 'spectra + 1D LC', 'spectra +  $\delta m - \delta t$ ', and 'spectra + 1D LC +  $\delta m - \delta t$ '. The top row of CMs in each subfigure is for the gold test set, and the bottom row of CMs is for the bronze test set.

providing more information than just the classification (for example, age, fairly accurate redshift, similarity to historical SNe, host galaxy characteristics, etc.). A more appropriate comparison can be made with DASH (Muthukrishna et al. 2019a), which also employs deep learning for automated classification purposes. In Muthukrishna et al. (2019a), DASH’s performance was tested on 212 spectra from OzDES ATELS released between 2015 and 2017, out of which 81% were SNe Ia, and DASH provided correct classifications for 93% of the 212 SNe. However, the same performance of DASH could not be attained on the SEDM spectra as tested in Fremling et al. (2021). Kim et al. (2024) compared the performance of SNID, NGSF (Goldwasser et al. 2022), and DASH on  $\sim 4600$  SEDM spectra and found the automatic accuracy for the five-class classification task (Ia, II, Ibc, SLSN, and notSN) to be  $\sim 63\%$  (SNID),  $\sim 75\%$  (NGSF), and  $\sim 62\%$  (DASH). Particularly for CCSNe, DASH achieved only  $\sim 29\%$  TPR at  $\sim 3\%$  FPR for Type II and  $\sim 79\%$  TPR at  $\sim 32\%$  FPR for Type Ibc, which is not suitable for reporting classifications to TNS. We see the same with DASH’s performance on our test sets, which is  $\sim 35\%$  TPR for the gold set and  $\sim 4\%$  TPR for the bronze set at a  $2\%$  FPR.

Figure 6.5 displays the confusion matrices (CMs) for the gold and bronze test sets derived from the predictions of our layer 1 models (the four input cases). We present the CM data in ‘number of samples’ instead of percentages to emphasize the number of misclassifications. The top row of CMs in both sub-figures (6.5a & 6.5b) are for the gold set and the bottom row of CMs are for the bronze set. The four columns of matrices are for the four input cases (from left to right, ‘only spectra’, ‘spectra + 1D LC’, ‘spectra +  $\delta m - \delta t$ ’, and ‘spectra + 1D LC +  $\delta m - \delta t$ ’). The ‘accuracy’ metric is printed under each CM. Henceforth, ‘only spectra’, ‘spectra + 1D LC’, ‘spectra +  $\delta m - \delta t$ ’, and ‘spectra + 1D LC +  $\delta m - \delta t$ ’ input cases will be referred to as cases ‘S’, ‘SL’, ‘SD’, and ‘SLD’ respectively.

Figure 6.5a shows the CMs constructed by including all samples of test sets without applying any quality cut on the predicted probabilities. As mentioned earlier in §6.4, the classifier that assigns the highest probability is chosen as the class for a test sample if the difference between the highest and the second highest probability is more than the sum of their uncertainties, otherwise, the test sample gets an ‘ambiguous’ tag. These ambiguous cases occupy the third column in the CMs of Figure 6.5a. When spectral quality is good (gold set), the case S model performs better than other input cases, has the lowest number of false and ambiguous predictions, and the highest accuracy of 93.5% (see Figure 6.5a). When spectral quality is poor (bronze

set), all cases perform similarly with case SL having slightly higher accuracy. The true usefulness of the light curve input can be seen in Figure 6.5b, which shows the CMs constructed from the subset of the test sets filtered by cuts on predicted probability ( $P$ ) and their uncertainties ( $P_{unc}$ ) determined heuristically to obtain the most confident classifications. The threshold cuts are  $P > 0.8, P_{unc} < 0.05$  for the gold set, and  $P > 0.9, P_{unc} < 0.05$  for the bronze set (slightly stricter). The filtered subset fraction is printed under each matrix in Figure 6.5b. A high probability threshold reduces false positives and increases accuracy, but discards the test samples that do not pass the threshold cuts. From Figure 6.5b, we note that a higher fraction of bronze test samples pass the cuts in cases SL, SD, and SLD while maintaining high accuracies. For gold test samples, this holds for case SL which has 82.8% confident classifications compared to 79.4% in case S. This increase in high-confidence classifications also slightly increases false positives and negatives, which for the gold set reduces the accuracy in case SL to 98% from 98.7% in case S. But for the bronze set the overall accuracy in case SLD still increases. Thus, multi-input channel models that can ingest auxiliary information relevant to classification are better suited for lesser-quality spectral data.

A caveat with our models is that they were trained on spectra that had been deredshifted (transformed from observed wavelengths to rest-frame wavelengths), and thus would require redshift information for real-time application. To analyze the effect of redshifting, we trained binary classifiers for H-rich and H-poor classes using only the spectral channel and redshifted spectra. We found that the classification accuracy for the whole set (gold + bronze) is  $\sim 85.9\%$ , the same as the performance of models trained on deredshifted spectra. This is expected as bi-directional LSTM layers are capable of capturing dependencies in sequences in both directions simultaneously.

Another caveat with our models is that they were trained using the full duration of light curves but for real-time application, only epochs up until the spectral phase will be available (mostly early-time or pre-peak phase). Thus the real-time performance of the models using light curve input will be different than presented. Hence, we plan on using the Case S models for real-time TNS reporting until the performance of partial light curve input is characterized.

Table 6.3 further lists the following metrics that quantify the performance of our layer 1 models:

$$\begin{aligned}
\text{Accuracy} &= \frac{TP + TN}{TP + FN + FP + TN} \\
\text{Precision (or Purity)} &= \frac{TP}{TP + FP} \\
\text{TPR (or Recall)} &= \frac{TP}{TP + FN} \\
\text{FPR} &= \frac{FP}{FP + TN} \\
\text{F1score} &= \frac{2 \times \text{Precision} \times \text{Recall}}{\text{Precision} + \text{Recall}}
\end{aligned} \tag{6.1}$$

where  $TP$  stands for true positives,  $FP$  for false positives,  $FN$  for false negatives, and  $TN$  for true negatives. Ambiguous cases were counted as  $FN$  for the TPR calculation and  $TN$  for the FPR calculation.

Table 6.3: Performance metrics of the layer 1 task models on the gold and bronze test sets. The total accuracy in the final row shows the combined performance on the gold and bronze sets.

		Only Spectra Case S		Spectra + 1D LCs Case SL		Spectra + $\delta m - \delta t$ Case SD		All channels Case SLD	
		H-rich	H-poor	H-rich	H-poor	H-rich	H-poor	H-rich	H-poor
Gold	F1 score	96.5%	90.3%	95.7%	88.5%	91.9%	78.4%	93.6%	80.3%
	Precision	99.0%	89.7%	99.3%	86.8%	96.7%	81.1%	96.8%	83.7%
	TPR	94.1%	90.8%	92.3%	90.2%	87.6%	75.8%	90.6%	77.1%
	FPR	3.9%	2.6%	2.6%	3.3%	12.4%	4.3%	12.4%	3.7%
	Accuracy	93.5%		91.9%		85.3%		87.9%	
Bronze	F1 score	86.1%	69.7%	87.7%	70.1%	85.4%	63.6%	86.9%	70.8%
	Precision	87.2%	85.4%	88.7%	84.5%	88.2%	87.9%	89.7%	90.7%
	TPR	85.1%	58.9%	86.8%	59.8%	82.6%	49.8%	84.3%	58.0%
	FPR	30.6%	4.1%	26.9%	4.5%	26.9%	2.8%	23.7%	2.4%
	Accuracy	77.5%		78.9%		73.1%		76.7%	
Total	Accuracy	85.6%		85.5%		79.3%		82.4%	

### Layer 1 misclassifications

From Figure 6.5b, there are 3, 2, 10, and 6 samples of the H-poor class from the gold set that get misclassified as H-rich even with confidence cuts in cases S, SL, SD, and SLD respectively. There are 14 unique misclassified samples out of these 21, with some common samples among cases, and the misclassifications share some similarities. The misclassifications in cases S and SL have weak H-poor spectral line features with a strong blue continuum, making them look similar to early-time

H-rich spectra. Out of the 10 misclassifications in case SD, 2 are the same as case S, and the remaining 8 have either long declining or peculiar light curves (unlike regular Type Ibc SNe) possibly influencing the incorrect decision. Finally, of the 6 case SLD misclassifications, 3 are common with case SD, and the remaining 3 are cases that completely lack *g*-band coverage.

Similarly, 5, 11, 15, and 8 gold samples of the H-rich class are misclassified as H-poor in cases S, SL, SD, and SLD respectively. Out of the 5 case S misclassifications, 3 are nebular spectra, 1 does not show  $H\alpha$  emission, and 1 seems to be a genuine mistake. Out of the 11 case SL misclassifications, 7 are nebular spectra from the same supernova, SN 2023rky—a Type IIL (that have a similar light curve shape to H-poor SNe), 1 does not show strong  $H\alpha$  emission, and the remaining 3 are genuine mistakes. Nine of 15 Case SD misclassifications are also from SN 2023rky, 2 do not show  $H\alpha$  emission and 4 are genuine mistakes. For case SLD, 6 out of 8 misclassifications are from SN 2023rky and the remaining 2 are genuine mistakes. There are 20 unique misclassified samples across all cases (39 total) from 12 unique SNe, and 9 samples belong to just one SN.

Considering the bronze set, there are many H-poor SNe misclassified as H-rich (Figure 6.5a), most of which are because of host contamination. For example, 56 out of the 67 bronze set misclassifications in case S are due to host contamination. The host-contamination cases are inherently difficult to classify with SEDM spectra even with the help of SNID or NGSF, and thus often require intervention at the level of raw data reduction. Another observation can be made from Figure 6.5a for the ambiguous cases. The bronze set has more ambiguous classifications for all the input cases, with more H-rich SNe classified as ambiguous (likely due to a higher occurrence of blue featureless spectra).

## **Layer 2: Sub-typing of H-rich and H-poor SNe**

The performance of CCSNscore’s layer 2a and layer 2b models which are trained for classification into subtypes of Type II and Type Ibc respectively are presented in Figure 6.6. The confusion matrices are created with the full set instead of splitting into gold and bronze sets as the rarer subsets already have limited samples. Looking at the effect of light curve input on classification accuracy, layer 2a (SN II subtypes; Figure 6.6a) seems to benefit marginally from the light curve input (particularly  $\delta m - \delta t$ ). While cases SL, SD, and SLD have fewer Type Iib-H and Type IIn samples misclassified as normal Type II, they also have more normal Type II

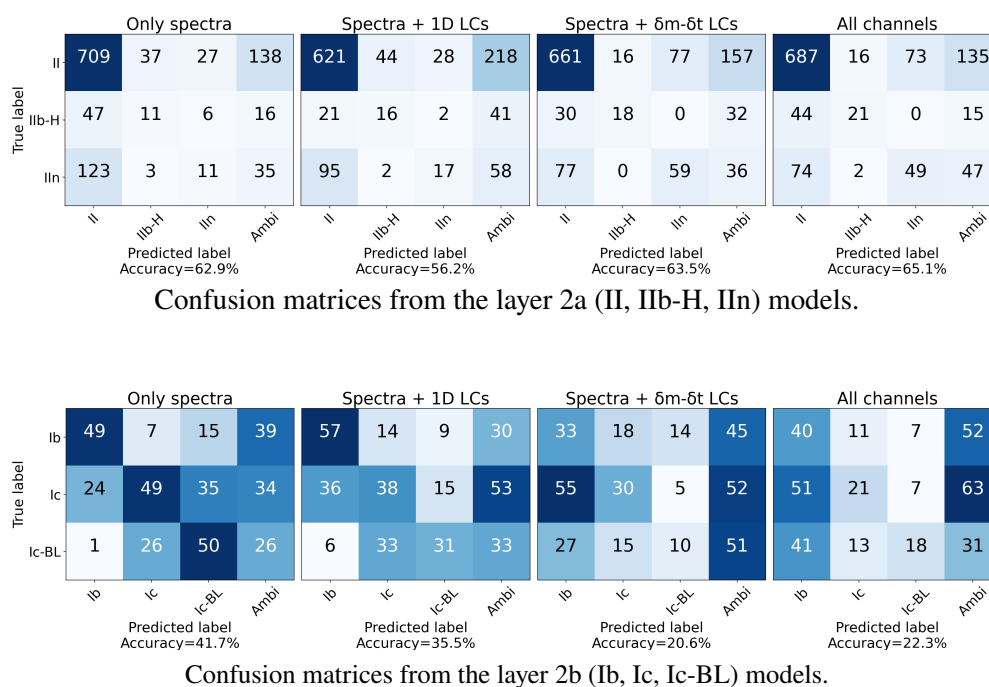


Figure 6.6: Confusion matrices for the whole test set derived from the layer 2 models. The four columns in subfigures are for the four input cases—‘only spectra’, ‘spectra + 1D LC’, ‘spectra +  $\delta m - \delta t$ ’, and ‘spectra + 1D LC +  $\delta m - \delta t$ ’. These confusion matrices were constructed considering all of the test samples’ classifications.

misclassified as the ‘IIc’ or ambiguous.

The opposite effect of light curve addition is seen for layer 2b (SN Ibc subtypes; Figure 6.6b). Cases SL, SD, and SLD have lower accuracies than in case S, with case SD performing the worst. As SESN light curve properties do not differ much among the subtypes, perhaps the extra input information leads to confusion in the models. On the other hand, SN II light curve properties of normal Type II, IIb, and IIc at least show some variety, thus making the extra input marginally useful. From Figure 6.6b, the case S accuracy is the highest at 41.7%, but many misclassifications are among Ic and Ic-BL samples. If Ic and Ic-BL samples are considered just one class (Ic) and accuracy is measured for a Type Ib vs. Type Ic classification, case S accuracy gets bumped up to 58.7% including ambiguous samples. If ambiguous samples are not considered, 72% of the total samples get a non-ambiguous (Ib or Ic) classification out of which 81.7% are correct. Though this might not be robust enough for fully automated classification, the subtype predictions from CCSNscore can be provided as additional information with the TNS reports.

## 6.6 Real-time implementation

CCSNscore will be integrated into the current SEDM pipeline which already runs SNID and SNIAscore. It will be used in conjunction with SNIAscore to infer the classification for real-time application. The following scenarios are possible based on figure 4 of Fremling et al. (2021). First,  $\sim 85\%$  of true SNe Ia and  $\sim 0.5\%$  of true CCSNe are likely to pass  $SNIAscore > 0.6$  cut, which has generally been robust enough for automated SN Ia classification reporting. Since CCSNscore has not been trained on SN Ia data, its performance on real SNe Ia is unreliable, and thus using CCSNscore prediction in this scenario will not help recover the  $0.5\%$  true CCSNe. Therefore, CCSNscore predictions will not be considered where  $SNIAscore > 0.6$ . Next,  $\sim 12\%$  true SNe Ia and  $\sim 9.5\%$  true CCSNe are likely to get  $0.1 < SNIAscore < 0.6$ . In this scenario, a H-rich classification by CCSNscore can mean host-contamination in the spectrum (which should not be sent to TNS), a bad classification, or a true SN II. A H-poor classification by CCSNscore does not provide any distinguishing information as SNe Ia are also hydrogen-poor. We will flag these cases for visual inspection and not report them automatically. In total,  $\sim 10\%$  of true CCSNe will not meet automatic classification criteria during real-time operations. Finally,  $\sim 90\%$  true CCSNe and  $\sim 3\%$  true SNe Ia will likely pass the  $SNIAscore < 0.1$  cut. The  $3\%$  SN Ia false negatives will comprise difficult cases of host contamination, peculiar SNe Ia, or bad classifications. From preliminary analysis, we found that with the strict threshold cuts on  $CCSNscore$  and  $numSNID$  that we apply for TNS reporting (described below), most of these SN Ia false negatives get filtered out and the number of true SNe Ia misclassified as CCSNe that might get sent to TNS goes down to  $\sim 0.5\%$ . From the BTS survey,  $\sim 800$  SNe with  $m_{pk} \leq 18.5$  are expected to be classified as SNe Ia annually, which translates to  $\sim 24$  SNe Ia getting a  $SNIAscore < 0.1$  and only  $\sim 4$  SNe Ia per year passing the further TNS reporting criteria, which is a small number objectively. Therefore, we will use this criteria ( $SNIAscore < 0.1$ ) to filter out potential CCSNe from SNe Ia and  $CCSNscore$ , and  $numSNID$  quality criteria will be used to determine their automatic reporting eligibility. Note that these numbers may change over time based on the real-time performance of the classifiers, so we will adjust the thresholds later on if needed<sup>7</sup>.

As the performance of models that include light curve input on only early-time light curve data has not been characterized, we will use the layer 1 ‘only spectra’ model

---

<sup>7</sup>The current TNS reporting criteria cuts are posted on the CCSNscore GitHub page and will be updated there if any changes are made.

predictions for TNS reporting for now while we further analyze the light curve input performance. Therefore, the  $CCSNscore$  and  $CCSNscore_{unc}$  are the prediction probability and uncertainty on prediction probability, respectively, obtained from the ‘only spectra’ model for H-rich (Type II) vs. H-poor (Type Ibc) task. The TNS reporting criteria will be as follows:

1. For  $numSNID \geq 30$ :  $CCSNscore > 0.8$  and  $CCSNscore_{unc} < 0.05$
2. For  $20 \leq numSNID < 30$ :  $CCSNscore > 0.9$  and  $CCSNscore_{unc} < 0.05$
3. For  $numSNID < 20$ :  $CCSNscore > 0.95$  and  $CCSNscore_{unc} < 0.05$

The number of samples that pass the above three criteria in our full test set (1535 samples) are 634, 49, and 275, respectively (62.4% of the full test set). Out of these, 598, 48, and 255 are correct classifications, which corresponds to a  $\sim 94\%$  accuracy rate and 6% misclassifications. Among the SESNe in the full test set, 174, 13, and 59 pass the three TNS reporting criteria respectively, which corresponds to  $\sim 66\%$  of the total SESNe (372). Again from the BTS survey,  $\sim 81$  SNe with  $m_{pk} \leq 18.5$  are expected to be classified as SESNe annually, and therefore  $\sim 66\%$  of them or  $\sim 53$  will pass the TNS reporting criteria. Therefore, the  $\sim 4$  SNe Ia that are expected to be falsely reported to TNS as SESNe annually will make up  $\sim 7.5\%$  of the total reported SESNe classifications. Improving the SN Ia automatic classifiers can help reduce these false positives in the future.

A breakdown of the true positive rate by phase and true type is shown in Table 6.4 for the samples that pass the TNS criteria. We do not see a significant difference with phase for Type II samples under any criteria. However, Type Ibc samples under  $numSNID \geq 30$  have a higher true positive rate and precision for earlier phases (phase  $\leq 10$  days), while for  $numSNID < 20$ , the true positive rate and precision are higher for the later phases. This indicates that the difficult cases have a better chance of successful classification with post-peak spectra. We plan on further testing and revising this selection scheme over the next few months before actually starting real-time TNS reporting.

## 6.7 Discussion and Summary

In this work, we have presented a new deep-learning based software for the automated classification of core-collapse supernovae from their ultra-low resolution spectra (from SEDM) called CCSNscore. CCSNscore consists of hierarchical classification

Table 6.4: Performance of the layer 1 ‘only spectra’ model predictions on the test samples that pass the TNS reporting criteria. The true positive rate and precision values are reported separately by phase ( $\leq 10$  days or  $> 10$  days) and the true type (II and Ibc). The number of samples that pass the different TNS criteria is shown in brackets in the first column.

True class:		Type II		Type Ibc	
Phase:		$\leq$ 10d	$>$ 10d	$\leq$ 10d	$>$ 10d
1.	TPR	99.7%	97.5%	83.2%	80.3%
(634)	Precision	94.0%	92.8%	98.9%	92.4%
2.	TPR	100%	100%	87.5%	100%
(49)	Precision	96.4%	100%	100%	100%
3.	TPR	96.4%	95.7%	78.4%	81.8%
(275)	Precision	95.3%	91.8%	82.8%	90.0%

tasks, with its layer 1 meant for classification between Type II (or H-rich) and Type Ibc (or H-poor) SNe, layer 2a meant for classification between subtypes of Type II (II, IIb, IIc), and layer 2b meant for classification between subtypes of Type Ibc (Ib, Ic, Ic-BL). CCSNscore can be trained with up to five input channels, the spectral channel for SEDM spectra being the required input, and the ZTF  $g$ - and  $r$ -band 1D light curves and their respective  $\delta m - \delta t$  representations as four additional inputs. We trained four different models for four input cases (‘only spectra’, ‘spectra + 1D LC’, ‘spectra +  $\delta m - \delta t$ ’, and ‘spectra + 1D LC +  $\delta m - \delta t$ ’) and quantified the benefit of light curves to the classification process. We list our main results below:

- CCSNscore’s layer 1 performance with just spectral data input is quite robust for real-time TNS reporting of the classifications when strict score and uncertainty cuts are applied. Adding light curve input boosts the number of samples with high scores while maintaining accuracy, which can be useful for difficult classification cases. With just spectra, only 79.4% (54.2%) of the gold (bronze) test set pass the threshold cuts, out of which 98.7% (87%) are accurate. Comparatively, with spectra and 1D light curves, 82.8% (57.4%) of the gold (bronze) test set pass the threshold cuts, out of which 98% (93.5%) are accurate.
- CCSNscore also provides subtype predictions from its layer 2 models, which can assist astronomers with manual classifications. The light curve input

marginally improves accuracy over the ‘only spectra’ case in the Type II subtyping task. On the other hand, given that SN Ib and Ic light curves are very similar, the light curve input actually reduces the classification accuracy for the Type Ibc subtyping task.

- RNN architecture seems optimal for ultra-low resolution spectral sequences, as found in this study and in Fremling et al. (2021). The biLSTM layers are also capable of deducing classification without needing redshift correction.
- CCSNscore misclassifies H-poor SNe as H-rich more frequently than it does the other way around because of host-contamination cases, thus making H-poor predictions more reliable until host-contamination is dealt with at the data processing level. The misclassified true H-rich samples come from multiple spectra of a few unique SNe. The misclassified true H-poor samples come less often from multiple spectra of a few unique SNe but often share similar characteristics (weak features, strong host lines, etc.).
- We will use SNIascore to filter out likely SNe Ia and select potential CCSNe candidates by applying a threshold cut of  $SNIascore < 0.1$ . Then, we will apply threshold cuts on  $numSNID$ ,  $CCSNscore$ , and  $CCSNscore_{unc}$  to determine eligible candidates for reporting to TNS as described in §6.6. Based on the BTS statistics on bright transients ( $m_{pk} \leq 18.5$ ) and expected SNIascore and CCSNscore performance, we expect  $\sim 0.5\%$  ( $\sim 4$ ) of true SNe Ia to be misclassified as SNe Ibc on TNS annually. For the classification of CCSNe into Type II or Type Ibc, we expect  $\sim 62\%$  of the total real-time true CCSNe spectra to qualify for TNS reporting, out of which we expect  $\sim 94\%$  correct classifications and  $\sim 6\%$  misclassifications.

Kim et al. (2024) suggests that the effect of instrument resolution might not be significant for SEDM spectra when it comes to classification by SNID, NGSF, and DASH, as all three programs appropriately preprocess the input (including smoothing and binning) to compare to the templates. But still, DASH’s performance on SEDM spectra does not compare to models trained specifically using SEDM spectra like SNIascore and CCSNscore. This arises from the fact that deep learning models can be sensitive to the data they are trained with and do not generalize well until trained with an extremely large quantity of data. Kim et al. (2024) also note that a two-category classification task has more accurate results than a five-category task, as CCSNe are more difficult to classify than SNe Ia, and CCSNe need more

than just spectral information to be classified robustly. CCSNscore addresses the above issues by

1. increasing the training data by including spectra from the Open Supernova Catalog, smoothed to match the varying resolutions to the SEDM training set,
2. splitting the classification tasks into hierarchical layers, which are based on the traditional supernova classification scheme, and training parallel binary classifiers instead of a single multi-class classifier,
3. using a model architecture that can ingest multiple types of inputs, and using photometry data as an additional input.

The dominant source of CCSNscore’s misclassifications is host contamination, which is difficult to eliminate from the final processed spectra. SEDM’s resolution augments the issue by blending the strong host lines around  $H\alpha$ , making them appear like SN II or SN IIn  $H\alpha$  features. There are efforts to separate the SN light from its host galaxy at the data reduction level for SEDM through careful contour separation (Kim et al. 2022) and hyperspectral scene modeling of the host galaxy (Lezmy et al. 2022), which could greatly improve CCSNscore’s automatic typing accuracy.

Another possible method to improve the fidelity of CCSNscore could be changing the way photometric input is supplied and modeled. A well-performing photometric supernova classifier architecture from the literature that has already been tested independently (Charnock et al. 2017; Pasquet et al. 2019; Möller et al. 2020; Burhanudin et al. 2022; Allam et al. 2023) could be added as an additional input channel. Moreover, models that can predict the classification using only early-time photometric data and host-galaxy information will be the most useful as additional channels to CCSNscore (Muthukrishna et al. 2019b; Qu et al. 2022).

CCSNscore is a small step towards handling the increased load of transient spectroscopic data, which will become more important for future photometric and spectroscopic surveys. Currently, CCSNscore is only capable of providing a robust broad Type (II vs. Ibc) and a prediction for a subtype (less accurately), but does not provide other crucial information that can be deduced from spectra (redshift and phase). Future work for CCSNscore could focus on attempting redshift prediction using a similar model structure and exploring auxiliary inputs that can aid in such a task.

## 6.8 Acknowledgment

Based on observations obtained with the Samuel Oschin Telescope 48-inch and the 60-inch Telescope at the Palomar Observatory as part of the Zwicky Transient Facility project. ZTF is supported by the National Science Foundation under Grants No. AST-1440341 and AST-2034437 and a collaboration including current partners Caltech, IPAC, the Weizmann Institute of Science, the Oskar Klein Center at Stockholm University, the University of Maryland, Deutsches Elektronen-Synchrotron and Humboldt University, the TANGO Consortium of Taiwan, the University of Wisconsin at Milwaukee, Trinity College Dublin, Lawrence Livermore National Laboratories, IN2P3, University of Warwick, Ruhr University Bochum, Northwestern University and former partners the University of Washington, Los Alamos National Laboratories, and Lawrence Berkeley National Laboratories. Operations are conducted by COO, IPAC, and UW. The ZTF forced-photometry service was funded under the Heising-Simons Foundation grant #12540303 (PI: Graham). The SED Machine is based upon work supported by the National Science Foundation under Grant No. 1106171. This work was supported by the GROWTH project (Kasliwal et al. 2019) funded by the National Science Foundation under Grant No 1545949. MMK acknowledges generous support from the David and Lucille Packard Foundation. The Gordon and Betty Moore Foundation, through both the Data-Driven Investigator Program and a dedicated grant, provided critical funding for SkyPortal.

Y. Sharma thanks the LSSTC Data Science Fellowship Program, which is funded by LSSTC, NSF Cybertraining Grant #1829740, the Brinson Foundation, and the Moore Foundation; her participation in the program has benefited this work. M.W.C. acknowledges support from the National Science Foundation with grant numbers PHY-2308862 and PHY-2117997. Zwicky Transient Facility access for N.R. was supported by Northwestern University and the Center for Interdisciplinary Exploration and Research in Astrophysics (CIERA). Y.-L.K. has received funding from the Science and Technology Facilities Council [grant number ST/V000713/1].

*Software:* pandas (team 2020), NumPy (Harris et al. 2020), astropy (Astropy Collaboration et al. 2013; Astropy Collaboration et al. 2018), Keras (Chollet et al. 2015), TensorFlow (Martín Abadi et al. 2015).

## 6.9 Appendix A: SNID ROC curve

To construct the SNID ROC curve of Figure 6.4, we ran SNID on our gold and bronze test sets with the following settings. We set  $lapmin = 0.1$ ,  $rlapmin = 0$ , set ‘Ia’ and ‘notSN’ as template types to avoid (as we wanted to obtain only CCSN predictions), set maximum redshift  $zmax = 0.2$ , and ran SNID with interactive and plotting disabled on all spectra. The top SNID match of each sample was set as the automatically predicted classification from SNID. For the subset of spectra that did not get any template matches with the above settings, we gradually increased  $zmax$  to 0.5 until all samples had at least one match. The predicted classifications were then labeled as H-rich or H-poor based on the SNID assigned type, and the  $rlap$  scores were used to measure the confidence in those predictions. Then to calculate the ROC curve, we used  $rlap$  thresholds in the range 0–25 with a step of 1, and at each threshold, we calculated the true positive rate and the false positive rate, considering H-rich as the true positive class.

## Chapter 7

### SUMMARY

In this final chapter, I summarize the advances made in this thesis and highlight the prospects in the context of the upcoming Vera Rubin Observatory.

#### 7.1 Probing the extent of CSM in SNe Ia

In Chapter 2, I present a systematic sample of 12 new SNe Ia-CSM from the ZTF Bright Transient Survey, nearly doubling the current sample size. These events show some distinct spectral features that can be used to distinguish them from normal SNe IIn, such as larger Balmer decrements and weaker  $H\beta$  strength. SNe Ia-CSM show strong mid-IR emissions and signs of new dust formation. Their host galaxies tend to be late-type with ongoing star formation. No pre-explosion precursors were found. I estimate that SNe Ia-CSM make up 0.02–0.2% of all SNe Ia, which is consistent with the theoretical rate from the common-envelope wind (CEW) model of Han et al. (2006).

Future surveys like the Legacy Survey of Space and Time (LSST) of the Rubin Observatory will be key to refining rates and understanding the progenitors of this class. With its unprecedented depth of  $\sim 24$  mag, Rubin will be able to put strong constraints on the precursors to SNe Ia-CSM. Rubin will also probe faint late-time excess emission in SNe Ia, and thus constrain the number of SNe Ia that have delayed CSM interaction of any degree. Furthermore, *JWST* can probe the formation of new dust in these objects.

#### 7.2 Building systematic samples of double-peaked SESNe

In Chapter 3, I analyze the observations of SN 2023aew—a unique double-peaked light curve with a bright precursor and a broad main peak with some undulations. Spectral evolution suggests the precursor showing at least broad velocity hydrogen, which disappears during the main peak that looks like typical stripped-envelope spectra, and reappears in late phases. The horned structure of prominent nebular lines of [O I], Mg I], [Ca II], and the emission around  $H\alpha$  suggests asphericity, possibly hidden CSM powering the SN. This event offers rare insight into the final stages of massive star evolution, warranting further theoretical investigations into the mechanisms of eruptive mass loss and asymmetric and clumpy CSM geometries

powering supernovae.

In Chapter 4, I analyze a systematic sample of clearly double-peaked Type Ibc SNe in ZTF (including SN 2023aew) with two particular SNe in the forefront: SN 2021uvy—a slow-evolving and luminous spectroscopically normal Type Ib, and SN 2022hgk—a typically luminous and spectroscopically normal Type Ib. SN 2021uvy shows a rise in photospheric temperature and a constant color evolution during the second peak, which indicates renewed energy injection, and matches the models put forth by Moriya et al. (2022); while SN2022hgk fits within a group consistent with being powered by a double-nickel distribution (Orellana et al. 2022). I quantify key light curve properties of this double-peaked sample and find a correlation between the absolute magnitudes and luminosities of the two peaks. The growing sample highlights the need for double-peaked SESNe to be studied as a sample.

The ongoing CATS150 survey of ZTF—a volume-limited survey of the local universe to 150 Mpc will collect a comprehensive sample of core-collapse SNe that will be followed up by the Next Generation Palomar Spectrograph on the Palomar 200-inch telescope. CATS150 will create a systematic sample of these double/multi-peaked SESNe, which will help constrain the observed rates of such objects. The higher cadence ZTF survey will catch the fast-duration peaks and bumps, while Rubin will provide the depth to detect any precursor and postcursor bumps.

### **7.3 SEDM-KP, a new supernova classifier on the horizon**

In Chapter 5, I present SEDM-KP, a fully robotic, ultra-low-resolution spectrograph on the Kitt Peak 84-inch (KP84) telescope, designed as an upgraded counterpart to the SEDM on the Palomar 60-inch (P60) telescope. With twice the effective area of the telescope as P60 and nearly twice the instrument efficiency as SEDM, SEDM-KP can classify fainter transients. The fully robotic operations enable rapid follow-up of fast-fading events, and the EMCCD imager enables fast cadence photometry. Despite challenges, including COVID delay, wildfire, and telescope mechanical failures, robotic operations were successfully established, and early science data were collected. Ongoing upgrades will optimize performance, positioning SEDM-KP as a key asset in the Rubin/LSST era.

### **7.4 Future of AI in supernova classification**

In Chapter 6, I present *CCSNscore* (see Figure 7.1), a deep-learning classifier for core-collapse supernovae using ultra-low-resolution SEDM spectra, with multi-modal capabilities to use ZTF light curves. Its hierarchical architecture distinguishes

between Type II and Ibc SNe with  $\sim 94\%$  accuracy for real-time classification. Performance is currently best for broad-type classification, though subtype accuracy varies, particularly due to host-galaxy contamination in SEDM spectra. *CCSNscore* improves over other AI tools like DASH by being trained specifically on SEDM data. Future upgrades include better host-light separation and integration of more sophisticated photometric classifiers to improve accuracy and early-time classification.

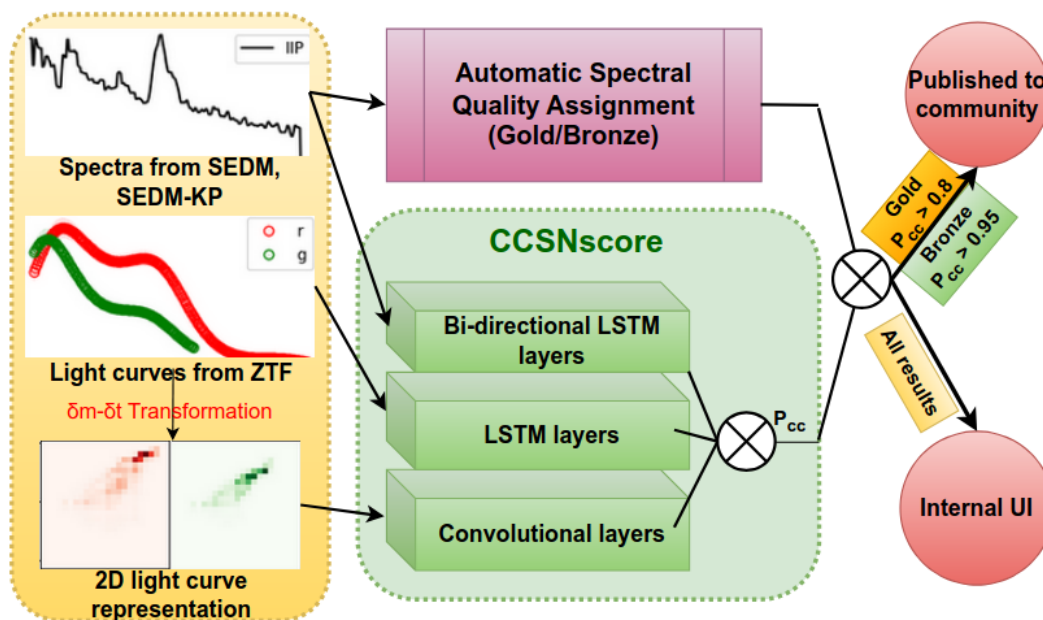


Figure 7.1: A schematic of *CCSNscore*'s workflow. Though it primarily uses SEDM spectra, *CCSNscore*'s multi-modal architecture allows for the use of ZTF  $g$  and  $r$ -band light curves in inference. Additional spectral quality criteria have also been implemented to determine if a spectrum is of good quality (good SNR, SN-like features) to generate reliable predictions.

*CCSNscore* employs a recurrent neural network architecture (Lipton et al. 2015), which is optimal in this case, given the  $\sim$ few thousand samples of CCSNe in the training set. More advanced deep-learning techniques like the Transformer architecture that employs attention mechanisms (Vaswani et al. 2023) can be used to build models that capture features at different scales in large supernova spectral datasets, improving multiclass classification.

Together, these developments lay the groundwork for systematic observations and intelligent automation to work in concert to unlock the full potential of Rubin and beyond.

## BIBLIOGRAPHY

- Abbott, B. P. et al. (Oct. 2017). “GW170817: Observation of Gravitational Waves from a Binary Neutron Star Inspiral”. In: *Phys. Rev. Lett.* 119 (16), p. 161101. DOI: 10.1103/PhysRevLett.119.161101.
- Ahn, C. P. et al. (Dec. 2012). “The Ninth Data Release of the Sloan Digital Sky Survey: First Spectroscopic Data from the SDSS-III Baryon Oscillation Spectroscopic Survey”. In: *ApJS* 203, 21, p. 21. DOI: 10.1088/0067-0049/203/2/21.
- Aldering, G. et al. (Oct. 2006). “Nearby Supernova Factory Observations of SN 2005gj: Another Type Ia Supernova in a Massive Circumstellar Envelope”. In: *ApJ* 650.1, pp. 510–527. DOI: 10.1086/507020.
- Allam Tarek, J. et al. (Oct. 2023). “Paying attention to astronomical transients: introducing the time-series transformer for photometric classification”. In: *RAS Techniques and Instruments* 3.1, pp. 209–223. DOI: 10.1093/rasti/rzad046.
- Andreoni, I. et al. (Sept. 2021). “Fast-transient Searches in Real Time with ZTFReST: Identification of Three Optically Discovered Gamma-Ray Burst Afterglows and New Constraints on the Kilonova Rate”. In: *ApJ* 918.2, 63, p. 63. DOI: 10.3847/1538-4357/ac0bc7.
- Angus, C. R. et al. (Dec. 2024). “Double “acct”: A Distinct Double-peaked Supernova Matching Pulsational Pair Instability Models”. In: *ApJ* 977.2, L41, p. L41. DOI: 10.3847/2041-8213/ad9264.
- Anupama, G. C. et al. (Oct. 2005). “The Peculiar Type Ib Supernova SN 2005bf: Explosion of a Massive He Star with a Thin Hydrogen Envelope?” In: *ApJ* 631.2, pp. L125–L128. DOI: 10.1086/497336.
- Arcavi, I. et al. (Dec. 2011). “SN 2011dh: Discovery of a Type IIb Supernova from a Compact Progenitor in the Nearby Galaxy M51”. In: *ApJ* 742.2, L18, p. L18. DOI: 10.1088/2041-8205/742/2/L18.
- Arcavi, I. et al. (Nov. 2017). “Energetic eruptions leading to a peculiar hydrogen-rich explosion of a massive star”. In: *Nature* 551.7679, pp. 210–213. DOI: 10.1038/nature24030.
- Arnett, W. D. (Feb. 1982). “Type I supernovae. I - Analytic solutions for the early part of the light curve”. In: *ApJ* 253, pp. 785–797. DOI: 10.1086/159681.
- Astropy Collaboration et al. (Oct. 2013). “Astropy: A community Python package for astronomy”. In: *A&A* 558, A33, A33. DOI: 10.1051/0004-6361/201322068.
- Astropy Collaboration et al. (Sept. 2018). “The Astropy Project: Building an Open-science Project and Status of the v2.0 Core Package”. In: *AJ* 156.3, 123, p. 123. DOI: 10.3847/1538-3881/aabc4f.

- Astropy Collaboration et al. (Aug. 2022a). “The Astropy Project: Sustaining and Growing a Community-oriented Open-source Project and the Latest Major Release (v5.0) of the Core Package”. In: *apj* 935.2, 167, p. 167. doi: 10.3847/1538-4357/ac7c74.
- Astropy Collaboration et al. (Aug. 2022b). “The Astropy Project: Sustaining and Growing a Community-oriented Open-source Project and the Latest Major Release (v5.0) of the Core Package”. In: *ApJ* 935.2, 167, p. 167. doi: 10.3847/1538-4357/ac7c74.
- Barbarino, C. et al. (July 2021). “Type Ic supernovae from the (intermediate) Palomar Transient Factory”. In: *A&A* 651, A81, A81. doi: 10.1051/0004-6361/202038890.
- Barbary, K. (Dec. 2016). *extinction v0.3.0*. Zenodo. doi: 10.5281/zenodo.804967.
- Barbon, R. et al. (May 1995). “SN 1993J in M 81: One year of observations at Asiago.” In: *A&AS* 110, p. 513.
- Barkat, Z. et al. (Mar. 1967). “Dynamics of Supernova Explosion Resulting from Pair Formation”. In: *Phys. Rev. Lett.* 18 (10), pp. 379–381. doi: 10.1103/PhysRevLett.18.379.
- Barmantloo, S. et al. (Sept. 2024). “Nebular nitrogen line emission in stripped-envelope supernovae - a new progenitor mass diagnostic”. In: *MNRAS* 533.2, pp. 1251–1280. doi: 10.1093/mnras/stae1811.
- Barnsley, R. M. et al. (Feb. 2012). “A fully automated data reduction pipeline for the FRODOSpec integral field spectrograph”. In: *Astronomische Nachrichten* 333.2, pp. 101–117. doi: 10.1002/asna.201111634.
- Becker, A. (Apr. 2015). *HOTPANTS: High Order Transform of PSF ANd Template Subtraction*. Astrophysics Source Code Library, record ascl:1504.004.
- Bellm, E. C. et al. (June 2019). “The Zwicky Transient Facility: Surveys and Scheduler”. In: *PASP* 131.6, p. 068003. doi: 10.1088/1538-3873/ab0c2a.
- Bellm, E. C. et al. (Feb. 2016). *pyraf-dbsp: Reduction pipeline for the Palomar Double Beam Spectrograph*. Astrophysics Source Code Library, record ascl:1602.002.
- Ben-Ami, S. et al. (Sept. 2012). “The SED Machine: a dedicated transient IFU spectrograph”. In: *Ground-based and Airborne Instrumentation for Astronomy IV*. Vol. 8446. Proc. SPIE, 844686, p. 844686. doi: 10.1117/12.926317.
- Benetti, S. et al. (Dec. 2006). “Supernova 2002ic: The Collapse of a Stripped-Envelope, Massive Star in a Dense Medium?” In: *ApJ* 653.2, pp. L129–L132. doi: 10.1086/510667.
- Benson, P. J. et al. (Apr. 1994). “Light Curves of SN 1993J From The Keck Northeast Astronomy Consortium”. In: *AJ* 107, p. 1453. doi: 10.1086/116958.

- Bersten, M. C. et al. (Apr. 2013). “Early Ultraviolet/Optical Emission of The Type Ib SN 2008D”. In: *ApJ* 767.2, 143, p. 143. doi: 10.1088/0004-637X/767/2/143.
- Bertin, E. et al. (June 1996). “SExtractor: Software for source extraction.” In: *A&AS* 117, pp. 393–404. doi: 10.1051/aas:1996164.
- Bianco, F. B. et al. (Nov. 2011). “Constraining Type Ia Supernovae Progenitors from Three Years of Supernova Legacy Survey Data”. In: *ApJ* 741.1, 20, p. 20. doi: 10.1088/0004-637X/741/1/20.
- Bianco, F. B. et al. (Aug. 2014). “Multi-color Optical and Near-infrared Light Curves of 64 Stripped-envelope Core-Collapse Supernovae”. In: *ApJS* 213.2, 19, p. 19. doi: 10.1088/0067-0049/213/2/19.
- Blagorodnova, N. et al. (Mar. 2018). “The SED Machine: A Robotic Spectrograph for Fast Transient Classification”. In: *PASP* 130.985, p. 035003. doi: 10.1088/1538-3873/aaa53f.
- Blondin, S. et al. (Mar. 2009). “A SECOND CASE OF VARIABLE Na I D LINES IN A HIGHLY REDDENED TYPE Ia SUPERNOVA”. In: *ApJ* 693.1, pp. 207–215. doi: 10.1088/0004-637x/693/1/207.
- Blondin, S. et al. (Sept. 2007). “Determining the Type, Redshift, and Age of a Supernova Spectrum”. In: *ApJ* 666.2, pp. 1024–1047. doi: 10.1086/520494.
- Bloom, J. S. et al. (Dec. 2011). “A COMPACT DEGENERATE PRIMARY-STAR PROGENITOR OF SN 2011fe”. In: *ApJ* 744.2, p. L17. doi: 10.1088/2041-8205/744/2/117.
- Branch, D. et al. (Feb. 2002). “Direct Analysis of Spectra of Type Ib Supernovae”. In: *ApJ* 566.2, pp. 1005–1017. doi: 10.1086/338127.
- Breeveld, A. A. et al. (Aug. 2011). “An Updated Ultraviolet Calibration for the Swift/UVOT”. In: *American Institute of Physics Conference Series*. Ed. by J. E. McEnery et al. Vol. 1358. American Institute of Physics Conference Series, pp. 373–376. doi: 10.1063/1.3621807.
- Brennan, S. J. et al. (Jan. 2024). “Spectroscopic observations of progenitor activity 100 days before a Type Ibn supernova”. In: *arXiv e-prints*, arXiv:2401.15148, arXiv:2401.15148. doi: 10.48550/arXiv.2401.15148.
- Brown, P. J. et al. (May 2009). “Ultraviolet Light Curves of Supernovae with the Swift Ultraviolet/Optical Telescope”. In: *AJ* 137.5, pp. 4517–4525. doi: 10.1088/0004-6256/137/5/4517.
- Brown, P. J. et al. (June 2012). “ASWIFTLOOK AT SN 2011fe: THE EARLIEST ULTRAVIOLET OBSERVATIONS OF A TYPE Ia SUPERNOVA”. In: *ApJ* 753.1, p. 22. doi: 10.1088/0004-637x/753/1/22.
- Brown, P. J. et al. (Sept. 2015). “The first ten years of Swift supernovae”. In: *Journal of High Energy Astrophysics* 7, pp. 111–116. doi: 10.1016/j.jheap.2015.04.007.

- Bruch, R. J. et al. (Aug. 2023). “The Prevalence and Influence of Circumstellar Material around Hydrogen-rich Supernova Progenitors”. In: *ApJ* 952.2, 119, p. 119. DOI: 10.3847/1538-4357/acd8be.
- Burhanudin, U. F. et al. (Dec. 2022). “Pan-chromatic photometric classification of supernovae from multiple surveys and transfer learning for future surveys”. In: *Monthly Notices of the Royal Astronomical Society* 521.2, pp. 1601–1619. DOI: 10.1093/mnras/stac3672.
- Burrows, D. N. et al. (Oct. 2005). “The Swift X-Ray Telescope”. In: *Space Science Reviews* 120.3-4, pp. 165–195. DOI: 10.1007/s11214-005-5097-2.
- Buzzoni, B. et al. (Dec. 1984). “The ESO Faint Object Spectrograph and Camera / EFOSC”. In: *The Messenger* 38, p. 9.
- Byler, N. et al. (May 2017). “Nebular Continuum and Line Emission in Stellar Population Synthesis Models”. In: *ApJ* 840.1, 44, p. 44. DOI: 10.3847/1538-4357/aa6c66.
- Calzetti, D. et al. (Apr. 2000). “The Dust Content and Opacity of Actively Star-forming Galaxies”. In: *ApJ* 533, pp. 682–695. DOI: 10.1086/308692.
- Cartier, R. et al. (Oct. 2024). “Unveiling the nature of SN 2022jli: the first double-peaked stripped-envelope supernova showing periodic undulations and dust emission at late times”. In: *arXiv e-prints*, arXiv:2410.21381, arXiv:2410.21381. DOI: 10.48550/arXiv.2410.21381.
- Cenko, S. B. et al. (Oct. 2006). “The Automated Palomar 60 Inch Telescope”. In: *PASP* 118, pp. 1396–1406. DOI: 10.1086/508366.
- Cenko, S. B. et al. (June 2013). “Discovery of a Cosmological, Relativistic Outburst via its Rapidly Fading Optical Emission”. In: *ApJ* 769.2, 130, p. 130. DOI: 10.1088/0004-637X/769/2/130.
- Chabrier, G. (July 2003). “Galactic Stellar and Substellar Initial Mass Function”. In: *PASP* 115, p. 763. DOI: 10.1086/376392.
- Chambers, K. C. et al. (Dec. 2016). “The Pan-STARRS1 Surveys”. In: *arXiv e-prints*, arXiv:1612.05560, arXiv:1612.05560.
- Charnock, T. et al. (Mar. 2017). “Deep Recurrent Neural Networks for Supernovae Classification”. In: *ApJ* 837.2, L28, p. L28. DOI: 10.3847/2041-8213/aa603d.
- Chen, J. et al. (Aug. 2014). “Optical Observations of the Type Ic Supernova 2007gr in NGC 1058”. In: *ApJ* 790.2, 120, p. 120. DOI: 10.1088/0004-637X/790/2/120.
- Chen, P. et al. (Jan. 2024). “A 12.4-day periodicity in a close binary system after a supernova”. In: *Nature* 625.7994, pp. 253–258. DOI: 10.1038/s41586-023-06787-x.
- Chen, T. -. et al. (Nov. 2018). “SN 2017ens: The Metamorphosis of a Luminous Broadlined Type Ic Supernova into an SN II<sub>n</sub>”. In: *ApJ* 867.2, L31, p. L31. DOI: 10.3847/2041-8213/aaeb2e.

- Chen, T.-W. (Oct. 2019). “ePESSTO+: survey and scientific output”. In: *The Extragalactic Explosive Universe: the New Era of Transient Surveys and Data-Driven Discovery*, 15, p. 15. DOI: 10.5281/zenodo.3478022.
- Chen, Z. H. et al. (Jan. 2023a). “The Hydrogen-poor Superluminous Supernovae from the Zwicky Transient Facility Phase I Survey. I. Light Curves and Measurements”. In: *ApJ* 943.1, 41, p. 41. DOI: 10.3847/1538-4357/aca161.
- Chen, Z. H. et al. (Jan. 2023b). “The Hydrogen-poor Superluminous Supernovae from the Zwicky Transient Facility Phase I Survey. II. Light-curve Modeling and Characterization of Undulations”. In: *ApJ* 943.1, 42, p. 42. DOI: 10.3847/1538-4357/aca162.
- Chevalier, R. A. (Nov. 1989). “Neutron Star Accretion in a Supernova”. In: *ApJ* 346, p. 847. DOI: 10.1086/168066.
- Chiba, R. et al. (Sept. 2024). “Characterization of Supernovae Interacting with Dense Circumstellar Matter with a Flat Density Profile”. In: *ApJ* 973.1, 14, p. 14. DOI: 10.3847/1538-4357/ad6c37.
- Childress, M. J. et al. (Nov. 2017). “OzDES multifibre spectroscopy for the Dark Energy Survey: 3-yr results and first data release”. In: *MNRAS* 472.1, pp. 273–288. DOI: 10.1093/mnras/stx1872.
- Chollet, F. et al. (2015). *Keras*. URL: <https://github.com/fchollet/keras>.
- Chu, M. et al. (Sept. 2021). “ZTF Transient Classification Report for 2021-09-13”. In: *Transient Name Server Classification Report 2021-3171*, pp. 1–3171.
- Chugai, N. N. (June 1991). “Evidence for energizing of H alpha emission in type II supernovae by ejecta-wind interaction.” In: *MNRAS* 250, p. 513. DOI: 10.1093/mnras/250.3.513.
- (Dec. 2009). “Circumstellar interaction in type Ibn supernovae and SN 2006jc”. In: *MNRAS* 400.2, pp. 866–874. DOI: 10.1111/j.1365-2966.2009.15506.x.
- Chugai, N. N. et al. (May 1994). “SN 1988Z: low-mass ejecta colliding with the clumpy wind?” In: *MNRAS* 268, pp. 173–180. DOI: 10.1093/mnras/268.1.173.
- Chugai, N. N. et al. (Dec. 2004a). “Circumstellar interaction of the type Ia supernova 2002ic”. In: *MNRAS* 355.2, pp. 627–637. DOI: 10.1111/j.1365-2966.2004.08347.x.
- Chugai, N. N. et al. (Feb. 2004b). “Type-Ia Supernovae in Dense Circumstellar Gas”. In: *AstL* 30, pp. 65–72. DOI: 10.1134/1.1646691.
- Chugai, N. N. et al. (May 2022). “Origin of post-maximum bump in luminous Type Ic supernova 2019stc”. In: *MNRAS* 512.1, pp. L71–L73. DOI: 10.1093/mnras/1/slab131.
- Clark, P. et al. (Nov. 2021). “Probing the progenitors of Type Ia supernovae using circumstellar material interaction signatures”. In: *MNRAS* 507.3, pp. 4367–4388. DOI: 10.1093/mnras/stab2038.

- Coughlin, M. W. et al. (Feb. 2019). “The Kitt Peak Electron Multiplying CCD demonstrator”. In: *Monthly Notices of the Royal Astronomical Society* 485.1, pp. 1412–1419. DOI: 10.1093/mnras/stz497.
- Coughlin, M. W. et al. (Aug. 2023). “A Data Science Platform to Enable Time-domain Astronomy”. In: *ApJS* 267.2, 31, p. 31. DOI: 10.3847/1538-4365/acdee1.
- Crawford, A. et al. (Mar. 2025). “Peaky Finders: Characterizing Double-Peaked Type IIb Supernovae in Large-Scale Live-Stream Photometric Surveys”. In: *arXiv e-prints*, arXiv:2503.03735, arXiv:2503.03735. DOI: 10.48550/arXiv.2503.03735.
- Damineli, A. et al. (July 1997). “Eta Carinae: a long period binary?” In: *New Astronomy* 2.2, pp. 107–117. DOI: 10.1016/S1384-1076(97)00008-0.
- Das, K. K. et al. (Sept. 2024). “Probing Presupernova Mass Loss in Double-peaked Type Ibc Supernovae from the Zwicky Transient Facility”. In: *ApJ* 972.1, 91, p. 91. DOI: 10.3847/1538-4357/ad595f.
- DBSP DRP* (2021).
- De, K. et al. (Feb. 2020a). “Palomar Gattini-IR: Survey Overview, Data Processing System, On-sky Performance and First Results”. In: *PASP* 132.1008, p. 025001. DOI: 10.1088/1538-3873/ab6069.
- De, K. et al. (Dec. 2020b). “The Zwicky Transient Facility Census of the Local Universe. I. Systematic Search for Calcium-rich Gap Transients Reveals Three Related Spectroscopic Subclasses”. In: *ApJ* 905.1, 58, p. 58. DOI: 10.3847/1538-4357/abb45c.
- Dekany, R. et al. (Mar. 2020). “The Zwicky Transient Facility: Observing System”. In: *PASP* 132.1009, p. 038001. DOI: 10.1088/1538-3873/ab4ca2.
- Deng, J. et al. (Apr. 2004). “Subaru Spectroscopy of the Interacting Type Ia Supernova SN 2002ic: Evidence of a Hydrogen-rich, Asymmetric Circumstellar Medium”. In: *ApJ* 605.1, pp. L37–L40. DOI: 10.1086/420698.
- Dexter, J. et al. (July 2013). “Supernova Light Curves Powered by Fallback Accretion”. In: *ApJ* 772.1, 30, p. 30. DOI: 10.1088/0004-637X/772/1/30.
- Dey, A. et al. (May 2019). “Overview of the DESI Legacy Imaging Surveys”. In: *AJ* 157.5, 168, p. 168. DOI: 10.3847/1538-3881/ab089d.
- Dhawan, S. et al. (Feb. 2022). “The Zwicky Transient Facility Type Ia supernova survey: first data release and results”. In: *MNRAS* 510.2, pp. 2228–2241. DOI: 10.1093/mnras/stab3093.
- Di Stefano, R. et al. (Nov. 2012). “The Absence of Ex-companions in Type Ia Supernova Remnants”. In: *ApJ* 759.1, 56, p. 56. DOI: 10.1088/0004-637X/759/1/56.

- Dilday, B. et al. (Aug. 2012). “PTF 11kx: A Type Ia Supernova with a Symbiotic Nova Progenitor”. In: *Science* 337.6097, p. 942. doi: 10.1126/science.1219164.
- Dilday, B. et al. (Apr. 2010). “Measurements of the Rate of Type Ia Supernovae at Redshift  $z \sim 0.3$  from the Sloan Digital Sky Survey II Supernova Survey”. In: *ApJ* 713.2, pp. 1026–1036. doi: 10.1088/0004-637X/713/2/1026.
- Dong, X.-F. et al. (July 2023). “Magnetar Flare-driven Bumpy Declining Light Curves in Hydrogen-poor Superluminous Supernovae”. In: *ApJ* 951.1, 61, p. 61. doi: 10.3847/1538-4357/acd848.
- Dubay, L. O. et al. (Feb. 2022). “Late-onset Circumstellar Medium Interactions are Rare: An Unbiased GALEX View of Type Ia Supernovae”. In: *ApJ* 926.1, 98, p. 98. doi: 10.3847/1538-4357/ac3bb4.
- Duev, D. A. et al. (2019). “Real-bogus classification for the Zwicky Transient Facility using deep learning”. In: *MNRAS* 489.3, pp. 3582–3590.
- Elmhamdi, A. et al. (Apr. 2006). “Hydrogen and helium traces in type Ib-c supernovae”. In: *A&A* 450.1, pp. 305–330. doi: 10.1051/0004-6361:20054366.
- Ergon, M. et al. (Aug. 2015). “The Type IIb SN 2011dh: Two years of observations and modelling of the lightcurves”. In: *A&A* 580, A142, A142. doi: 10.1051/0004-6361/201424592.
- Evans, P. A. et al. (July 2007). “An online repository of Swift/XRT light curves of  $\gamma$ -ray bursts”. In: *A&A* 469.1, pp. 379–385. doi: 10.1051/0004-6361:20077530.
- Evans, P. A. et al. (Aug. 2009). “Methods and results of an automatic analysis of a complete sample of Swift-XRT observations of GRBs”. In: *MNRAS* 397.3, pp. 1177–1201. doi: 10.1111/j.1365-2966.2009.14913.x.
- Fang, Q. et al. (Mar. 2019). “A hybrid envelope-stripping mechanism for massive stars from supernova nebular spectroscopy”. In: *Nature Astronomy* 3, pp. 434–439. doi: 10.1038/s41550-019-0710-6.
- Fang, Q. et al. (Apr. 2022). “Statistical Properties of the Nebular Spectra of 103 Stripped-envelope Core-collapse Supernovae”. In: *ApJ* 928.2, 151, p. 151. doi: 10.3847/1538-4357/ac4f60.
- Fang, Q. et al. (Oct. 2023). “An aspherical distribution for the explosive burning ash of core-collapse supernovae”. In: *Nature Astronomy*. doi: 10.1038/s41550-023-02120-8.
- Fausnaugh, M. M. et al. (Feb. 2021). “Early-time Light Curves of Type Ia Supernovae Observed with TESS”. In: *The Astrophysical Journal* 908.1, p. 51. doi: 10.3847/1538-4357/abcd42.
- Filippenko, A. V. et al. (Feb. 1999). “Supernova 1999aa in NGC 2595”. In: *IAU Circ.* 7108, p. 2.

- Filippenko, A. V. (Jan. 1997). “Optical Spectra of Supernovae”. In: *ARA&A* 35, pp. 309–355. DOI: 10.1146/annurev.astro.35.1.309.
- Filippenko, A. V. et al. (Jan. 1992). “The Peculiar Type IA SN 1991T: Detonation of a White Dwarf?” In: *ApJ* 384, p. L15. DOI: 10.1086/186252.
- Fitzpatrick, E. L. (Jan. 1999). “Correcting for the Effects of Interstellar Extinction”. In: *PASP* 111.755, pp. 63–75. DOI: 10.1086/316293.
- Folatelli, G. et al. (Apr. 2006). “SN 2005bf: A Possible Transition Event between Type Ib/c Supernovae and Gamma-Ray Bursts”. In: *ApJ* 641.2, pp. 1039–1050. DOI: 10.1086/500531.
- Foley, R. J. et al. (Feb. 2007). “SN 2006jc: A Wolf-Rayet Star Exploding in a Dense He-rich Circumstellar Medium”. In: *ApJ* 657.2, pp. L105–L108. DOI: 10.1086/513145.
- Ford, C. H. et al. (Sept. 1993). “CCD Photometry of Three Types Ia Supernovae: V,R, and I Light Curves”. In: *AJ* 106, p. 1101. DOI: 10.1086/116708.
- Förster, F. et al. (May 2021). “The Automatic Learning for the Rapid Classification of Events (ALeRCE) Alert Broker”. In: *AJ* 161.5, 242, p. 242. DOI: 10.3847/1538-3881/abe9bc.
- Fox, O. D. et al. (Nov. 2011). “A Spitzer Survey for Dust in Type IIn Supernovae”. In: *ApJ* 741.1, 7, p. 7. DOI: 10.1088/0004-637X/741/1/7.
- Fox, O. D. et al. (Feb. 2015). “On the nature of Type IIn/Ia-CSM supernovae: optical and near-infrared spectra of SN 2012ca and SN 2013dn”. In: *MNRAS* 447.1, pp. 772–785. DOI: 10.1093/mnras/stu2435.
- Fremling, C. (Aug. 2021). “ZTF Transient Discovery Report for 2021-08-04”. In: *Transient Name Server Discovery Report 2021-2682*, pp. 1–2682.
- (Apr. 2022). “ZTF Transient Discovery Report for 2022-04-10”. In: *Transient Name Server Discovery Report 2022-932*, p. 1.
- Fremling, C. et al. (Sept. 2016). “PTF12os and iPTF13bvn. Two stripped-envelope supernovae from low-mass progenitors in NGC 5806”. In: *A&A* 593, A68, A68. DOI: 10.1051/0004-6361/201628275.
- Fremling, C. et al. (Oct. 2018). “Oxygen and helium in stripped-envelope supernovae”. In: *A&A* 618, A37, A37. DOI: 10.1051/0004-6361/201731701.
- Fremling, C. et al. (May 2020). “The Zwicky Transient Facility Bright Transient Survey. I. Spectroscopic Classification and the Redshift Completeness of Local Galaxy Catalogs”. In: *ApJ* 895.1, 32, p. 32. DOI: 10.3847/1538-4357/ab8943.
- Fremling, C. et al. (Aug. 2021). “SNIascore: Deep-learning Classification of Low-resolution Supernova Spectra”. In: *The Astrophysical Journal Letters* 917.1, p. L2. DOI: 10.3847/2041-8213/ac116f.

- Frohmaier, C. et al. (Apr. 2023). “SN2023aew: Spectroscopic observation during a significant rebrightening”. In: *Transient Name Server AstroNote* 97, p. 1.
- Fuller, J. et al. (May 2018). “Pre-supernova outbursts via wave heating in massive stars - II. Hydrogen-poor stars”. In: *MNRAS* 476.2, pp. 1853–1868. DOI: 10.1093/mnras/sty369.
- Gaffet, B. (Sept. 1977). “Pulsar theory of supernova light curves. I. Dynamical effect and thermalization of the pulsar strong waves.” In: *ApJ* 216, pp. 565–577. DOI: 10.1086/155498.
- Gal-Yam, A. et al. (Apr. 2009). “A massive hypergiant star as the progenitor of the supernova SN 2005gl”. In: *Nature* 458.7240, pp. 865–867. DOI: 10.1038/nature07934.
- Gal-Yam, A. et al. (Feb. 2021). “Introducing a new Supernova classification type: SN Icn”. In: *TNSAN* 76, pp. 1–76.
- Gal-Yam, A. et al. (Jan. 2022). “A WC/WO star exploding within an expanding carbon-oxygen-neon nebula”. In: *Nature* 601.7892, pp. 201–204. DOI: 10.1038/s41586-021-04155-1.
- Gal-Yam, A. et al. (Sept. 2024). “Introducing a new supernova classification type: SN Ien”. In: *Transient Name Server AstroNote* 239, p. 1.
- Gal-Yam, A. (2017). “Observational and Physical Classification of Supernovae”. In: *Handbook of Supernovae*. Ed. by A. W. Alsabti et al. Cham: Springer International Publishing, pp. 195–237. DOI: 10.1007/978-3-319-21846-5\_35.
- Gal-Yam, A. et al. (Feb. 2007). “On the Progenitor of SN 2005gl and the Nature of Type IIn Supernovae”. In: *ApJ* 656.1, pp. 372–381. DOI: 10.1086/510523.
- Galama, T. J. et al. (Oct. 1998). “An unusual supernova in the error box of the  $\gamma$ -ray burst of 25 April 1998”. In: *Nature* 395.6703, pp. 670–672. DOI: 10.1038/27150.
- Gehrels, N. et al. (Aug. 2004). “The Swift Gamma-Ray Burst Mission”. In: *ApJ* 611.2, pp. 1005–1020. DOI: 10.1086/422091.
- Germany, L. M. et al. (Apr. 2000). “SN 1997CY/GRB 970514: A New Piece in the Gamma-Ray Burst Puzzle?” In: *ApJ* 533.1, pp. 320–328. DOI: 10.1086/308639.
- Goldwasser, S. et al. (Sept. 2022). “The Next Generation SuperFit (NGSF) tool is now available for online execution on WISeREP”. In: *Transient Name Server AstroNote* 191, p. 1.
- Gomez, S. et al. (June 2021). “The Luminous and Double-peaked Type Ic Supernova 2019stc: Evidence for Multiple Energy Sources”. In: *ApJ* 913.2, 143, p. 143. DOI: 10.3847/1538-4357/abf5e3.
- Gomez, S. et al. (Dec. 2022). “Luminous Supernovae: Unveiling a Population between Superluminous and Normal Core-collapse Supernovae”. In: *ApJ* 941.2, 107, p. 107. DOI: 10.3847/1538-4357/ac9842.

- Goobar, A. et al. (2023). “Uncovering a population of gravitational lens galaxies with magnified standard candle SN Zwicky”. In: *Nature Astronomy* 7.9, pp. 1098–1107. DOI: 10.1038/s41550-023-01981-3.
- Graham, M. L. et al. (July 2017). “PTF11kx: A Type Ia Supernova with Hydrogen Emission Persisting after 3.5 Years”. In: *ApJ* 843.2, 102, p. 102. DOI: 10.3847/1538-4357/aa78ee.
- Graham, M. J. et al. (July 2019). “The Zwicky Transient Facility: Science Objectives”. In: *PASP* 131.1001, p. 078001. DOI: 10.1088/1538-3873/ab006c.
- Graham, M. L. et al. (Mar. 2022a). “Supernova siblings and their parent galaxies in the Zwicky Transient Facility Bright Transient Survey”. In: *MNRAS* 511.1, pp. 241–254. DOI: 10.1093/mnras/stab3802.
- (Mar. 2022b). “Supernova siblings and their parent galaxies in the Zwicky Transient Facility Bright Transient Survey”. In: *MNRAS* 511.1, pp. 241–254. DOI: 10.1093/mnras/stab3802.
- Guillochon, J. et al. (Jan. 2017). “An Open Catalog for Supernova Data”. In: *ApJ* 835.1, 64, p. 64. DOI: 10.3847/1538-4357/835/1/64.
- Gutiérrez, C. P. et al. (July 2021). “The double-peaked Type Ic supernova 2019cad: another SN 2005bf-like object”. In: *MNRAS* 504.4, pp. 4907–4922. DOI: 10.1093/mnras/stab1009.
- Hamuy, M. et al. (Aug. 2003). “An asymptotic-giant-branch star in the progenitor system of a type Ia supernova”. In: *Nature* 424.6949, pp. 651–654. DOI: 10.1038/nature01854.
- Han, Z. et al. (May 2006). “A single-degenerate model for the progenitor of the Type Ia supernova 2002ic”. In: *MNRAS* 368.3, pp. 1095–1100. DOI: 10.1111/j.1365-2966.2006.10185.x.
- Harris, C. R. et al. (Sept. 2020). “Array programming with NumPy”. In: *Nature* 585.7825, pp. 357–362. DOI: 10.1038/s41586-020-2649-2.
- Harutyunyan, A. H. et al. (Sept. 2008). “ESC supernova spectroscopy of non-ESC targets”. In: *A&A* 488.1, pp. 383–399. DOI: 10.1051/0004-6361:20078859.
- Hayden, B. T. et al. (Oct. 2010). “Single or Double Degenerate Progenitors? Searching for Shock Emission in the SDSS-II Type Ia Supernovae”. In: *ApJ* 722.2, pp. 1691–1698. DOI: 10.1088/0004-637X/722/2/1691.
- HI4PI Collaboration et al. (Oct. 2016). “HI4PI: A full-sky H I survey based on EBHIS and GASS”. In: *A&A* 594, A116, A116. DOI: 10.1051/0004-6361/201629178.
- Hiramatsu, D. et al. (May 2023). “Multiple Peaks and a Long Precursor in the Type II<sub>n</sub> Supernova 2021qqp: An Energetic Explosion in a Complex Circumstellar Environment”. In: *arXiv e-prints*, arXiv:2305.11168, arXiv:2305.11168. DOI: 10.48550/arXiv.2305.11168.

- Ho, A. Y. Q. et al. (Jan. 2019). “AT2018cow: A Luminous Millimeter Transient”. In: *ApJ* 871.1, 73, p. 73. DOI: 10.3847/1538-4357/aaf473.
- Ho, A. Y. Q. et al. (Dec. 2020). “ZTF20aajksq (AT 2020blt): A Fast Optical Transient at  $z \approx 2.9$  with No Detected Gamma-Ray Burst Counterpart”. In: *ApJ* 905.2, 98, p. 98. DOI: 10.3847/1538-4357/abc34d.
- Ho, A. Y. Q. et al. (Nov. 2023). “Minutes-duration optical flares with supernova luminosities”. In: *Nature* 623.7989, pp. 927–931. DOI: 10.1038/s41586-023-06673-6.
- Hodgkin, S. T. et al. (Aug. 2021). “Gaia Early Data Release 3. Gaia photometric science alerts”. In: *A&A* 652, A76, A76. DOI: 10.1051/0004-6361/202140735.
- Hoogendam, W. et al. (May 2023). “SN2023aew: SCAT Spectroscopic Observations During Significant Rebrightening”. In: *Transient Name Server AstroNote* 111, p. 1.
- Hosseinzadeh, G. et al. (Feb. 2017). “Type Ibn Supernovae Show Photometric Homogeneity and Spectral Diversity at Maximum Light”. In: *ApJ* 836.2, p. 158. DOI: 10.3847/1538-4357/836/2/158.
- Howell, D. A. et al. (Dec. 2005). “Gemini Spectroscopy of Supernovae from the Supernova Legacy Survey: Improving High-Redshift Supernova Selection and Classification”. In: *ApJ* 634.2, pp. 1190–1201. DOI: 10.1086/497119.
- Howell, D. (Jan. 2019). “The Global Supernova Project”. In: *American Astronomical Society Meeting Abstracts #233*. Vol. 233. American Astronomical Society Meeting Abstracts, 258.16, p. 258.16.
- Humphreys, R. M. et al. (Oct. 1994). “THE LUMINOUS BLUE VARIABLES: ASTROPHYSICAL GEYSERS”. In: *Publications of the Astronomical Society of the Pacific* 106.704, p. 1025. DOI: 10.1086/133478.
- Hunter, J. D. (2007a). “Matplotlib: A 2D graphics environment”. In: *Computing in Science & Engineering* 9.3, pp. 90–95. DOI: 10.1109/MCSE.2007.55.
- Hunter, J. D. (2007b). “Matplotlib: A 2D Graphics Environment”. In: *Computing in Science & Engineering* 9.3, pp. 90–95. DOI: 10.1109/MCSE.2007.55.
- Iben I., J. et al. (Feb. 1984). “Supernovae of type I as end products of the evolution of binaries with components of moderate initial mass.” In: *ApJS* 54, pp. 335–372. DOI: 10.1086/190932.
- Inserra, C. et al. (Jan. 2014). “SN2012ca: a stripped envelope core-collapse SN interacting with dense circumstellar medium”. In: *MNRAS* 437.1, pp. L51–L55. DOI: 10.1093/mnrasl/slt138.
- Inserra, C. et al. (July 2016). “On Type II<sub>n</sub>/Ia-CSM supernovae as exemplified by SN 2012ca\*.” In: *MNRAS* 459.3, pp. 2721–2740. DOI: 10.1093/mnras/stw825.
- Irani, I. et al. (Mar. 2022). “Less Than 1% of Core-collapse Supernovae in the Local Universe Occur in Elliptical Galaxies”. In: *ApJ* 927.1, 10, p. 10. DOI: 10.3847/1538-4357/ac4709.

- IRSA (2022). *Zwicky Transient Facility Image Service*. DOI: 10.26131/IRSA539.
- Ivezić, Ž. et al. (Mar. 2019). “LSST: From Science Drivers to Reference Design and Anticipated Data Products”. In: *ApJ* 873, 111, p. 111. DOI: 10.3847/1538-4357/ab042c.
- Jensen-Clem, R. et al. (Jan. 2018). “The Performance of the Robo-AO Laser Guide Star Adaptive Optics System at the Kitt Peak 2.1 m Telescope”. In: *AJ* 155.1, 32, p. 32. DOI: 10.3847/1538-3881/aa9be6.
- Jerkstrand, A. et al. (Jan. 2015). “Late-time spectral line formation in Type IIb supernovae, with application to SN 1993J, SN 2008ax, and SN 2011dh”. In: *A&A* 573, A12, A12. DOI: 10.1051/0004-6361/201423983.
- Jin, H. et al. (Mar. 2021). “The Effect of Circumstellar Matter on the Double-peaked Type Ic Supernovae and Implications for LSQ14efd, iPTF15dtg, and SN 2020bvc”. In: *ApJ* 910.1, 68, p. 68. DOI: 10.3847/1538-4357/abe0b1.
- Johnson, B. D. et al. (June 2021). “Stellar Population Inference with Prospector”. In: *ApJS* 254.2, 22, p. 22. DOI: 10.3847/1538-4365/abef67.
- Justham, S. (Apr. 2011). “Single-degenerate Type Ia Supernovae Without Hydrogen Contamination”. In: *ApJ* 730.2, L34, p. L34. DOI: 10.1088/2041-8205/730/2/L34.
- Kangas, T. et al. (Jan. 2024). “The enigmatic double-peaked stripped-envelope SN 2023aew”. In: *arXiv e-prints*, arXiv:2401.17423, arXiv:2401.17423. DOI: 10.48550/arXiv.2401.17423.
- Karamahmetoglu, E. et al. (Oct. 2023). “A population of Type Ibc supernovae with massive progenitors. Broad lightcurves not uncommon in (i)PTF”. In: *A&A* 678, A87, A87. DOI: 10.1051/0004-6361/202245231.
- Kasen, D. et al. (July 2010). “Supernova Light Curves Powered by Young Magnetars”. In: *ApJ* 717.1, pp. 245–249. DOI: 10.1088/0004-637X/717/1/245.
- Kasen, D. et al. (Apr. 2016). “Magnetar-driven Shock Breakout and Double-peaked Supernova Light Curves”. In: *ApJ* 821.1, 36, p. 36. DOI: 10.3847/0004-637X/821/1/36.
- Kashi, A. et al. (Nov. 2010). “Periastron Passage Triggering of the 19th Century Eruptions of Eta Carinae”. In: *ApJ* 723.1, pp. 602–611. DOI: 10.1088/0004-637X/723/1/602.
- Kasliwal, M. M. et al. (2017). “Illuminating gravitational waves: A concordant picture of photons from a neutron star merger”. In: *Science* 358.6370, pp. 1559–1565. DOI: 10.1126/science.aap9455.
- Kasliwal, M. M. et al. (Feb. 2019). “The GROWTH Marshal: A Dynamic Science Portal for Time-domain Astronomy”. In: *PASP* 131.997, p. 038003. DOI: 10.1088/1538-3873/aafbc2.

- Khatami, D. K. et al. (June 2019). “Physics of Luminous Transient Light Curves: A New Relation between Peak Time and Luminosity”. In: *ApJ* 878.1, 56, p. 56. DOI: 10.3847/1538-4357/ab1f09.
- (Sept. 2024). “The Landscape of Thermal Transients from Supernovae Interacting with a Circumstellar Medium”. In: *ApJ* 972.2, 140, p. 140. DOI: 10.3847/1538-4357/ad60c0.
- Kiewe, M. et al. (Jan. 2012). “Caltech Core-Collapse Project (CCCP) Observations of Type II<sub>n</sub> Supernovae: Typical Properties and Implications for Their Progenitor Stars”. In: *ApJ* 744.1, 10, p. 10. DOI: 10.1088/0004-637X/744/1/10.
- Kim, Y. -. et al. (Feb. 2022). “New Modules for the SEDMachine to Remove Contaminations from Cosmic Rays and Non-target Light: BYECR and CONTSEP”. In: *PASP* 134.1032, 024505, p. 024505. DOI: 10.1088/1538-3873/ac50a0.
- Kim, Y.-L. et al. (Nov. 2024). “How Accurate are Transient Spectral Classification Tools?— A Study Using 4646 SEDMachine Spectra”. In: *Publications of the Astronomical Society of the Pacific* 136.11, p. 114501. DOI: 10.1088/1538-3873/ad85cd.
- Kochanek, C. S. et al. (Oct. 2017). “The All-Sky Automated Survey for Supernovae (ASAS-SN) Light Curve Server v1.0”. In: *PASP* 129.980, p. 104502. DOI: 10.1088/1538-3873/aa80d9.
- Kool, E. et al. (Dec. 2022). “A thermonuclear supernova interacting with helium rich circumstellar material”. In: *Nature Astronomy*.
- Kotak, R. et al. (Dec. 2005). “Optical and Near-Infrared Observations of SN 2002ic”. In: *1604-2004: Supernovae as Cosmological Lighthouses*. Ed. by M. Turatto et al. Vol. 342. Astronomical Society of the Pacific Conference Series, p. 264.
- Kulkarni, S. R. (Apr. 2020). “Towards An Integrated Optical Transient Utility”. In: *arXiv e-prints*, arXiv:2004.03511, arXiv:2004.03511. DOI: 10.48550/arXiv.2004.03511.
- Kuncarayakti, H. et al. (July 2015). “Nebular phase observations of the Type-Ib supernova iPTF13bvn favour a binary progenitor”. In: *A&A* 579, A95, A95. DOI: 10.1051/0004-6361/201425604.
- Kuncarayakti, H. et al. (Dec. 2022). “Late-time H/He-poor Circumstellar Interaction in the Type Ic Supernova SN 2021ocs: An Exposed Oxygen-Magnesium Layer and Extreme Stripping of the Progenitor”. In: *ApJ* 941.2, L32, p. L32. DOI: 10.3847/2041-8213/aca672.
- Kuncarayakti, H. et al. (Oct. 2023). “The broad-lined Type-Ic supernova SN 2022xxf and its extraordinary two-humped light curves. I. Signatures of H/He-free interaction in the first four months”. In: *A&A* 678, A209, A209. DOI: 10.1051/0004-6361/202346526.
- Lang, D. (May 2014). “unWISE: Unblurred Coadds of the WISE Imaging”. In: *AJ* 147, 108, p. 108. DOI: 10.1088/0004-6256/147/5/108.

- Lang, D. et al. (May 2010). “Astrometry.net: Blind Astrometric Calibration of Arbitrary Astronomical Images”. In: *AJ* 139.5, pp. 1782–1800. DOI: 10.1088/0004-6256/139/5/1782.
- Leloudas, G. et al. (Feb. 2015). “Supernova spectra below strong circumstellar interaction”. In: *A&A* 574, A61, A61. DOI: 10.1051/0004-6361/201322035.
- Leung, S.-C. et al. (Dec. 2019). “Pulsational Pair-instability Supernovae. I. Pre-collapse Evolution and Pulsational Mass Ejection”. In: *ApJ* 887.1, 72, p. 72. DOI: 10.3847/1538-4357/ab4fe5.
- Leung, S.-C. et al. (Dec. 2021). “Wave-driven Mass Loss of Stripped Envelope Massive Stars: Progenitor-dependence, Mass Ejection, and Supernovae”. In: *ApJ* 923.1, 41, p. 41. DOI: 10.3847/1538-4357/ac2c63.
- Lezmy, J. et al. (Dec. 2022). “HyperGal: Hyperspectral scene modeling for supernova typing with the SED Machine integral field spectrograph”. In: *A&A* 668, A43, A43. DOI: 10.1051/0004-6361/202244740.
- Li, W. et al. (Dec. 2011). “Exclusion of a luminous red giant as a companion star to the progenitor of supernova SN 2011fe”. In: *Nature* 480.7377, pp. 348–350. DOI: 10.1038/nature10646.
- Lintott, C. et al. (Jan. 2011). “Galaxy Zoo 1: data release of morphological classifications for nearly 900 000 galaxies”. In: *MNRAS* 410.1, pp. 166–178. DOI: 10.1111/j.1365-2966.2010.17432.x.
- Lipton, Z. C. et al. (May 2015). “A Critical Review of Recurrent Neural Networks for Sequence Learning”. In: *arXiv e-prints*, arXiv:1506.00019, arXiv:1506.00019. DOI: 10.48550/arXiv.1506.00019.
- Lipunov, V. M. et al. (Apr. 2019). “The Concept of a Multi-Functional Astronomy Complex and Dynamically Integrated Database Applied to Multi-Channel Observations with the MASTER Global Network”. In: *Astronomy Reports* 63.4, pp. 293–309. DOI: 10.1134/S1063772919040073.
- Liu, Y.-Q. et al. (Aug. 2016). “Analyzing the Largest Spectroscopic Data Set of Stripped Supernovae to Improve Their Identifications and Constrain Their Progenitors”. In: *ApJ* 827.2, 90, p. 90. DOI: 10.3847/0004-637X/827/2/90.
- Livio, M. et al. (Sept. 2003). “Have the Elusive Progenitors of Type Ia Supernovae Been Discovered?” In: *ApJ* 594.2, pp. L93–L94. DOI: 10.1086/378765.
- Lunnan, R. et al. (Nov. 2016). “PS1-14bj: A Hydrogen-poor Superluminous Supernova With a Long Rise and Slow Decay”. In: *ApJ* 831.2, 144, p. 144. DOI: 10.3847/0004-637X/831/2/144.
- Lunnan, R. et al. (Aug. 2021). “ZTF superluminous supernova candidates”. In: *Transient Name Server AstroNote* 218, pp. 1–218.

- Lyman, J. D. et al. (Feb. 2014). “Bolometric corrections for optical light curves of core-collapse supernovae”. In: *MNRAS* 437.4, pp. 3848–3862. DOI: 10.1093/mnras/stt2187.
- Maeda, K. et al. (Sept. 2007). “The Unique Type Ib Supernova 2005bf at Nebular Phases: A Possible Birth Event of a Strongly Magnetized Neutron Star”. In: *ApJ* 666.2, pp. 1069–1082. DOI: 10.1086/520054.
- Maguire, K. et al. (Nov. 2013). “A statistical analysis of circumstellar material in Type Ia supernovae”. In: *MNRAS* 436.1, pp. 222–240. DOI: 10.1093/mnras/stt1586.
- Mahabal, A. et al. (Nov. 2017). “Deep-learned classification of light curves”. In: *2017 IEEE Symposium Series on Computational Intelligence (SSCI)*. Vol. 39. IEEE, pp. 1–8. DOI: 10.1109/ssci.2017.8280984.
- Mainzer, A. et al. (Sept. 2014). “Initial Performance of the NEOWISE Reactivation Mission”. In: *ApJ* 792.1, 30, p. 30. DOI: 10.1088/0004-637X/792/1/30.
- Maoz, D. et al. (Nov. 2012). “The delay-time distribution of Type Ia supernovae from Sloan II”. In: *MNRAS* 426.4, pp. 3282–3294. DOI: 10.1111/j.1365-2966.2012.21871.x.
- Margutti, R. et al. (Jan. 2014). “A Panchromatic View of the Restless SN 2009ip Reveals the Explosive Ejection of a Massive Star Envelope”. In: *ApJ* 780.1, 21, p. 21. DOI: 10.1088/0004-637X/780/1/21.
- Martin, D. C. et al. (Jan. 2005). “The Galaxy Evolution Explorer: A Space Ultraviolet Survey Mission”. In: *ApJ* 619.1, pp. L1–L6. DOI: 10.1086/426387.
- Martín Abadi et al. (2015). *TensorFlow: Large-Scale Machine Learning on Heterogeneous Systems*. Software available from tensorflow.org.
- Masci, F. J. et al. (Jan. 2019). “The Zwicky Transient Facility: Data Processing, Products, and Archive”. In: *PASP* 131.1, p. 018003. DOI: 10.1088/1538-3873/aae8ac.
- Masci, F. J. et al. (May 2023). “A New Forced Photometry Service for the Zwicky Transient Facility”. In: *arXiv e-prints*, arXiv:2305.16279, arXiv:2305.16279. DOI: 10.48550/arXiv.2305.16279.
- Matheson, T. et al. (Sept. 2000). “Detailed Analysis of Early to Late-Time Spectra of Supernova 1993J”. In: *AJ* 120.3, pp. 1499–1515. DOI: 10.1086/301519.
- Matheson, T. et al. (Mar. 2001). “Optical Spectroscopy of Type IB/C Supernovae”. In: *AJ* 121.3, pp. 1648–1675. DOI: 10.1086/319390.
- Matsumoto, T. et al. (Sept. 2022). “Supernova Precursor Emission and the Origin of Pre-explosion Stellar Mass Loss”. In: *ApJ* 936.2, 114, p. 114. DOI: 10.3847/1538-4357/ac892c.

- Mauerhan, J. C. et al. (Apr. 2013). “The unprecedented 2012 outburst of SN 2009ip: a luminous blue variable star becomes a true supernova”. In: *MNRAS* 430.3, pp. 1801–1810. DOI: 10.1093/mnras/stt009.
- Meisner, A. M. et al. (Aug. 2018). “Time-resolved WISE/NEOWISE Coadds”. In: *AJ* 156.2, 69, p. 69. DOI: 10.3847/1538-3881/aacbcd.
- Meng, X. et al. (Dec. 2019). “The common-envelope wind model for type Ia supernovae”. In: *IAU Symposium* 343, pp. 470–471. DOI: 10.1017/S1743921318006543.
- Milisavljevic, D. et al. (Dec. 2015). “Metamorphosis of SN 2014C: Delayed Interaction between a Hydrogen Poor Core-collapse Supernova and a Nearby Circumstellar Shell”. In: *ApJ* 815.2, 120, p. 120. DOI: 10.1088/0004-637X/815/2/120.
- Milisavljevic, D. et al. (Feb. 2010). “Doublets and Double Peaks: Late-Time [O I]  $\lambda\lambda 6300, 6364$  Line Profiles of Stripped-Envelope, Core-Collapse Supernovae”. In: *ApJ* 709.2, pp. 1343–1355. DOI: 10.1088/0004-637X/709/2/1343.
- Miller, A. A. et al. (July 2020a). “The Spectacular Ultraviolet Flash from the Peculiar Type Ia Supernova 2019yvq”. In: *ApJ* 898.1, 56, p. 56. DOI: 10.3847/1538-4357/ab9e05.
- Miller, A. A. et al. (Oct. 2020b). “ZTF Early Observations of Type Ia Supernovae. II. First Light, the Initial Rise, and Time to Reach Maximum Brightness”. In: *ApJ* 902.1, 47, p. 47. DOI: 10.3847/1538-4357/abb13b.
- Miller, J. et al. (1987). *The CCD Cassegrain Spectrograph at the Shane Reflector*.
- Modjaz, M. et al. (July 2006). “Early-Time Photometry and Spectroscopy of the Fast Evolving SN 2006aj Associated with GRB 060218”. In: *ApJ* 645.1, pp. L21–L24. DOI: 10.1086/505906.
- Modjaz, M. et al. (Nov. 2008). “Double-Peaked Oxygen Lines Are Not Rare in Nebular Spectra of Core-Collapse Supernovae”. In: *ApJ* 687.1, p. L9. DOI: 10.1086/593135.
- Modjaz, M. (Jan. 2007). “Varied deaths of massive stars: Properties of nearby type IIb, Ib and Ic supernovae”. PhD thesis. Harvard University, Massachusetts.
- Modjaz, M. et al. (Dec. 2016). “The Spectral SN-GRB Connection: Systematic Spectral Comparisons between Type Ic Supernovae and Broad-lined Type Ic Supernovae with and without Gamma-Ray Bursts”. In: *ApJ* 832.2, 108, p. 108. DOI: 10.3847/0004-637X/832/2/108.
- Möller, A. et al. (Jan. 2020). “SuperNNova: an open-source framework for Bayesian, neural network-based supernova classification”. In: *MNRAS* 491.3, pp. 4277–4293. DOI: 10.1093/mnras/stz3312.
- Morales-Garoffolo, A. et al. (Nov. 2015). “SN 2011fu: a type IIb supernova with a luminous double-peaked light curve”. In: *MNRAS* 454.1, pp. 95–114. DOI: 10.1093/mnras/stv1972.

- Moriya, T. J. et al. (July 2019a). “Fallback Accretion-powered Supernova Light Curves Based on a Neutrino-driven Explosion Simulation of a 40 M<sub>⊙</sub> Star”. In: *ApJ* 880.1, 21, p. 21. DOI: 10.3847/1538-4357/ab2643.
- (July 2019b). “Fallback Accretion-powered Supernova Light Curves Based on a Neutrino-driven Explosion Simulation of a 40 M<sub>⊙</sub> Star”. In: *ApJ* 880.1, 21, p. 21. DOI: 10.3847/1538-4357/ab2643.
- Moriya, T. J. et al. (July 2022). “Variable thermal energy injection from magnetar spin-down as a possible cause of stripped-envelope supernova light-curve bumps”. In: *MNRAS* 513.4, pp. 6210–6218. DOI: 10.1093/mnras/stac1352.
- Munoz-Arancibia, A. et al. (Jan. 2023). “ALeRCE/ZTF Transient Discovery Report for 2023-01-23”. In: *Transient Name Server Discovery Report 2023-166*, p. 1.
- Muthukrishna, D. et al. (Nov. 2019a). “DASH: Deep Learning for the Automated Spectral Classification of Supernovae and Their Hosts”. In: *The Astrophysical Journal* 885.1, p. 85. DOI: 10.3847/1538-4357/ab48f4.
- Muthukrishna, D. et al. (Nov. 2019b). “RAPID: Early Classification of Explosive Transients Using Deep Learning”. In: *PASP* 131.1005, p. 118002. DOI: 10.1088/1538-3873/ab1609.
- Nakar, E. et al. (June 2014). “Supernovae with Two Peaks in the Optical Light Curve and the Signature of Progenitors with Low-mass Extended Envelopes”. In: *ApJ* 788.2, 193, p. 193. DOI: 10.1088/0004-637X/788/2/193.
- Nicholl (Dec. 2018a). *mnicholl/superbol: superbol v1.0*. Version v1.0. Zenodo. DOI: 10.5281/zenodo.2155821.
- Nicholl, M. (Dec. 2018b). “SuperBol: A User-friendly Python Routine for Bolometric Light Curves”. In: *Research Notes of the American Astronomical Society* 2.4, 230, p. 230. DOI: 10.3847/2515-5172/aaf799.
- Nicholls, B. et al. (Aug. 2018). “ASAS-SN Transient Discovery Report for 2018-08-11”. In: *TNSCR 2018-1144*, p. 1.
- Nordin, J. et al. (Nov. 2019). “Transient processing and analysis using AMPEL: alert management, photometry, and evaluation of light curves”. In: *A&A* 631, A147, A147. DOI: 10.1051/0004-6361/201935634.
- Nugent, P. E. et al. (Dec. 2011). “Supernova SN 2011fe from an exploding carbon-oxygen white dwarf star”. In: *Nature* 480.7377, pp. 344–347. DOI: 10.1038/nature10644.
- Nyholm, A. et al. (Aug. 2017). “The bumpy light curve of Type II<sub>n</sub> supernova iPTF13z over 3 years”. In: *A&A* 605, A6, A6. DOI: 10.1051/0004-6361/201629906.
- Ofek, E. O. et al. (July 2014). “Precursors Prior to Type II<sub>n</sub> Supernova Explosions are Common: Precursor Rates, Properties, and Correlations”. In: *ApJ* 789.2, 104, p. 104. DOI: 10.1088/0004-637X/789/2/104.

- Oke, J. B. et al. (June 1982). “An Efficient Low Resolution and Moderate Resolution Spectrograph for the Hale Telescope”. In: *PASP* 94, p. 586. DOI: 10.1086/131027.
- Oke, J. B. et al. (Apr. 1995). “The Keck Low-Resolution Imaging Spectrometer”. In: *PASP* 107, p. 375. DOI: 10.1086/133562.
- Orellana, M. et al. (Nov. 2022). “Supernova double-peaked light curves from double-nickel distribution”. In: *A&A* 667, A92, A92. DOI: 10.1051/0004-6361/202244124.
- Ostriker, J. P. et al. (Mar. 1971). “Do Pulsars Make Supernovae?” In: *ApJ* 164, p. L95. DOI: 10.1086/180699.
- Ouyed, R. et al. (Dec. 2013). “SN 2009ip and SN 2010mc as dual-shock Quark-Novae”. In: *Research in Astronomy and Astrophysics* 13.12, 1463-1470, pp. 1463–1470. DOI: 10.1088/1674-4527/13/12/007.
- Parrent, J. T. et al. (Mar. 2016). “Line Identifications of Type I Supernovae: On the Detection of Si II for These Hydrogen-poor Events”. In: *ApJ* 820.1, 75, p. 75. DOI: 10.3847/0004-637X/820/1/75.
- Pasquet, J. et al. (July 2019). “PELICAN: deeP architecturE for the LIght Curve ANalysis”. In: *A&A* 627, A21, A21. DOI: 10.1051/0004-6361/201834473.
- Pastorello, A. et al. (Jan. 2004). “Low-luminosity Type II supernovae: spectroscopic and photometric evolution”. In: *MNRAS* 347.1, pp. 74–94. DOI: 10.1111/j.1365-2966.2004.07173.x.
- Pastorello, A. et al. (Sept. 2008). “Massive stars exploding in a He-rich circumstellar medium - I. Type Ibn (SN 2006jc-like) events”. In: *MNRAS* 389.1, pp. 113–130. DOI: 10.1111/j.1365-2966.2008.13602.x.
- Pastorello, A. et al. (Apr. 2013). “Interacting Supernovae and Supernova Impostors: SN 2009ip, is this the End?” In: *ApJ* 767.1, 1, p. 1. DOI: 10.1088/0004-637X/767/1/1.
- Patat, F. et al. (Aug. 2007). “Detection of Circumstellar Material in a Normal Type Ia Supernova”. In: *Science* 317.5840, p. 924. DOI: 10.1126/science.1143005.
- Patat, F. et al. (July 2001). “The Metamorphosis of SN 1998bw”. In: *ApJ* 555.2, pp. 900–917. DOI: 10.1086/321526.
- Patterson, M. T. et al. (Jan. 2019). “The Zwicky Transient Facility Alert Distribution System”. In: *PASP* 131.995, p. 018001. DOI: 10.1088/1538-3873/aae904.
- Payne, A. V. et al. (Mar. 2019). “SCAT Transient Classification Report for 2019-03-07”. In: *TNSCR* 2019-343, p. 1.
- Pedregosa, F. et al. (2011). “Scikit-learn: Machine Learning in Python”. In: *JMLR* 12, pp. 2825–2830.

- Pellegrino, C. et al. (May 2022). “The Diverse Properties of Type Icn Supernovae Point to Multiple Progenitor Channels”. In: *arXiv e-prints*, arXiv:2205.07894, arXiv:2205.07894.
- Pellegrino, C. et al. (Sept. 2023). “SN 2020bio: A Double-peaked, H-poor Type IIb Supernova with Evidence of Circumstellar Interaction”. In: *ApJ* 954.1, 35, p. 35. DOI: 10.3847/1538-4357/ace595.
- Perley, D. et al. (May 2022a). “ZTF Transient Classification Report for 2022-05-20”. In: *Transient Name Server Classification Report 2022-1362*, p. 1.
- Perley, D. A. (Aug. 2019). “Fully Automated Reduction of Longslit Spectroscopy with the Low Resolution Imaging Spectrometer at the Keck Observatory”. In: *PASP* 131.8, p. 084503. DOI: 10.1088/1538-3873/ab215d.
- Perley, D. A. et al. (Nov. 2020). “The Zwicky Transient Facility Bright Transient Survey. II. A Public Statistical Sample for Exploring Supernova Demographics”. In: *ApJ* 904.1, p. 35. DOI: 10.3847/1538-4357/abbd98.
- Perley, D. A. et al. (Mar. 2022b). “The Type Icn SN 2021csp: Implications for the Origins of the Fastest Supernovae and the Fates of Wolf-Rayet Stars”. In: *ApJ* 927.2, 180, p. 180. DOI: 10.3847/1538-4357/ac478e.
- Phillips, M. M. et al. (2017). “The Peak Luminosity–Decline Rate Relationship for Type Ia Supernovae”. In: *Handbook of Supernovae*. Ed. by A. W. Alsabti et al. Cham: Springer International Publishing, pp. 2543–2561. DOI: 10.1007/978-3-319-21846-5\_100.
- Piasek, A. S. et al. (July 2014). “SPRAT: Spectrograph for the Rapid Acquisition of Transients”. In: *Ground-based and Airborne Instrumentation for Astronomy V*. Vol. 9147. Proc. SPIE, 91478H, 91478H. DOI: 10.1117/12.2055117.
- Piro, A. L. (Aug. 2015). “Using Double-peaked Supernova Light Curves to Study Extended Material”. In: *ApJ* 808.2, L51, p. L51. DOI: 10.1088/2041-8205/808/2/L51.
- Piro, A. L. et al. (Mar. 2021). “Shock Cooling Emission from Extended Material Revisited”. In: *ApJ* 909.2, 209, p. 209. DOI: 10.3847/1538-4357/abe2b1.
- Planck Collaboration et al. (Sept. 2020). “Planck 2018 results. VI. Cosmological parameters”. In: *A&A* 641, A6, A6. DOI: 10.1051/0004-6361/201833910.
- Poidevin, F. et al. (Aug. 2021). “SGLF Transient Classification Report for 2021-08-13”. In: *Transient Name Server Classification Report 2021-2800*, pp. 1–2800.
- Popov, D. V. (Sept. 1993). “An Analytical Model for the Plateau Stage of Type II Supernovae”. In: *ApJ* 414, p. 712. DOI: 10.1086/173117.
- Prentice, S. et al. (July 2020). “TCD Transient Classification Report for 2020-07-26”. In: *TNSCR 2020-2285*, p. 1.

- Prentice, S. J. et al. (May 2016). “The bolometric light curves and physical parameters of stripped-envelope supernovae”. In: *MNRAS* 458.3, pp. 2973–3002. DOI: 10.1093/mnras/stw299.
- Prentice, S. J. et al. (May 2019). “Investigating the properties of stripped-envelope supernovae; what are the implications for their progenitors?” In: *MNRAS* 485.2, pp. 1559–1578. DOI: 10.1093/mnras/sty3399.
- Prentice, S. J. et al. (Aug. 2022). “Oxygen and calcium nebular emission line relationships in core-collapse supernovae and Ca-rich transients”. In: *MNRAS* 514.4, pp. 5686–5705. DOI: 10.1093/mnras/stac1657.
- Prieto, J. L. et al. (June 2007). “A Study of the Type Ia/II<sub>n</sub> Supernova 2005gj from X-ray to the Infrared: Paper I”. In: *arXiv e-prints*, arXiv:0706.4088, arXiv:0706.4088.
- Prochaska, J. X. et al. (2020). “PypeIt: The Python Spectroscopic Data Reduction Pipeline”. In: *Journal of Open Source Software* 5.56, p. 2308. DOI: 10.21105/joss.02308.
- Qu, H. et al. (Jan. 2022). “Photometric Classification of Early-time Supernova Light Curves with SCONE”. In: *The Astronomical Journal* 163.2, p. 57. DOI: 10.3847/1538-3881/ac39a1.
- Quataert, E. et al. (June 2012). “Wave-driven mass loss in the last year of stellar evolution: setting the stage for the most luminous core-collapse supernovae”. In: *MNRAS* 423.1, pp. L92–L96. DOI: 10.1111/j.1745-3933.2012.01264.x.
- Quimby, R. M. (2011). “Superluminous Supernovae”. In: *Proceedings of the International Astronomical Union* 7.S279, pp. 22–28. DOI: 10.1017/S174392131201263X.
- Rakavy, G. et al. (Oct. 1967). “Carbon and Oxygen Burning Stars and Pre-Supernova Models”. In: *ApJ* 150, p. 131. DOI: 10.1086/149318.
- Reguitti, A. (Dec. 2020). “Padova-Asiago Transient Classification Report for 2020-12-17”. In: *TNSCR* 2020-3825, p. 1.
- Rehemtulla, N. et al. (Oct. 2023). “SN 2023tyk: discovery to spectroscopic classification performed fully automatically”. In: *Transient Name Server AstroNote* 265, p. 1.
- Rehemtulla, N. et al. (Sept. 2024). “The Zwicky Transient Facility Bright Transient Survey. III. BTSbot: Automated Identification and Follow-up of Bright Transients with Deep Learning”. In: *ApJ* 972.1, 7, p. 7. DOI: 10.3847/1538-4357/ad5666.
- Renzo, M. et al. (Aug. 2020). “Predictions for the hydrogen-free ejecta of pulsational pair-instability supernovae”. In: *A&A* 640, A56, A56. DOI: 10.1051/0004-6361/202037710.
- Richmond, M. W. et al. (Mar. 1994). “UBVRI Photometry of SN 1993J in M81: The First 120 Days”. In: *AJ* 107, p. 1022. DOI: 10.1086/116915.
- Richmond, M. W. et al. (Aug. 1996). “UBVRI Photometry of SN 1993J in M81: Days 3 to 365”. In: *AJ* 112, p. 732. DOI: 10.1086/118048.

- Ricker, G. R. (June 2014). “The Transiting Exoplanet Survey Satellite Mission”. In: *JAAVSO* 42.1, p. 234.
- Riddle, R. L. et al. (2012). “The Robo-AO software: fully autonomous operation of a laser guide star adaptive optics and science system”. In: *Adaptive Optics Systems III*. Ed. by B. L. Ellerbroek et al. Vol. 8447. International Society for Optics and Photonics. SPIE, pp. 993–1001. DOI: 10.1117/12.925475.
- Ridley, E. et al. (Aug. 2021). “ePESSTO+ Transient Classification Report for 2021-08-13”. In: *Transient Name Server Classification Report 2021-2795*, pp. 1–2795.
- Rigault, M. et al. (July 2019). “Fully automated integral field spectrograph pipeline for the SEDMachine: pysedm”. In: *A&A* 627, A115, A115. DOI: 10.1051/0004-6361/201935344.
- Rigault, M. (Aug. 2018). *ztfquery, a python tool to access ZTF data*. Zenodo. Version doi. DOI: 10.5281/zenodo.1345222.
- Roberson, M. et al. (Feb. 2022). “DBSP\_DRP: A Python package for automated spectroscopic data reduction of DBSP data”. In: *The Journal of Open Source Software* 7.70, 3612, p. 3612. DOI: 10.21105/joss.03612.
- Rodrigo, C. et al. (July 2020). “The SVO Filter Profile Service”. In: *XIV.0 Scientific Meeting (virtual) of the Spanish Astronomical Society*, 182, p. 182.
- Rodrigo, C. et al. (Oct. 2012). *SVO Filter Profile Service Version 1.0*. IVOA Working Draft 15 October 2012. DOI: 10.5479/ADS/bib/2012ivoa.rept.1015R.
- Rodríguez, Ó. et al. (Apr. 2024). “Stripped-envelope supernova light curves argue for central engine activity”. In: *Nature* 628.8009, pp. 733–735. DOI: 10.1038/s41586-024-07262-x.
- Roming, P. W. A. et al. (Oct. 2005). “The Swift Ultra-Violet/Optical Telescope”. In: *Space Science Reviews* 120.3-4, pp. 95–142. DOI: 10.1007/s11214-005-5095-4.
- Salamanca, I. et al. (Oct. 1998). “The circumstellar medium of the peculiar supernova SN1997ab”. In: *MNRAS* 300.2, pp. L17–L21. DOI: 10.1046/j.1365-8711.1998.02093.x.
- Schlafly, E. F. et al. (Aug. 2011). “MEASURING REDDENING WITH SLOAN DIGITAL SKY SURVEY STELLAR SPECTRA AND RECALIBRATING SFD”. In: *ApJ* 737.2, p. 103. DOI: 10.1088/0004-637x/737/2/103.
- Schlegel, E. M. (May 1990). “A new subclass of type II supernovae ?” In: *MNRAS* 244, pp. 269–271.
- Schmidt, B. P. et al. (Oct. 1994). “SN 1991T: Reflections of Past Glory”. In: *ApJ* 434, p. L19. DOI: 10.1086/187562.

- Schulze, S. et al. (Aug. 2021). “The Palomar Transient Factory Core-collapse Supernova Host-galaxy Sample. I. Host-galaxy Distribution Functions and Environment Dependence of Core-collapse Supernovae”. In: *ApJS* 255.2, 29, p. 29. DOI: 10.3847/1538-4365/abff5e.
- Schulze, S. et al. (Mar. 2024a). “1100 days in the life of the supernova 2018ibb. The best pair-instability supernova candidate, to date”. In: *A&A* 683, A223, A223. DOI: 10.1051/0004-6361/202346855.
- Schulze, S. et al. (Sept. 2024b). “A cosmic formation site of silicon and sulphur revealed by a new type of supernova explosion”. In: *arXiv e-prints*, arXiv:2409.02054, arXiv:2409.02054. DOI: 10.48550/arXiv.2409.02054.
- Shappee, B. et al. (Jan. 2014). “All Sky Automated Survey for SuperNovae (ASAS-SN or “Assassin”)”. In: *American Astronomical Society Meeting Abstracts #223*. Vol. 223. American Astronomical Society Meeting Abstracts, 236.03, p. 236.03.
- Sharma, Y. et al. (May 2023). “A Systematic Study of Ia-CSM Supernovae from the ZTF Bright Transient Survey”. In: *ApJ* 948.1, 52, p. 52. DOI: 10.3847/1538-4357/acbc16.
- Sharma, Y. et al. (May 2024). “Dramatic Rebrightening of the Type-changing Stripped-envelope Supernova SN 2023aew”. In: *ApJ* 966.2, 199, p. 199. DOI: 10.3847/1538-4357/ad3758.
- Sharma, Y. et al. (2025). “CCSNscore: A Multi-input Deep Learning Tool for Classification of Core-collapse Supernovae Using SED-machine Spectra”. In: *PASP* 137.3, p. 034507. DOI: 10.1088/1538-3873/adb4b.
- Sheinis, A. I. et al. (Aug. 2002). “ESI, a New Keck Observatory Echellette Spectrograph and Imager”. In: *PASP* 114.798, pp. 851–865. DOI: 10.1086/341706.
- Shingles, L. et al. (Jan. 2021). “Release of the ATLAS Forced Photometry server for public use”. In: *Transient Name Server AstroNote* 7, pp. 1–7.
- Shivvers, I. et al. (Jan. 2019). “The Berkeley sample of stripped-envelope supernovae”. In: *MNRAS* 482.2, pp. 1545–1556. DOI: 10.1093/mnras/sty2719.
- Silverman, J. M. et al. (Aug. 2013a). “Late-time Spectral Observations of the Strongly Interacting Type Ia Supernova PTF11kx”. In: *ApJ* 772.2, 125, p. 125. DOI: 10.1088/0004-637X/772/2/125.
- Silverman, J. M. et al. (June 2013b). “TYPE Ia SUPERNOVAE STRONGLY INTERACTING WITH THEIR CIRCUMSTELLAR MEDIUM”. In: *ApJS* 207.1, p. 3. DOI: 10.1088/0067-0049/207/1/3.
- Simon, J. D. et al. (Aug. 2009). “VARIABLE SODIUM ABSORPTION IN A LOW-EXTINCTION TYPE Ia SUPERNOVA,” in: *ApJ* 702.2, pp. 1157–1170. DOI: 10.1088/0004-637x/702/2/1157.
- Skrutskie, M. F. et al. (Feb. 2006). “The Two Micron All Sky Survey (2MASS)”. In: *AJ* 131, pp. 1163–1183. DOI: 10.1086/498708.

- Smartt, S. J. et al. (July 2015). “PESSTO: survey description and products from the first data release by the Public ESO Spectroscopic Survey of Transient Objects”. In: *A&A* 579, A40, A40. DOI: 10.1051/0004-6361/201425237.
- Smith, K. W. et al. (Aug. 2020). “Design and Operation of the ATLAS Transient Science Server”. In: *PASP* 132.1014, 085002, p. 085002. DOI: 10.1088/1538-3873/ab936e.
- Smith, N. (Aug. 2011). “Explosions triggered by violent binary-star collisions: application to Eta Carinae and other eruptive transients”. In: *MNRAS* 415.3, pp. 2020–2024. DOI: 10.1111/j.1365-2966.2011.18607.x.
- (Aug. 2014). “Mass Loss: Its Effect on the Evolution and Fate of High-Mass Stars”. In: *ARA&A* 52, pp. 487–528. DOI: 10.1146/annurev-astro-081913-040025.
- (2017). “Interacting Supernovae: Types IIn and Ibn”. In: *Handbook of Supernovae*. Ed. by A. W. Alsabti et al., p. 403. DOI: 10.1007/978-3-319-21846-5\_38.
- Smith, N. et al. (Oct. 2008). “SN 2006tf: Precursor Eruptions and the Optically Thick Regime of Extremely Luminous Type IIn Supernovae”. In: *ApJ* 686.1, pp. 467–484. DOI: 10.1086/591021.
- Soker, N. (Aug. 2001). “The departure of  $\eta$  Carinae from axisymmetry and the binary hypothesis”. In: *MNRAS* 325.2, pp. 584–588. DOI: 10.1046/j.1365-8711.2001.04439.x.
- (Sept. 2004). “Why a Single-Star Model Cannot Explain the Bipolar Nebula of  $\eta$  Carinae”. In: *ApJ* 612.2, pp. 1060–1064. DOI: 10.1086/422599.
- (Mar. 2022). “Common Envelope to Explosion Delay time Distribution (CEEDTD) of Type Ia Supernovae”. In: *RAA* 22.3, 035025, p. 035025. DOI: 10.1088/1674-4527/ac4d25.
- Soker, N. et al. (Feb. 2013a). “Explaining the Supernova Impostor SN 2009ip as Mergerburst”. In: *ApJ* 764.1, L6, p. L6. DOI: 10.1088/2041-8205/764/1/L6.
- Soker, N. et al. (May 2013b). “Explaining the Type Ia supernova PTF 11kx with a violent prompt merger scenario”. In: *MNRAS* 431.2, pp. 1541–1546. DOI: 10.1093/mnras/stt271.
- Sollerman, J. et al. (July 2000). “SN 1998bw at Late Phases”. In: *ApJ* 537.2, pp. L127–L130. DOI: 10.1086/312763.
- Sollerman, J. et al. (May 2002). “Supernova 1998bw - the final phases”. In: *A&A* 386, pp. 944–956. DOI: 10.1051/0004-6361:20020326.
- Sollerman, J. et al. (Nov. 2020). “Two stripped envelope supernovae with circumstellar interaction. But only one really shows it”. In: *A&A* 643, A79, A79. DOI: 10.1051/0004-6361/202038960.
- Sollerman, J. et al. (Jan. 2022). “Maximum luminosities of normal stripped-envelope supernovae are brighter than explosion models allow”. In: *A&A* 657, A64, A64. DOI: 10.1051/0004-6361/202142049.

- Soraisam, M. et al. (Mar. 2021). “AT2020caa: A Type Ia Supernova with a Prior Outburst or a Statistical Fluke?” In: *RNAAS* 5.3, 62, p. 62. DOI: 10.3847/2515-5172/abf1f7.
- Soraisam, M. et al. (Feb. 2022). “Optical Rebrightening of Extragalactic Transients from the Zwicky Transient Facility”. In: *ApJ* 926.2, L11, p. L11. DOI: 10.3847/2041-8213/ac4e99.
- Soumagnac, M. T. et al. (July 2018). “catsHTM: A Tool for Fast Accessing and Cross-matching Large Astronomical Catalogs”. In: *PASP* 130.989, p. 075002. DOI: 10.1088/1538-3873/aac410.
- Steele, I. A. et al. (Oct. 2004). “The Liverpool Telescope: performance and first results”. In: *Ground-based Telescopes*. Ed. by J. Oschmann Jacobus M. Vol. 5489. Society of Photo-Optical Instrumentation Engineers (SPIE) Conference Series, pp. 679–692. DOI: 10.1117/12.551456.
- Stein, R. et al. (Aug. 2018a). “ePESSTO Transient Classification Report for 2018-08-13”. In: *TNSCR* 2018-1168, p. 1.
- (Aug. 2018b). “ePESSTO Transient Classification Report for 2018-08-13”. In: *TNSCR* 2018-1168, p. 1.
- Stein, R. et al. (Feb. 2021). “A tidal disruption event coincident with a high-energy neutrino”. In: *Nature Astronomy* 5, pp. 510–518. DOI: 10.1038/s41550-020-01295-8.
- Stein, R. D. et al. (Mar. 2025). *winter-telescope/mirar: v0.20.0*. Version v0.20.0. DOI: 10.5281/zenodo.14968811.
- Sternberg, A. et al. (Aug. 2011). “Circumstellar Material in Type Ia Supernovae via Sodium Absorption Features”. In: *Science* 333.6044, p. 856. DOI: 10.1126/science.1203836.
- Stritzinger, M. D. et al. (Feb. 2018). “The Carnegie Supernova Project I. Photometry data release of low-redshift stripped-envelope supernovae”. In: *A&A* 609, A134, A134. DOI: 10.1051/0004-6361/201730842.
- Strotjohann, N. L. et al. (Feb. 2021a). “Bright, Months-long Stellar Outbursts Announce the Explosion of Interaction-powered Supernovae”. In: *ApJ* 907.2, 99, p. 99. DOI: 10.3847/1538-4357/abd032.
- (Feb. 2021b). “Bright, Months-long Stellar Outbursts Announce the Explosion of Interaction-powered Supernovae”. In: *ApJ* 907.2, 99, p. 99. DOI: 10.3847/1538-4357/abd032.
- Taddia, F. et al. (July 2013). “Carnegie Supernova Project: Observations of Type II supernovae”. In: *A&A* 555, A10, A10. DOI: 10.1051/0004-6361/201321180.
- Taddia, F. et al. (Feb. 2015). “Early-time light curves of Type Ib/c supernovae from the SDSS-II Supernova Survey”. In: *A&A* 574, A60, A60. DOI: 10.1051/0004-6361/201423915.

- Taddia, F. et al. (Aug. 2016). “iPTF15dtg: a double-peaked Type Ic supernova from a massive progenitor”. In: *A&A* 592, A89, A89. DOI: 10.1051/0004-6361/201628703.
- Taddia, F. et al. (Jan. 2018a). “PTF11mnb: First analog of supernova 2005bf. Long-rising, double-peaked supernova Ic from a massive progenitor”. In: *A&A* 609, A106, A106. DOI: 10.1051/0004-6361/201629874.
- Taddia, F. et al. (Feb. 2018b). “The Carnegie Supernova Project I. Analysis of stripped-envelope supernova light curves”. In: *A&A* 609, A136, A136. DOI: 10.1051/0004-6361/201730844.
- Taggart, K. (Dec. 2020). “The environments and progenitors of extreme supernovae in the low-redshift Universe”. PhD thesis. Liverpool John Moores University. DOI: 10.24377/LJMU.t.00014104.
- Takei, Y. et al. (Dec. 2024). “Detached Circumstellar Matter as an Explanation for Slowly-Rising Interacting Type Ibc Supernovae”. In: *The Open Journal of Astrophysics* 7, 119, p. 119. DOI: 10.33232/001c.127610.
- Tartaglia, L. et al. (June 2021). “SN 2018ijp: the explosion of a stripped-envelope star within a dense H-rich shell?” In: *A&A* 650, A174, A174. DOI: 10.1051/0004-6361/202039068.
- Taubenberger, S. et al. (Aug. 2009). “Nebular emission-line profiles of Type Ib/c supernovae - probing the ejecta asphericity”. In: *MNRAS* 397.2, pp. 677–694. DOI: 10.1111/j.1365-2966.2009.15003.x.
- Taubenberger, S. et al. (July 2013). “‘Super-Chandrasekhar’ Type Ia Supernovae at nebular epochs”. In: *MNRAS* 432.4, pp. 3117–3130. DOI: 10.1093/mnras/stt668.
- team, T. pandas development (Feb. 2020). *pandas-dev/pandas: Pandas*. Version latest. DOI: 10.5281/zenodo.3509134.
- Thévenot, M. et al. (Aug. 2021). “Supernovae detected in NEOWISE-R 2021”. In: *Transient Name Server AstroNote* 212, pp. 1–212.
- Tody, D. (Jan. 1986). “The IRAF Data Reduction and Analysis System”. In: *Instrumentation in astronomy VI*. Ed. by D. L. Crawford. Vol. 627. Proc. SPIE, p. 733. DOI: 10.1117/12.968154.
- Tody, D. (Jan. 1993). “IRAF in the Nineties”. In: *Astronomical Data Analysis Software and Systems II*. Ed. by R. J. Hanisch et al. Vol. 52. Astronomical Society of the Pacific Conference Series, p. 173.
- Tominaga, N. et al. (Nov. 2005). “The Unique Type Ib Supernova 2005bf: A WN Star Explosion Model for Peculiar Light Curves and Spectra”. In: *ApJ* 633.2, pp. L97–L100. DOI: 10.1086/498570.
- Tonry, J. et al. (Oct. 1979). “A survey of galaxy redshifts. I. Data reduction techniques.” In: *AJ* 84, pp. 1511–1525. DOI: 10.1086/112569.

- Tonry, J. L. et al. (June 2018). “ATLAS: A High-cadence All-sky Survey System”. In: *PASP* 130.6, p. 064505. DOI: 10.1088/1538-3873/aabadf.
- Tsuna, D. et al. (Jan. 2024). “Bright Supernova Precursors by Outbursts from Massive Stars with Compact Object Companions”. In: *arXiv e-prints*, arXiv:2401.02389, arXiv:2401.02389. DOI: 10.48550/arXiv.2401.02389.
- Tucker, M. A. et al. (Mar. 2018). “SCAT Classifications of 5 Supernovae with the UH88/SNIFS”. In: *The Astronomer’s Telegram* 11444, p. 1.
- Valenti, S. et al. (Feb. 2008a). “The broad-lined Type Ic supernova 2003jd”. In: *MNRAS* 383.4, pp. 1485–1500. DOI: 10.1111/j.1365-2966.2007.12647.x.
- Valenti, S. et al. (Feb. 2008b). “The Carbon-rich Type Ic SN 2007gr: The Photospheric Phase”. In: *ApJ* 673.2, p. L155. DOI: 10.1086/527672.
- van Baal, B. F. A. et al. (July 2023). “Modelling supernova nebular lines in 3D with EXTRASS”. In: *MNRAS* 523.1, pp. 954–973. DOI: 10.1093/mnras/stad1488.
- van Driel, W. et al. (Oct. 1993). “BVRI Photometry of SN 1993J in M81. I. Period April 01–30 1993”. In: *PASJ* 45, pp. L59–L62.
- van Paradijs, J. et al. (Jan. 2000). “Gamma-Ray Burst Afterglows”. In: *ARA&A* 38, pp. 379–425. DOI: 10.1146/annurev.astro.38.1.379.
- Vaswani, A. et al. (2023). *Attention Is All You Need*.
- Virtanen, P. et al. (Feb. 2020). “SciPy 1.0: fundamental algorithms for scientific computing in Python”. In: *Nature Methods* 17, pp. 261–272. DOI: 10.1038/s41592-019-0686-2.
- Walt, S. J. van der et al. (May 2019). “SkyPortal: An Astronomical Data Platform”. In: *Journal of Open Source Software* 4.37. DOI: 10.21105/joss.01247.
- Wang, L. et al. (July 1997). “Supernovae and Their Host Galaxies”. In: *ApJ* 483.1, pp. L29–L32. DOI: 10.1086/310737.
- Wang, L. et al. (Mar. 2004). “On the Hydrogen Emission from the Type Ia Supernova SN 2002ic”. In: *ApJ* 604.1, pp. L53–L56. DOI: 10.1086/383411.
- Webbink, R. F. (Feb. 1984). “Double white dwarfs as progenitors of R Coronae Borealis stars and type I supernovae.” In: *ApJ* 277, pp. 355–360. DOI: 10.1086/161701.
- Whelan, J. et al. (Dec. 1973). “Binaries and Supernovae of Type I”. In: *ApJ* 186, pp. 1007–1014. DOI: 10.1086/152565.
- Wilson, J. C. et al. (Sept. 2004). “Mass producing an efficient NIR spectrograph”. In: *Ground-based Instrumentation for Astronomy*. Ed. by A. F. M. Moorwood et al. Vol. 5492. Society of Photo-Optical Instrumentation Engineers (SPIE) Conference Series, pp. 1295–1305. DOI: 10.1117/12.550925.
- Wise, J. et al. (Apr. 2023). “ZTF Transient Classification Report for 2023-04-09”. In: *Transient Name Server Classification Report 2023-750*, p. 1.

- Wood-Vasey, W. M. et al. (Nov. 2004). “Photometry of SN 2002ic and Implications for the Progenitor Mass-Loss History”. In: *ApJ* 616.1, pp. 339–345. DOI: 10.1086/424826.
- Woosley, S. E. (Aug. 2010). “Bright Supernovae from Magnetar Birth”. In: *ApJ* 719.2, pp. L204–L207. DOI: 10.1088/2041-8205/719/2/L204.
- (Feb. 2017). “Pulsational Pair-instability Supernovae”. In: *ApJ* 836.2, 244, p. 244. DOI: 10.3847/1538-4357/836/2/244.
- Woosley, S. E. et al. (Nov. 2007). “Pulsational pair instability as an explanation for the most luminous supernovae”. In: *Nature* 450.7168, pp. 390–392. DOI: 10.1038/nature06333.
- Woosley, S. E. et al. (Sept. 2015). “The Remarkable Deaths of 9-11 Solar Mass Stars”. In: *ApJ* 810.1, 34, p. 34. DOI: 10.1088/0004-637X/810/1/34.
- Wright, A. H. et al. (July 2016). “Galaxy And Mass Assembly: accurate panchromatic photometry from optical priors using LAMBDA”. In: *MNRAS* 460.1, pp. 765–801. DOI: 10.1093/mnras/stw832.
- Wright, E. L. et al. (Dec. 2010). “The Wide-field Infrared Survey Explorer (WISE): Mission Description and Initial On-orbit Performance”. In: *AJ* 140.6, pp. 1868–1881. DOI: 10.1088/0004-6256/140/6/1868.
- Wu, S. et al. (Jan. 2021). “A Diversity of Wave-driven Presupernova Outbursts”. In: *ApJ* 906.1, 3, p. 3. DOI: 10.3847/1538-4357/abc87c.
- Xu, Y. et al. (Feb. 1992). “Hydrogen Recombination at High Optical Depth and the Spectrum of SN 1987A”. In: *ApJ* 386, p. 181. DOI: 10.1086/171003.
- Yang, S. et al. (Dec. 2023). “HAFFET: Hybrid Analytic Flux Fitter for Transients”. In: *ApJS* 269.2, 40, p. 40. DOI: 10.3847/1538-4365/acfcb4.
- Yang, Y. et al. (Nov. 2022). “The Interaction of Supernova 2018evt with a Substantial Amount of Circumstellar Matter - An SN 1997cy-like Event”. In: *MNRAS*. DOI: 10.1093/mnras/stac3477.
- Yao, Y. et al. (Dec. 2019). “ZTF Early Observations of Type Ia Supernovae. I. Properties of the 2018 Sample”. In: *ApJ* 886.2, 152, p. 152. DOI: 10.3847/1538-4357/ab4cf5.
- Yaron, O. et al. (July 2012). “WiSeREP—An Interactive Supernova Data Repository”. In: *PASP* 124.917, p. 668. DOI: 10.1086/666656.
- Yoon, S. -. et al. (Dec. 2010). “Type Ib/c Supernovae in Binary Systems. I. Evolution and Properties of the Progenitor Stars”. In: *ApJ* 725.1, pp. 940–954. DOI: 10.1088/0004-637X/725/1/940.
- Yuan, F. et al. (Sept. 2015). “OzDES multifibre spectroscopy for the Dark Energy Survey: first-year operation and results”. In: *MNRAS* 452.3, pp. 3047–3063. DOI: 10.1093/mnras/stv1507.

- Zackay, B. et al. (Oct. 2016). “Proper Image Subtraction - Optimal Transient Detection, Photometry, and Hypothesis Testing”. In: *ApJ* 830, 27, p. 27. DOI: 10.3847/0004-637X/830/1/27.
- Zhang, T. et al. (Nov. 2012). “Type II<sub>n</sub> Supernova SN 2010jl: Optical Observations for over 500 Days after Explosion”. In: *AJ* 144.5, 131, p. 131. DOI: 10.1088/0004-6256/144/5/131.
- Zhang, W. et al. (May 2008). “Fallback and Black Hole Production in Massive Stars”. In: *ApJ* 679.1, pp. 639–654. DOI: 10.1086/526404.
- Zhu, J.-P. et al. (Aug. 2024). “Bumpy Superluminous Supernovae Powered by a Magnetar–Star Binary Engine”. In: *ApJ* 970.2, L42, p. L42. DOI: 10.3847/2041-8213/ad63a8.
- Zwicky, F. (Dec. 1938). “On the Frequency of Supernovae.” In: *ApJ* 88, p. 529. DOI: 10.1086/144007.